

Institute of Geography
University of Fribourg

**EXTRACTING QUANTITATIVE
SUB-PIXEL HETEROGENEITY INFORMATION
FROM OPTICAL REMOTE SENSING DATA**

THESIS

submitted to the Faculty of Sciences
of the University of Fribourg in Switzerland
in accordance with the requirements for the degree of
Doctor rerum naturalis

by

Jean-Luc WIDLowski

from

Luxembourg

N°: 1358
Uniprint, Miséricorde, Fribourg
2001

Accepted by the Faculty of Sciences of the University of Fribourg in Switzerland, as recommended by Prof. Bernard Pinty and Dr. Michel Verstraete from the Space Applications Institute of the Joint Research Centre of the European Union in Ispra, Italy.

Fribourg, *20th* November 2001

The thesis supervisor:

The dean:

Prof. Martin Beniston

Prof. Alexander von Zelewsky

*Wisdom cannot be pass'd from one having it to another not having it,
Wisdom is of the soul, is not susceptible of proof, is its own proof,
Applies to all stages and objects and qualities and is content.*

Song of the open Road
Walt Whitman

Acknowledgments

I would first like to express my gratitude towards Alan Belward, head of the Global Vegetation Monitoring unit at the Institute for Environment and Sustainability of the EC Joint Research Centre. He welcomed me within his unit and provided the necessary freedom for scientific activities and excellent research conditions. At the same time I would also like to thank Martin Beniston, head of the Institute of Geography within the Department of Geosciences at the University of Fribourg in Switzerland, for his kindness in accepting me as a doctoral student, and offering to provide access to the Swiss Center for Scientific Computing.

This work would not have been possible without the dedicated support of both Bernard Pinty and Michel Verstraete. They were instrumental in setting up this research project and introducing me to the international scientific community. They shared with me their scientific skills, radiation transfer knowledge and many fruitful discussions. I am deeply grateful for their generosity and help.

I would also like to thank Anthony Davis, who spent his time with me discussing the ins and outs of multifractal formalism; Dave Diner, who funded my visit to the AGU Spring Meeting in Boston and the MISR Science Meeting in Passadena; Nadine Gobron, who shared both her radiation transfer model code and her scientific knowledge with me; and Yves Govaerts, who provided essential background information on the usage of his Monte Carlo ray-tracing model.

Furthermore I would like to thank the various STARS members: Gabriela Bucini, Dulce Lajas, Gianni Napoli, Fausto Roveda, Malcolm Taberner and Peter Vogt, as well as all my working colleagues at the GVM unit for many stimulating and interesting interactions.

I also want to express my appreciation for interacting with the following persons, who—in their own and varied ways—have helped for this research to come to a successful conclusion: Nicholas Doering, Marc Fuentes, Federico Gallopin, Nick Hibma, Constanze Leemhuis, Alberto Reggiori, Daniela Sebeledi, Carlotta Segre, Jean-Michel Terres and Kamila Zdenikova.

Finally, I would especially like to thank Daniela and Cathérine for their continuing support and motivation during the years that lead to this work.

Contents

| | |
|---|-----------|
| Table of Contents | i |
| Abstract | iv |
| Résumé | v |
| List of Acronyms | vi |
| | |
| 1 Outline of the Thesis | 1 |
| | |
| 2 Remote Sensing of the Biosphere | 3 |
| 2.1 Prerequisites for the extraction of quantitative information from remote sensing data | 3 |
| 2.2 Optical remote sensing of terrestrial surfaces | 4 |
| 2.2.1 Atmospheric signal transmission | 4 |
| 2.2.2 Target specific signal modulations | 6 |
| 2.2.3 Target variability and signal perturbations | 11 |
| 2.3 The role and importance of models | 12 |
| 2.4 Conclusion | 14 |
| | |
| 3 Radiation Transfer Modeling | 15 |
| 3.1 Overview of radiation transfer models | 15 |
| 3.2 The Raytran model of Govaerts, 1995 | 17 |
| 3.2.1 Description of the model | 18 |
| 3.2.2 Verification and application of the model | 20 |
| 3.3 The Semi-Discrete model of Gobron et al, 1997 | 22 |
| 3.3.1 Description of the model | 22 |
| 3.3.2 Verification and application of the model | 23 |
| 3.4 The radiative transfer model intercomparison exercise | 24 |
| 3.4.1 Evaluation strategy | 24 |
| 3.4.2 Overview of the RAMI results | 25 |
| 3.5 Conclusion | 30 |
| | |
| 4 Extracting Quantitative Information From Optical Remote Sensing | 31 |
| 4.1 The inversion of radiation transfer models | 31 |
| 4.1.1 Classical model inversion strategy | 32 |
| 4.1.2 Look-up-table based inversion schemes | 34 |
| 4.2 LUT-based inversion of the Raytran model | 35 |
| 4.2.1 Radiative discrimination of the pre-defined surface types | 36 |
| 4.2.2 New directions for LUT-based inversion methods | 39 |
| 4.3 Discussion | 41 |
| 4.4 Conclusion | 42 |

| | | |
|----------|---|-----------|
| 5 | The Plane-parallel RT Model Bias Over Heterogeneous Forest Scenes | 43 |
| 5.1 | Assessing the radiative separability of 1-D and 3-D surfaces | 43 |
| 5.1.1 | Raytran simulated reflectance anisotropy at multiple spatial scales | 45 |
| 5.1.2 | Defining the TOC height level across multiple spatial scales | 48 |
| 5.2 | The scale dependent separability of 1-D' and 3-D canopies | 50 |
| 5.2.1 | The radiative separability of 1-D' and 3-D canopies at multiple scales | 50 |
| 5.2.2 | The plane-parallel bias in the retrieval of LAI at multiple scales | 57 |
| 5.3 | Discussion | 59 |
| 5.4 | Conclusion | 62 |
| 6 | The Reflectance Anisotropy Shape | 63 |
| 6.1 | Characterization of the spectral reflectance anisotropy shape | 63 |
| 6.2 | The reflectance anisotropy shape of homogeneous canopies | 66 |
| 6.2.1 | The Minnaert function parameter of homogeneous leaf canopies | 66 |
| 6.2.2 | The Minnaert function parameter for the uncollided, single-collided | 68 |
| 6.2.3 | The relative contributions of ρ_{UC} , ρ_{SC} and ρ_{MC} | 70 |
| 6.2.4 | The effect of θ_0 on the Minnaert function parameter | 71 |
| 6.3 | Reflectance anisotropy as a surface heterogeneity indicator | 73 |
| 6.4 | Concluding remarks | 75 |
| 7 | Surface Reflectance and Structure: Combining Anisotropy Indicators | 79 |
| 7.1 | Surface Heterogeneity Descriptors | 79 |
| 7.1.1 | The Semivariogram | 80 |
| 7.1.2 | Fractals | 81 |
| 7.2 | Intermittency and non-stationarity of geophysical data | 82 |
| 7.2.1 | Structure-function analysis | 83 |
| 7.2.2 | Singularity analysis | 85 |
| 7.3 | Combining surface structure and reflectance information | 87 |
| 7.4 | Discussion | 88 |
| 7.5 | Conclusion | 90 |
| 8 | Summary and Outlook | 91 |
| | Bibliography | 95 |

Annexes:

| | | |
|----------|---|------------|
| A | Detection and Characterization of Boreal Coniferous Forests from Remote Sensing Data | 115 |
| A-1 | Introduction | 115 |
| A-2 | Strategy of the retrieval | 116 |
| A-2.1 | Forest canopy modelling | 117 |
| A-2.2 | Physics of the retrieval | 121 |
| A-2.3 | Mathematical approach | 123 |
| A-2.4 | Simulation tests of the inverse procedure | 125 |
| A-3 | Application to actual data | 126 |
| A-3.1 | Forest identification | 127 |
| A-3.2 | Forest characterization | 129 |
| A-4 | Conclusions | 132 |

| | |
|---|------------|
| B Radiation Transfer in Vegetation Canopies | 133 |
| B-1 The radiation transfer equation in vegetation canopies | 133 |
| B-2 The hot-spot formulation of Verstraete et al. 1990 | 134 |
| B-3 The distribution function of leaf normal orientations | 134 |
| B-4 The Ross function, $G(\Omega)$ | 136 |
| B-5 The leaf scattering transfer function, $f(\Omega^i \rightarrow \Omega, \Omega_L)$ | 136 |
| B-6 The area scattering transfer function, $\Gamma(z_k; \Omega^i \rightarrow \Omega)$ | 137 |
| C Uniqueness of Multiangular Measurements Part 1: An Indicator of Subpixel Surface Heterogeneity from MISR | 139 |
| C-1 Introduction | 139 |
| C-2 Interpretation of the anisotropy of surface leaving radiance fields | 140 |
| C-2.1 Surface anisotropy as a unique feature | 140 |
| C-2.2 Anisotropy pattern as an indicator of surface heterogeneity | 142 |
| C-2.3 Potential and limitation in the exposure of surface heterogeneity | 144 |
| C-3 Sun angle and background brightness effects | 148 |
| C-4 Application | 149 |
| C-5 Miscellaneous issues | 153 |
| C-6 Concluding remarks | 155 |
| C-7 Acknowledgements | 156 |
| D Characterization of surface heterogeneity detected at the MISR/TERRA sub-pixel scale | 157 |
| D-1 Introduction | 157 |
| D-2 Canopy height field characterization | 158 |
| D-3 Combining canopy height field and reflectance anisotropy descriptors | 159 |
| D-4 Conclusion | 160 |

Abstract

This work describes two approaches for the extraction of quantitative information on the degree of surface heterogeneity at the subpixel scale of optical remote sensing data.

The first approach is a look-up-table based inversion scheme, where the spectral reflectances of realistically modelled three-dimensional vegetation canopies are pre-computed for a variety of atmospheric optical depths, and subsequently compared against actual satellite observations under identical conditions of observation and illumination. An optimal solution is selected from amongst the set of predefined surface type candidates, using criteria such as temporal consistency and required accuracy, as defined by the difference between the simulated and measured reflectances. An exhaustive characterization of the surface heterogeneity at the subpixel scale can subsequently be derived from the imposed set of optical and structural surface properties. A series of multi-scale assessments concerning the radiative uniqueness of structurally heterogeneous surface types lead to the conjecture that structurally homogeneous surface representations will generally be capable of explaining the measured (angular and spectral) reflectance data, at least over some range of spatial resolutions.

The second approach is based on quantifying the ‘shape’ of the spectral reflectance field using the modified Minnaert function parameter, k in the parametric RPV model of Rahman et al. (1993a). Values of $k < 1$ refer to ‘bowl-shaped’ reflectance anisotropy patterns which may be indicative of optically thick 1-D leaf canopies, for example. Values of $k > 1$ refer to ‘bell-shaped’ anisotropy patterns that may occur for both, structurally homogeneous and heterogeneous vegetation canopies, if their dominant structures are dark, vertically oriented, sufficiently opaque and sparsely distributed over a relatively brighter background surface. Bell-shaped reflectance anisotropy patterns are most likely to occur in the red spectral band. They are spatial resolution dependent and vary with the degree of soil brightness. Variations of k as a function of the solar zenith angle were shown to characterize the preferred vertical orientation of the dominant structures in spatially homogeneous leaf canopies, *i.e.*, the leaf normal distribution. Finally it is shown that vegetation canopy structure may be characterized in the small scale limit by statistical measures such as non-stationarity ($\langle H_1 \rangle$) and intermittency ($\langle C_1 \rangle$) exponents, using an ensemble of canopy height transects of different orientations and origins. More importantly, however, surface types with a bell-shaped reflectance field (in the red) are documented to form clusters with illumination dependent sizes in $\langle H_1 \rangle$, $\langle C_1 \rangle$ space.

In essence, this thesis shows that information on the structure of vegetation canopies can be derived from satellite remote sensing data, provided such measurements are acquired as a function of observation angles. The recent availability of multiangular instruments (such as MISR) permitted to evaluate the feasibility of these approaches and the validity of the associated concepts. These results, in turn, will lead to improved land cover classifications and innovative designs for future Earth Observation instruments.

Keywords: BRDF, Heterogeneity, Spatial Resolution

Résumé

Ce travail présente le développement et l'utilisation de deux approches pour quantifier le degré d'hétérogénéité intra-pixel des surfaces terrestres à partir de données de télédétection spatiale.

La première approche utilise une technique d'inversion qui consiste à comparer les données mesurées par un satellite avec celles contenues dans une table de recherche pour les mêmes conditions géométriques de mesures. La table contient les valeurs modélisées de champs radiatifs émergeant du système couplé végétation-atmosphère dans le cas de plusieurs types d'atmosphère et de couverts végétaux. Les réflectances spectrales sont modélisées de manière réaliste puisque que le transfert radiatif dans les couverts végétaux est représenté selon les trois dimensions de l'espace. Parmi les milieux géophysiques possibles proposés dans la table, une solution probable est sélectionnée grâce à des critères de convergence, tels que la cohérence temporelle et un niveau d'incertitude, qui peut être défini par une valeur minimale de différence entre les réflectances modélisées et celles mesurées. Une caractérisation complète de l'hétérogénéité intra-pixel de surface peut être déduite à partir de critères imposés sur les propriétés de structure et optiques des surfaces. Une série d'études portant sur l'estimation de l'unicité de différents types d'hétérogénéité de structure de surface est conduite à plusieurs échelles spatiales et montre que la modélisation radiative de surfaces terrestres homogènes est généralement capable de représenter les mesures (spectrales et angulaires) de réflectance, au moins pour un éventail donné de résolution spatiale.

La seconde approche est basée sur l'étude de la 'forme' de la courbe de la réflectance en fonction des angles d'observation, qui représente les propriétés d'anisotropie radiatives. On utilise le paramètre k de la fonction modifiée de Minnaert (incluse dans le modèle paramétrique RPV développé par Rahman et al. 1993) pour quantifier le degré d'hétérogénéité intra-pixel des surfaces terrestres. Une valeur de $k < 1$ se réfère à une courbe en 'cratère' (les bords incurvés vers le haut) qui est indicative d'une représentation radiative 1-D des couverts végétaux. La valeur de $k > 1$ se réfère à la courbe en 'cloche' (les bords incurvés vers le bas) qui correspond soit à une structure homogène soit à une structure hétérogène d'un couvert végétal, à condition que ses objets présentent une structure érectophile, suffisamment sombres et opaques et avec une distribution clairesemée sur une surface relativement plus brillante. De telles conditions se produisent la plupart du temps dans la bande rouge du spectre solaire. Elles dépendent de la résolution spatiale et varient avec la brillance du sol sous-jacent. Dans un premier temps, une étude est menée sur les variations des valeurs de k en fonction de l'angle zénithal solaire pour caractériser l'orientation principale des feuilles dans les canopées homogènes, c'est-à-dire la distribution normale des feuilles. Dans un deuxième temps, on montre que la structure des couverts végétaux peut être caractérisée par des statistiques décrivant la non-stationnarité ($\langle H_1 \rangle$) et l'intermittance ($\langle C_1 \rangle$). Finalement, le plus important est la documentation de l'organisation des types de surfaces avec des propriétés d'anisotropie $k > 1$ dans le repère ($\langle H_1 \rangle, \langle C_1 \rangle$), pour la bande rouge du spectre solaire.

L'essentiel de ce manuscrit montre que l'information sur la structure des couverts végétaux peut être dérivée à partir de données multi-angulaires de télédétection spatiale. La disponibilité récente d'instruments multi-angulaires (tel que MISR) permet d'évaluer les performances de ces deux approches, et la validité des concepts qui leur sont associés. Ces résultats vont à la fois permettre d'améliorer les cartes d'occupation du sol et surtout aider à l'élaboration innovatrice de futurs instruments d'observation de la Terre.

Mot-clés: BRDF, Hétérogénéité, Résolution Spatiale

List of Acronyms

| | |
|--------|---|
| ATSR | Along-Track Scanning Radiometer |
| AVHRR | Advanced Very High Resolution Radiometer |
| BRDF | Bidirectional Reflectance Distribution Function |
| BRF | Bidirectional Reflectance Factor |
| CSG | Constructive Solid Geometry |
| EGO | European GOloniometer |
| FAPAR | Fraction of Absorbed Photosynthetically Active Radiation |
| FMERS | Forest Monitoring in Europe with Remote Sensing |
| FOV | Field Of View |
| GO | Geometric-Optical |
| HRD | Horizontal Ray Distance |
| IPA | Independent Pixel Approximation |
| JRC | Joint Research Centre |
| LAD | Leaf Area Density |
| LAI | Leaf Area Index |
| LND | Leaf Normal Distribution |
| LUT | Look-Up-Table |
| MC | Monte Carlo |
| MERIS | MEDium Resolution Imaging Spectrometer |
| MISR | MultiangLe Imaging Spectro-Radiometer |
| MODIS | MODERate-resolution Imaging Spectrometer |
| MPI | Message Passing Interface |
| NIR | Near InfraRed |
| NOAA | National Oceanic and Atmospheric Administration |
| RAMI | RAdiative transfer Model Intercomparison |
| RT | Radiation Transfer |
| 6S | Second Simulation of the Satellite Signal in the Solar Spectrum |
| PDF | Probability Distribution Function |
| PELCOM | Pan-European Land use and land COVer Monitoring |
| POLDER | POLarization and Directionality of the Earth's Reflectances |
| PP | Plane-Parallel |
| RMS | Root-Mean-Square |
| RPV | Rahman-Pinty-Verstraete |
| TOA | Top-Of-Atmosphere |
| TOC | Top-Of-Canopy |

Chapter 1

Outline of the Thesis

Anthropogenic activities are suspected to be responsible of many environmental degradation and climatic change processes. Any attempt at quantifying the nature, extend and dynamics of these processes, or, enforcing, supervising and controlling international regulations for their reversal, must rely on both an accurate understanding of the mechanisms involved and a set of tools to monitor continuously and repetitively the Earth's surface. This monitoring activity is necessary to evaluate the nature, location, duration and intensity of the problem, as well as to assess the effectiveness of any measure that is taken to address this issue. Clearly the data acquisition must occur at spatial scales and resolutions appropriate for the task at hand. In many cases satellite remote sensing constitutes the sole cost-effective source of data suitable for the generation of the required information, assuming the proper interpretation models do exist. Of particular interest in this context are the exchanges of water, energy and carbon at the interface between the biosphere and atmosphere. Physically based radiation transfer models can be applied to the extraction of quantitative information on the state of the environment from optical remote sensing data. Such information, in turn, may be used to specify initial and boundary conditions in general circulation, global climate and soil-vegetation-atmosphere transfer models, amongst others. There is an increasing demand for high resolution information on vegetation structure and composition, whether this is to satisfy national forest inventory requirements, landscape management, habitat studies, carbon and nutrient cycling, or biogeochemical modelling, *e.g.*, Asner et al. (1998) or Tomppo (2000). It is commonly accepted that vegetation structure and its intrinsic dynamics can have a profound effect on ecosystem productivity, a key variable in understanding the vegetation response to climate change (Shugart 2000).

Until recently, the characterization of surface properties from optical remote sensing data was often based on simple linear combinations of radiometric values (spectral indices), (un)supervised classification techniques of single, multi-temporal and/or multi-sensor data, or metrics derived thereof, as well as spectral unmixing, the use of expert knowledge and a wide variety of ancillary validation data. However, with the recent availability of several quasi-simultaneous multispectral and multiangular instruments like the Along-Track Scanning Radiometer-2 (ATSR-2), the Polarization and Directionality of the Earth's Reflectances (POLDER) and the Multiangle Imaging Spectro-Radiometer (MISR), the accuracy and reliability of commonly retrieved information can be substantially improved. These instruments further offer new and unique opportunities to quantify the spatial structure at the level of the individual pixel. This is the major aim of this research, namely, to extract reliable quantitative information on the subpixel-heterogeneity of the environment from optical remote sensing data.

This thesis is organised in three main parts. The first one is dedicated to the description of the formal constraints on using Earth observation data for the quantitative extraction of terres-

trial surface properties. Chapter 2 introduces the rationale behind the usage of physically-based radiation transfer models in the analysis of optical remote sensing data. Chapter 3 presents two such state of the art radiation transfer models in detail, and documents their performances when compared to several other models during the RADIATION transfer Model Intercomparison (RAMI) exercise. The second part of the thesis is dedicated to the retrieval of reliable quantitative canopy information from optical remote sensing measurements. Chapter 4 presents the various issues that are related to classical and look-up-table (LUT) based inversion methods, with specific emphasis on the discrimination of the predefined, structurally heterogeneous surface type solutions in the latter approach. Annex A applies a LUT-based inversion method to the identification and characterization of boreal conifer forests in northern Europe. Chapter 5 investigates the ranges of applicability of such a 3-D inversion scheme, by documenting the scale dependent radiative separability of structurally homogeneous and heterogeneous canopy representations. Finally, the third part of this thesis is dedicated to the establishment of a link between the information contained within the angular ‘shape’ of the spectral reflectance field and the structural aspects of the vegetation canopies that gave rise to these radiative signatures. Chapter 6 introduces the RPV model parameter k as a means to quantify one important aspect of the reflectance anisotropy shape, and documents how this parameter varies with the structural, optical and illumination conditions for homogeneous leaf canopies. Annex C provides a similar description for structurally heterogeneous vegetation canopies and establishes a qualitative link between the values of the k parameter and the degree of surface heterogeneity within the observed pixel. Finally, in chapter 7 and annex D a quantitative characterization of the vegetation structure is proposed, and subsequently related to the measured values of the reflectance anisotropy indicator k in the red spectral domain.

Overall, this work documents the feasibility of extracting quantitative information on the structural organisation of vegetation canopies at the scale of individual pixels, using multiangular satellite remote sensing data. The findings are suited for improving existing land cover classification approaches, and for providing new directions in the design of future Earth Observation strategies.

Chapter 2

Remote Sensing of the Biosphere

This chapter provides an overview of the various issues relating to the accurate and reliable retrieval of information about the state of the terrestrial surface from remote sensing observations. Section 2.1 introduces the formal constraints on using Earth observation data for the quantitative extraction of terrestrial surface parameters, section 2.2 describes the radiative characteristics of the various signal contributing elements within the atmosphere-biosphere radiative system, and section 2.3 introduces the rationale behind the usage of physically-based radiation transfer models in the analysis of optical remote sensing data.

2.1 Prerequisites for the extraction of quantitative information from remote sensing data

Observation of land surfaces from space began formally with the launch of LANDSAT-1 in 1972¹. A large variety of satellite instruments with different scientific objectives, spatial, spectral and temporal resolutions have been operated since. In order, for calibrated, remotely sensed measurements to qualify as a basis for the extraction of accurate and reliable information about the state of a specific terrestrial target, three general conditions have to be satisfied (Verstraete and Pinty 1999) :

1. a *signal* must have been transmitted from the target to the detector.
2. the measurable characteristics of this signal *must depend on the properties of the target* of interest.
3. the signal *must not be perturbed* by other processes to such an extent that the information carried about the target of interest is irretrievable.

To detect the contribution of the target property within the measured signal, an optimal observation strategy needs to be elaborated. This can be best achieved using validated, quantitative radiation transfer (RT) models, capable of simulating all relevant processes in the various intervening media between the original source of radiation and the detector optics of a space-borne radiometer. Apart from identifying optimal observation and illumination geometries for specific wavelengths and exhaustive lists of naturally occurring and explicitly described geophysical scenarios, such models actually allow to designate those variables that are directly

¹Although LANDSAT-1, originally called Earth Resource Technology Satellite (ERTS), was the first satellite designed to provide near global coverage at relatively high resolution and on a regular and predictable basis, it was the Television InfraRed Observation Satellite (TIROS-1)—launched on 1st April 1960—that actually delivered the first series of cloud cover images of the Earth.

responsible and therefor also retrievable from remote sensing observations. Given the existence of efficient inversion procedures, the latter information thus allows to envisage the necessity of additional sources of information (models and/or auxiliary data) to relate one or more of the so retrievable radiation transfer state variables to the target properties of interest.

2.2 Optical remote sensing of terrestrial surfaces

The sun is the only significant source of radiation for passive remote sensing in the visible (0.3 – 0.7 μm) and infrared (0.7 – 3.0 μm) spectral regions. Nevertheless, prior to asserting the appropriateness of optical remote sensing measurements to partake in the identification and characterization process of terrestrial surfaces, evidence for the validity of the three statements in section 2.1 is required. Initially, this involves the determination and understanding of the various processes within the atmosphere-biosphere radiative system that are capable of altering the statistical properties of the incident electromagnetic radiation. Ultimately, however, it will be the combinations and co-occurrences of these interactions that determine, in conjunction with the capabilities of the space-borne instrument and the conditions of observation, whether a quantitative assessment of the target property of interest from remotely sensed data-strings is indeed a meaningful proposition.

2.2.1 Atmospheric signal transmission

A terrestrial target may only be observable by a space-borne sensor if it scatters radiation in the appropriate wavelength(s) and direction(s) to the observing instrument. In the absence of emission this requires it 1) to be well irradiated by some external light source, and 2) to deviate a sufficient fraction of this incident radiation directly into the field-of-view (FOV) of the space-borne radiometer. Irrespective of these requirements, however, it is the opacity of the overlying atmosphere, at the time of measurement, that determines whether or not a surface reflected energy stream actually illuminates the detector optics of a space-borne instrument. By the same token, it is the transmission of solar radiation through the atmosphere that constitutes, either directly or through varying degrees of scattering interactions, the sole source of incident radiation at the Earth's surface. The reflection of this incident radiation, on the other hand, is dependent on a variety of factors, like the spectral and geometrical properties of the terrestrial target, the conditions of observation and illumination, and ultimately also the space sensor characteristics, which will be discussed in more detail in subsections 2.2.2 and 2.2.3.

The total flux density of incoming solar radiation at the top of the atmosphere (TOA), which is also known as the total solar irradiance at the TOA, varies in accordance with the annual change in the Earth-Sun distance, the 11 year solar sunspot cycle and the 30 day rotation period of the sun (Froehlich and Lean 1998). The spectral distribution of this extra-atmospheric solar irradiance is largely in agreement with that predicted by Planck's law for a blackbody of ~ 5900 K, that is, half of its energy lies within the visible part of the solar spectrum. The selective opacity of the atmosphere, however, allows only a fraction of this incident radiation to pass through it and reach the Earth's surface. Absorption by various atmospheric constituents, most notably water vapor, CO_2 and O_3 , result in substantial losses of energy at some wavelengths, whilst at others the atmosphere remains—with the exception of scattering processes—virtually transparent to the incoming radiation (see Figure 2.1). These latter spectral intervals—which include most of the visible and near-infrared—define the wavelength regimes within which the Earth's surface may effectively be observed from space.

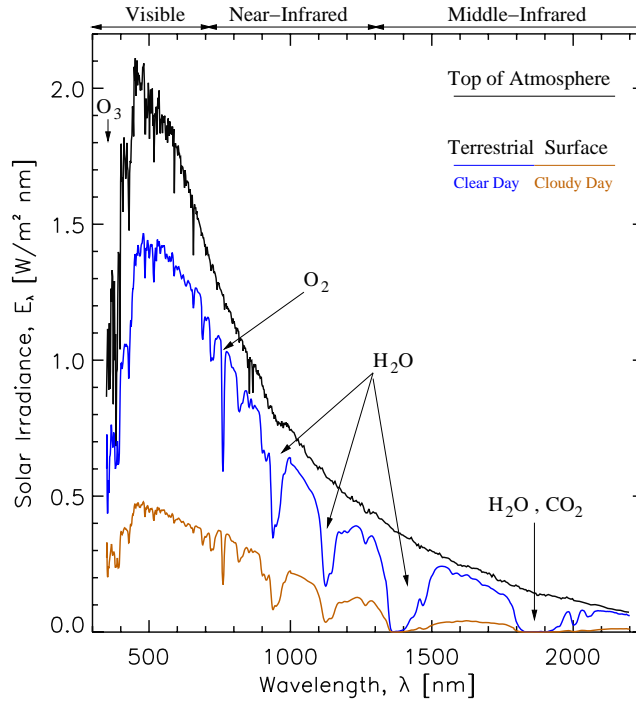


Figure 2.1: The visible to middle-infrared part of the standard solar irradiance spectrum of Wehrli (1985) at the top of the atmosphere (black), together with solar irradiance measurements at the terrestrial surface for clear (blue) and cloudy (brown) days recorded at similar solar zenith angles (courtesy of Analytical Spectral Devices Inc. – <http://www.asdi.com>). Some major atmospheric absorption bands are indicated.

Under clear sky conditions, it is primarily the scattering of solar radiation by gaseous, liquid and solid atmospheric constituents that affects the intensity and polarization of radiation impinging upon the Earth’s surface. The amount of radiation scattered whilst traversing the atmosphere depends largely on its wavelength, the distance traveled within the media and the concentration and size distribution of the atmospheric gases, aerosols and cloud droplets along its path. Three major scattering regimes are of importance here: Rayleigh scattering, Mie scattering, and Non-selective scattering:

- *Rayleigh scattering* occurs when particles are very small compared to the wavelength of the radiation. The effect of Rayleigh scattering is inversely proportional to the fourth power of the wavelength, proportional to the density of the air, and results in equipartitioned forward and backscattering components.
- *Mie scattering* is defined for spherical scatterers of comparable dimensions to the wavelength of the colliding radiation. The effect of Mie scattering is to redistribute the exiting ray paths preferentially along the forward direction.
- *Non-selective scattering* occurs when the particles are much larger than the wavelength of the colliding radiation. Nonselective scattering affects all wavelengths about equally.

Atmospheric attenuation is typically of the order of 50% at 450 μm and 20% at 850 μm (Tanré et al. 1990), however, cloud cover can significantly reduce the passage of light, effectively absorbing and redirecting large fractions of it (compare with Figure 2.1). Hence the directionality of the incident radiation at the Earth’s surface is commonly decomposed into a direct and a diffuse component.

2.2.2 Target specific signal modulations

For remote sensing observations to yield quantifiable information about the state of a terrestrial target, the latter must lie at the origin of some measurable characteristics in the energy flux collected by one or more detectors on board of an Earth-orbiting satellite. More specifically, the target must possess at least some properties that are capable of modulating the exiting radiation in a dominant and preferably unique manner with respect to the energy fields emanating from other nearby objects in the direction(s) and wavelength(s) of observation. In the visible and near-infrared (NIR) regions of the solar spectrum three different types of target properties may give rise to such characteristic behavior: spectral, directional and polarizational signatures.

Spectral properties of some terrestrial surfaces

Laboratory and field measured reflectance spectra², in general, relate to bi-conical reflectances at successive wavelengths.

- Typical reflectance spectra of soils exhibit an almost monotonical increase in the visible and NIR with two major water absorption bands showing around 1.4 μm , 1.9 and 2.7 μm (see Figure 2.2). Moisture content is one of the main factors affecting the overall reflectance level of bare soils although the chemical and physical properties of their components, their texture, surface roughness as well as organic matter and iron-oxide content also play a role (*e.g.*, Hunt and Salisbury 1970, Stoner and Baumgardner 1981). For any specific wavelength, in general, wetter soils appear darker, whereas organic matter, iron-oxide content and small particle sizes tend to increase the reflectance. The latter, however, is not so straightforward since in the field it is the aggregate size (or roughness)—which may change over a small time frame due to tillage, soil erosion, eolian accumulation or physical crust formation—that is important in altering the soil spectra (*e.g.*, Cierniewski 1987, Jackson et al. 1990).
- Although the spectrally integrated value may vary, the general shape of the reflectance spectra for green leaves is similar for all species (Gates et al. 1965). Foliar absorption dominates the visible part of the solar spectrum whereas strong reflection and transmission values characterize the NIR. Living leaves reflect less than 10% in the visible due to the fact that most of the incident radiation interacts with the internal leaf components (and structures) where it is strongly absorbed by chlorophyll and other pigments, especially in the blue and red wavelengths (Knipling 1970). Approximately half of the total reflectance in the visible originates from the *surface* of the leaf although this is dependent on the actual leaf surface characteristics and the angle of incidence (Gates et al. 1965). Around 700 nm lies a sharp increase in the leaf reflectance and transmission values, that remain almost constant thereafter until about 1100 nm (see Figure 2.2). This reflectance and transmittance plateau ($\sim 50\%$) originates from multiple reflections within the internal leaf structure caused by different refractive indices of the cell walls and intercellular cavities. Only 5% of the incident radiation is absorbed in the NIR primarily by H_2O , cellulose and other carbon based compounds (Gaussman 1977). Leaf maturity tends to increase the visible reflectance whereas that of the NIR is reduced (Guyot 1989). Various other kinds of stresses, like the availability of nutrients or the salinity level, may also affect the reflectance properties of leaves. In the middle infrared water content dominates the leaf

²Reflectance [dimensionless] is defined as the ratio of some specified portion of the reflected flux to the incident flux. More precisely, the reflectance must be qualified by two adjectives ('hemispherical', 'conical' or 'directional') to indicate how the incident and collected fluxes are distributed, *i.e.*, over the entire hemisphere, a finite solid angle less than 2π steradian, or else confined to essentially one direction (Judd 1967 and Nicodemus et al. 1977).

absorption (1.4, 1.9 and 2.7 μm).

- The reflectance spectrum of snow depends on the intrinsic properties of the snow itself, that is the geometry of its grains, the liquid water inclusions as well as the solid and soluble impurities. In general, snow reflectance decreases with age, impurities, grain size and melting conditions at all wavelengths (Nolin and Liang 2000). The reflectance of water is of the order of 5% in the visible and slightly less in the NIR, continuously decreasing thereafter until absorption is essentially complete. Shallow or turbid waters, however, are altered by the spectral properties of their underlying or suspended materials.

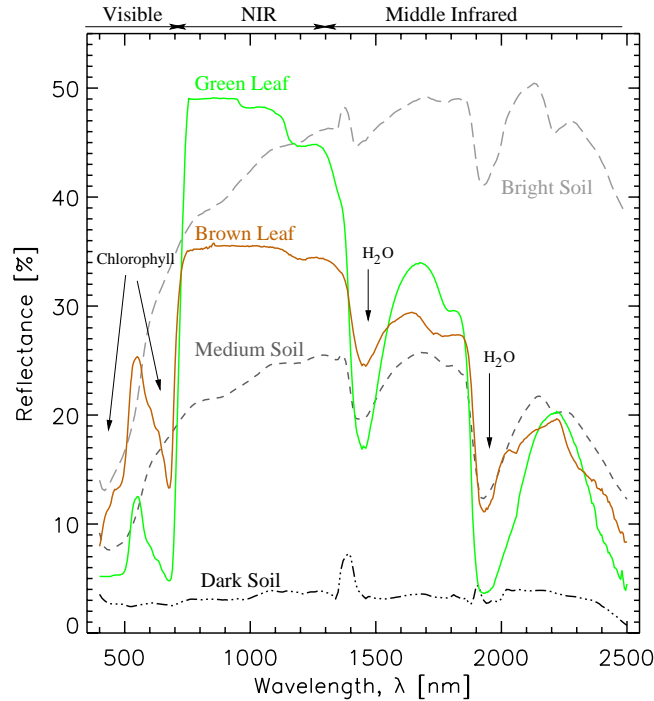


Figure 2.2: The reflectance spectra of bright (light grey), medium (dark grey) and dark (black) soils (Price 1995), together with that of live (green) and dry (brown) leaves in the visible and infrared (generated with PROSPECT, Jacquemoud and Baret 1990). Some major absorption bands are indicated.

Apart from wavelength dependent reflectance variations the bi-conical or bi-directional reflectance properties of terrestrial surfaces, at specific wavelengths and illumination and viewing conditions, may also provide a means of target characterization.

Reflectance anisotropy of terrestrial surfaces

Surfaces that appear equally bright³ from all directions are known as *Lambertian* reflectors at the wavelength(s) of observation. With the exception of some artificial materials like *Spectralon*[®], however, natural surfaces in general do not adhere to this behavior. In fact even Spectralon is not perfectly Lambertian for different spectral conditions, *e.g.*, Flasse et al. (1993). Soils (*e.g.*, Coulson et al. 1965, Coulson 1966), leaves (Breece and Holmes 1971, Brakke et al. 1989, Walter-Shea 1989) and snow (Dirmhirn and Eaton 1975) have all been shown to scatter light

³The concept of brightness relates to radiance, L [$\text{W m}^{-2} \text{sr}^{-1}$], which is the radiant flux Φ [W] per unit solid angle ω [sr], incident or leaving an element of surface A [m^2] in a given direction (making a polar angle θ with the surface normal), per unit projected area in that direction: $L = d\Phi / (dA \cos\theta d\omega) = dE / (\cos\theta d\omega)$, where E [W m^{-2}] is the irradiance (see Nicodemus et al. 1977).

anisotropically, that is, for a given illumination angle and wavelength, the amount of reflected radiance is not equal in all directions.

In order to ‘geometrically’ characterize the anisotropy of the surface leaving reflectance field, Nicodemus et al. (1977) formalized a nomenclature based on the spectral bidirectional reflectance distribution function (BRDF), γ_r [sr^{-1}], which, for any given point on a surface element, relates the incident (i) irradiance $dE_i(\theta_i, \phi_i)$ [W m^{-2}] to the reflected (r) radiance in the outgoing direction $dL_r(\theta_i, \phi_i; \theta_r, \phi_r)$ [$\text{W m}^{-2} \text{sr}^{-1}$] for any given pair of directions:

$$\gamma_r(\theta_i, \phi_i; \theta_r, \phi_r) = \frac{dL_r(\theta_i, \phi_i; \theta_r, \phi_r; E_i)}{dE_i(\theta_i, \phi_i)} = \frac{dL_r(\theta_i, \phi_i; \theta_r, \phi_r; E_i)}{L_i(\theta_i, \phi_i) \cos \theta_i d\omega_i} \quad [\text{sr}^{-1}] \quad (2.1)$$

where $d\omega$ is an infinitesimal element of solid angle, θ and ϕ are the zenith and azimuth angles, respectively, and L_i stands for the incident radiance (see Figure 2.3 for a definition of the geometry of the system). For any tangible source of light or sensor, however, the solid angles (of incidence ω_i and reflection ω_r) are not infinitesimal so that the radiant flux $d\Phi$ per surface element dA is the integral of the various directional radiances $L(\theta, \phi)$ within the respective solid angle element: $d\Phi/dA = \int_{\omega} L(\theta, \phi) \cos \theta d\omega$. Thus, given that the reflectance factor ρ [dimensionless] of a planar surface, can be defined as the radiant flux density ($d\Phi_r/dA$) reflected into a finite solid angle (ω_r) divided by the radiant flux density reflected by an ideal perfectly diffusing⁴ reference target ($d\Phi_{r:pd}/dA$) into the same finite solid angle under identical conditions of illumination:

$$\frac{d\Phi_r}{d\Phi_{r:pd}} = \frac{\int_{\omega_r} \int_{\omega_i} \gamma_r(\theta_i, \phi_i; \theta_r, \phi_r) L_i(\theta_i, \phi_i) \cos \theta_i d\omega_i \cos \theta_r d\omega_r}{\frac{1}{\pi} \int_{\omega_r} \int_{\omega_i} L_i(\theta_i, \phi_i) \cos \theta_i d\omega_i \cos \theta_r d\omega_r}$$

If L_i is isotropic within the full solid angle of incidence ω_i , the general expression for the biconical reflectance factor can be written as (Nicodemus et al. 1977):

$$\rho_{(\omega_i; \omega_r)} = \frac{\int_{\omega_r} \int_{\omega_i} \gamma_r(\theta_i, \phi_i; \theta_r, \phi_r) \cos \theta_i d\omega_i \cos \theta_r d\omega_r}{\frac{1}{\pi} \int_{\omega_r} \int_{\omega_i} \cos \theta_i d\omega_i \cos \theta_r d\omega_r}$$

which for an infinitesimally small field of view yields the bidirectional reflectance factor (BRF):

$$\rho_{(\theta_i, \phi_i; \theta_r, \phi_r)} = \pi \gamma_r(\theta_i, \phi_i; \theta_r, \phi_r) \quad [\text{dimensionless}] \quad (2.2)$$

Strictly speaking the above equations are only valid for planar surfaces of uniform reflectance properties. If the latter characteristics, however, are changing, the BRDF becomes a function of spatial position (x, y), which, in the case of non-planar (continuous) surfaces, must also include the height (z) as a dependent variable. Earth observing sensors, however, possess finite FOVs, such that—in accordance with the above definition of ρ —any BRF measurements have to be interpreted as if the gathered fluxes were reflected from some reference surface ΔA , corresponding to the nominal footprint area of the sensor, that is located at height level z . Increasing the vertical position of ΔA implies that the number and origin of the photons that pass through it, and thus contribute to the perceived (reflected) flux that functions as a descriptor of the target properties below, are also changing. In the case of a planar ground surface, the reasons for

⁴A perfectly diffusing surface—also known as white Lambertian—is one that isotropically reflects all incident radiation, that is $\gamma_{r:pd} = 1/\pi$ and from Equation 2.1 it follows that its reflected radiance $L_{r:pd} = E_i/\pi$ is a constant.

this are simply the reduced (increased) flux contributions of areas, that lie within (outside) the downward projected reference surface area ΔA as its height level z is being increased. Whether the differences in reflected fluxes from different height levels (z_0, z_H) are actually noticeable, depends on 1) the dimensions of ΔA , 2) the height levels (z_0, z_H), 3) the structural heterogeneity of the target, 4) the spatial variability of the reflectance properties of the target, and 5) the topography of the ground surface and its positioning with respect to the illumination direction. In general, BRDF measurements should always be quoted in terms of the height level z of the reference surface they refer to, *i.e.*, $\rho(z; \theta_i, \phi_i; \theta_r, \phi_r)$.

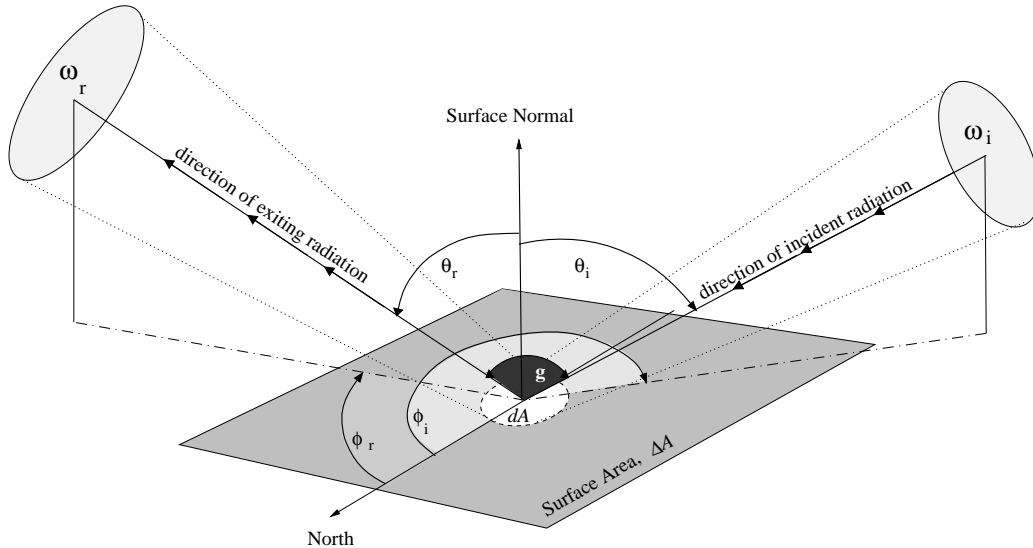


Figure 2.3: Viewing and illumination geometry for an infinitesimal surface element dA : The zenith angle of the incident (θ_i) and reflected (θ_r) radiation is defined with respect to the local vertical – which in the case of a horizontal plane coincides with the surface normal. The azimuth angle of the incident (ϕ_i) and reflected (ϕ_r) radiation is defined (in a clockwise manner) with respect to the North pointing surface tangent. The solid angle of the incident and reflected radiation are denoted by ω_i and ω_r respectively. The phase angle g is the angle defined by the incident and reflected radiation directions. The *principal plane* is the one containing both the local vertical and the direction vector of the incoming solar radiation. For any measurement in the principal plane, the absolute value of the relative azimuth angle $|\phi|$ between the view and illumination direction is either zero or π radians. The complementary *orthogonal* or *cross plane* is perpendicular to the principal plane, such that $|\phi|$ is either $\frac{\pi}{2}$ or $\frac{3\pi}{2}$ radians. If $\theta_0 = 0^\circ$ neither planes are defined.

In the context of terrestrial surface characterization from space, one aims at retrieving directional reflectance properties with respect to the sensor's nominal footprint area ΔA , located at the Top-Of-Canopy (TOC) height level z^{TOC} . Given that the geophysical medium representing the terrestrial surface target, is actually an agglomeration of separate objects of finite sizes (*i.e.* discontinuous for any given level of z), the contribution towards the overall surface reflectance at z^{TOC} by the BRDF of some scatterer that lies in the line of sight of the observer, will also depend on the direct and diffuse illumination components (and their incident angles with respect to the local normal) at that location. The natural three-dimensionality of terrestrial soils and vegetation covers thus implies that 1) the incident radiance L_i (in absence of any dominant multiple scattering and diffuse illumination component) will in general not be uniformly distributed across all the scatterers within the footprint area of a remote sensor, and 2) the non-zero size of this FOV makes the retrieved reflectance factors at height z^{TOC} the result of the *ensemble* of all underlying surface elements (with their individual BRDFs, local normals and illumination and reflection geometries) that are capable of sufficiently contributing towards the exiting radiation (through the reference surface ΔA) in the direction of observation. Hence, it is the

surface structure, or more specifically the number, size, shape, position and orientation of its various building blocks, that produce the illumination and viewing direction dependent patterns of ‘mutual shading’, which, in conjunction with the spectral and directional reflectance properties of the ‘visible’ objects, are responsible for the anisotropy in the exiting radiation field at the top of canopy (TOC). Any increase of the reference height level of ΔA above z^{TOC} will result in additional atmospheric and terrestrial contributions towards the gathered BRF measurement.

Several laboratory and field measurements of canopy reflectance anisotropies have been performed (*e.g.*, Kriebel 1978, Kimes et al. 1986, Deering 1989 and Sandmeier et al. 1998). In general, both the angular shape and the overall intensity of the exiting radiation field at the TOC are controlled by factors that operate at different scales within the vegetation canopy: At the *leaf* level, the optical properties of the various individual canopy elements, *e.g.* the leaves, stems and substratum particles, represent the building blocks from which the illumination dependent surface reflectance field is constituted. Exactly how (the magnitudes and angular dependencies of) these elementary BRDFs are combined at the level of the *tree crown*, however, depends not only on the position of the sun, but also on the amount of foliage surface, its orientation and spatial distribution within the crown⁵. Obviously the geometric shape of the scatterers and the amount of woody material within the crown volume and below may also have an impact (Goel 1989, Nilson and Peterson 1991). At the level of the *forest* (canopy) it is the spatial distribution of the tree crowns, their geometric shapes and optical properties, as well as the topography, the fraction of the shaded and visible ground cover, and the optical and geometrical properties of its constituents, that determine the overall intensity and anisotropy of the canopy reflectance field.

Of particular interest here is the so called *hot spot effect*, a sudden rise in the BRF values due to vanishing shadow fractions as the directions of illumination and observation converge. This retro-reflection peak occurs whenever mutual-shading is present within the geophysical medium under observation. Its angular width and intensity are determined by the visible fractions and reflectivity differences, respectively, of the shaded and illuminated scatterers within the FOV of the observer. Whereas the intensity of the hot spot may be affected by the presence of multiple scattering and diffuse light components, its angular width is a direct consequence of the composition, density and geometric structure of the reflective medium (within the footprint area of the remote sensor) and thus presents an intrinsic characteristic of the imaged terrestrial surface at the time of observation (Hapke 1981, Gerstl 1988, Verstraete et al. 1990 and Hapke et al. 1996). However, since mutual-shading can occur at a variety of spatial scales (*i.e.*, individual scatterers, agglomerations of scatterers, topography) satellite measured hot spot effects may actually be the result of several nested contributions of increasing angular width. Thus, for bare soils and leaf canopies (grasses and dense crops) it is the shapes, sizes and gaps in between the elementary scatterers that control the angular width of the hot spot effect. In forest canopies, or at even larger scales these contributions may, however, be dwarfed by the corresponding structural properties of the tree crowns and the topographic shadowing of hills and other landforms (Meerkoetter 1989, Qin and Xiang 1994, Goel et al. 1997).

Complementary to directional reflectance measurements the degree of linear polarization of solar radiation may also be used as a means to characterize specific properties of a terrestrial target. However, due to atmospherically induced polarization of the solar radiation in the optical domain, space-borne measurements of such properties have never become widely exploited, and will not feature any further within the remainder of this work. Nevertheless it is considered

⁵The latter quantities are commonly expressed in terms of the Leaf Area Index LAI [m^2/m^2], the Leaf Normal Distribution LND, and the Leaf Area Density LAD [m^{-1}], respectively (compare with Annex B).

appropriate to provide a short description of some of the scientific activities in this field.

Polarization properties of some terrestrial surfaces

The degree of linear polarization is computed as the ratio of the difference and the sum of the polarization in two orthogonal directions, that are perpendicular to the direction of propagation of the electromagnetic wave (Coulson 1966). Polarization data for soils, vegetation and other surface types have been acquired for multiple illumination and observation geometries:

- Loamy soils and darker substrates generally polarize light to a greater degree than very bright surfaces such as desert sands (Coulson et al. 1965). Coulson (1966) and Woessner and Hapke (1978) concluded that the phase angle g is the primary geometric variable controlling the degree of polarization of soils. There is a general decrease in polarization from 0.4 – 1.0 μm whereas the polarization increases with increasing soil moisture content (Genda and Okayama 1978).
- The relationship between the light-polarizing and biophysical properties of foliage and plant canopies have been amply documented (*e.g.*, Ross 1981, Curran 1981, Egan 1985, and Vanderbilt et al. 1991). Coulson et al. (1965) concluded that the polarization of light scattered from leaves is primarily due to Fresnel reflection from specularly oriented surfaces, hence its intensity is mainly controlled by the phase angle g . Polarization measurements of vegetation canopies, in general, may contain information about the physiological state of the leaf surface with the degree of polarization in the visible varying from 10% in the red to 50% in the blue (Grant et al. 1987).
- Light reflected from both snow and water surfaces is also well known to be partly polarized (horizontally) with the degree of polarization being maximal at large zenith angles.

Both laboratory and field measurements of the spectral, directional and polarizing properties, of individual surface elements and their agglomerations, have demonstrated, that—in absence of any atmospheric effects—it is feasible to differentiate (and even characterize) the various constituents of terrestrial surfaces, whether they are vegetated or not. What remains to be described is how these property-specific signal modulations translate, through the perturbing effects of the overlying atmosphere, into the measurements of the observing instrument.

2.2.3 Target variability and signal perturbations

The upward traveling energy flux, collected by a space-borne radiometer viewing the Earth, carries information on myriads of photon interactions with different types of geophysical media. Consequently, any single measurement collected in the optical domain at the TOA (\mathcal{M}_{TOA}), may be attributed to the radiative characteristics of both the atmosphere A, and the underlying terrestrial surface S, under the given conditions of measurement M:

$$\mathcal{M}_{TOA} = \mathcal{M}_{TOA}(A; S | M) \quad (2.3)$$

where the conditions of measurement, M include the wavelength (λ), the time of data acquisition (t), the spatial coordinates of the terrestrial target (x, y, z), the geometric conditions of illumination (θ_o, ϕ_o) and observation (θ_v, ϕ_v), as well as the polarization (p):

$$M = M(\lambda; t; x, y, z; \theta_o, \phi_o; \theta_v, \phi_v; p) \quad (2.4)$$

The radiative characteristics of the atmosphere are dependent on the various factors listed in subsection 2.2.1. More specifically, a horizontally homogeneous atmospheric layer of depth Δz , can be characterized by its optical thickness (τ), its single scattering albedo (ω_o), and the scattering phase function ($P_{(g)}$) with respect to the passing radiation⁶:

$$A_{\Delta z} = A_{\Delta z}(\tau; \omega_o; P_{(g)})$$

Similarly, the radiative characteristics of the terrestrial surface are due to the modulation of the incident radiation by the optical and geometric properties of the vegetation and other ground cover types, as well as their fractional coverages and spatial arrangements within the topography of the terrain. The various contributing factors to bidirectional reflectance properties of vegetation canopies have already been described in section 2.2.2.

The radiative regime of the atmosphere and the biosphere are strongly coupled through non-linear processes such as multiple scattering at the common interface between these geophysical media. Obviously the intensity and directionality of the downward traveling radiation at the TOC is not only dependent on the radiative characteristics of the atmosphere (A), but also on the magnitude of the incident solar radiation at the TOA and the upward traveling radiation at the TOC. Conversely, the latter depends both on the radiative characteristics of the surface layer (S) and the intensity and directionality of the downward traveling radiation at the TOC. Ultimately, however, it will be the conditions of measurement (M) that determine to what degree the various surface and atmosphere induced energy modulations, contained within the upward traveling radiation field at the TOA, will actually translate into the measured signal characteristics at the space-borne sensor. For example, it has been shown that some plant elements exhibit polarization sensitivity at the TOC. The latter characteristics will, however, almost always be masked by atmospherically induced polarization effects (largely as a result of Rayleigh scattering). Hence the prospects of actually deriving useful information (about the state of vegetation) from such characteristics of the electromagnetic radiation field at the TOA are rather reduced (Deschamps et al. 1994). This suggests that both the conditions of measurements and the characteristics of the space-borne detector should be selected using *a priori* considerations of all relevant aspects of the system under study such that the *richness* and *quality* of the gathered data is maximized with respect to the target properties of interest (Verstraete and Pinty 1999). Clearly, the availability of appropriate tools for the quantitative simulation of the radiation transfer, from the light source to the actual detector optics, for arbitrary geophysical scenarios would help in specifying both the optimal sensor characteristics and the best observation strategy. Such tools would also promote the development of algorithms to extract information on the values of the variables that control the measured radiometer counts at the TOA. It is, however, unsatisfactory to derive empirical relationships without understanding the mechanisms that lead to the observed measurements (or the factors that may alter them). Indeed, if one wishes to physically interpret data strings gathered from satellite, it becomes mandatory to develop theories and models that can describe how the various media composing the radiative system under observation interact with the radiation to produce the observed sensor response.

⁶The optical thickness is the integral of the extinction coefficient (which describes the fraction of radiation taken from the direct beam by absorption and scattering processes) along the vertical as radiation travels from level z_1 to z_2 within a media. The single scattering albedo is the fraction of scattering from the total extinction, and the scattering phase function describes the angular distribution of the scattered radiation (see for example Kaufman 1989).

2.3 The role and importance of models

Models are conceptual tools that provide a link between measurements and the variables and processes that control these observations. Fundamentally, the interpretation of remotely sensed data always implies the use of a model. This can be implicit, as in the case of the various *statistical* methods that correlate raw data or vegetation indices (VI) with environmental parameters of interest, or explicit, as in *physically-based* approaches to extract information about the parameters that influence the propagation of radiation (*e.g.*, Tucker et al. 1985, Myneni et al. 1995a, Gobron et al. 2000a). In any case, models should only be used after substantial validations and then solely to retrieve information on variables that are contained within them (Pinty and Verstraete 1992).

In the context of Earth Observation, signals are carried by electromagnetic radiation. Consequently, a physical interpretation of remote sensing measurements can provide reliable quantitative information only on the relevant *state variables* that control the interactions of the radiation field with all intervening media from the light source to the detector (Verstraete et al. 1996). The simulation of such processes, using physically based RT models, thus allows to estimate the most probable value of a remote sensing measurement, given that the values of all state variables in the model, the conditions of observation and the nature and role of all relevant radiative processes in the system are specified in advance (Verstraete and Pinty 1999). This modeling approach is known as the **direct** or **forward mode** and will be presented more thoroughly in chapter 3. It provides ample testing ground for the intercomparison of different radiation transfer models (Pinty et al. 2001a) and can be used, for example, to determine which state variable in a given model is primarily responsible for the observed signal variability under specific conditions of observations and illumination (*e.g.*, Gobron et al. 1997b). The interpretation of remote sensing data, on the other hand, requires to apply the same model in **inverse mode**, or more specifically to *invert the model against the data set* (Verstraete et al. 1996), in order to retrieve the state variables of interest. The many problems to be faced when addressing such an inversion have been extensively discussed by Goel and Strebel (1983), Pinty and Verstraete (1991), Verstraete and Pinty (1999) and Kimes et al. (2000) among others, and will be dealt with in greater detail in the context of chapter 4.

Strictly speaking, statistical or empirical approaches are valid only, when applied to data sets and conditions they were derived from (Verstraete et al. 1996). In the case of physically based approaches the hypotheses on which the models are based can be explicitly stated. This is an advantage when setting the limits of applicability or to evaluate the model. Most importantly, however, is that physically based models, preferably with a small number of state-variables, can be validated. This is essential, since any model, whether of conceptual or mathematical design, must allow the experimental verification of the theories inherent in its formulation. In the context of quantitative information retrieval from satellite observations, this implies that RT models need to be validated both in the forward and in the inverse mode for a given terrestrial surface. Pinty and Verstraete (1992) provided a robust validation scheme, consisting of the comparison of simulated BRDF values with actual measurements by a space-borne detector, the subsequent retrieval (with the same RT model) of the state variables from these observations, and finally the validation of the retrieved optical and structural properties with the corresponding parameters gathered in the field and used in the initial forward modeling procedure. Such an exhaustive validation scheme might, however, not always be feasible, in which case a comparison with other RT models should be attempted. This is the approach pursued in chapter 3 when validating two state of the art RT models requiring very different computer requirements, radiation transfer formulations and vegetation representation capabilities.

2.4 Conclusion

The analysis of remote sensing data may yield information about a specific target property only if the latter contributes substantially to the measured characteristics of an energy signal collected by a space-borne radiometer. At the Earth's surface, the spectral, directional and polarization signatures of the various scattering elements together with their number, geometry and spatial distribution, are responsible for the radiative characteristics of the reflected signal in the optical part of the solar spectrum. The conditions of observation and illumination, as well as the state of the atmosphere at the time of the measurement, may significantly modulate the reflectance values of terrestrial surfaces. In order to identify the terrestrial source(s) that lie behind the signal characteristics measured by a space-borne detector, validated radiation transfer models can be run on predefined scenarios of canopy architecture, leaf and soil optical properties as well as illumination, observation and atmospheric state conditions. Physically based RT models have several advantages over statistical or empirical approaches, most notably, in that they can predict new situations, have state-variables with precise meanings, and in general have the potential to be inverted and thus also to be validated.

Chapter 3

Radiation Transfer Modeling

This chapter focuses on the presentation and validation of two state of the art physically based radiation transfer models that differ widely in their computer requirements, radiation transfer formulations and vegetation representation capabilities. Section 3.1 provides an overview of the various physically based approaches to simulate reflectance fields over vegetated surfaces in the optical domain. Section 3.2 and 3.3 introduce the RT models of Govaerts (1995) and Gobron et al. (1997c) respectively. Section 3.4 describes the performances of these two models when compared to several other models during the RAdiation transfer Model Intercomparison (RAMI) exercise (Pinty et al. 2001a).

3.1 Overview of radiation transfer models

A panoply of optical RT models are in existence today, capable of simulating the bidirectional or hemispherically integrated reflectances from individual leaves to entire soil-vegetation-atmosphere radiative systems (*e.g.*, Jacquemoud and Baret 1990, Liang and Strahler 1993, Vermote et al. 1997). Detailed reviews of these models and the concepts behind them have been performed in the past and shall not be repeated here (*e.g.*, Goel 1988, Myneni et al. 1989, Hapke 1993, Disney et al. 2000). A brief summary of the various approaches to model the radiation transfer in vegetation canopies, where the leaf is treated without acknowledgement of its internal cell structure and the exiting reflectance field conveniently simulated at the TOC, will nevertheless be presented.

Many of the current RT models were derived from the classical theory of radiation transfer in stellar atmospheres (Chandrasekhar 1960), and approximate the vegetation canopy as a *plane-parallel, turbid medium*—that is, a horizontally infinite slab, homogeneously filled with infinitesimal scatterers—with a specific foliage density, leaf scattering and orientation distribution function (*e.g.*, Ross 1981, Camillo 1987, Shultis and Myneni 1988, Nilson and Kuusk 1989, Knyazikhin and Marshak 1991). The motivation behind these simplifications is essentially twofold: 1) the need to characterize the medium under observation with a minimum number of essential (and preferably measurable) state variables, such as to maximize the accuracy in the forward mode, and 2) the wish to obtain a tractable solution to the integro-differential transfer equation of monochromatic radiation within vegetated surface layers (Pinty and Verstraete 1998). A review of the proposed methodologies to achieve the latter is given in Goel 1988 and Asrar 1989. Although numerical techniques are hampered by their increased computation times, they have the definite advantage over analytical approaches, that they can be less stringent in their assumptions about the canopy geometry and the radiation regime there within. During the last decade or so, the specific accounting for the finite size of the scatterers lead to the formulation of a series of hot-spot models more realistic in their foliage description than the original far

field¹ approach (Marshak 1989, Verstraete et al. 1990, Jupp and Strahler 1991, Kuusk 1991). Similarly, the assumption of an infinitely deep canopy (Ross 1981) has been progressively removed by some of the more recent models, in that they included a proper treatment of the role of the soil reflectance (*e.g.*, Privette et al. 1995, Gobron et al. 1997c). For a brief description of some of these concepts see Annex B. However, with the exception of some implementations (Myneni and Asrar 1993, Peltoniemi 1993), most **plane parallel** RT models remain spatially continuous in their conception, that is they generally assume an infinite, horizontally homogeneous vegetation cover, not really representative of the architectural properties of many known vegetation cover types.

To account for the macroscopic heterogeneity of vegetation canopies, and in particular the sizes, shapes and spatial aggregations of individual trees or plants, the approaches of Brown and Pandolfo (1969) and Richardson et al. (1975), among others, were further developed to allow for bidirectional reflectance simulations in complex vegetation arrangements (*e.g.*, Li and Strahler 1985, Nilson and Peterson 1991, Chen and Leblanc 1997a). The common theme of such **geometric-optical** (GO) models is the abstracted representation of foliage entities, most commonly in the form of simple geometrical volumes (boxes, cones, spheres, cylinders) of known average optical properties (*e.g.*, Egbert 1977, Otterman 1983, Meerkoetter 1989). Thus, neglecting the accurate representation and distribution of individual canopy elements within the tree crowns (and approximating the multiple scattering component within the canopy as a whole), GO models generally estimate the canopy reflectance field using an area-weighted combination of several sunlit and shaded components, as defined by the geometry of the protrusions (*e.g.*, Franklin and Strahler 1988, Strahler and Jupp 1990, Gerard and North 1997).

With the recent advances in computer graphics and visualisation techniques the scene² creation process is becoming an ever more involved and comprehensive part of the radiation transfer modeling activity. Bio-mechanical, fractal or L-system based approaches are being used to enhance the realism of plant architecture modelling (*e.g.*, Goel et al. 1991a, Myneni 1991, Kranigk and Gravenhorst 1993, De Reffye and Houllier 1997, Lewis 1999). In general, such **complex geometric** or **computer simulation** models employ Monte Carlo ray-tracing or radiosity methods to simulate the radiation transfer within the modelled canopies (*e.g.*, Ross and Marshak 1988, Borel et al. 1991, Goel et al. 1991b, Gerstl and Borel 1992, North 1996, Govaerts and Verstraete 1998). However, despite the usage of optimization techniques, many of these models remain prohibitively demanding in computer resources, such that they have been primarily used for the benchmarking of other less refined RT models, or else, in the evaluation of information extraction algorithms.

Finally, and although not physically based, **parametric** models contain empirical functions that are capable of representing almost any shape of reflectance field. The RPV model of Rahman et al. (1993a) capitalizes on the original work by Minnaert (1941). It was extensively evaluated by Engelsen et al. (1996) and modified by Martonchik et al. (1998b) for operational use in the generation of MISR products. Other models in this category include the work of Walthall et al. (1985), Hapke (1981) and Dickinson et al. (1990) as well as the kernel driven approaches of Roujean et al. (1992), Wanner et al. (1997) and others. The main advantages

¹The *far field* assumptions relates to media with sufficiently isolated particles such that their individual scattering patterns are independent of all other particles in the medium.

²The term *scene* refers to a simulated vegetation canopy representation that is either implied by the RT model definition or else specifically generated as an input to the model at hand. The spatial extend and architectural detail of this canopy representation may either be defined by the user or else is inherent to the type of RT model being used.

of parametric models are that 1) they can simulate measurements in conditions not actually measured or even measurable, 2) they can provide the necessary boundary conditions for the (atmosphere/biosphere) radiative system under study, 3) they can be integrated to retrieve spectral albedos (Lyapustin 1999, Pinty et al. 2000a), and 4), they allow for a fast inversion because of their small (3 to 5) number of parameters (Privette et al. 1997). Although, these models do not contain state-variables of the radiative transport, their parameters are nevertheless functional in the description of the surface-leaving reflectance field. Work is currently under way to determine, when and how these parameters might become associated with something more tangible in terms of actually observable features or measurable quantities (Pinty et al. 2001b).

Radiation transfer models, like any other models for that matter, contain their own sets of assumptions and approximations which in the case of the above physically based RT models, relate both to the description of the canopy architecture and its optical properties, and to the method of resolving the ensuing radiation transfer problem. What model to select for a particular forward modeling task depends primarily on the accuracy requirements for the resulting BRDF values, the computing constraints, and the available set of input parameters describing both the structural and optical canopy characteristics. In the following, two specific, physically based RT models with different degrees of canopy representation capabilities will be presented:

- 1 The **Raytran** computer simulation model of Govaerts (1995), that can describe a scene in arbitrarily fine detail using a very large number of parameters to describe the structural and optical properties of the vegetation canopy, and that returns a statistical estimate of various radiation transfer properties using a Monte Carlo ray-tracing approach.
- 2 The plane-parallel **Semi-Discrete** model of Gobron et al. (1997c), that needs only 7 input parameters, and that accurately accounts for the effects of finite sized leaves when describing the first two orders of scattering, whilst using a turbid medium approach to include the higher orders of scattering.

3.2 The Raytran model of Govaerts, 1995

Raytran is a Monte Carlo (MC) ray-tracing model, designed as a *virtual laboratory*, where three-dimensional (3-D) scenes of arbitrary complexity can be described, and where the relevant radiative processes can be evaluated in great detail and at scales appropriate for the simulation of actual satellite observations (Govaerts and Verstraete 1998). MC ray-tracing techniques lend themselves nicely to the simulation of reflectance fields over complex canopy representations in that they stochastically sample the various interactions of the incident radiation within the scene until a certain level of stability is reached. Similar to other MC ray-tracing models (for a recent review see Disney et al. 2000), **Raytran** describes the radiative transfer on a ray-by-ray basis, following individual ray trajectories from their energy source, through all relevant interactions, until an eventual absorption or exit from the simulated scene. However, rather than relying on variance reduction techniques—that is, optimization methods to limit the number of ray paths, usually to the detriment of accurate physical representations—**Raytran**, has been designed to take advantage of recent hardware and software parallelization developments. Indeed, the speed-up achieved by using the Message Passing Interface (MPI) as a communicating layer within a distributed memory, parallel processor architecture increases almost linearly with the number of processors available (Govaerts and Verstraete 1996).

3.2.1 Description of the model

The **Raytran** model assumes that 1) light propagation can be described entirely with geometrical optics, 2) incident radiation can be simulated with a finite number of non-interacting rays, and 3) whenever a ray-matter interaction occurs, the ray is scattered in one and only one direction under elastic scattering conditions. In its current form this model would thus not be appropriate to simulate physical processes at spatial scales of the order of, or smaller than, the wavelength of the radiation, or phenomena resulting from the wave nature of the radiation, such as diffraction or interference. To set up an experiment with this model, the structural and optical properties of the medium of interest have to be defined prior to the computation of the ray trajectories. A set of 11 geometric primitives (*e.g.*, disc, cone, sphere, cylinder), may be combined using Constructive Solid Geometry (CSG) techniques to produce objects of great complexity. Every object within the bounding volume of the scene (known as the *world* object) will be characterized by its position with respect to the world cartesian coordinate system, its spatial extension and an interaction model that specifies the object's scattering properties if a ray intersects its outer envelope or is to be propagated within the spatially homogeneous media defined inside its (closed) interior. Figure 3.1 shows some examples of structurally homogeneous (top) and heterogeneous (bottom) vegetation canopies, that are depicted both in a *deterministic* manner (right), where every primitive is explicitly described, and in a *stochastic* manner (left), where the statistical foliage properties are represented by volumes of spatially homogeneous media with identical characteristics³. Additionally, the extent and location of an energy source from which the rays are to be generated in accordance with a specified lighting model have to be defined. These energy sources may be located either inside or outside of the world object and can be combined to simulate complex illumination conditions. Last but not least, specific measurement procedures may be specified to generate the desired information from the ray paths.

Ray generation and event tracking

Upon emission from a light source, a ray k is tagged by a set of parameters describing that event: $\epsilon_{k_j} = \{\mathbf{r}_j; \boldsymbol{\Omega}_j; T_j; O_l\}$, where \mathbf{r}_j is a position vector indicating the origin of the ray, $\boldsymbol{\Omega}_j$ is a unit vector describing the travelling direction, T_j marks the type of j -th interaction (emission, absorption, reflection or transmission) and O_l identifies the l -th object within the scene where the interaction occurs⁴. For every new interaction between the ray and the scene another event is added to the profile of the ray path, thus allowing for an easy way to extract any relevant kind of information later on. In order to determine the position of the next point of intersection (\mathbf{r}_{j+1}) an optimized geometric-sorting algorithm, based on the uniform subdivision of the scene into smaller volumes called 'voxels', is applied (Arvo and Kirk 1989).

Ray interaction at the interface between two media

If a ray falls onto an open surface, or the envelope surrounding a homogeneous scattering and absorbing medium, the type of interaction and subsequently also the outgoing direction are both determined with respect to the local coordinate system (l) at the point of intersection. Knowing the incoming direction of the ray ($\boldsymbol{\Omega}'_j$) as well as the bidirectional reflectance and transmission distribution functions (from the interaction model of the object), it is possible to compute the hemispherically integrated probabilities of reflection $P_\rho(\boldsymbol{\Omega}'_j)$, transmission $P_\tau(\boldsymbol{\Omega}'_j)$ and absorption $P_\alpha(\boldsymbol{\Omega}'_j) = 1 - P_\rho(\boldsymbol{\Omega}'_j) - P_\tau(\boldsymbol{\Omega}'_j)$, *e.g.*, Glassner 1989, Antyufeev and Marshak 1990.

³Govaerts (1995) referred to deterministic canopy representation as being composed of 'discrete' entities, whereas stochastic representation of finite-sized (or point-like) canopy elements are made of 'pseudo-turbid' (or turbid) media. The corresponding notations will be used interchangeably.

⁴Although light sources are not actual objects—in the sense that they cannot intercept rays emitted from another source—they are nevertheless included in the first event description.

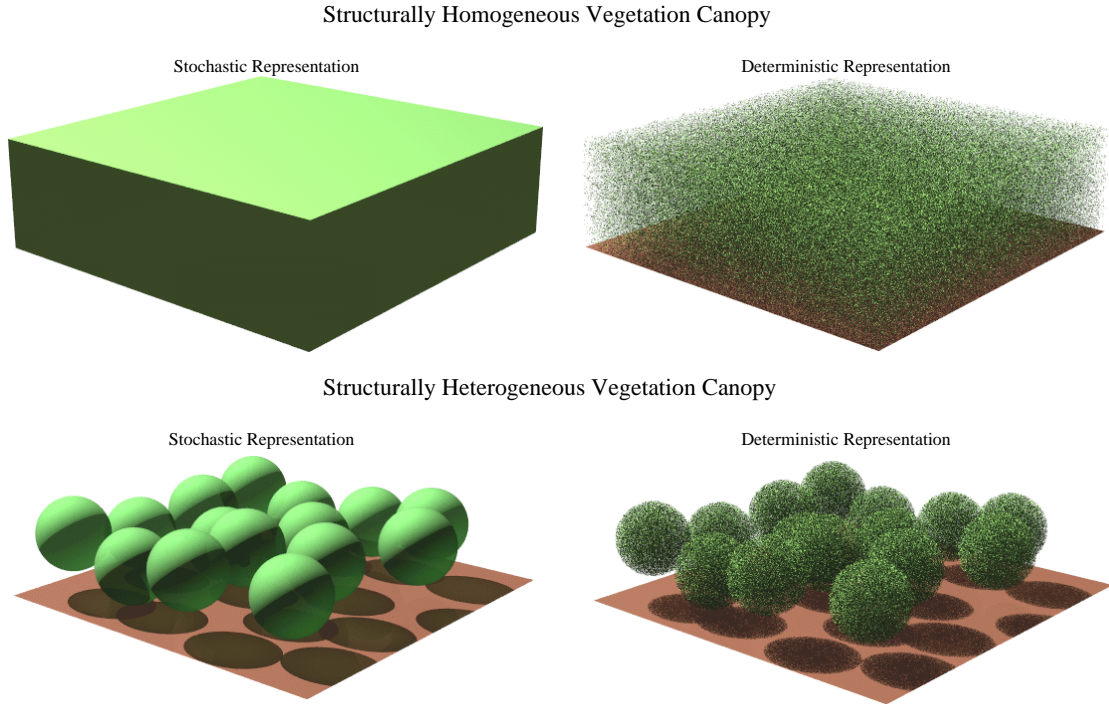


Figure 3.1: Four Raytran canopy representations of equal scene dimension, LAI and TOC height. The top panels depict two structurally homogeneous vegetation canopies, where the foliage is uniformly distributed throughout the available volume. The bottom panels visualize two structurally heterogeneous vegetation architectures, where the scatterers are confined within the volumes of several non overlapping spherical objects. In the right hand panels, the discrete foliage elements are represented in a deterministic manner, in the left hand panels, they are displayed in a stochastic manner using pseudo-turbid objects.

The type of interaction T_{j+1} is simulated by generating a random number \mathcal{R} over the interval $[0, 1]$, such that a reflection event occurs if $\mathcal{R} < P_\rho(\Omega'_j)$, a transmission if $P_\rho(\Omega'_j) \leq \mathcal{R} < P_\rho(\Omega'_j) + P_\tau(\Omega'_j)$ and an absorption event if $P_\rho(\Omega'_j) + P_\tau(\Omega'_j) \leq \mathcal{R}$. In the former two cases the acceptance-rejection method (Devroye 1986) is used to relate the BRDF, normalized by $P_\rho(\Omega'_j)$, via two random numbers to the outgoing direction, first in the local coordinate system—where the surface normal always points to $(0, 0, 1)$ —and then in the coordinate system of the world object (Ω_{j+1}). In order to represent the boundary condition at the soil interface, Lambertian, Gaussian as well as the Torrance-Sparrow (Torrance and Sparrow 1967) and SOILSPEC (Jacquemoud et al. 1992) scattering distribution functions have been implemented.

Ray propagation within a scattering medium

Ray propagation within a spatially homogeneous medium, containing finite-sized or point-like scatterers is controlled not only by the simulations of the interaction types and scattering angles as before, but also by the reckoning of the actual distances between successive interactions. Rays are expected to travel over distances of the order of the mean free path of photons in the real world, with a probability of interaction with the pseudo-turbid medium that increases exponentially with the distance travelled since the last interaction (Spanier and Gelbard 1969). The actual path length $d_a(\Omega_j)$ that a ray may travel since its last point of interaction \mathbf{r}_j inside a pseudo-turbid medium of optical depth $\tau(\Omega_j)$, is simulated using a random number \mathcal{R} (bound in the interval $[0, 1]$) such that $d_a(\Omega_j) = -\ln \mathcal{R} / \tau(\Omega_j)$, and an interaction will occur only if d_a is contained within the medium. The next position of interaction \mathbf{r}_{j+1} is thus given by $\mathbf{r}_{j+1} = \mathbf{r}_j + d_a \cdot \Omega_j$ with the type of interaction being determined as mentioned before. The formulation

of $\tau(\Omega_j)$ for finite-sized scatterers makes use of the geometric-statistical hot spot model of Verstraete et al. (1990) which requires some assumptions as to the shape and organisation of the scatterers within the medium (compare with Annex B). Comparison of **Raytran** simulated hemispherical reflectances for both deterministic and stochastic canopy representations with identical properties, revealed very little differences, especially in the NIR and when the radius of the scatterers was not too large (Govaerts 1995).

Energy conservation and measurements

Within **Raytran**, the computations associated with a ray are pursued until 1) an absorption event occurs, 2) the ray exits the world object upwards, or 3) a user-specified maximum event number is reached. To simulate the horizontal exchange of rays with neighbouring areas *cyclic boundary* conditions may be applied, that is, laterally exiting rays are re-ingested into the world object through the side opposite that of their departure without being affected in their direction of travel. This approach assumes, however, that the simulated scene is part of a larger and similarly structured area (compare with section 5.1.1). Since every ray-path is composed of a series of event descriptors, **Raytran** can associate virtual filters (and logical operations thereof) to specific measurements. This allows, for example, to apply a given measurement only to rays that have had a certain type of interaction with a specific group of objects, or that have experienced a specific number of interactions of a particular kind. The most commonly applied measurements include, 1) the simulation of BRDF values over user-specified angular intervals for predefined azimuthal planes or the entire upper hemisphere, 2) the estimation of vertical fluxes at user-specified height intervals, and 3) the counting of rays that satisfy a series of predefined event criteria (Govaerts 1995). However, since the uncertainty in the Monte Carlo estimate of any measurement improves as the inverse of the square root of the number of incident rays, a compromise has to be found between the tolerable level of uncertainty in a measurement and the time it takes to generate this. Figure 3.2 documents, for a structurally homogeneous vegetation canopy (much alike that in the top right panel of Figure 3.1) composed of 40.000 disc-like scatterers and illuminated at $\theta_0 = 30^\circ$ and $\phi_0 = 0^\circ$, how the average BRDF accuracy in the principal plane (left panel) and the runtime (right panel) of **Raytran** depend on the number of incident rays. Shown are averages of 5 different realisations.

3.2.2 Verification and application of the model

Govaerts (1995) compared the **Raytran** model against the radiative transfer MC model of Ross and Marshak (1988). The main difference was that the latter (RM model) used a weighting mechanism to adjust the reflectance contributions from successive collisions of individual rays with the explicit canopy representation of circular leaves attached to vertical cylindrical stems. Additionally **Raytran** sampled the canopy reflectance field with finite sized angular buckets whereas the RM model, due to its implemented variance reduction technique, accounted only for those rays leaving in the specified direction of observation. Several simulations were performed for different solar zenith angles, LAI conditions and soil brightnesses in both the red and NIR spectral domain. For LAI = 1, the relative differences did not exceed 1% on average, at LAI = 3 they were 5% and for very dense canopies (LAI = 5) they amounted to 15% on average (Govaerts and Verstraete 1998). The systematic underestimation of the reflectance values by the RM model had already been reported by Liang and Strahler (1995) and was found to be due to the implementation of the optimization technique. **Raytran** was subsequently compared to the discrete-ordinate canopy reflectance model of Iaquinata (1995). In the NIR, for several scatterer sizes and LAI values of 1, 3 and 8, the mean relative difference of the models was very low (around $\pm 2\%$), especially when the structural properties of the homogeneous canopy approached turbid medium conditions. The multiple-scattering contributions were accurately

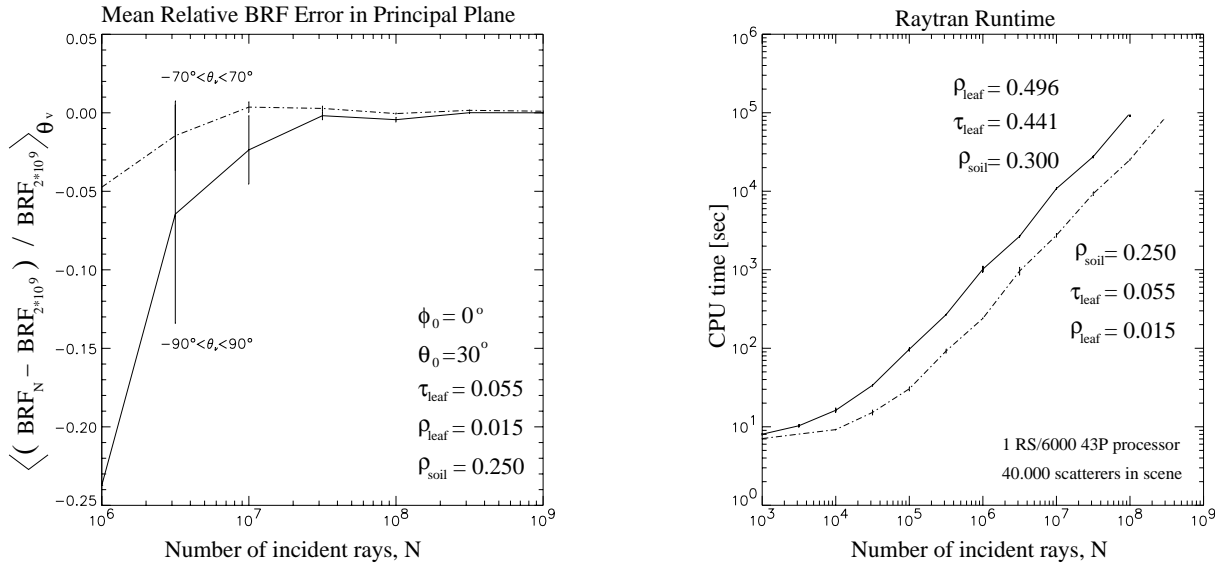


Figure 3.2: Left Panel: θ_v -averaged relative BRF difference between a 2 billion ray reference solution and several runs with fewer incident rays. The BRF values were sampled in 90 angular bins of 2° width. Right Panel: **Raytran** runtime, for the same scene and illumination conditions, as a function of the number of incident rays for two sets of reflectance properties.

accounted for in both models. However, it was found that **Raytran**, because of its discrete angular binning strategy, underestimated the reflectance values around the hot spot.

The accuracy of the **Raytran** model was further evaluated against actual laboratory BRF measurements carried out in the European Goniometer (EGO) laboratory (Koechler et al. 1994). The EGO allows for the independent positioning of a light source and a detector anywhere on a 2 m radius hemisphere around a target located at its centre. The reflectance field of an artificial target, consisting of a lattice of cubes over a planar surface of duraluminium with known micro-structural properties, was measured using a HeNe laser source at 632.8 nm and a detector FOV of 28° . The Torrance-Sparrow model (Torrance and Sparrow 1967) was inverted against these measurements using the technique developed by Renders and Flasse (1996) to yield the parameters of the interaction model for the artificial target within **Raytran**. The subsequent comparison of the modelled and measured BRF values showed that the reflectance variations were correctly simulated both in shape and in intensity. The major sources of discrepancy were due to 1) the omission of **Raytran** to simulate exactly the micro-roughness of the duraluminium surface, 2) the inadequacy of the Torrance-Sparrow model to represent the actual scattering distribution function of the artificial target and 3) the errors in the measurements (Govaerts and Verstraete 1998).

Raytran thus compares favorably with other reflectance models and is capable of reproducing actual observations, even in the case of an anisotropic surface. It can therefore be exploited to interpret actual observations. Govaerts et al. (1996) modeled the internal 3D cell structure of a *dicotyledon* leaf and simulated its spectral and bidirectional reflectances properties. The results compared well with actual observations indicating that an accurate description of the geometry of the leaf tissues, their optical characteristics, and the physical principles behind the radiation transfer are essential to the accurate simulation of reflectance fields in the optical domain. To increase the realism of the plant architecture Govaerts and Verstraete (1994) used an L-system approach to generate a series of explicitly described tree structures, of differing heights, leaf content and stem densities within **Raytran**. This model was exploited in a tropical detection project, where a patch of rainforest was simulated and its spectral BRF values were

subsequently compared to satellite remote sensing data from NOAA-AVHRR in order to derive a spatial distribution of forest cover (Govaerts et al. 1997).

3.3 The Semi-Discrete model of Gobron et al, 1997

The **Semi-Discrete** model is a plane-parallel (PP) radiation transfer model, developed as a tool of sufficient accuracy and speed to be attractive for operational usage. Like other PP models (for a recent review see Qin and Liang 2000) it assumes a horizontally infinite canopy layer of finite depth, but allows for the explicit representation of finite-sized canopy elements in the first two orders of scattering. Higher orders of scattering are approximated with a turbid medium approach, that is, without taking account of the increased retro-reflection probability due to the discrete nature of the foliage elements. Whereas MC based models are capable of offering highly detailed but specific representations of a particular canopy architecture situation, the **Semi-Discrete** model proposes a *generic* solution, applicable to all vegetation canopies that meet its structural homogeneity assumption within some predefined level of uncertainty (see also chapter 5).

3.3.1 Description of the model

The **Semi-Discrete** model idealizes vegetation canopies as a collection of K non-overlapping layers of leaf area index ℓ . Vertical homogeneity is often assumed so that the canopy is composed of a large but finite number of flat leaves, that are uniformly distributed between the TOC and the underlying soil. The canopy foliage is characterized by a specified leaf reflectance and transmittance probabilities, a bi-Lambertian scattering phase function, one of the trigonometric LND functions of Bunnik (1978), and a finite leaf size. The latter implies that the radiation interception process is spatially discontinuous, which—especially for scatterer sizes much larger than the wavelength—constitutes a significant deviation from the classical turbid medium hypothesis. The radiative impact of finite-sized canopy elements manifests itself most notably in the occurrence of a hot spot effect, primarily controlled by the first few orders of scattering, whereas the multiple-scattering component has a tendency to ‘smear out’ the radiative signature of the various architectural features within the canopy. Thus, in accordance with Marshak (1989) and others, the **Semi-Discrete** model separates the overall intensities into two single-scattering contributions, from the soil (zero order scattering or uncollided radiation) and the leaves (first order scattering or single collided radiation), and a multiple-scattering component (multiply collided). Both the uncollided ρ_{UC} and single collided ρ_{SC} BRF components can be solved for explicitly using the hot spot model of Verstraete et al. (1990) as well as an adaptation of the discrete model of Verstraete (1987) for the extinction of the direct solar radiation:

$$\rho_{\text{UC}}(z^{\text{TOC}}; \mathbf{\Omega}_0; \mathbf{\Omega}_v) = \rho_{\text{soil}}(z_0; \mathbf{\Omega}_0; \mathbf{\Omega}_v) \left[1 - \ell \frac{G(\mathbf{\Omega}_0)}{|\mu_0|} \right]^K \left[1 - \ell \frac{\|\mathcal{V}_\bullet\|}{\|\mathcal{V}_2\|} \frac{G(\mathbf{\Omega}_v)}{\mu} \right]^K \quad (3.1)$$

$$\rho_{\text{SC}}(z^{\text{TOC}}; \mathbf{\Omega}_0; \mathbf{\Omega}_v) = \frac{\Gamma(\mathbf{\Omega}_0 \rightarrow \mathbf{\Omega}_v)}{\mu|\mu_0|} \sum_{i=K}^1 \ell \left[1 - \ell \frac{G(\mathbf{\Omega}_0)}{|\mu_0|} \right]^i \left[1 - \ell \frac{\|\mathcal{V}_\bullet\|}{\|\mathcal{V}_2\|} \frac{G(\mathbf{\Omega}_v)}{\mu} \right]^i \quad (3.2)$$

where $G(\mathbf{\Omega}_x)$ is the function of Ross (1981), $\Gamma(\mathbf{\Omega}_0 \rightarrow \mathbf{\Omega}_v)$ is the canopy scattering phase function of Shultis and Myneni (1988), and $\|\mathcal{V}_\bullet\| / \|\mathcal{V}_2\|$ is the correcting factor of Verstraete et al. (1990) to account for the existence of free spaces in between the finite-sized scatterers inside the canopy (see annex B). Finally, and essentially because of the practical unsolvability of the radiation transfer problem for finite-sized scatterers in the multiple-scattering regime (Myneni

et al. 1991), the multiply-collided ρ_{MC} contribution is approximated with a discrete ordinate method using an azimuthally averaged expression of the bi-Lambertian scattering phase function, as proposed by Shultis and Myneni (1988). Typically, the **Semi-Discrete** model needed ~ 3.5 seconds when computing 90 BRF values on a IBM RS-6000 workstation with one 43P processor.

3.3.2 Verification and application of the model

Gobron et al. (1997c) compared the output of their **Semi-discrete** model with that generated by the **Raytran** model of Govaerts and Verstraete (1998) for several geophysical scenarios. These consisted of horizontally infinite, homogeneous vegetation canopies characterized by flat oriented discs of various diameters, erectophile, planophile and uniform LNDs and LAI values of 1, 3 and 8. Different illumination zenith angles, TOC heights and soil conditions were also considered. Overall, the **Semi-Discrete** model very accurately reflected the magnitude and variations of the **Raytran** simulated BRF values in the principal plane (which contains the strongest anisotropy). This good performance was particularly effective in the red, since most of the signal there is due to the very first orders of scattering by the leaves and soil. In the NIR, especially for increased LAI values and bright soil conditions, the **Semi-Discrete** model began to underestimate the BRF values, most likely because of its approximative formulation of the multiple-scattering component, so prominent in the NIR. Nevertheless, the differences between the results obtained (for all canopy conditions) with the two models were bias free, and amounted to an average of $\sim 5\%$ of the BRF values in the red and $\sim 3\%$ of the BRF values in the NIR. The linear correlation between the two models was 0.997 in the red and 0.998 in the NIR.

The performance of the **Semi-Discrete** model in simulating the reflectance field of actual canopies was investigated using the soybean plant canopy data of Ranson et al. (1984). Despite several assumptions and approximations to obtain the required set of model input parameters (*e.g.*, imposing a mean leaf size, an uniform foliage distribution, soil albedo, and the directionality of the incoming solar radiation at the time of the field measurements), reasonable agreements were obtained between the simulated and measured BRF values. In the NIR the linear correlation coefficient was greater than 0.85 for all considered solar zenith and azimuth angles, and the root-mean-square (RMS) error of the fit between the measured and modelled distributions corresponded to $\sim 5\%$ of the BRF values. In the red, however, some significant discrepancies with RMS values as large as 15–20 % of the BRF values were noted. Reasons for these differences could be: 1) the model idealization of the soy bean canopy, 2) the heuristics associated with the deduction of some of the required model input parameters that were missing in the field data, and 3) the possible existence of measurement errors in the field data. In the NIR the differences were less pronounced due to the tendency of the multiple-scattering component to smooth out these effects. The **Semi-Discrete** model was subsequently inverted against the field observations, and the resulting estimators of the model input parameters were used to compute the reflectance field of the soybean canopy anew. This time the agreement between model simulations and field measurements were much better. In the NIR the linear correlation coefficient was now greater than 0.91 for all solar illumination conditions, and in the red wavelength regime the RMS errors now corresponded to $\sim 5\%$ of the measured BRF values (Gobron et al. 1997c).

Given that the **Semi-Discrete** model is capable to represent the variability of bidirectional reflectance fields with sufficient speed and accuracy (both in the forward and inverse mode), Gobron et al. (1997a) generated a series of look-up-tables (LUT) containing the BRF values of 35 radiatively distinct biome types under specific illumination and viewing conditions. This pool of predefined surface type solutions was subsequently used to estimate the most probable LAI values on a global scale from red and NIR AVHRR/GVI data ($15 \times 15 \text{ km}^2$), previously

processed by Berthelot et al. (1997). The capability of the **Semi-Discrete** model to efficiently compute large amounts of reflectance data, was further used in a series of algorithms aimed at retrieving instrument specific estimators of the fraction of absorbed photosynthetically active radiation (FAPAR). These so called *optimized vegetation indices* are designed to be as insensitive as possible (on a global basis) to both atmospheric perturbation and soil properties, whilst accounting for the directionality of both the observation and illumination at the time of measurement, *e.g.*, Verstraete and Pinty (1996), Gobron et al. (1999b), Gobron et al. (2000b).

Having outlined both the **Raytran** and the **Semi-Discrete** RT models, as well as the verification efforts of their respective authors, it remains to investigate how the two models perform 1) when compared to an *ensemble* of otherwise derived and benchmarked reflectance models, and 2) with respect to their energy conservation compliance when tested under conservative scattering conditions. Both of these aspects are of vital importance for the confidence that may be placed into any future forward modelling activities of the **Raytran** and the **Semi-Discrete** models and can be documented in a straightforward manner with the results obtained from their participation in the Radiative transfer Model Intercomparison (RAMI) exercise.

3.4 The radiative transfer model intercomparison exercise

The RAMI initiative was a self organized activity of the radiative transfer modelling community to 1) help developers improve their models, 2) provide a rationale for the acquisition of more or better data, 3) inform the user community on the performance of the various models available, and 4) progressively develop a community consensus on the best ways to simulate the transfer of radiation at and near the Earth's surface (Pinty et al. 2001a). A formal intercomparison exercise was defined, where the participating models were required to simulate the radiative transfer in strictly defined configurations so as to allow the comparison of their results. The proposed geophysical scenarios consisted of both turbid and discrete representations of the structurally homogeneous and heterogeneous vegetation scenes depicted in Figure 3.1. The participating models (see Table 3.1) were required to perform a set of measurements for each of the applicable canopy representations, under both red and NIR spectral conditions, solar zenith angles of 20° and 50°, and a variety of LND's. The full documentation on the experimental protocol for all the proposed simulations can be found at the following World Wide Web address: <http://www.enamors.org/>.

3.4.1 Evaluation strategy

The intercomparison of model results raises a number of fundamental issues related to the notion of absolute truth and model verification. Oreskes et al. (1994) provides elements to support the conclusion that model results cannot be compared against an absolute reference *per se*, simply because such an actual 'truth' cannot be established⁵. As such, this statement implies that an absolute 'model verification' is impossible. Therefore, rather than looking for the 'truth' in the analysis of an ensemble of model results, the establishment of a set of 'most credible solutions', representative of both the knowledge contained within the models and the description of the scenario under study is required. Although it is tempting to derive this surrogate from the estimation of the various moments of the distributions of model results, it must be recognized that, for instance, model deviations with respect to an ensemble arithmetic average are difficult to interpret in the presence of potential 'outlier' that could bias this estimation (Pinty et al. 2001a).

⁵It should be noted here that this topic touches upon a wider and intensely fought debate as to the validity of science *e.g.*, Gross and Levitt (1997), Smith and Plotnitsky (1997), Sokal and Bricmont (1997).

Table 3.1: List of the models participating in the RAMI exercise.

| Model type | Model name | Reference |
|--------------------------------|---------------|--|
| 1-D homogeneous scenes | ProSAIL | Verhoef (1984) & Jacquemoud and Baret (1990) |
| | ProKuusk | Kuusk (1995) & Jacquemoud and Baret (1990) |
| | Semi-Discrete | Gobron et al. (1997c) |
| 3-D heterogeneous scenes | Flight | North (1996) |
| | DART | Gastellu-Etchegorry et al. (1996) |
| | Sprint | Thompson and Goel (1998) |
| | Raytran | Govaerts and Verstraete (1998) |
| | RGM | Qin and Gerstl (2000) |

It is however feasible to compare an ensemble of model results against each other in order to document their relative differences. In the context of RAMI, the primary criterion to quantify the inter-model variability was a measure of distance between BRF fields generated under identical geophysical and geometrical conditions. Specifically, the following metric was computed to estimate how the results of a given model m , behaves with respect to those of all other participating models:

$$\delta_m(\theta_v) = \frac{1}{\mathcal{N}} \sum_{i=1}^{N_{\theta_o}} \sum_{s=1}^{N_{scenes}} \sum_{\lambda=1}^{N_{\lambda}} \sum_{k=1, k \neq m}^{N_{models}} \frac{|\rho_m(\theta_v, i, s, \lambda) - \rho_k(\theta_v, i, s, \lambda)|}{\rho_m(\theta_v, i, s, \lambda) + \rho_k(\theta_v, i, s, \lambda)} \quad (3.3)$$

where $\delta_m(\theta_v)$ expresses local angular deviation of model m at the specific exiting angle θ_v with respect to the ensemble of N_{models} models. This deviation, normalized by the number of cases considered (\mathcal{N}), is estimated for all simulations of the BRF fields, emerging from N_{scenes} at N_{λ} wavelengths, illuminated with N_{θ_o} incident source angles. $\rho_m(\theta_v, i, s, \lambda)$ and $\rho_k(\theta_v, i, s, \lambda)$ correspond to the BRF values generated by model m and any other RAMI model k participating in the experiment, respectively.

The larger the number of participating models, the easier the identification of ‘outliers’ if any. However, in the absence of an absolute ‘truth’, there are no definite reasons to exclude such ‘outliers’ on the sole basis of statistical analyses. An inspection of the underlying physics (and its implementation) within these RT models is definitely mandatory to get a rationale regarding their deviations.

3.4.2 Overview of the RAMI results

Of the various intercomparison results that were generated in the context of the RAMI exercise, only the following three will be presented here: 1) the relative credibility with which the BRF values could be generated by a given model, 2) the performance of a given model under conservative scattering conditions, and 3) the actual discernability between different models, given a tolerable level of discrepancies in their simulated BRF values.

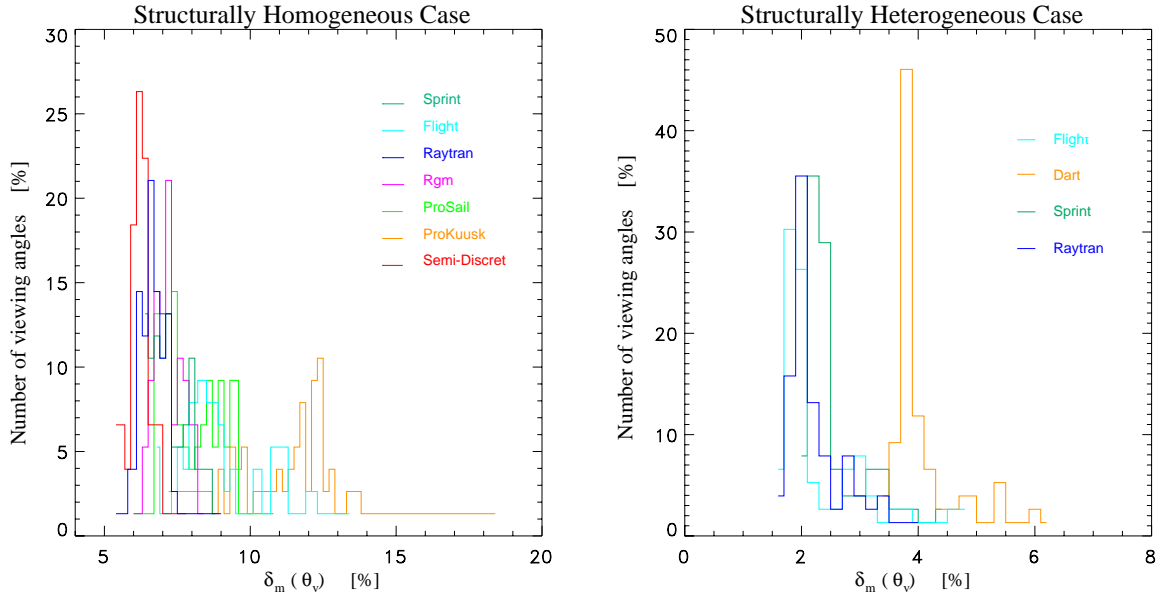


Figure 3.3: Histograms for local angular model deviation values estimated over all 152 viewing conditions in the principal and orthogonal plane for both the red and NIR wavelengths and two solar illumination zenith angles. In the case of the structurally homogeneous scene (left) both the turbid and discrete canopy representation reflectance fields were included, whereas the histogram of the structurally heterogeneous scene (right) contains only the BRF values from its discrete representation.

Local angular model deviations

Figure 3.3 shows the histograms of local angular deviations $\delta_m(\theta_v)$ for all models that participated in the RAMI exercise. These histograms were derived over all 152 viewing conditions in the principal and orthogonal planes and the two solar illumination zenith angles. In the case of the structurally homogeneous canopy (left panel) the BRF values of both the turbid and discrete canopy representations were included, whereas for the structurally heterogeneous canopy (right panel) only the BRF values from its discrete representation were used⁶. Seven models participated in the homogeneous test case (left panel) with their local angular deviations ranging from about 5 – 18%. The envelope of their combined histograms reveals the presence of a well marked peak around 5 – 8% and a less pronounced secondary peak close to 12%. A detailed inspection of the results revealed that the former peak was lower in the NIR (3 – 6%) than in the red (8 – 12%), a direct consequence of the different methods used by the various models to estimate the multiple-scattering contributions (in the NIR) and the effects of finite-sized leaves (in the red). The bimodal nature of this histogram envelope indicates the presence of one or more ‘outliers’ in the sense that these models produce BRF values which are distinctly different from those delivered by the other RAMI models. The left panel of Figure 3.3 thus reveals that, in a statistical sense, both the **ProKuusk** and **Flight** models deviate the most from the other models. Additionally, it can be seen that both the **Raytran** (deep blue) and **Semi-Discrete** (red) models contributed significantly to the local angular deviation peak with the lower δ_m in the histogram envelope. Thus, for most viewing angles, their BRF values deviated very little from those of most other participating models.

In the heterogeneous case (right panel) the histograms of the 4 participating models had local angular deviations ranging from about 3 – 6%. Again, a primary peak (around $\delta_m \sim 2\%$)

⁶The DART model did not participate in the turbid heterogeneous case.

and a secondary peak (at $\delta_m \sim 4\%$) can be seen. The latter was entirely contributed by the DART model, and found to be due to a systematic (10%) underestimate of its multiple-scattering component with respect to the other three models. Again, the *Raytran* (deep blue) model contributed significantly to the lower of the local angular deviation peaks.

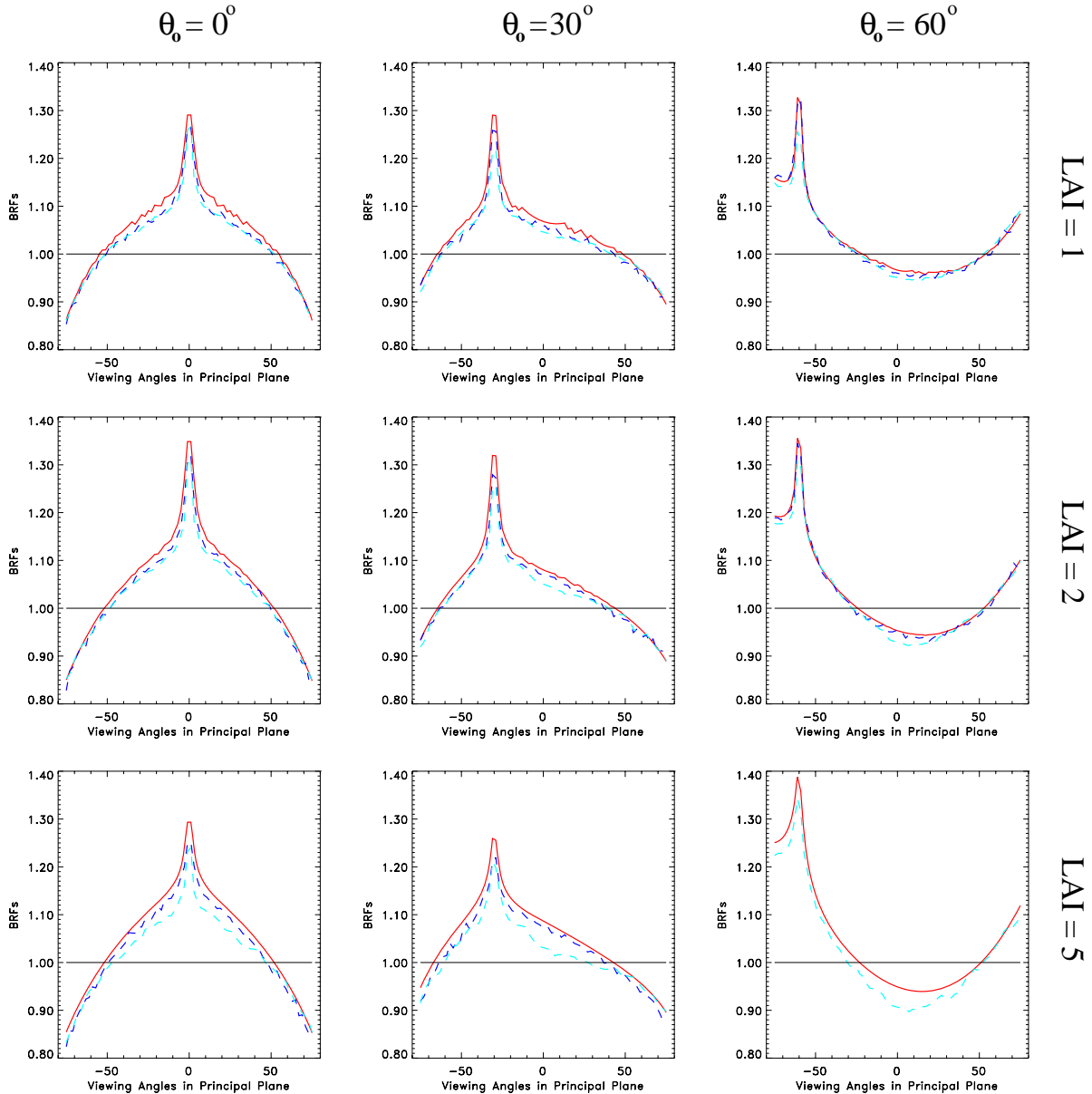


Figure 3.4: Various plots of the BRF values simulated by the *Flight* (light blue curve), *Raytran* (deep blue curve) and *Semi-Discrete* (red curve) models, in the principal plane for a homogeneous scene with an erectophile leaf angle distribution function and conservative scattering properties (view zenith angles are in degrees).

Energy conservation compliance

The verification of model compliance with respect to energy conservation was addressed on the basis of a set of conservative scattering experiments, where the scatterer reflectance and transmittance values were both equal to 0.5 and the soil reflectance unity. The additional variables were fixed at 0.1 m for the leaf diameter, $1.0 \text{ m}^2/\text{m}^2$ for the LAI and 1.0 m for the height of the canopy. Erectophile and planophile LNDs had been suggested for the simulations at three

different illumination zenith angles (0° , 30° and 60°). However, the large computing times requested by some of the three-dimensional models prevented many participants to attempt these *purist* cases. Figures 3.4 and 3.5 illustrate the BRF fields simulated in the principal plane by **Flight**, **Raytran** and **Semi-Discrete** for deterministic representations of structurally homogeneous canopies with erectophile and planophile LNDs, respectively. The overall agreement between the three model results, especially when considering an erectophile leaf angle distribution function and the lowest LAI values, is quite impressive under such drastic scattering conditions. The differences in the simulated BRF results increase almost systematically in the forward scattering direction, most notably in the planophile case (see Figure 3.5).

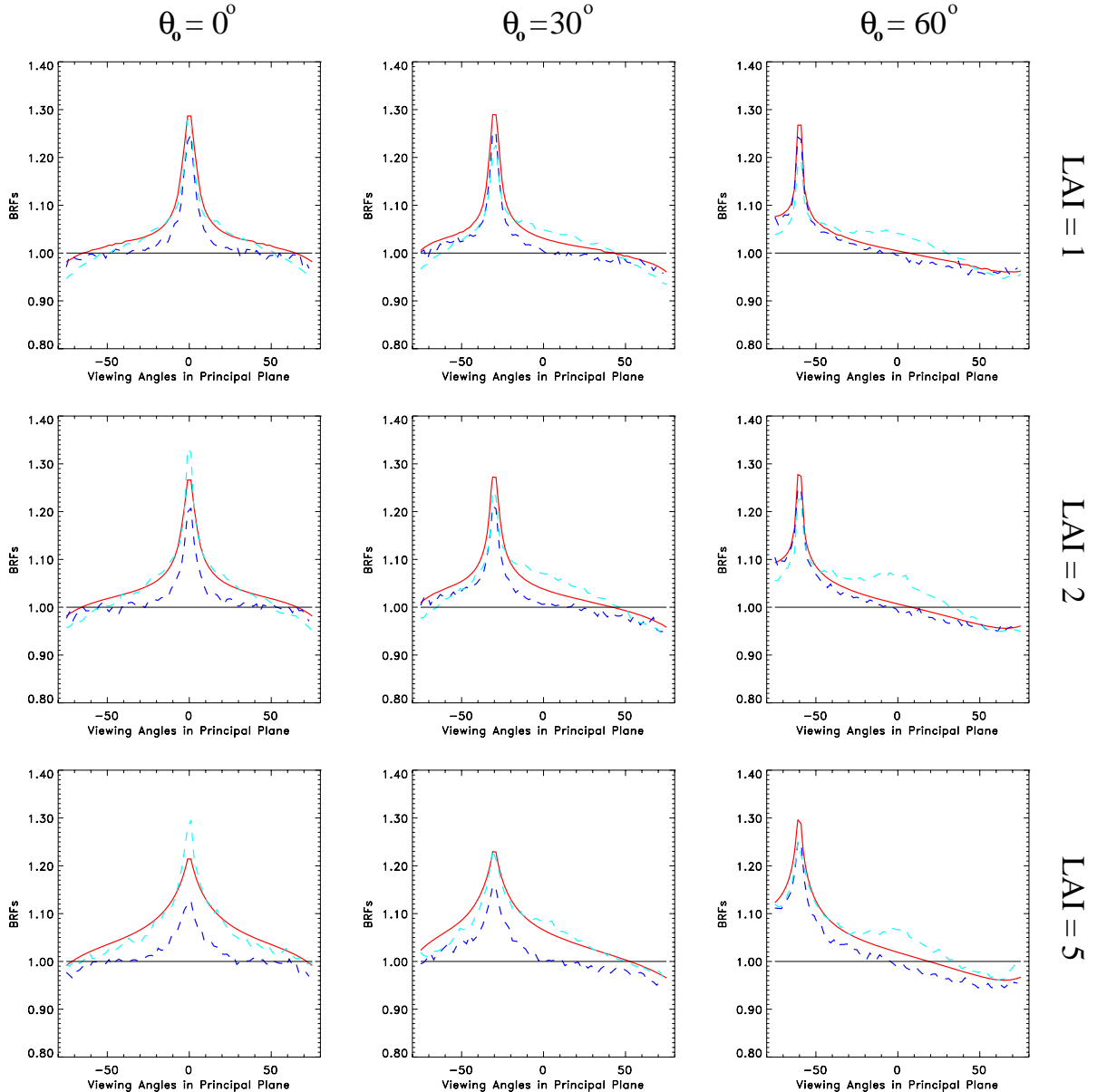


Figure 3.5: Various plots of the BRF values simulated by the **Flight** (light blue curve), **Raytran** (deep blue curve) and **Semi-Discrete** (red curve) models, in the principal plane for a homogeneous scene with an planophile leaf angle distribution function and conservative scattering properties (view zenith angles are in degrees).

In all of the above experiments, except in the case of planophile canopy illuminated at 60° for which the simulation results are not available, the **Raytran** model recovers the theoretical

albedo (1.0) and absorption factor (0.0) values with a numerical accuracy of about 10^{-5} . The **Semi-Discrete** model delivers absolute albedo and absorption factor values which are off by 0.02 (0.045) in the worst case using an erectophile (planophile) leaf normal distribution.

Model discernability

In a pragmatic sense, the differences between RT models matter only to the extent that they exceed the level of uncertainty associated with the measured BRF fields. During the RAMI exercise, a χ^2 approach, similar to that of Kahn et al. (1997), was implemented to assess how the errors of measurement compared to the variability exhibited by the different models in their representation of the reality. The goal of this discernability metrics was to identify which models would cease to produce distinguishable BRF values at a given level of accuracy whilst others would continue to behave differently:

$$\chi^2 = \frac{1}{\mathcal{N}} \sum_{i=1}^{N_{\theta_o}} \sum_{j=1}^{N_{\theta_v}} \sum_{s=1}^{N_{scenes}} \sum_{\lambda=1}^{N_{\lambda}} \frac{[\rho(i, j, s, \lambda) - \rho^{Credible}(i, j, s, \lambda)]^2}{\sigma^2(\lambda)} \quad (3.4)$$

where $\rho^{Credible}(i, j, s, \lambda)$ was estimated as being the mean of the corresponding BRF values generated by the N_{3D} ‘most credible’ of the three-dimensional RT models, namely **RGM**, **Raytran** and **Sprint**. $\sigma^2(\lambda)$ which corresponds to the sum of the variances associated to each individual model and the actual measurements (Kahn et al. 1997), may be estimated by assuming that the uncertainties linked to the measurements are identical to those associated with the models. The latter being straightforward to quantify using the variance of the N_B BRF values taken from the N_{3D} ‘most credible’ three-dimensional RT models:

$$\sigma_{3D}^2(\lambda) = \frac{1}{N_B - 1} \sum_{m=1}^{N_{3D}} \sum_{i=1}^{N_{\theta_o}} \sum_{j=1}^{N_{\theta_v}} \sum_{s=1}^{N_{scenes}} [\rho^{3D}(i, j, s, \lambda) - \rho^{Credible}(i, j, s, \lambda)]^2 \quad (3.5)$$

Thus, on the basis of the BRF values generated by the **RGM**, **Raytran** and **Sprint** models, $\sigma_{3D}^2(\lambda)$ values of 1.6E-03 and 1.0E-02 were obtained at the red and NIR wavelengths, respectively. These values correspond approximately to 5% and 2% of the typical BRF values that can be measured over a plant canopy system at the red and near-infrared wavelengths, respectively.

The resulting χ^2 metrics, for all those models participating in the BRF simulations over structurally homogeneous canopy scenes, are graphically shown in Figure 3.6. The dashed, vertical line at $\chi^2 = 1.0$ defines two sub-spaces in the diagram. All models falling to the left of this dashed line ($0 < \chi^2 < 1.0$) are indistinguishable on the basis of the available sample of measurements, while those that stand on the right ($\chi^2 > 1.0$) generate BRF fields that are statistically different at the prescribed level of error (σ_{3D}^2). In other words the **Raytran**, **RGM**, **Semi-Discrete** and **Sprint** models are generating BRF fields which are not discernible, in the sense that the statistical deviations between their results are smaller than the typical errors in their simulations. By contrast, the models **Flight**, **ProSAIL** and **ProKuusk** do not represent the BRF fields, from the ensemble of structurally homogeneous scenes, in a correct enough manner.

In summary, the RAMI exercise demonstrated that both the **Raytran** and the **Semi-Discrete** model could be used as a standard to evaluate other RT models. More specifically, they were amongst the models with the least deviating BRF fields, if tested under a variety of illumination and surface conditions. Their compliance with respect to energy conservation was also

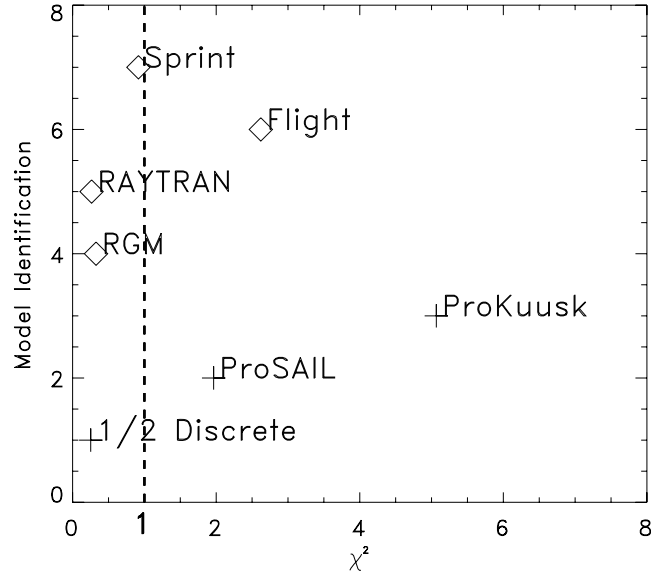


Figure 3.6: Plot of the discernability metrics χ^2 for each of the RAMI models in the case of the structurally homogeneous scenes. The cross and diamond signs identify the one and three dimensional models, respectively.

remarkable, especially since the *Semi-Discrete* model was merely approximating the multiple-scattering component. Finally, both models were deemed undiscernible when compared over structurally homogeneous vegetation canopies under accuracy requirements of 5 and 2% of the BRF values in the red and the NIR, respectively. These tests, together with those performed by their respective authors, thus provide an acceptable baseline from which the necessary confidence for any of their future forward modeling activities (both in terms of intensity and anisotropy of the simulated reflectance fields) may be derived. Although both models have already been applied to the interpretation of data-strings gathered by satellite, chapters 4 and 5 will aim at comparing these efforts both in terms of the results achieved and the resources required to do so.

3.5 Conclusion

A large variety of physically based radiation transfer models are in existence today. *Raytran* is a Monte Carlo ray-tracing model, capable of describing the relevant radiative processes within arbitrarily complex three-dimensional scenes and at scales appropriate for the simulation of actual satellite observations. The plane-parallel *Semi-Discrete* model accounts for finite-sized canopy elements in the first two orders of scattering and was developed as a generic solution to all homogeneous vegetation canopies that meet its required hypotheses. Both the *Raytran* and the *Semi-Discrete* model have been extensively tested against simulated and observed reflectance measurements. In the context of the RAMI exercise, they were proven consistent with the bulk of participating RT models, faithful to energy conservation under conservative scattering conditions, and undiscernible over structurally homogeneous vegetation canopies if the prescribed accuracy levels were set at 5% of the BRF values in the red and 2% of those in the NIR, respectively.

Chapter 4

Extracting Quantitative Information From Optical Remote Sensing Data

This chapter documents and discusses the utility of LUT-based inversion schemes for the extraction of a comprehensive set of quantitative canopy information from remote sensing measurements in the optical domain. Section 4.1 provides an overview of the various approaches to the inversion of physically based RT models. Section 4.2 documents the feasibility of LUT-based approaches to retrieve extensive (structural and optical) canopy information using three-dimensional RT models like **Raytran**. Finally, section 4.3 discusses some aspects of the fundamental issue of RT model complexity in the context of LUT-based inversion schemes.

4.1 The inversion of radiation transfer models

Physically based RT models can be applied in forward mode to assess the impact of individual state variables on the magnitude of a satellite gathered signal under clearly defined simulation conditions. In practice, however, remotely sensed measurements are acquired and reliable information on the governing state variables that gave rise to these observations is desired. This is feasible provided these RT models can indeed be meaningfully inverted against an appropriate set of measurements. In the specific case where only one state variable, Z is needed to describe the physics behind the measurement \mathcal{M} , the inverse problem can be solved analytically or numerically, usually to a great precision¹:

$$\mathcal{M} = f(Z) \quad \rightarrow \quad Z = f^{-1}(\mathcal{M})$$

In general, however, more than one state variable is required to describe the radiation transfer within the atmosphere-biosphere system (see section 2.2.3), which necessitates the performing of multiple observations of the target of interest in order to extract the desired estimates of the RT model input parameters. Such measurements, however, will prove useless, if 1) they involve new state variables (and therefore new RT models to retrieve these), 2) the target system changes between successive measurements (and no model exists to account for its temporal evolution without introducing new state variables), and, 3) identical measurements are simply repeated (Verstraete and Pinty 1999). Hence, to acquire information on an invariant system by inversion of a model, one has to introduce a number of *independent* variables such that their varying allows for the acquisition of multiple—yet different—observations without increasing the number of unknown state variables. In the context of optical remote sensing these independent

¹In this work, bold fonts indicate vector quantities *e.g.*, \mathbf{X} relates to the multiple occurrence of elements of type X . Subscripts may be used to indicate the number of dimensions *e.g.*, $\mathbf{X}_N = \{X_1, X_2, X_3, \dots, X_N\}$ relates to N different elements of type X .

variables must relate to some or all of the conditions of measurement, that is, the spatial, temporal, spectral, directional (illumination and viewing) as well as polarization aspects of a space-borne measurement² (Gerstl 1990). Of immediate interest here, however, are the N independent variables \mathbf{X}_N , that need to be altered in between K successive observations of a specific terrestrial target, such that any given RT model f featuring these same independent variables is capable of simulating the ensemble of measurements ($\mathcal{M}_1 \dots \mathcal{M}_K$) without changing the number L of its state variables \mathbf{Z} (Verstraete et al. 1996):

$$\begin{aligned}\mathcal{M}_1 &= f(\mathbf{X}_{1,N}; \mathbf{Z}_L) + \varepsilon_1 \\ \mathcal{M}_2 &= f(\mathbf{X}_{2,N}; \mathbf{Z}_L) + \varepsilon_2 \\ &\dots \\ \mathcal{M}_K &= f(\mathbf{X}_{K,N}; \mathbf{Z}_L) + \varepsilon_K\end{aligned}$$

where the system remains undetermined (ill-posed problem) if the number of measurements, K is lower than that of the state variables, L . On the other hand, if $K = L$, a solution can be found only if the measurements are without error, and the model describes the system in a perfect manner ($\varepsilon = 0$). Finally, if $K > L$, the system is overdetermined and the goal of the inversion now has to be shifted from finding *the mathematically correct solution* to finding *an optimal solution* for the various state variables; one that best accounts for the observed variability in the measurements given the errors inherent to both the model solutions and the actual observations (Verstraete and Pinty 1999).

4.1.1 Classical model inversion strategy

In the light of the above considerations the mathematical nature of an inverse problem is simply to find the optimal (but not necessarily unique) solution of an over-determined system of equations. Classical approaches aim at minimizing the inversion errors using a merit function:

$$\delta^2 = \sum_{k=1}^K W_k \left[\mathcal{M}_k - f(\mathbf{X}_{k,N}; \mathbf{Z}_L) \right]^2 \quad (4.1)$$

where W_k is the weight³ given to the measurement \mathcal{M}_k , and $f(\mathbf{X}_{k,N}; \mathbf{Z}_L)$ is the model simulated value corresponding to the state variables \mathbf{Z}_L and the effective independent variables $\mathbf{X}_{k,N}$ (Goel and Strelbel 1983). More specifically, the strategy of finding the minimum value of the merit function in equation 4.1 involves the following four-step procedure (Verstraete and Pinty 1999):

1. select arbitrary initial guess values for each of the L state variables \mathbf{Z}_L ,
2. use the known values of the N effective, independent variables \mathbf{X}_N to simulate the $k = 1, 2, \dots, K$ values of $f(\mathbf{X}_{k,N}; \mathbf{Z}_L)$ given that $K > L$,
3. compute the corresponding δ^2 and store the values of \mathbf{Z}_L if δ^2 can be considered small enough to stop the minimization procedure,
4. otherwise modify the values of \mathbf{Z}_L and reiterate the procedure from 2.

It should be noted, however, that the optimal solution identified by this inversion procedure may actually be dependent on the choices that are made during the execution of each one of its individual stages. In general, the performance (both in terms of speed and accuracy) of the

²For every remote sensing measurement \mathcal{M} there are at least 10 independent variables (equation 2.4). However, depending on the complexity of the RT model only a few of these might actually be contained in its formulation, and—depending on the properties of the available data sets—fewer still (N) have to be effectively included as independent variables \mathbf{X}_N , in order to allow for the model's successful inversion against these measurements.

³This should include the errors associated with the model and measurement uncertainties, *i.e.*, $W_k \propto 1/\langle \varepsilon^2 \rangle$.

various numerical algorithms that can be applied to solve this optimization problem is directly related to the way they search the available model parameter space. This, however, may make their solutions dependent on the initial guess values of \mathbf{Z}_L , with the possibility that the retrieved solution vector is actually a representative of a local—rather than the global—minimum of δ^2 . To overcome this issue the ‘genetic algorithm’ approach, for example, tracks a population of candidate solutions, initially distributed over the whole parameter space of \mathbf{Z}_L , before locating the subdomain within which the global minimum of δ^2 is to be found (Renders and Flasse 1996). The fidelity of the RT model, that is the validity of its underlying hypotheses and assumptions when generating $f(\mathbf{X}_{k,N}; \mathbf{Z}_L)$ is another issue that may affect the outcome of the δ^2 minimization procedure. Similarly, the results reported by an inversion algorithm may also depend on the *exit criterion* that is used to stop the optimization process. For example, if $\delta^2 \ll \langle \varepsilon^2 \rangle$ the RT model may include too many state variables or try to interpret actual measurement noise, whereas, if $\delta^2 \gg \langle \varepsilon^2 \rangle$ the RT model may not be capable to account for all of the variability in the gathered measurements (Verstraete and Pinty 1999). In either case the retrieved solutions cannot be considered reliable, and a re-evaluation of the RT model as well as the stability of the retrieved solutions in the presence of (not necessarily Gaussian) noise might be appropriate. Finally, the choice of the next set of values of the state variables in step 4 may also prove critical, since the way by which the model parameter space is searched can profoundly affect the content of the results vector that is taken as the optimal solution once the exit criterion has been reached. Commonly used optimization methods in the context of optical remote sensing include: Kalman filters as well as ‘Quasi-Newton’ or ‘Simplex’ hill-climbing algorithms (*e.g.*, Nelder and Mead 1965, Gill and Murray 1972, Goel and Thompson 1984, Pinty et al. 1989).

Another fundamental issue of model inversions is the occurrence of *multiple solutions*. This situation may arise because of 1) the uncertainties associated with the actual observations, as well as the simplifications and assumptions of the model, 2) the ‘flatness’ of the valley containing the global minimum of the merit function, 3) the choice of the exit criterion value, and, more perfidiously, 4) the number of available state variables in a given model. The latter point arises from the fact that, the larger the number of variables which can be adjusted in a model, the easier it is to find multiple combinations thereof which fit the observations in accordance with some specified value of the exit criterion. Pinty and Verstraete (1992) consider it mandatory to limit as much as possible the number of the state variables that need to be retrieved, since even for 3–4 state variables the uniqueness of the retrieved solution vector cannot be guaranteed. One obvious reason for this would be that certain state variables play only minor roles under certain conditions whilst at others they dominate the signal completely (*e.g.*, the structural parameters that describe the shape of the hot-spot). A reliable and accurate retrieval of such parameters would thus be strongly dependent on the sampling strategy, that is, the availability of measurements which highlight the variability of the signal due to the influence of these state variables. Additionally, the RT models that best fit the observations (*i.e.*, those with a large number of free parameters) are not necessarily those that are most physically correct or yield the best estimates of the state variables (Pinty and Verstraete 1991). In general, it can be said that the smaller the number of model input parameters, and the larger the number of actual observations that can be explained by that model, the higher the confidence that can be placed into its capability to represent the variance of the measurements (Verstraete et al. 1996). Overall, the only way to properly address the issue of multiple solutions, short of acquiring new or more accurate data, is to repeat the above optimization procedure with different starting values of \mathbf{Z}_L , with RT models of varying complexity, and with changing convergence criteria.

Since remote sensing observations are intrinsically related to the conditions of measurement—*i.e.*, the set of independent variables relating to the spectral, spatial, temporal, directional and

polarizational aspects of the observation—at least one independent variable has to be varied in order to allow for the retrieval of model parameters that are themselves unperturbed by variations in this independent variable (Verstraete et al. 1996). Consequently, it is reasonable to first extract information that is independent of the particular geometry of the observations, and only then to attempt the derivation of spectrally independent parameters if any increase in the complexity of interpreting the extracted results is to be avoided. This issue, however, does not apply as such to LUT-based inversions, as they are described below, since here the entire set(s) of structural and optical properties, that were used in the generation of the surface type solution(s), are known prior to any inversion attempts.

4.1.2 Look-up-table based inversion schemes

An alternative to the iterative inversion procedure is provided by the so called LUT approach. Here, the complete set of instrument specific observations, associated with any conceivable terrestrial target systems and under all possible conditions of observation and illumination, are pre-computed before any inversion attempts are being made. These data are then stored in a set of LUTs which can be searched to retrieve the optimal (pre-defined) solution to the inverse problem, given some specified conditions of selection. The latter criterion is commonly based on a χ^2 formalism and can be adapted in accordance with the complexity of the problem to be addressed (*e.g.*, Kahn et al. 1997, Gobron et al. 1997a, Martonchik et al. 1998a, Knyazikhin et al. 1999, Pinty et al. 2000a, Gobron et al. 2000a and Kahn et al. 2001). In its most general form, such a metric⁴ is analogous to equation 4.1 with the addition of a denominator in the summation part, that explicitly quantifies the tolerable level of discrepancy between the observed and simulated signal values. The search mechanism thus identifies all surface type solutions whose entries (under identical conditions of illumination and observation as the satellite measurements) in the LUTs abide, as a whole, by the selected uncertainty level (in the denominator of the χ^2 metric) such that they are equally probable to lie at the origin of the satellite measured data strings. LUT-based approaches, thus, make the non-uniqueness of model inversions apparent and, more interestingly, they can also provide a ranking of the retrieved solutions (in terms of their likelihood to explain the observed signal). Furthermore, the set of acceptable solutions provides an estimate of the accuracy of the retrieval of individual state variables. However, since the reflectance anisotropy (of the BRDF field) of a vegetated surface may well serve as an indicator of its structural appearance (see for example Figures 3.4 and 3.5, and chapter 6) we will avoid the summation over all (spectral and directional) observations when looking for optimal matches between pre-computed LUT entries and actual satellite measurements. This is because such an approach (equation 4.1 and the above χ^2 formulations) will inevitably retrieve surface type solutions that are not faithful in mirroring the observed reflectance anisotropy at *every view angle and spectral band* (to within the bounds of the imposed uncertainty level). Therefor, a *piece-wise* χ^2 metric will be applied to each and every measurement in order to assure the verisimilitude of the simulated $f(\mathbf{X}_{k,N}; \mathbf{Z}_L)$ and observed \mathcal{M}_k signals throughout the ensemble of available data points, K :

$$\chi_k^2 = \frac{[\mathcal{M}_k - f(\mathbf{X}_{k,N}; \mathbf{Z}_L)]^2}{\sigma_k^2} \quad k = 1, 2, \dots, K \quad (4.2)$$

where the uncertainty level σ_k^2 is conveniently expressed as a percentage ϵ of the observed signal \mathcal{M}_k . The value of ϵ should be derived from calibration specifications of the sensor as well as

⁴A *metric* is defined as a mathematical function that associates, with each pair of elements of a set, a real nonnegative number with the general properties of distance such that the number is zero only if the two elements are identical, and the number is the same regardless of the order in which the two elements are taken

from uncertainty estimates associated to the model simulations (*e.g.*, Gobron et al. 1997a). However, depending on the application it can be adjusted to account for the spatial variability of the surface that is being observed, the spectral band of the sensor, and—in the case of monodirectional instruments—the viewing geometry (*e.g.*, Kahn et al. 2001). From the selected sets of surface types, whose LUT entries satisfy $\chi_k^2 < 1$ at any one particular measurement condition, k ($S\{\chi_k^2 < 1 \mid \epsilon, \mathbf{X}_N, \mathbf{Z}_L\}$), only those that are contained within all K sets become a valid solution to the inverse problem:

$$S\{\text{valid solutions} \mid \epsilon, \mathbf{X}_N, \mathbf{Z}_L, K\} = \bigcap_{k=1}^K S\{\chi_k^2 < 1 \mid \epsilon, \mathbf{X}_N, \mathbf{Z}_L\} \quad (4.3)$$

such that the set of retrieved surface type solutions is explicitly dependent on the selected error criterion ϵ , the number of observations K , the number of RT model state variables \mathbf{Z}_L , and the effective independent variables \mathbf{X}_N . On the other hand, any dependency on the order of the inversions that existed for classical inversion strategies has disappeared from equation 4.3. Furthermore, the range of every state variable in the above set of valid solutions expresses the uncertainty in interpreting the set of K available, instrument specific measurements (\mathbf{X}_N) using the RT model f .

LUT-based inversion approaches give also rise to a series of questions that are in essence but reformulations of the issues associated with the iterative inversion procedure of section 4.1. The first one relates to the determination of the upper and lower bounds of the various state variables that serve as input parameters to the RT model. In practice, this information can be derived from the general knowledge of the system under study, or, by limiting the analysis to very particular situations for which *ancillary* information in the form of actual field measurements is available. Obviously the fidelity of the RT model remains an issue since it is instrumental in specifying the magnitude of the LUT entries. To this end, great care should be taken that only validated RT models are applied to the extraction of quantitative information from remote sensing data. As to the value of the exit criterion: this reduces to finding what constitutes an appropriate upper limit to the uncertainty level σ_k for which a given terrestrial surface type must be rejected from the set of probable solutions. Clearly the answer to this question depends both on the application at hand, and the accuracy requirements of the end user. However, care has to be taken here, since the selection of a particular surface type solution can always be achieved (even in the case of geographically incompatible biome types) if the value of the uncertainty level is high enough. Last but not least, the discretization step of the LUTs, both in terms of the state variables and the conditions of illumination and observation, predefines the interval between successive choices of \mathbf{Z}_L , and therefore must be chosen such as to avoid irrelevant computations as well as the existence of too many surface type solutions with essentially undistinguishable radiative characteristics. To address this point, the LUT-based inversion scheme presented in Annex A (and summarized below) is entirely based upon *in-situ* measurements of actual coniferous forest stands. Although this scheme may mean that the discretization steps of the state variables in the LUTs are not regular, it assures that each of the retrieved solutions will always correspond to a forest type that was observed in nature.

4.2 LUT-based inversion of the Raytran model

LUT-based inversion schemes are computer memory intensive, but they allow the use of 3-D radiation transfer models to simulate the reflectance fields of explicitly modelled heterogeneous canopy architecture representations. In section 3.2 the **Raytran** model was introduced and the validation efforts of its authors were presented. In section 3.4 the RAMI intercomparison

exercise compared it with a set of other RT models. This evaluation turned out to be very favorable, most notably in terms of its accurate representation of the signal’s angular variability, and, with respect to energy conservation under conservative scattering conditions. Since the **Raytran** model is capable of accurately describing the relevant radiative processes within arbitrarily complex three-dimensional scenes, and computations can be carried out once and for all in advance, the LUT-based approach is an appropriate inversion procedure to apply it to the extraction of a comprehensive set of structural and optical vegetation canopy parameters from remote sensing observations.

Annex A documents the inversion of the **Raytran** model against multispectral data gathered by the **VEGETATION** sensor over northern Europe, aimed at retrieving and characterizing the structure of explicitly modelled 3-D coniferous forest stands in that region. This work is published in Widlowski et al. (2001a). In essence, the three-step method includes: 1) the generation of an accurate 3-D representation of the structural and optical canopy properties at the spatial resolution of the sensor based on field measurements, 2) the simulation of the TOA spectral reflectance fields for a variety of atmospheric aerosol conditions and the view and illumination geometries that can occur with that sensor over this region, and 3) the selection of the optimal solution from amongst the set of pre-defined surface types such that both temporal consistency and the necessary agreement in terms of the specified uncertainty level are guaranteed. More specifically, the study in Annex A utilizes five different surface types consisting of mature Scots Pine (*Pinus sylvestris*) forests with tree densities of 100, 200, 400, 800 and 1200 stem/hectare. For each of these surface types the reflectance field in the blue, red and NIR bands at the TOA were simulated using a subarctic summer model with aerosol optical depths of 0.05, 0.15, 0.25, 0.35 and 0.45 at 550 nm. A piece-wise χ^2 approach, like that of section 4.1.2 was adopted to select the set of most likely solutions to the inverse problem. Maps can then be generated showing the spatial distribution of the retrieved surface types (or any known structural and optical variable thereof), their associated atmospheric optical depth on the day of retrieval, as well as the error criterion ϵ associated with this retrieval. The methodology behind this approach is completely generic, and thus can easily be prototyped for different instruments and biome types. One important aspect behind this kind of LUT based inversion approach, however, still remains to be addressed in more detail. This concerns the actual discernability of the predefined solutions in the LUTs, and how this may affect the outcome of any inversion attempt – especially if a great number of surface types solutions are available.

4.2.1 Radiative discrimination of the pre-defined surface types

As more surface types are being added to the set of potential solutions, the question arises as to how different these biomes remain at the TOA (in terms of their spectral BRF values). The importance of this issue derives from the fact that two or more solutions in the LUTs will never be distinguishable on the basis of actual measurements if their differences are smaller than the likely errors of measurements, *i.e.*, the instrument calibration accuracy. Conversely, if it is essential for a given application to distinguish between two given states of the environment, then the observational strategy and instruments must be designed to permit the reliable observation of such differences. Obviously, the radiative discernability amongst the pre-defined surface types in the LUT depends both on the increments and ranges of the selected aerosol types, the structural and optical canopy generation parameters, as well as the number of simultaneous satellite observations that are available to discriminate between them. In the case of the monodirectional **VEGETATION** instrument, the conditions imposed by equation 4.3 require the blue, red and near-infrared TOA BRF simulations all to lie within ϵ % of their corresponding satellite observations if they are to be identified as a solution to the inverse problem.

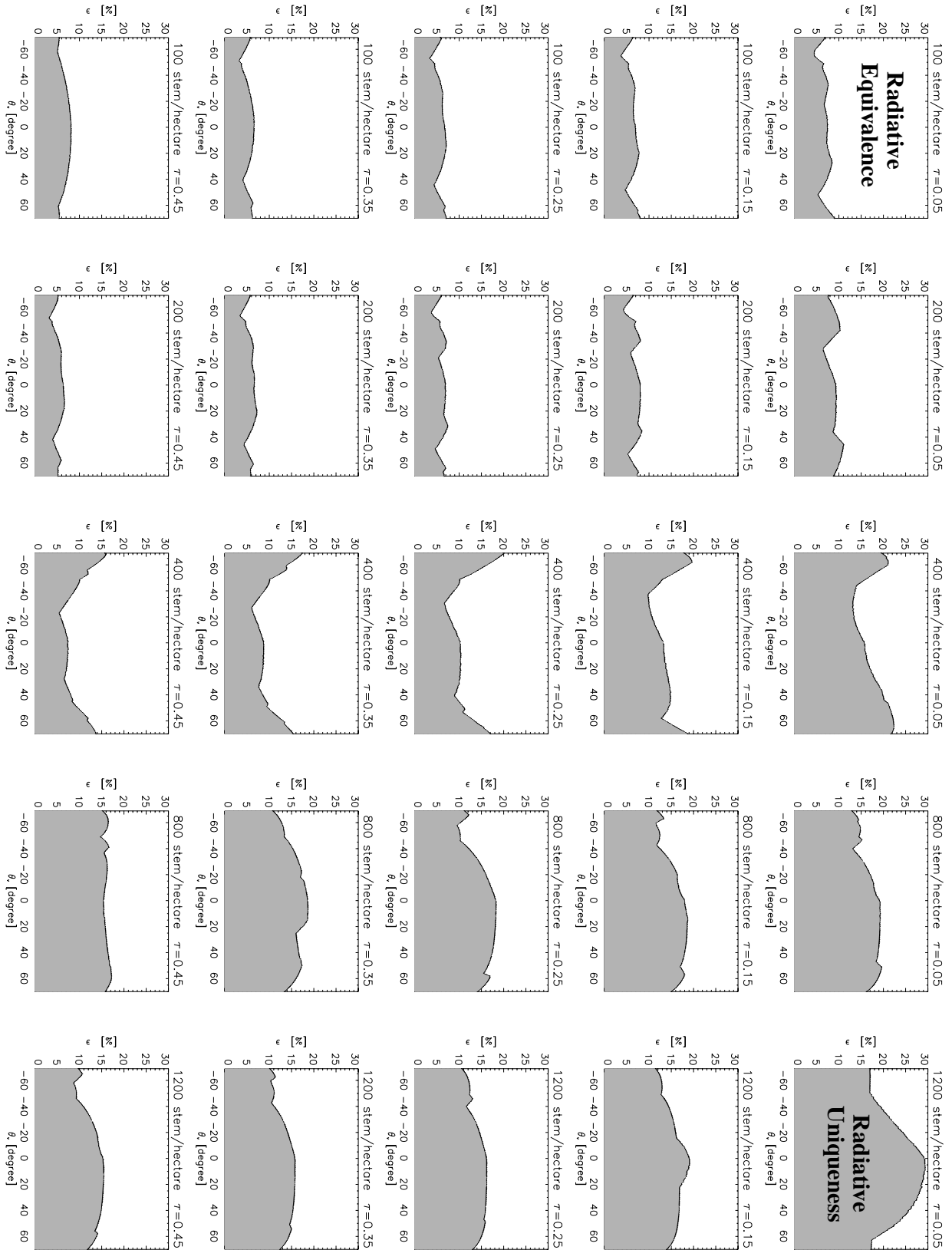


Figure 4.1: Variations in the radiative separability limit, $\hat{\epsilon}$, of the 25 reference surface type/atmospheric depth combinations (indicated on the top of each panel), with respect to all other pre-defined surface types (regardless of their associated atmospheric depths) on the basis of their TOA spectral BRF values in the principal plane and for $\theta_o = 49^\circ$. $\hat{\epsilon}$, which is expressed as a percentage of the reference BRF values, represents the transition level between the regimes where radiative uniqueness ($\epsilon < \hat{\epsilon}$) and radiative equivalence ($\epsilon > \hat{\epsilon}$) of the reference solution with respect to all remaining predefined candidate solutions exists.

When assessing the radiative discernability of the pre-defined surface types in a LUT, one has to determine the smallest value of ϵ such that at least one solution amongst the remaining set of predefined LUT candidates will provide equivalent BRF values to those of the reference surface type/atmospheric depth solution (for all measurement configurations under the specific conditions of illumination and observation)⁵. This value is denoted by $\hat{\epsilon}$, and represents the transition level between the regimes where radiative uniqueness ($\epsilon < \hat{\epsilon}$) and radiative equivalence ($\epsilon > \hat{\epsilon}$) of the reference solution with respect to all remaining predefined candidate surface types exists. Figure 4.1 documents the variations of $\hat{\epsilon}$ amidst the 25 predefined surface type/atmospheric depth combinations of annex A, for a range of view zenith angles (θ_v) and for $\theta_o = 49^\circ$. Any value of ϵ outside the grey shaded area will thus result in at least one further surface type becoming a ‘probable’ solution (under some atmospheric aerosol conditions), capable of explaining the measured BRF values within the limits of this ϵ .

In Figure 4.1 the radiative separability limit of a particular reference surface type (*i.e.*, the boundary between the grey and white areas) tends to be reduced in value if its associated atmospheric depth is increased. A similar trend can be observed if, for a given atmospheric depth condition, the tree density of the reference surface type is being reduced. This development can be anticipated since an increase in vegetation cover implies higher (lower) BRF values in the NIR (red) spectral bands, whilst an increase in the atmospheric depth reduces (augments) the corresponding TOA BRF values—with respect to those at the TOC—such that they will become more similar to the reflectance values of lower tree density solutions at that wavelength. Whereas the 400 stem/hectare forest type benefits from an enhanced radiative separability limit at large view zenith angles, the 1200 (and for low atmospheric depth conditions also the 800) stem/hectare forest type retains its radiative uniqueness longest under small view zenith angles. Low tree densities (100 and 200 stem/hectare) are least discernible and their similar behaviour of $\hat{\epsilon}$ indicates that they may become radiatively equivalent to each other above $\sim 3\%$ for some selected view zenith angles (11% under all viewing and atmospheric depth conditions). In annex A the error criterion ϵ , was raised from 3 to 8%, with the lower value being related to the instruments absolute radiometric resolution limit (Henry and Meygret 2000), and the upper value, to the in-flight, root-mean-square deviation from the reference calibration over bright sands and deserts in the blue, red and near-infrared bands. Consequently, VEGETATION measurements with BRF values that fall in between (or within the intersection of) the TOA spectral BRF envelopes—compare with Figure A-3—of the pre-defined surface types, will always yield more than one probable surface type solution if the error criterion is raised above the level of grey-shaded areas in Figure 4.1. For the lower tree-density surface types this implies that (as soon as ϵ is raised above 3%) the selection of the most likely surface type (in the sense of section A-2.3) will depend on such trivial issues as the number of pre-defined aerosol loads in the LUTs and the viewing conditions with which a surface location is being observed. Although this might not have had any significant implications as to the retrieved surface type maps in annex A (simply because less than 1% of the pixels were identified as belonging to these two surface types and even so the viewing conditions might have been such as to guarantee an unbiased retrieval at these locations); nevertheless, the consequences of these findings should not be underestimated – especially if a LUT-based inversion scheme with a multitude of predefined surface types, or under many different types and loads of atmospheric aerosol is to be attempted. Strictly speaking,

⁵The radiative separability limit, $\hat{\epsilon}$ between a reference surface type S_r (with associated aerosol load τ_r), and a series of $c = 1, \dots, C$ different candidate surface types S_c (with $a = 1, \dots, A$ conditions of associated aerosol loads τ_a) is defined in accordance with equation 4.2, where for any specific measurement condition k the largest acceptable error criterion is: $\epsilon_{r,p,k} = 100 |f_{r,k} - f_{p,k}| / f_{r,k}$; with $r = (S_r; \tau_r)$, $p = (S_c; \tau_a)$, and f indicating the output of a particular RT model (for actual measurements $f_{r,k}$ would have to be replaced by \mathcal{M}_k). To satisfy equation 4.3 under these conditions requires $\epsilon_{r,p} = \text{Max}(\epsilon_{r,p,1}; \epsilon_{r,p,2}; \dots; \epsilon_{r,p,K})$ for any potential candidate solution $p = 1, \dots, P = CA$, and overall if $\epsilon_r = \text{Min}(\epsilon_{r,1}; \epsilon_{r,2}; \dots; \epsilon_{r,P})$ then $\hat{\epsilon} \equiv \epsilon_r$.

every surface type/atmospheric depth solution should only be retrieved up to the limit defined by its radiative separability $\hat{\epsilon}$ under the given conditions of illumination and observation. One way to increase this value (for a given number of pre-defined surface types), is by adding a multi-angular component to the spectral measurements.

Indeed, both Gobron et al. (2000a) and Vogt et al. (2000) have recently shown that, not only the number of probable solutions but also the error in the retrieved reflectance field is greatly reduced when multidirectional information is taken into consideration. This has obvious consequences on the quality of information that may be extracted from optical remote sensing data. In the context of space-borne observations of the biosphere, multiangular sampling of the terrestrial reflectance anisotropy has already led to a better decoupling of the atmosphere from surface BRDF retrievals and hence also to improved estimates of photosynthesis, FAPAR, LAI, crown size, leaf normal distributions and land cover classification, *e.g.*, Kimes and Sellers (1985), Sellers (1987), Pinty and Verstraete (1991), Sellers et al. (1992), Clevers et al. (1994), Martonchik et al. (1998a), Martonchik et al. (1998b), Diner et al. (1999), Pinty et al. (2000b), Pinty et al. (2000a). Table 4.1 compares the smallest radiative separability limits of the 25 surface type/atmospheric depth combinations in Figure 4.1 to what $\hat{\epsilon}$ would be if all nine MISR view zenith angles ($0^\circ, \pm 26.1^\circ, \pm 45.6^\circ, \pm 60.0^\circ, \pm 70.5^\circ$) were available in the principal plane to discriminate between the LUT entries. Indeed the radiative separabilities of the various predefined solutions have all been increased with respect to the minimum values in Figure 4.1. However, although the values of $\hat{\epsilon}$ have almost doubled on average, both the 100 and 200 stem/hectare forest types—with their very low LAI levels of 0.15 and 0.30, respectively—remain partially inseparable at the 8% error criterion level used in annex A. As mentioned before, the identification of a ‘most likely’ solution from amongst the set of predefined surface types should only be accepted if this selection occurs within its range of radiative uniqueness with respect to all other, realistically modelled, LUT solutions (under the given conditions of observation and illumination). Hence as a general guideline, LUT based inversion schemes should be carried out with 1) a minimum amount of predefined surface types still capable of expressing the natural variations in the land cover types within the region of interest, 2) sensors possessing the best radiometric accuracy to avoid the indistinguishability of the predefined solutions within the uncertainty range of the sensor, and 3) instruments capable of collecting sufficient (spectral and directional) measurements to provide the necessary criteria for the discrimination of the predefined surface types. As regards the level of the maximum tolerable error criterion in LUT based inversion schemes - this should not be smaller than the instrument specific calibration accuracy, and should not exceed (on an individual basis) the radiative separability limit of the predefined surface type/atmospheric depth combinations under the precise conditions of observation and illumination.

The results from Figure 4.1 and further sensitivity tests can thus be summarized by stating that 1) the radiative separability limit of any given surface type is substantially reduced at the TOA, 2) different magnitudes of $\hat{\epsilon}$ exist for different surface types under identical viewing and illumination conditions, 3) different optimal viewing conditions exist for the correct retrieval of these surface types, and 4) both comments 2 and 3 depend on the actual number of predefined surface types and aerosol loads, as well as the available number of (spectral and directional) measurement conditions.

4.2.2 New directions for LUT-based inversion methods

An alternative way to enhance the separability of the pre-defined surface types may come from the approach for designing optimized vegetation indices *e.g.*, Verstraete and Pinty (1996), Gobron et al. (1999b), Govaerts et al. (1999), Gobron et al. (2000b), Gobron et al. (2001c). Here,

Table 4.1: The radiative separability limit of the 25 predefined surface type/atmospheric depth combinations of Figure 4.1 for mono-directional and multi-directional observations in the principal plane and for θ_0 being 49° . For any value of $\epsilon > \hat{\epsilon}$ at least one of the remaining candidate surface types will become radiative equivalence to the reference solution.

| Tree density [stem/ha] | Smallest monodirectional $\hat{\epsilon}$ [%] | | | | | Multidirectional $\hat{\epsilon}$ [%] [†] | | | | |
|---------------------------|---|-------|-------|-------|-------|--|-------|-------|-------|-------|
| | $\tau = 0.05$ | 0.15 | 0.25 | 0.35 | 0.45 | $\tau = 0.05$ | 0.15 | 0.25 | 0.35 | 0.45 |
| 100 | 4.31 | 3.54 | 3.22 | 3.06 | 4.92 | 8.89 | 7.88 | 6.98 | 6.44 | 7.98 |
| 200 | 6.30 | 4.13 | 3.60 | 3.32 | 3.08 | 10.95 | 7.90 | 6.82 | 6.82 | 6.21 |
| 400 | 12.95 | 9.66 | 6.54 | 5.90 | 5.30 | 22.10 | 18.59 | 20.25 | 17.48 | 16.15 |
| 800 | 12.78 | 11.40 | 9.41 | 10.64 | 14.55 | 19.06 | 18.36 | 18.02 | 18.48 | 17.06 |
| 1200 | 16.82 | 11.33 | 10.44 | 9.96 | 8.60 | 28.95 | 18.84 | 16.01 | 15.58 | 15.18 |

[†] Multidirectional refers to the 9 MISR view zenith angles, *i.e.*, $0^\circ, \pm 26.1^\circ, \pm 45.6^\circ, \pm 60.0^\circ, \pm 70.5^\circ$

the satellite measured BRF values at the TOA in the red and NIR are *rectified* to the level of the TOC on the basis of information about the atmospheric state contained within the blue spectral band, and in the case of mono-directional instruments some assumptions about the anisotropy properties of the reflectance field. More specifically, the rectified reflectances in the red ($\rho_{R_{red}}$) and NIR ($\rho_{R_{nir}}$) are given by:

$$\begin{aligned}\rho_{R_{red}} &= g_1[\rho_0(\lambda_{blu}), \rho_0(\lambda_{red})] \\ \rho_{R_{nir}} &= g_2[\rho_0(\lambda_{blu}), \rho_0(\lambda_{nir})]\end{aligned}$$

where $\rho_0(\lambda_i)$ corresponds to the optimal value of the amplitude parameter of the BRF field derived from the RPV model (Annex C, section C-2.1) at the spectral band i . The value of this parameter can be optimally retrieved using a new inversion scheme of the RPV model fully described in Gobron and Lajas (2001). The formula used for parameterizing the polynomials g_1 and g_2 in the case of the VEGETATION instrument is given by (Gobron et al. 1998):

$$g_n[\rho_0(\lambda_{blu}), \rho_0(\lambda_i)] = \frac{l_{n,1}(\rho_0(\lambda_{blu}) + l_{n,2})^2 + l_{n,3}(\rho_0(\lambda_i) + l_{n,4})^2 + l_{n,5}\rho_0(\lambda_{blu})\rho_0(\lambda_i)}{l_{n,6}(\rho_0(\lambda_{blu}) + l_{n,7})^2 + l_{n,8}(\rho_0(\lambda_i) + l_{n,9})^2 + l_{n,10}\rho_0(\lambda_{blu})\rho_0(\lambda_i) + l_{n,11}}$$

where the values of the m coefficients $l_{(n,m)}$ of each polynomial function g_n ($n=1,2$) are estimated once and for all using an optimization procedure that minimizes the following cost function:

$$\delta_{g_n}^2 = \sum_{\zeta_\lambda} \left[g_n \left(\rho_0(\lambda_{blu})^{TOA}, \rho_0(\lambda_i)^{TOA} \right) - \rho_0(\lambda_i)^{TOC} \right]^2 \rightarrow 0$$

ζ_λ represents the domain within the spectral space where the optimization is sought. This cost function forces the polynomial functions g_1 and g_2 to deliver rectified values which are as close as possible to the optimal value of the amplitude parameter of the BRF derived from the RPV model, namely $\rho_0(\lambda_i)$, estimated at the TOC for each and every surface type and atmospheric condition included in the training BRF data sets (Gobron et al. 2001a).

Thus, given the values of the various polynomial coefficients for the VEGETATION instrument (Gobron et al. 1998), the satellite observations could be rectified to $\rho_{R_{red}}$ and $\rho_{R_{nir}}$ which, in turn could then be compared against similar entries in the LUTs to identify any appropriate surface type solutions. Such an approach would not only eliminate the need for lengthy computations to generate the spectral TOA BRF values, it would also reduce the computer memory requirements since only 2 values ($\rho_{R_{red}}$ and $\rho_{R_{nir}}$) would have to be stored in the

LUTs for every illumination condition and surface type. However, by assuming a shape for the reflectance anisotropy of the BRF field (in the case of mono-directional observations), one obviously eliminates the use of all information contained within the angular function of the RPV model (equation C-2). This approach might also compromise the accuracy of the rectified reflectance values. Multi-angular instruments, on the other hand, possess the advantage that they allow the quantification of the anisotropy of the reflectance field at the TOA. Hence the rectification procedure could be performed using ρ_0 parameters that were retrieved without any assumptions about the shape of the reflectance anisotropy. Recently, Gobron et al. (2001a) showed that multiangular data from MISR permits the reconstitution of k_{red}^{TOC} from k_{red}^{TOA} using a rectification procedure that is based on the information contained in the RPV model parameter Θ_{red}^{TOA} . In the context of LUT-based inversion strategies, this would then provide another source of information, which may have interesting applications in terms of land cover classification.

4.3 Discussion

A successful, LUT-based inversion of three-dimensional RT models offers a plenitude of optical and structural canopy parameters for interpretation. Ideally, it would be desirable to have the radiative separability limit of all the predefined solutions as large as possible, and greater than the sensor calibration accuracy. Multiangular measurements can add an extra information component to multispectral data and thus enhance the discrimination of the LUT entries. Similarly, improved sensor calibration accuracies, narrowed spectral bands and a minimum set of predefined surface type solutions will also add to the success of a LUT-based inversion scheme – if the radiation transfer within the canopy (and atmosphere) is modelled in an appropriate manner. Three dimensional RT models like *Raytran* can generate canopy representations with almost any degree of complexity; their main limitation being the available computer memory. The number of their (structural and optical) state variables L_{3D} can become very large as the realism of the simulated canopy representation approaches that of nature. As such their usage in a LUT-based inversion scheme may necessitate the inclusion of an increased number of predefined surface types. This, however, will inevitably reduce the separability of the LUT entries, since the many more combinations of state variables may all yield reflectance values that lie within the bounds of some specified error criterion. Furthermore, from the discussion at the end of section 4.1 it can be expected that, with increasing number, some of the many L_{3D} state variables may become inconsequential (or only under specific conditions contributors) to the measured digital number at the TOA. The reliability of their retrieved values might thus be seriously compromised (Verstraete et al. 1996). In fact, it is clear that remote sensing data can only provide information on those processes and variables that noticeably affect the radiation being measured. Consequently, the number of state variables for a given RT model should be kept as close as possible to the number of effective state variables that are needed in order to account (within ϵ %) for the observed variability in the signal. The question thus arises as to how many state variables are actually needed to explain a given set of space-borne measurements within some specified range of uncertainty? Or more pragmatically, was it actually necessary to utilize a three-dimensional RT model for the simulation of the coniferous forest stands in annex A? Could a one-dimensional canopy representation not have yielded identical results (to within ϵ %), both in terms of the generated spectral reflectance fields, and the retrieved land cover maps?

The answers to these questions, however, are slightly more involved than may be expected. The first point to consider is obviously related to the type of information that a user might want to retrieve. Is it actually possible to obtain this kind of information with a plane-parallel RT model? And if so, does that involve the extraction of multiple or individual state variables? What about the accuracy of these retrievals? Do all state variables have to be extracted within

similar accuracy bounds? How does the user justify these requirements? Is it actually meaningful to attach an accuracy criterion on (information relating to) the retrieved state variables of a RT model inversion? After all, remote sensing observations can only describe the most pertinent *radiative* surface characteristics, and solutions to the inverse problem are selected in accordance to how well they match the observed reflectance data and not on the accuracy of their state variables – which cannot be known at the time of retrieval anyway. In general, the question as to what may actually constitute an acceptable match, between the modelled and measured data-strings, ultimately hinges on 1) the extent (global, regional) of the application at hand, *i.e.*, the size and content of the LUT, 2) the type, accuracy and reliability of the information to be retrieved, and 3) the available resources (time, money, people, computers, etc). Suffice to say that the interpretation of remotely sensed data with one-dimensional RT models should only be considered for the extraction of quantitative information over spatially homogeneous surfaces, or when average quantities are sufficient for the intended purposes.

In the context of LUT based inversion schemes of quasi-simultaneously gathered satellite observations, the possibility to utilize plane-parallel surface type representations would not only reduce the size of the required LUTs, but also increase the radiative separability limit between these candidate solutions. In order to investigate the validity of this homogeneity assumption, chapter 5 will assess the capability of a plane-parallel RT model to fit the BRDF values that were simulated over three-dimensional canopy representation, as well as the bias that can be expected when such RT models are utilized in retrieving a major state variable (LAI). More specifically, multi-angular simulations over structurally heterogeneous coniferous forests at different wavelengths, illumination conditions and spatial resolutions will be documented in terms of their radiative separability limit and LAI bias with respect to a LUT of plane-parallel surface type solutions.

4.4 Conclusion

The inversion of physically based RT models against multiple sets of measurements was discussed both for classical and LUT-based inversion. It was argued that, when attempting to select the set of valid solutions in a LUT-based inversion scheme, a *piece wise* χ^2 approach was preferential to the more standard *summation* approach, since the former ensures that the simulations match the observations at *every* view angle and spectral band. This approach was then used to invert the **Raytran** model against multispectral VEGETATION observations for the identification and characterization of boreal conifer forests in northern Europe (see annex A). It was subsequently noted, that a large number of predefined surface types will tend to decrease their mutual radiative separability limits in the LUTs. On the other hand, an increase in both the quality and quantity of the reflectance data (sampled in the spectral and angular domain) enhances the radiative discrimination between competing solutions in a LUT based inversion scheme.

Chapter 5

The Plane-parallel RT Model Bias Over Heterogeneous Forest Scenes

This chapter will investigate the scale dependent separability of BRF and LAI values that were simulated and retrieved over structurally homogeneous and heterogeneous canopy representations by the `Semi-Discrete` and `Raytran` RT models, respectively. Section 5.1 presents some of the motivations and caveats regarding the setup of such a discernability exercise. Section 5.2 documents the results obtained for different surface types, viewing, illumination and soil albedo conditions, whilst section 5.3 discusses some of the implications of these findings.

5.1 Assessing the radiative separability of 1-D and 3-D surfaces at different spatial resolutions: Motivations and caveats

Heterogeneity in the structural and optical properties of terrestrial surfaces gives rise to mutual shading and photon channeling effects, which—depending on the solar zenith angle and the spatial resolution of interest—can have a significant impact on the observed reflectance anisotropy of the BRF field at the TOC. To account for such radiative crosstalk, increasingly exhaustive canopy architecture representations are being included in physically based RT models that simulate the angular signatures of terrestrial surfaces at medium to high spatial resolutions. However, due to the various issues regarding the inversion of RT models with many state variables (see section 4.1), such an approach should not be seen as a justification *per se* for the unconditional inclusion of three-dimensional RT models in the interpretation of remotely sensed data. Rather, it should be the quality and quantity of the available (directional and spectral) reflectance data together with the tolerable level of BRF uncertainty (when attempting to simulate these observations), that has to serve as the primary criterion for the acceptance or rejection of the 1-D surface type hypothesis. So far, the computational advantage of many one-dimensional RT models accounted for the widely used assumption of partial or complete pixel homogeneity (amongst inversion algorithms) in the remote sensing literature, *e.g.*, Borel and Gerstl (1994), Adams et al. (1995), Hall et al. (1995), and Gobron et al. (1999a). With the advent of LUT based inversion techniques, this is, however, going to change, since the retrieval of biophysical structure parameters from remote sensing data can now be performed operationally with both 1-D and 3-D RT models, *e.g.*, Govaerts et al. (1997), Myneni et al. (1997), Gobron et al. (1999a), Knyazikhin et al. (1999), Pinty et al. (2000a), and Widlowski et al. (2001a). Thus, assuming that a given set of (spectral and angular) BRF measurements could equally well be explained (to within ϵ %) by both a 1-D and 3-D RT model, how was one to decide whether the state variables of the structurally homogeneous or heterogeneous surface type solution, respectively,

were to be used for further interpretation? One possible approach is provided by the ‘principle of parsimony’, which states that *plurality should not be posited without necessity*¹. This is an often used guideline in situations which require the selection amidst two competing theories that make exactly the same predictions. Together with some of the previous considerations, ‘Occam’s razor’ would thus favour the inversion of the 1-D physically based RT model over that of its more complicated 3-D counterpart (under the assumption that the two approaches were equal in all other aspects). An important implication of such a choice would be the effective loss of surface heterogeneity (from a radiative point of view) as soon as the user required accuracy level was such as to allow for the existence of 1-D surface type solutions. Whether or not the values of the retrieved state variables in the 1-D case would actually be the same as those of their corresponding counterparts in the 3-D RT model is—without the addition of further, independent data or selection criteria—essentially irrelevant. Both surface type definitions constitute equivalent solutions to the electromagnetic observations that were gathered by the detector optics of some remote sensor. The 1-D solution, however, has the advantage, that its choice of state variables is in all likelihood closer to those effectively needed to describe the radiation transfer (within ϵ %), which translates into their more efficient accounting of the observed variability in the signal, a smaller set of valid solutions during inversions, and a greater reliability in the retrieved values of these state variables.

Similar considerations have led to substantial efforts in comparing 1-D RT models with actual observations as well as sophisticated 3-D MC simulations in the context of retrieving cloud optical properties, *e.g.*, Welch and Wielicki (1984), Coakley (1991), Cahalan et al. (1994b), or Loeb and Davies (1996). Cahalan et al. (1994a) showed that within-cloud variations in stratocumulus cloud liquid water can cause albedos to be lower than the plane-parallel values by about 15% over mesoscale regions. However, this bias is significantly reduced when the independent pixel approximation (IPA)—which is but an area averaged combination of different 1-D RT model calculations, that ignores any horizontal radiation transport between its members—is compared to MC estimates of the domain-averaged (kilometer scale) albedo. At the same time, however, the IPA’s biases at the local scales can be quite dramatic (Marshak et al. 1995b). This is because at spatial scales below the typical mean free path of photons, the horizontal exchange of photons between columns of scatterers can no longer be ignored, *e.g.*, Davis et al. (1997), and Oreopoulos et al. (2000). However, since the IPA benefits from a definite computational advantage with respect to MC approaches considerable attention has been devoted to its improvement (Gabriel and Evans 1996, or Marshak et al. 1998), and accuracy assessment (Cahalan et al. 1994b, Barker 1996, Chambers et al. 1997). Marshak et al. (1995a), for example, found that the IPA is also capable of representing the variability of the cloud optical depth field, while Zuidema and Evans (1998), who added vertical structure variations, observed that local shading now competed with radiative smoothing² and thus added to the biases at the smaller spatial scales. This latter issue of (subpixel scale) cloud-top structure has been thoroughly investigated by Loeb et al. (1997), Loeb and Coakley (1998) and Várnai and Davies (1999), among others, with cloud top height variations being shown to have very different and usually stronger effects on the scene averaged reflectivity, than volume extinction coefficient variations (Várnai 2000).

In the context of optical remote sensing of vegetated surfaces, the influence of surface heterogeneity and non-linear interactions between the scattering elements at the scale of observation

¹*Pluritas non est ponenda sine necessitate*, a statement commonly known as ‘Occam’s razor’, first postulated by William of Ockham (1285 - 1347).

²*Radiative smoothing* refers to the multiple scattering induced radiative interactions among nearby (point-like) scatterers of dissimilar optical properties in an IPA environment; with the consequence that radiance fields tend to be smoother than optical thickness fields (Davis et al. 1997).

have been recognized long ago, *e.g.*, Myneni et al. (1995b). However, as yet, little work has been directed towards a systematic evaluation of the bias that 1-D RT models may introduce. Whilst some attempts at assessing the errors associated with linear-(un)mixing methods (*e.g.*, Bastin 1997, or Settle and Campbell 1998), were performed, most studies were concerned with the effects of sensor resolution and landscape heterogeneity on statistical image interpretation techniques, *e.g.*, Cushnie (1987), Puech (1994), Moody and Woodcock (1995), Benson and MacKenzie (1995), Friedl (1997). On a more fundamental level, Pinty et al. (1996) pointed out that by adding height to an initially 1-D representation of turbid canopy rows, the albedo of that surface could under certain illumination and scene architecture conditions diminish by as much as a factor of 2 with respect to the initial IPA hypothesis. Recently, Knyazikhin et al. (1998), who simulated the vertical structure of vegetation canopies in a fractal-like manner, found that the canopy transmittance no longer followed Beer's law³ as soon as the small-scale variability was taken into account. In order to assess the effect of structure with respect to the scale of observation this chapter will investigate the conditions for which the spectral reflectance fields of explicitly modelled 3-D vegetation canopies can be approximated using a simpler canopy architecture formulation. More specifically, the level of separability is sought, beyond which plane-parallel RT models⁴ become capable of delivering surface type solutions that are equivalent (in terms of their spectral and directional BRDF values) to those generated by more complex, three-dimensional MC ray-tracing models at a variety of spatial scales. In addition, the dependence of these effects on the solar illumination conditions and the optical and structural characteristics of the underlying surface type will be assessed. However, prior to presenting the results of these investigations, two experimental aspects of MC simulations of surface reflectance fields at multiple spatial scales have to be addressed, namely, the spatial extend of the scene and the choice of the TOC height level.

5.1.1 Raytran simulated reflectance anisotropy at multiple spatial scales

Nicodemus et al. 1977, defines the ratio of the directional fluxes traveling upward and downward through an infinitesimal area dA (*i.e.*, the bidirectional reflectance), as the product of the BRDF at that point and the projected direction of reflection: $d\Phi_r/d\Phi_i = \gamma_r d\Omega_r$. This allows to express the BRDF values originating from a non-zero surface area ΔA located at a height level z^{TOC} , such that they can be simulated with a Monte-Carlo ray-tracing model like **Raytran** (Ross and Marshak 1988):

$$\rho(z^{TOC}; \theta_i, \phi_i; \theta_r, \phi_r) = \frac{\Delta\Phi_r}{\gamma_r; pd \Delta\Phi_i d\Omega_r} = \frac{\pi \Delta L_r}{\Delta L_i d\Omega_r} \cong \frac{\pi N^\uparrow}{N^\downarrow \Delta\Omega_r} \quad (5.1)$$

where, N^\downarrow indicates the number of rays that are incident upon the surface area ΔA at z^{TOC} , and N^\uparrow represents the number of rays that are exiting through the same ΔA such that the projected solid angle of their exiting direction is $\Delta\Omega_r$ (Govaerts 1995). Since the uncertainty in the MC estimate of any given measurement improves as $1/\sqrt{N^\downarrow}$, it is not considered appropriate to sample the reflectance field of a large scale forest scene over successively smaller spatial areas if the latter regions are not receiving a high enough density of incident rays (compare also with Figure 3.2). One obvious way to mimic such an increase in spatial resolution, without loosing

³Beer's law relates the fraction of monochromatic radiation I_z/I_0 , that is transmitted from level 0 to level z , to the exponential of the optical thickness, $\tau_{(z)}$ along that path: $I_z = I_0 \exp(-\tau_{(z)})$.

⁴Throughout this work, the **Semi-Discrete** RT model is utilized to simulate the reflectance fields of plane-parallel vegetation canopies with finite sized leaves. Strictly speaking, it is thus capable of simulating the BRDF values of three-dimensional albeit structurally homogeneous vegetation canopies. Hence to differentiate this type of canopy architecture from purley turbid plane-parallel media (1-D) as well as structurally heterogeneous canopy representations (3-D) the notation 1-D' has been adopted.

any accuracy in the measurements due to the number of rays, is by reducing the dimensions of the scene under investigation. However, such an approach cannot yield identical results to a true ‘zoom-in’ of a larger identically structured forest scene.

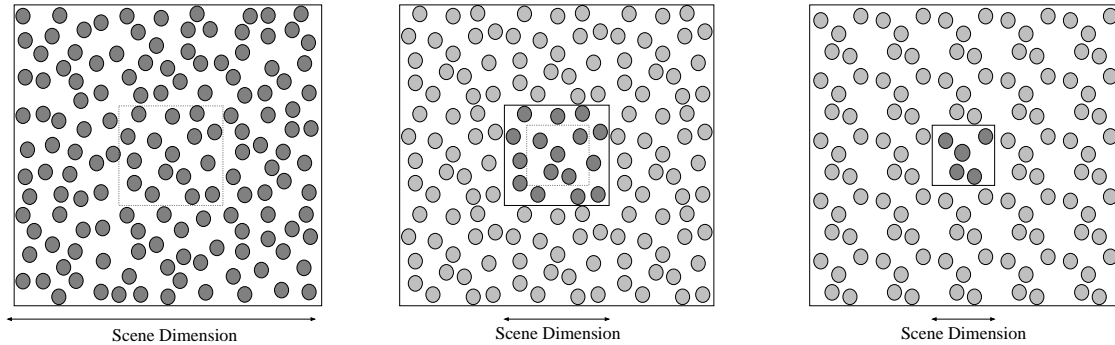


Figure 5.1: Increased regularity in the spatial arrangement of structural entities as the scene dimensions are reduced and cyclic boundary conditions apply. From left to right the dimensions of the world object (square with dark shaded circles) are reduced. Duplicated scene structures (light shaded circles) are shown up to the dimensions of the left most scene.

This is simply due to the cyclic boundary conditions (compare with section 3.2.1) that MC ray-tracing models, like *Raytran*, apply to simulate the horizontal photon fluxes that would enter a given scene if it were part of a greater, spatially continuous landscape pattern of similar structural and optical properties. Such an approach is conceptually equivalent to the replication of identical scenes and their placement, in a honeycomb manner, one next to the other. On the other hand, it may introduce artificial regularities in the spatial distribution of objects amidst the various instances of the original world object, especially when the latter is not densely populated and its dimensions are relatively small. Figure 5.1 illustrates this by showing how the ‘order’ of the dominant structures in the world object (*i.e.*, tree crowns) augments, as the dimensions of the scene (square with dark shaded circles) are reduced and duplicates thereof (light shaded circles) are utilized to cover the spatial extent of the original area. Whereas the mean horizontal distance that rays may travel between interactions remains relatively similar for all azimuthal directions in the left most illustration, this is no longer the case in the right most illustration where rays now may experience quasi-unbound trajectories if reflected in an appropriate direction from the underlying soil. Hence, if the dimensions of the world object fall significantly below the mean horizontal distance that a ray may travel inside it, then the directionality of the laterally entering and exiting rays (*i.e.*, the diffuse horizontal illumination component) will in all likelihood be altered, and so will also the azimuthal anisotropy of the measured reflectance field. In all generality, it can thus be stated that for MC simulations the reflectance field of a heterogeneous vegetation canopy at very high spatial resolution will differ from that obtained for the same vegetation patch when the *true variability* of the biome type *outside* the immediate area of coverage is taken into consideration.

To achieve such MC measurements, corresponding to a true zoom-in, it is proposed here to generate a large scale representation of a heterogeneous vegetation canopy (like those in annex A), and to illuminate successively smaller patches thereof for the purpose of retrieving the required reflectance fields within these areas. Such an approach requires however to know what distance rays may travel on average between their point of entry and exit on the upper surface of the world object (which was set to the same height as the TOC). This information can then be used to downsize the illumination-source area in order to perform higher spatial-resolution BRF measurements without introducing any significant accuracy losses (at least for

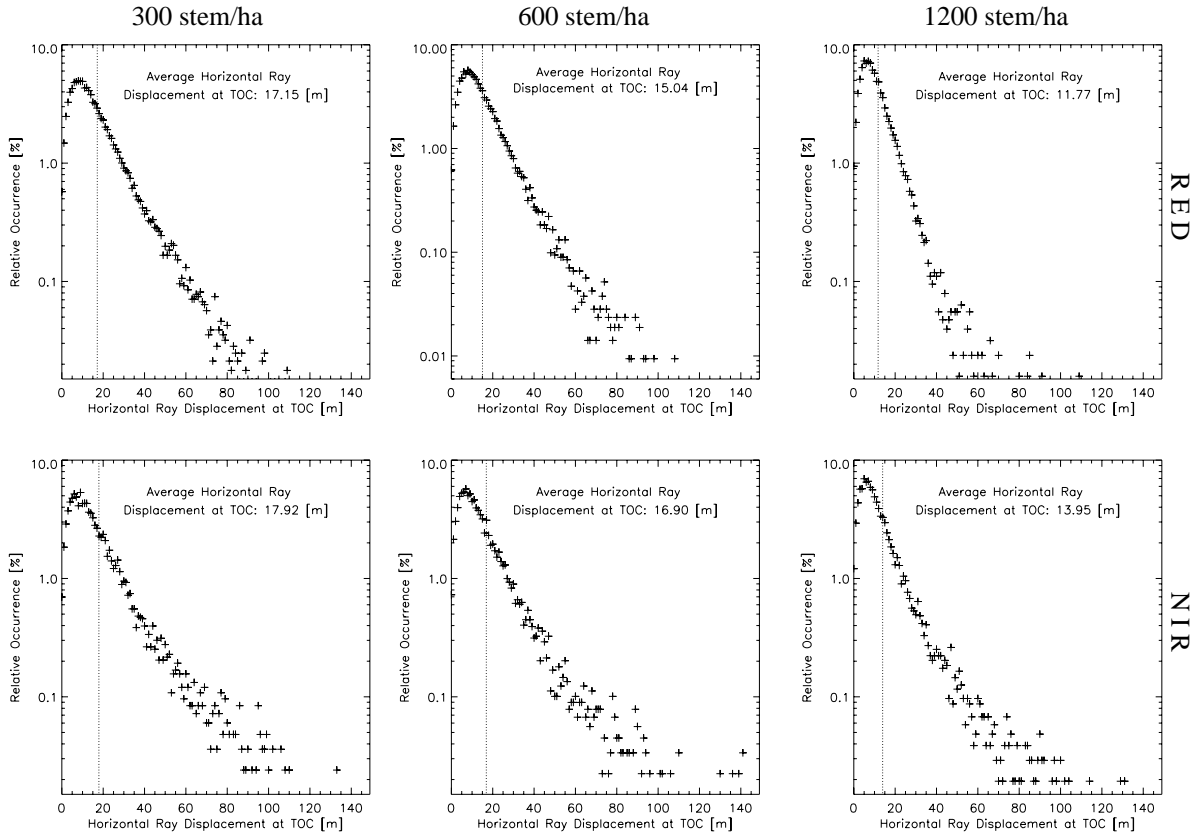


Figure 5.2: PDFs of the horizontal ray displacement (between the incoming and outgoing locations) at the TOC, for the optical and structural coniferous forest type properties described in annex A. Columns relate to different tree densities (indicated on top) whereas rows relate to different spectral conditions (indicated on the far right). In the red (NIR) it is the high absorption (scattering) of the foliage elements that accounts for the reduction in the average horizontal ray displacement as the tree density is increased. The scene dimensions are: $900 \times 900 \text{ m}^2$, and $\sim 10^4$ ray paths were used in the simulations ($\theta_0 = 30^\circ$, $\phi_0 = 0^\circ$).

$\theta_v < \sim 60^\circ$). The probability distribution functions (PDF) of these horizontal TOC distances can be obtained by illuminating the large scale canopy representations under identical conditions and for the same surface types for which the BRDF values are to be simulated at increased spatial resolutions later on. Figure 5.2 displays the PDF of these horizontal ray distances (HRD) at the TOC for three different tree densities (columns) and two spectral bands (rows). It was found that, if the BRDF values of a square-shaped area ΔA_i (smaller than the scene dimensions) were to be measured, then the sidelength of the directional illumination source in *Raytran* should be chosen approximatively equal to $\sqrt{\Delta A_i} + 4 \times \text{HRD}$. Such an approach would include $\sim 99\%$ (98%) of all rays in the red (NIR) spectral band - with those not contributing leaving the scene at zenith angles greater than $\sim 60^\circ$. Hence, by launching a large number of rays ($\sim 2^{31}$) from this source area, it becomes possible to gather different sets of BRDF measurements over consecutively smaller ground-areas without incurring more than a few percent of BRDF error due to the reduced number of rays. Tests indicated that it was best not to reduce the area from which the BRDF measurements were gathered below $\frac{1}{25}$ -th of ΔA_i , but instead to repeat the above procedure with different illumination source areas to cover the entire range of scales for which BRDF measurements were to be retrieved. To achieve this, four different illumination sources of sidelength 900, 405, 180, 105 m were used to illuminate square-shaped areas of sidelength 900, 300, 100, 33.33 m, respectively. The mean BRDF deviation that occurs with the above illumination scheme between the *Semi-Discrete* and *Raytran* models, in the case of structurally homogeneous leaf canopy of uniform leaf orientations, darkish soil conditions and an LAI of 0.5 in the principal (orthogonal) plane, were found to range from 2.7% (0.8%) to

5.1% (4.0%) in the red and 3.4% (1.9%) to 4.2% (2.7%) in the NIR as the spatial resolution of the 3-D scenes was reduced from 900 m to about 7 m, and if the rays were collected in angular bins of $\sim 3.5^\circ$ centered along the direction of the 7 innermost MISR view zenith angles. Here, the increase in the BRF deviations along the principal plane is due to the two models' differing representation of the hot spot effect ($\theta_0 = 30^\circ$) which is still partially captured by the 26.1° view zenith angle.

5.1.2 Defining the TOC height level across multiple spatial scales

The explicit reference of z^{TOC} in equation 5.1 requires that the height level of the BRF measurement at the TOC is selected such as to provide the best possible characterization of the underlying surface type at any spatial resolution (that is without introducing any significant new sources—or sinks—of illumination). In the context of the **Raytran** simulations earlier mentioned for the spectral reflectance fields over heterogeneous forest scenes at multiple spatial resolutions, it thus becomes mandatory to agree upon appropriate height levels for the various reference surface areas over which the upward and downward traveling rays are to be collected. At coarse spatial resolutions the TOC reference height (z^{TOC}) is very well defined for a slab-like canopy architecture: it coincides with the highest vertical extent of the leaf canopy (\hat{H}) that exists within the world object. For three-dimensional canopy representations the same definition may likewise apply, at sufficiently large spatial scales and in the absence of any significant topography. Figure 5.3 provides a graphical definition of these concepts, both for slab-like (top panel) and heterogeneous (bottom panel) forest architecture representations.

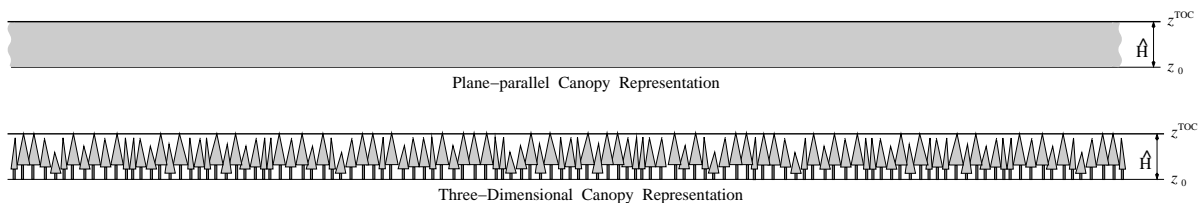


Figure 5.3: Graphical definition of the top of canopy height level (z^{TOC}), the highest vertical extent of the canopy (\hat{H}) and the ground level height (z_0) for slab-like (top panel) and heterogeneous (bottom panel) forest architecture representations at sufficiently large spatial resolutions and in absence of any significant topography.

In the case of 3-D Monte Carlo simulations of $\rho_{(z^{TOC})}$, it appears appropriate to identify the TOC reference height with the tallest point inside the simulated area of the (topographically flat) canopy representation. In the context of multi-scale characterizations of specified surface areas this may, however, lead to surprising findings. Consider, for example, an ideal space-borne sensor (*i.e.*, one that possesses a square wave modulation transfer function and orbits around a planet without atmosphere), capable of performing instantaneous TOC BRF measurements at multiple spatial scales i , such that 4^i pixels/observations would cover the same surface area ΔA_0 , as its coarsest scale ($i = 0$). Assuming further, that this ideal sensor was flying over a flat and uniformly covered forest area of very large extent—much greater than the coarsest scale of observation—and that the spatial extent of one pixel at the latter scale was significantly larger than the maximum height \hat{H} , encountered within its footprint area. Now, whereas, at this and subsequent low resolutions ($i = 0, 1, \dots, i$) the differences between the $z_{i,n}^{TOC}$ values of neighbouring pixels $n = 1, \dots, 4^i$ would be essentially negligible, at finer spatial resolutions ($i > i$), these variations in $z_{i,n}^{TOC}$ values would, however, become more and more accentuated due to the natural variability of tree heights in mature forest stands and the random placement of the pixels. This implies that the reflectance field of a three-dimensional forest stand that uniformly covers a spatial area much larger than ΔA_0 , were dependent on the spatial resolution

with which ΔA_0 were observed, *i.e.*, $\rho_0 \neq \sum_{n=1}^{4^i} \rho_{i,n}$ with $i > i$. The reason for this apparent lack of energy conservation is entirely due to the different reference heights of $z_{i,n}^{TOC}$ at different spatial positions n and resolutions i - as depicted in the top panels of Figure 5.4. Individual rays are capable of contributing to BRF measurements at different spatial positions n (via their local N_n^\downarrow and N_n^\uparrow numbers). These contributions depend however on the spatial scale of investigation, since the height levels, $z_{i,n}^{TOC}$ of the reference surfaces $\Delta A_{i,n}$ are constantly changing due to the spatial heterogeneity of the surface structure.

A better approach might thus consist in keeping the TOC height level fixed as the zooming-in is performed. This will guarantee identical reflectance fields over specified regions regardless of the scale of observation. On the other hand, such an approach may generate apparent increases (decreases) in the BRF values of a given pixel position l , if the neighbouring pixel k —along the line of sight of the sun—has a larger (smaller) $z_{i,k}^{TOC}$ value. This is because the presence (absence) of foliage at pixel k , may thus reduce (augment) the effective amount of incoming light $I_{0\text{eff}}^\downarrow$, that enters within the vegetation canopy at the position of the pixel l when compared to I_0^\downarrow , the expected intensity of light incident at $z_{i,l}^{TOC}$. This is made explicit in the bottom panels of Figure 5.4 which show graphically how the perceived brightness in a fixed TOC-height level approach can be affected by variations in the surface structure adjacent to the area of interest. The same behavior has also been noticed by Zuidema and Evans (1998) and Várnai (2000), who looked at cloud-top-height variations (under oblique illumination conditions) and the effect this had on the measured pixel brightness values.

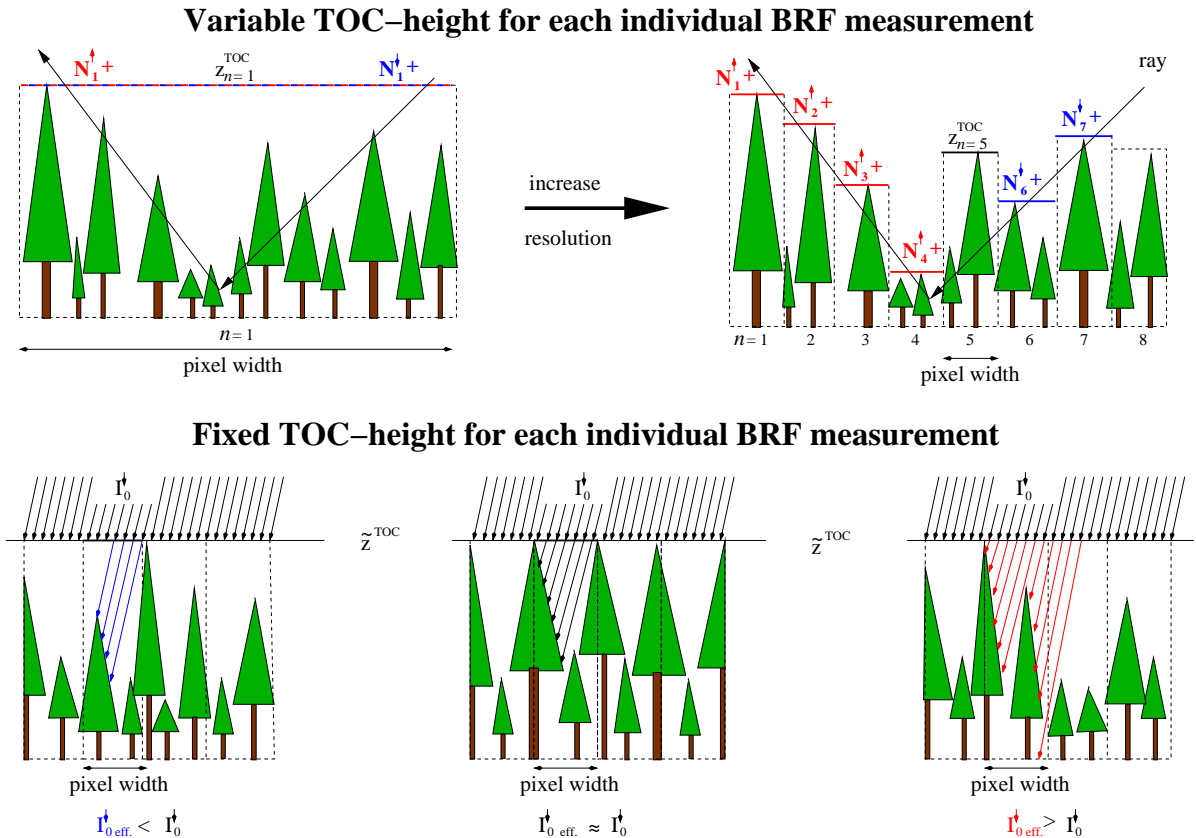


Figure 5.4: Top panels: Variable TOC height level approach for BRF measurements. When comparing low (left) and high (right) spatial resolution reflectance simulations over the same spatial area, energy conservation appears no longer maintained since individual rays may contribute to different numbers of BRF measurements at successive pixel resolutions. Bottom panels: Fixed TOC height level approach for BRF measurements. Variations in canopy height can lead to apparent increases (decreases) in brightness due to the effective illumination, $I_{0\text{eff}}^\downarrow$ being greater (smaller) than the direct illumination at the TOC, I_0^\downarrow .

In order to compare `Raytran` simulations from several spatial scales with one another it thus seems most appropriate to utilize a fixed z^{TOC} approach. However, from the above discussion it has become apparent that neither scheme is completely satisfactory in leading to a just characterization of the surface type below ΔA_i at higher spatial resolutions. This is because the radiative description of the canopy features contained within the volume below z^{TOC} is no longer independent of the structural and optical surface characteristics adjacent to the area of interest – if the spatial resolution of the sensor becomes comparable to (or smaller than) the horizontal mean free path of the photons, or, the height of the structures in the medium. Inter-pixel shading and illumination effects may induce significant variations in the effective (directional and diffuse) illumination components at these scales, such that the natural arrangement of the structures in the close vicinity of the area of interest may assert a strong effect on the recorded reflectance values unless the multiple scattering component in the canopy is very dominant. This situation appears somewhat analogous to the classical uncertainty relations of Heisenberg in the sense that an accurate characterization of the surface properties through its radiative signatures entails a limitation in the spatial position these properties can be assigned to. In other words, the more precise the location of the surface properties is to be determined (*i.e.*, pixel sizes that are smaller than the horizontal mean free path), the less reliable the resulting radiation measurement may become in terms of describing the actual properties of the content within these pixels, and vice versa. The reasons for this are, however, entirely related to the fact that the BRF definitions of section 2.2.2 imply a *plane of reference*, and thus, are being applied to situations for which they were not originally derived for.

5.2 The scale dependent separability of 1-D' and 3-D canopies

To address the scale dependent bias of plane-parallel RT models over heterogeneous forest scenes, the `Raytran` and `Semi-Discrete` models are to simulate the spectral reflectance fields at the TOC for a series of structurally heterogeneous (3-D) and homogeneous (1-D') forest environments, respectively. More specifically, the `Semi-Discrete` model will be used to generate a series of LUTs containing the TOC spectral BRF values, corresponding to the structural and optical surface type properties in Table 5.1 under specific illumination conditions ($\theta_0 = 30^\circ$ and 55°). For differently sized subregions of a 3-D representation of spatially continuous conifer forests that are structurally equivalent to those in annex A (see Table 5.2), the red and NIR reflectance fields at the TOC are then generated with the `Raytran` RT model in accordance with the considerations in section 5.1. A piece-wise χ^2 approach, which must be satisfied at every spectral and directional measurement condition, will then be applied to find the closest matching candidate(s)—under identical view and illumination conditions—between the LUT entries and the BRF values of the 3-D forest representation. These findings can then be analyzed both in terms of the separability between the 1-D' and 3-D BRF values, and the error associated with the retrieved LAI of the structurally homogeneous solution. Since the LAI constitutes the information that is to be extracted, both the plane-parallel and 3-D canopy representations possess identical leaf optical properties, and the 2505 1-D' surface type solutions contained within the LUTs have been generated almost exclusively in terms of the state variable of interest.

5.2.1 The radiative separability of 1-D' and 3-D canopies at multiple scales

The left hand panel in Figure 5.5 presents the radiative separability limit, $\hat{\epsilon}$ of a structurally heterogeneous forest with a tree density of 600 stem/ha under experimental conditions A (described in Table 5.2) as the spatial resolution is decreased from 900 to ~ 7 m. More specifically the results apply to the BRF values in the red spectral band, when the target area is being observed under viewing conditions corresponding to the 7 innermost MISR view zenith angles

Table 5.1: Structural and optical properties of the plane-parallel surface types in the LUTs.

| Variable | Value(s) |
|---------------------------------|---|
| Canopy Height | 10 m |
| Leaf Area Index | 0.0 ... 10.0 (in steps of 0.1) |
| Leaf Normal Distr. [†] | planophile, plagiophile, extremophile, erectophile, uniform |
| Leaf Radius | 5 cm |
| Leaf Reflectance | 0.0542 (red) 0.4964 (NIR) |
| Leaf Transmittance | 0.0144 (red) 0.4418 (NIR) |
| Soil Albedo (red) | 0.0722, 0.1255, 0.1724, 0.2382, 0.2986 |
| Soil Albedo (NIR) | 0.0845, 0.1593, 0.2070, 0.2923, 0.3555 |
| Scattering Law | bi-Lambertian (leaf), Lambertian (soil) |

[†]The leaf normal distributions are simulated with beta (trigonometric) functions in the case of the *Raytran* (*Semi-Discrete*) RT model (compare with section B-3).

Table 5.2: Experimental setup for the heterogeneous conifer forest types[†] covering 900 m².

| Experiment Tag | θ_0 [°] | Mean LAI per Tree | Soil Albedo RED | Soil Albedo NIR | Tree Height [m] | LND |
|----------------|----------------|-------------------|-----------------|-----------------|-----------------|---------|
| A | 30 | 3.37 | 0.1255 | 0.1593 | 12.0 ±1.0 | uniform |
| B | 30 | 3.37 | 0.2382 | 0.2923 | 12.0 ±1.0 | uniform |
| C | 30 | 10.11 | 0.1255 | 0.1593 | 12.0 ±1.0 | uniform |
| D | 55 | 3.37 | 0.1255 | 0.1593 | 12.0 ±1.0 | uniform |

[†]Every 3-D canopy representation was characterized by a needle area equivalent to a 5 cm (1 mm) long (wide) cylinder, and identical foliage optical properties as in Table 5.1.

(*i.e.*, $\pm 60.0^\circ$, $\pm 45.6^\circ$, $\pm 26.1^\circ$, and 0°) along the principal plane. Every star-symbol indicates the level of the mean separability between the BRF values corresponding to a typical 3-D forest patch (at that spatial resolution), and its closest matching 1-D' surface type solution from the LUT. In other words, if the user-specified level of BRF accuracy is equal to that indicated by one of the star-symbol (at that spatial resolution), then the surface type solutions provided by a 1-D' RT model are, on average, capable of providing equivalent BRF values at the TOC than those generated with a structurally heterogeneous vegetation canopy. The vertical bars that cross the star-symbols represent the largest and smallest separability values that were encountered when performing up to 25 different estimates of the 1-D' to 3-D BRF deviations at specific spatial scales. The grey shaded area at the bottom of the left hand graph indicates the mean BRF error between the *Semi-Discrete* and *Raytran* model, when generating the reflectance field of a structurally homogeneous canopy of average structural and optical properties equivalent to the 900 m² three-dimensional conifer forest representation under experimental conditions A. The various vertical bars indicate how this model difference changes in accordance with the number of rays that (given the procedure of section 5.1.1) were available at the various spatial scales at which the radiative separability limit of the 1-D' and 3-D RT models were evaluated.

The radiative separability limit⁵, $\hat{\epsilon}$ in the left panel of Figure 5.5 remains almost constant from spatial resolutions of 900 m down to ~ 80 m. At smaller spatial scales both the mean and range of $\hat{\epsilon}$ become continuously larger. This can be explained by the fact that the “statistics” of

⁵For a mathematical definition of the *radiative separability limit* see the footnote on page 38.

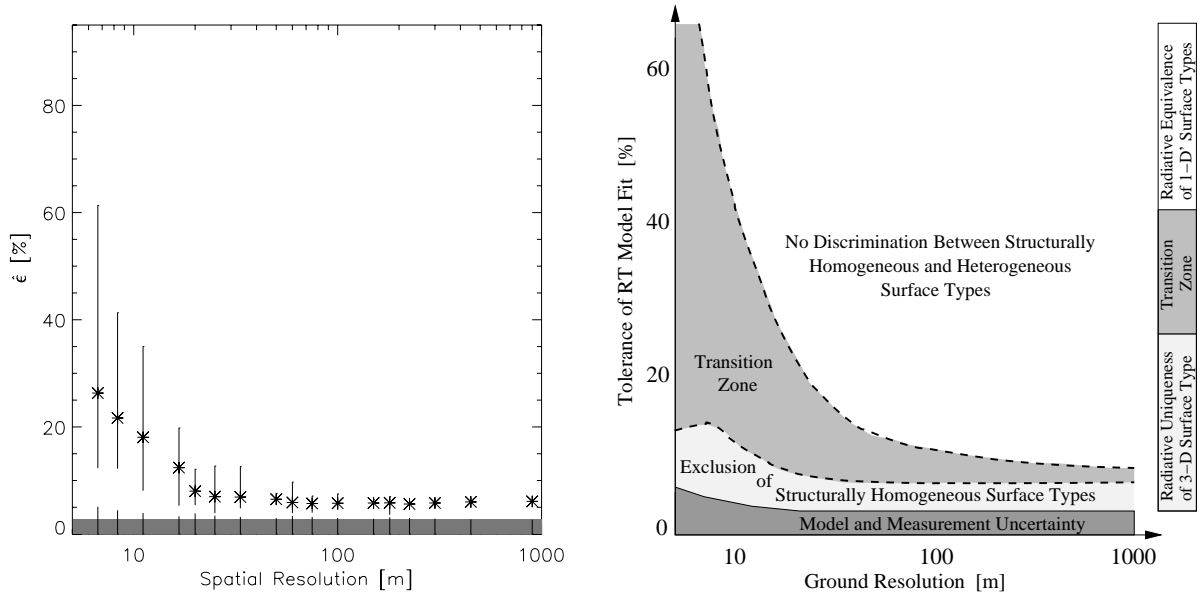


Figure 5.5: Left panel: The radiative separability limit, $\hat{\epsilon}$ of a 600 stem/ha 3-D forest representation and its closest matching 1-D' surface type from the LUT (experimental conditions A in Table 5.2), in the red spectral band using the 7 innermost MISR view zenith angles along the principal plane. Right panel: Conceptual partitioning of the left hand side panel in the context of interpreting remotely sensed observations of such a forest type with physically based RT models.

the 3-D forest representation contained within the area under observation (pixel) remains relatively unchanged for spatial resolutions larger than or equivalent to 80 m (indeed the 3-D forest scenes were generated to satisfy their specific tree densities at the hectare level). Below ~ 80 m the vegetation content will become different between neighbouring pixels since the statistics of what is contained within the area, over which the BRFs are being sampled, now depends on the exact location of the pixel with respect to the structures in the 3-D forest representations. This situation is exacerbated as the sidelength of the pixel becomes equivalent to or smaller than the typical size/height of the structures in the forest scene under study. The radiative separability limit of the BRF values gathered at any individual pixel location now depends both on what is contained within that area and what is adjacent to it (taking account of the illumination direction). Very complex three-dimensional situations can thus arise if a high resolution pixel area partially covers one or two tree crowns with the underlying soil far below (in addition, each of these components may be partially illuminated or shaded). Such a configuration will inevitably give rise to larger separability values, *i.e.*, the 1-D' surface type solutions will not match the actual (3-D) observations easily. On the other hand, if a pixel were to fall exactly in between the tree crowns of a forest stand, such that it would only contain soil (and no shadows), then the separability between the 1-D' and 3-D reflectance fields would be relatively small. The latter situation is, however, less likely to occur than the former, and will depend both on the tree density and on an accurate sampling of all possible placement of the pixel areas above the forest scene. Nevertheless, the range of separability should increase at the highest spatial resolutions simulated, with its minimum becoming eventually reduced again.

The right hand panel in Figure 5.5 shows a conceptual partitioning of the findings just described in the context of interpreting remotely sensed observations of this forest type with physically based RT models. Large tolerances of fit between the measured and modelled reflectance fields (white zone) will result in the radiative equivalence of 1-D' and 3-D RT models (especially at large spatial scales) to provide a surface type solution. On the other hand, small tolerances of fit—outside the modelling and measurement uncertainties (dark grey region)—

demand the usage of 3-D RT model to match the observed reflectance values (light grey zone). In between these regions lies a transition zone (medium grey) where the dimensionality of the RT model depends on the exact magnitude and shape of the observed reflectance field, *i.e.*, the validity of the homogeneity assumption within this zone is subject to the exact placement of the pixel area with respect to the constituents of the forest scene. However, since it is not known *a priori* what a given (high resolution) sensor covers within its footprint area, 3-D RT models will always have to be used in practice when satellite observations have to be matched with a tolerance of fit that lies within the area labeled as transition zone in the right hand panel of Figure 5.5. Given the nominal resolution of the MISR instrument (275 m), a 1-D' RT model would thus be appropriate if the BRF signature (of the above 600 stem/ha forest type) were to be reconstituted (in the red and NIR along the directions of the 7 innermost MISR view zenith angles in the principal plane) at a prescribed accuracy of 10 % of the observed values, whereas a 3-D RT model would be needed if the same operation had to be performed at a mere 5 %. On the other hand, if one were to fix the prescribed accuracy at the 10 % level, then the three-dimensionality of the forest type yielding the results in Figure 5.5, would only be maintainable (from a radiative point of view) up to spatial resolutions of ~ 80 m. This is because the retrieval of structural information beyond the level of individual scatterers becomes unjustified (according to Occam's razor) as soon as at least one plane-parallel surface type solution can match the observations within the required ϵ percent. Surface heterogeneity at the subpixel level is thus a scale dependent feature when described from a radiative point of view. For nadir viewing measurements in the red and NIR only, tests have indicated that the extent of the white area in the left hand panel of Figure 5.5 increases towards smaller values of the fitting tolerance, that is, such monodirectional observations reduce the ability to discriminate between structurally heterogeneous and homogeneous surface types. Or in other words, for a given fitting tolerance within the white area of the left hand panel in Figure 5.5, the number of solutions in the nadir-viewing case will be greater than for the multidirectional cases mentioned earlier (see also Gobron et al. 2000a).

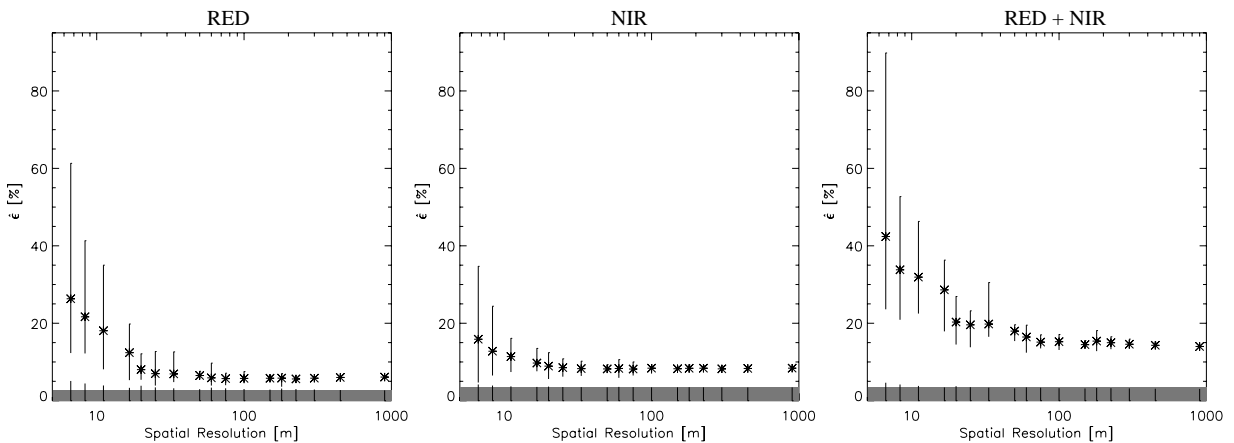


Figure 5.6: The radiative separability limit of a 600 stem/ha forest in the red (left), NIR (middle) and, red and NIR (right) spectral bands using the 7 innermost MISR view zenith angles along the principal plane (experimental conditions A in Table 5.2).

Figure 5.6 shows the radiative separability limit, $\hat{\epsilon}$ of the same 600 stem/hectare coniferous forest under experimental conditions A (see Table 5.2), if the 7 innermost MISR view zenith angles in the principle plane are utilized in the red (left), NIR (middle) and both, red and NIR (right) spectral bands. As expected, in the latter case the area of radiative equivalence between 1-D' and 3-D RT models is substantially reduced (compared to situations where only the information content within one single spectral band alone is being exploited). Interestingly, for

this particular forest type and experimental setup, the radiative separability limit in the NIR is larger than the corresponding one in the red spectral band at coarse spatial resolutions. However, at high spatial resolutions both the range and mean of $\hat{\epsilon}$ are larger in the red wavelength regime, presumably due to the reduced multiple scattering there.

Given the observations made in section 4.2.1 regarding the enhanced discrimination of the set of predefined surface types if the scope of the angular and spectral sampling of the surface leaving radiation fields was extended, the remainder of this chapter will only deal with results obtained from comparing the BRF values of 1-D' and 3-D RT models along the directions of the 7 innermost MISR view zenith angles for both the red and NIR spectral bands. Figure 5.7 thus shows the variations in separability of a 300 (red), 600 (black), 1200 (green) and 1800 (blue)⁶ stem/hectare coniferous forest under experimental conditions A (see Table 5.2) in both the principal (left graph) and orthogonal (right graph) plane. At coarse resolutions, the BRF separability of the low tree density forest is smallest, due to the reduced influence of its structural components (*i.e.*, the trees) on the angular signature of its reflectance field, which is predominantly controlled by the soil optical properties in this case. As the LAI increases (more trees) the three-dimensional nature of the forests becomes more important in terms of shadows and occlusions and as such the mean separability level rises. At very large tree densities, the gaps between the trees are getting smaller and the canopy eventually will become (almost) closed again. As a consequence the radiative resemblance with a highly vegetated 1-D' surface type increases and the BRF separability decreases again (at coarse resolutions). This trend can be observed both in the principal and orthogonal plane, with the separability in the former being generally larger due to the (partial) sampling of the hot spot effect with the -26.1° view zenith angle in the case of the 3-D forest representations. The level of the modelling uncertainty corresponding to the 600 stem/hectare forest type is being indicated at the bottom of both graphs in Figure 5.7.

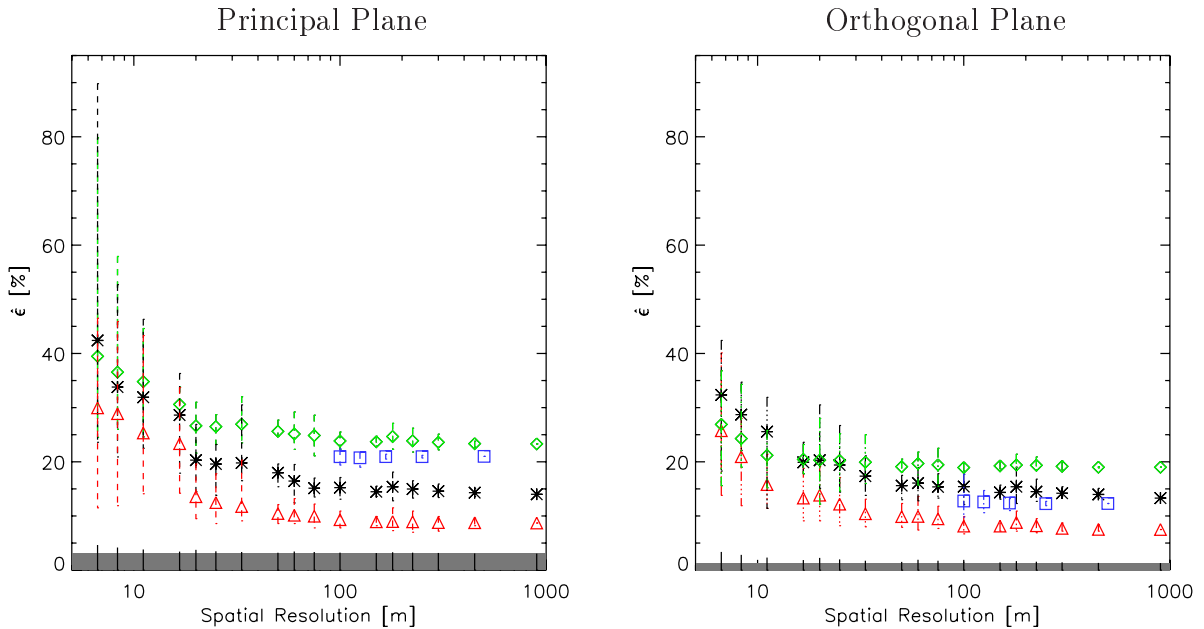


Figure 5.7: The radiative separability limit, $\hat{\epsilon}$ of a 300 (red), 600 (black), 1200 (green) and 1800 (blue) stem/ha coniferous forest under experimental conditions A (see Table 5.2), if the 7 innermost MISR view zenith angles in the principal (left graph) or orthogonal (right graph) plane and both the red and NIR spectral bands are utilized to identify the radiatively most alike 1-D' surface type solution.

⁶Only one set of 5 zoom-ins was performed for the 1800 stem/hectare forest type covering 500 m².

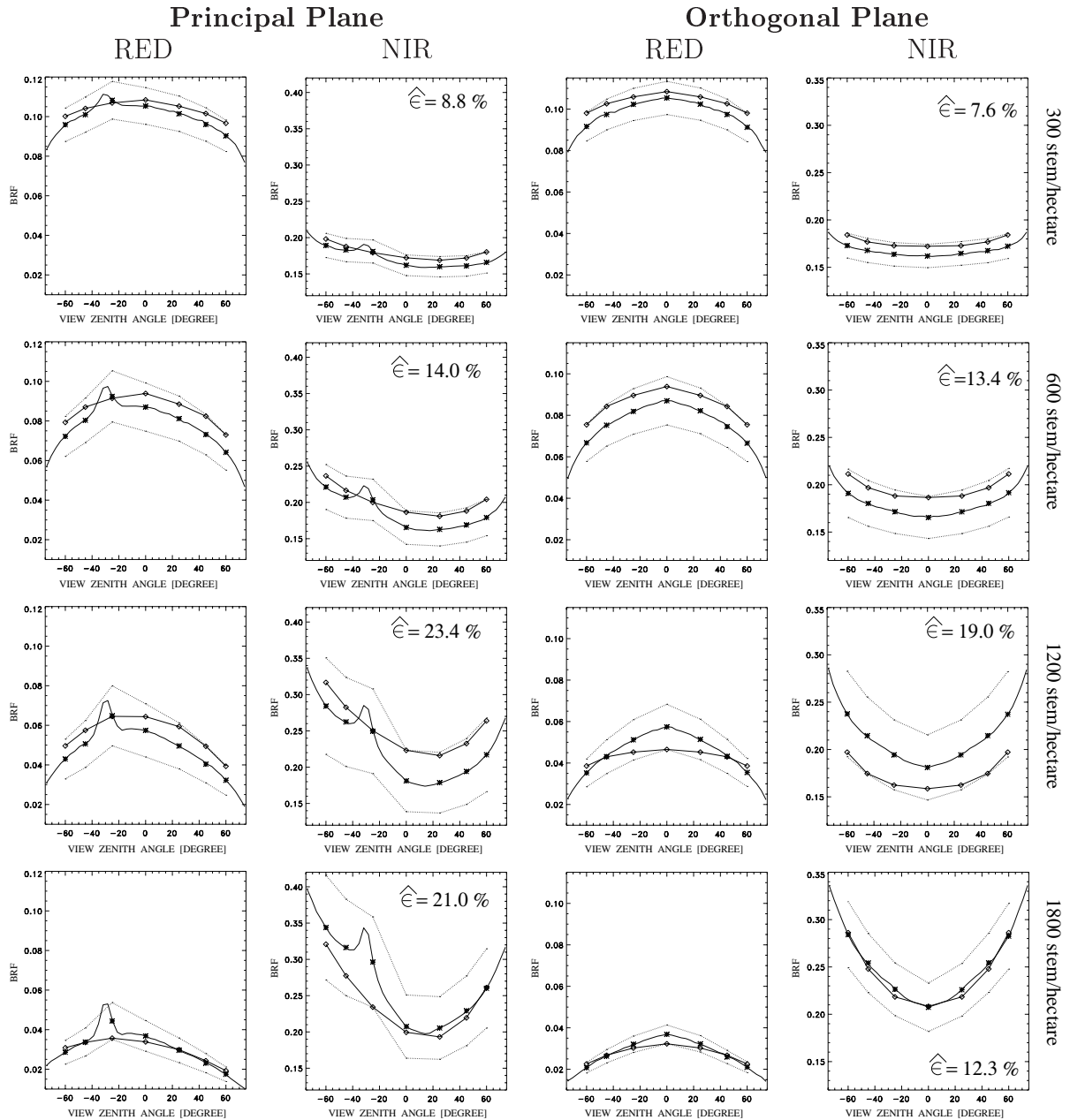


Figure 5.8: The BRF values of the best fitting 1-D' surface types (diamonds) compared to those of the 3-D forest representations (stars) if the 7 innermost MISR view zenith angles in both the red and NIR spectral bands had to lie within the limits of the imposed error criterion (dotted lines). The two leftmost (rightmost) columns present the results for the principal (orthogonal) plane for the 4 heterogeneous forest tree-densities (rows) indicated on the far right (experimental conditions A in Table 5.2).

Figure 5.8 indicates in greater detail how the best fitting 1-D' surface type (diamonds) from the LUTs matched the 3-D BRF data (stars) both in the principal (2 leftmost columns) and orthogonal (2 rightmost columns) planes at a spatial resolution of 900 m (500 m in the case of the 1800 stem/hectare forest type). Whereas in the case of the 1800 stem/hectare forest type the selection of the 1-D' solution in the principal plane is determined by the -26.1° view zenith angle, at lesser tree densities it is the largest forward zenith angle ($+70.0^\circ$) that constrains the radiative separability limit either in the red or NIR spectral band. In the $+70.0^\circ$ case the magnitudes of the 3-D BRF field are systematically overestimated by the selected 1-D' solution both in the red and NIR spectral bands, and with the misfit increasing with the prominence of the hot spot, that is, with increasing tree density. A similar behavior can be observed in the orthogonal

plane, where the lower tree density forest types are constrained by their largest forward and backward viewing zenith angles in the red and NIR, whereas in the 1200 and 1800 stem/hectare it is the nadir observation in the red that determines the separability level. Notice how good the fit in the 1800 stem/hectare case is, a fact that is not really apparent from the separability values in the right hand graph of Figure 5.7 due to the low magnitude of the reference BRF values. Furthermore it is interesting to note that the rise of the $\hat{\epsilon}$ values in Figure 5.7 and their subsequent decrease at high stem density values, coincides with the waxing and waning of the bell shaped appearance of the angular reflectance anisotropy in the red spectral band of Figure 5.8 (especially in the orthogonal plane). The anisotropy in the NIR, on the other hand, is marked by an increased asymmetry in the BRF values along the principal plane together with an enhancing of its bowl shaped feature (that is most visible in the orthogonal plane).

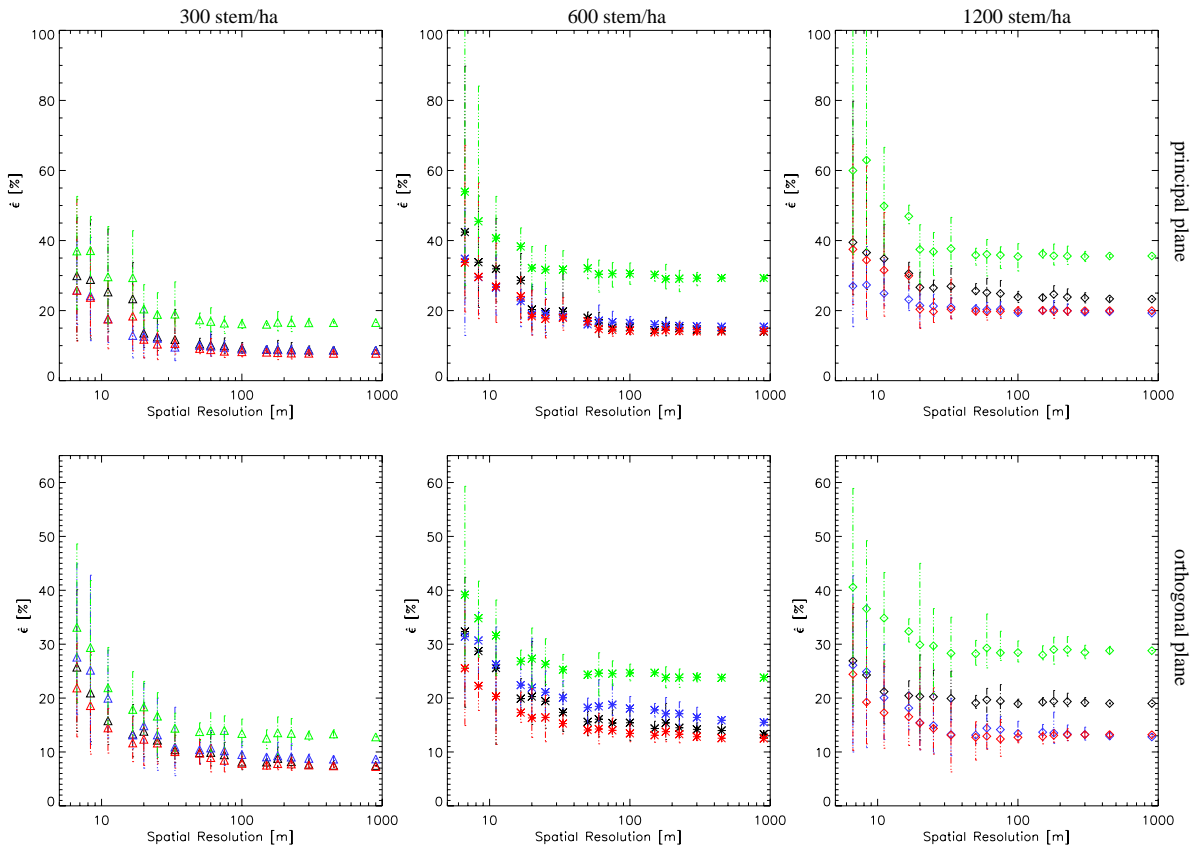


Figure 5.9: The radiative separability limit of a 300 (left), 600 (middle) and 1200 (right) stem/ha coniferous forest under experimental conditions A (black), B (red), C (green) and D (blue) - compare with Table 5.2 - if the 7 (or 5 for experimental conditions D) innermost MISR view zenith angles in the principle (top graphs) or orthogonal (bottom graphs) plane and both the red and NIR spectral bands are utilized to identify the radiatively most alike 1-D' surface type solution.

An analysis of the radiative separability limit of a 300 (left), 600 (middle) and 1200 (right) stem/ha coniferous forest under experimental conditions A (black), B (red), C (green) and D (blue)—compare with Table 5.2—is presented in Figure 5.9 for the principal (top graphs) and orthogonal (bottom graphs) planes. For experimental conditions B (red) the soil albedo was almost twice as bright as for conditions A (black), whereas for conditions C (green) the mean tree LAI was 3 times larger than for A. Notice that the range of the $\hat{\epsilon}$ values for the orthogonal plane (bottom graphs) is about half of that in the principal plane (top graphs). In general an increase in the mean tree LAI has a greater effect on the radiative separability than an increase in the soil brightness (at medium to large spatial scales). This can be related to an enhancing of

the three-dimensional effects in the pine forest reflectance signature when the opacity of the tree crowns is increased, *e.g.*, more efficient shadowing as well as occlusion of the soil under larger view zenith angles is occurring. Very large separabilities at high spatial resolutions can occur in the principal plane (with the 1200 stem/hectare forest type reaching almost 250% at ~ 9 m resolution!) predominantly when the BRF of the $+70.0^\circ$ view zenith angle is characterized by very low magnitudes in the red (0.009 in this case)⁷. In general, $\hat{\epsilon}$ increases with tree density - although under experimental conditions B, it remains almost constant between the 600 and 1200 stem/hectare forest densities at large resolutions. This could be related to the larger BRF values under bright soil conditions as well as the discretization steps of the LUTs. The radiative separability limit for experimental conditions E (blue) in Figure 5.9 was computed using only the 5 innermost MISR view zenith angles in order to avoid any increase in the model uncertainty due to the larger zenith angle of the incident rays (55° rather than the 30° for experimental conditions A). Tests indicated that the value of $\hat{\epsilon}$ in A was not noticeably affected when choosing only 5 MISR view zenith angles. Thus when comparing the results of experiments A (black) and E (blue) one notices that the larger solar zenith angles reduces $\hat{\epsilon}$ only for the relatively dense (1200 stem/hectare) forest type, whereas at lower tree densities the shadow component amidst the trees and on the soil is enhanced which tends to increase the radiative separability limit in E.

As a final comment to the results obtained in this section, it should be noted that coniferous forests, with their reduced needle reflectance and transmission values (Gates et al. 1965), as well as their vertically elongated crown shapes, are particularly suited to increase the values of $\hat{\epsilon}$. 3-D grassland representations, for example, would have resulted in substantially lower radiative separability limits at the spatial resolutions under investigation. Thus, having documented the scale dependent differences between the TOC reflectance fields of 3-D coniferous forest representations and their best matching 1-D' vegetation canopies from amongst a large set of potential candidates under a variety of structural, optical and illumination conditions, it now remains to investigate how well the state variable of interest (LAI) can actually be retrieved using the so identified 1-D' canopy candidates.

5.2.2 The plane-parallel bias in the retrieval of LAI at multiple scales

The leaf area index is a quantitative indicator of the amount of live green leaf material per unit ground area within a vegetation canopy. It is commonly used in agrometeorology and functions as a parameterizing agent of the vegetation cover and its interactions with the atmosphere in both biogeochemical and atmospheric general circulation models *e.g.*, Avissar and Verstraete (1990), Dickinson et al. (1990), Sellers et al. (1996). Due to the crucial role that the biosphere may play in the balance of the global carbon budget, continued efforts are underway to (operationally) determine its LAI values on a global basis, *e.g.*, Gobron et al. (1997a), Myneni et al. (1997), Knyazikhin et al. (1999). In section 5.2.1 the 1-D' vegetation canopy types that were best suited to lie at the origin of the BRF values measured above three-dimensional forest representations were identified. In the following, both the absolute and relative error in their LAI variable will be assessed.

Figure 5.10 indicates the absolute (top row) and relative (bottom row) LAI difference between the 3-D coniferous forests and their radiatively most alike 1-D' candidates from Figure 5.7. The mean LAI of the heterogeneous forest scenes at their largest resolution amounts to 0.27 for the 300 stem/hectare (red), 0.54 for the 600 stem/hectare (black), 1.09 for the 1200 stem/hectare (green) and 1.63 for the 1800 stem/hectare (blue) forest types. At coarse spatial resolutions

⁷This is a drawback when defining the separability in terms of a *relative* difference. The usage of absolute error values, on the other hand, has the disadvantage that equation 4.3 becomes dominated by the shorter wavelengths.

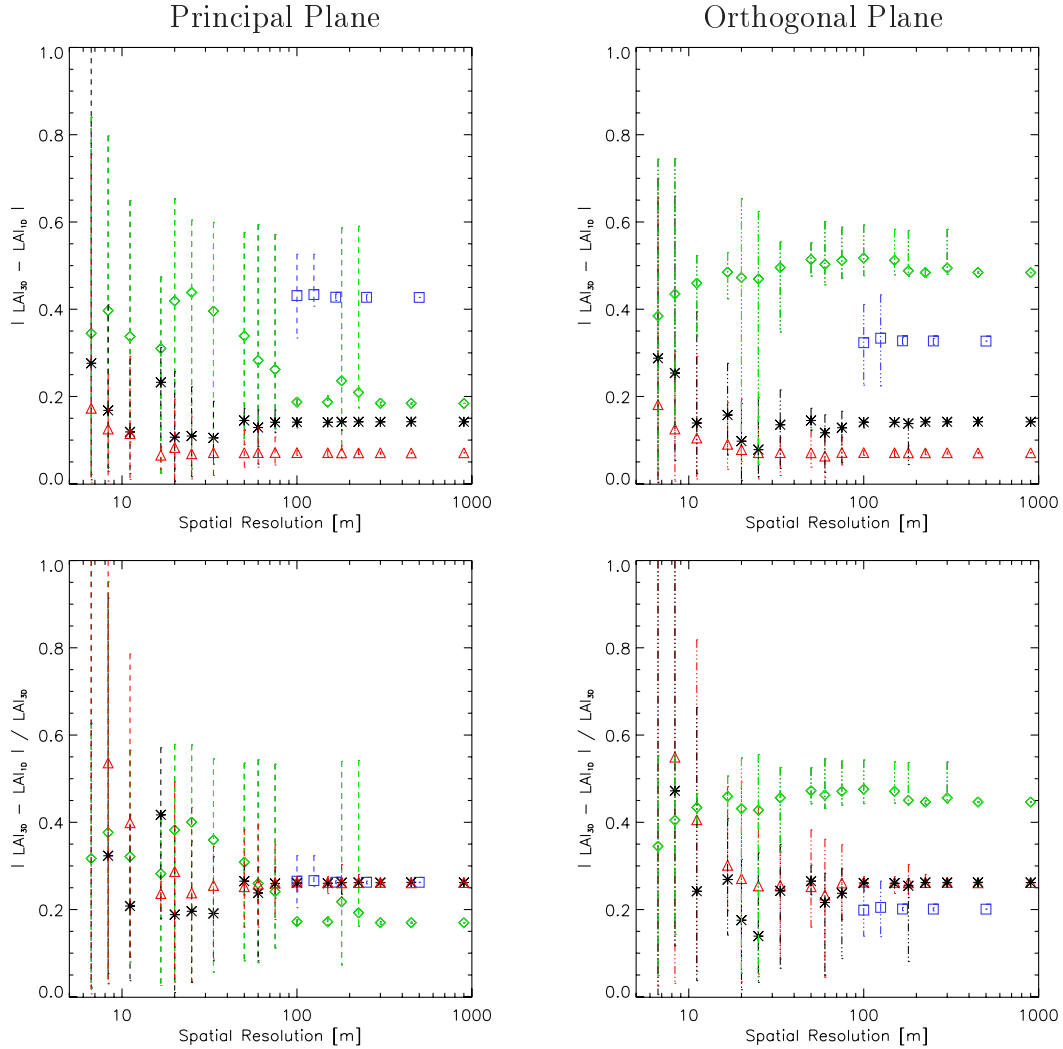


Figure 5.10: The absolute (top row) and relative (bottom row) LAI retrieval error for a 300 (red), 600 (black), 1200 (green) and 1800 (blue) stem/ha coniferous forest under experimental conditions A (see Table 5.2), if the 7 innermost MISR view zenith angles in the principal (left graph) or orthogonal (right graph) plane and both the red and NIR spectral bands are utilized to select the radiatively most alike 1-D' surface type.

the absolute LAI error increases continuously with the tree density in the principal plane (top left graph) whereas it is reduced at very high tree densities in the orthogonal plane (top right graph). In relative terms, the accuracy of the LAI retrieval stays almost constant at $\sim 25\%$ in both the principal and orthogonal plane, and for almost all surface types apart from the 1200 stem/hectare forest. The error of the latter is especially pronounced in the orthogonal plane, and it is precisely this configuration that produced the least convincing fit—as far as the shape of the BRDF profile is concerned—in the corresponding graph of the red spectral band in Figure 5.8. Interestingly, those surface types where the best fitting 1-D' solution was not constrained by the $+70.0^\circ$ angles had the largest absolute LAI difference (both in the principal and orthogonal plane). These 1-D' surface type solutions were, however, the only ones that retrieved the correct soil brightness value, whereas all others overestimated the soil albedo in order to compensate for their underestimation of the LAI. Thus, whilst the 1-D' surface type solution in the 1200 stem/hectare case provides a better estimate of the soil brightness in the orthogonal plane, its LAI estimate is better in the principal plane, and vice versa. As a last comment it should be noted that both the relative and absolute LAI differences can become very large at small spatial scales. This observation (together with the comments made at the end of section 5.1.2 about the

possible irrelevance of remotely sensed measurements for the accurate and reliable description of the underlying surface properties at very high spatial resolutions), is thus a prime example not to embrace high spatial resolution sensors as the most obvious means to improve the quantitative characterization of terrestrial targets on the basis of remotely sensed data-strings.

In Figure 5.11 the radiative separability limit values are shown as a function of the absolute LAI difference for the 300 (triangle), 600 (stars) and 1200 (diamonds) stem/hectare coniferous forest under experimental conditions A,B,C and D in the principal (left graph) and orthogonal (right graph) plane for three different scale ranges (colors), and by accounting for the BRF values of the 7 innermost MISR view zenith angles both in the red and NIR spectral bands. In both graphs, the LAI differences tend to become smaller as the radiative separability limit decreases, *i.e.*, as the 1-D' and 3-D BRF fields are becoming more alike. The largest LAI differences occur over surface types with elevated LAIs (experimental condition C in Table 5.2). As the scales of investigation are reduced, the $\hat{\epsilon}$ values tend to fluctuate more than the corresponding (absolute) LAI differences. At scales below 50 m this spread is becoming much greater (not shown), with some experimental conditions (C and D) supporting the relationship between the BRF separability limit and the LAI retrieval error in Figure 5.11 better than others (A and B).

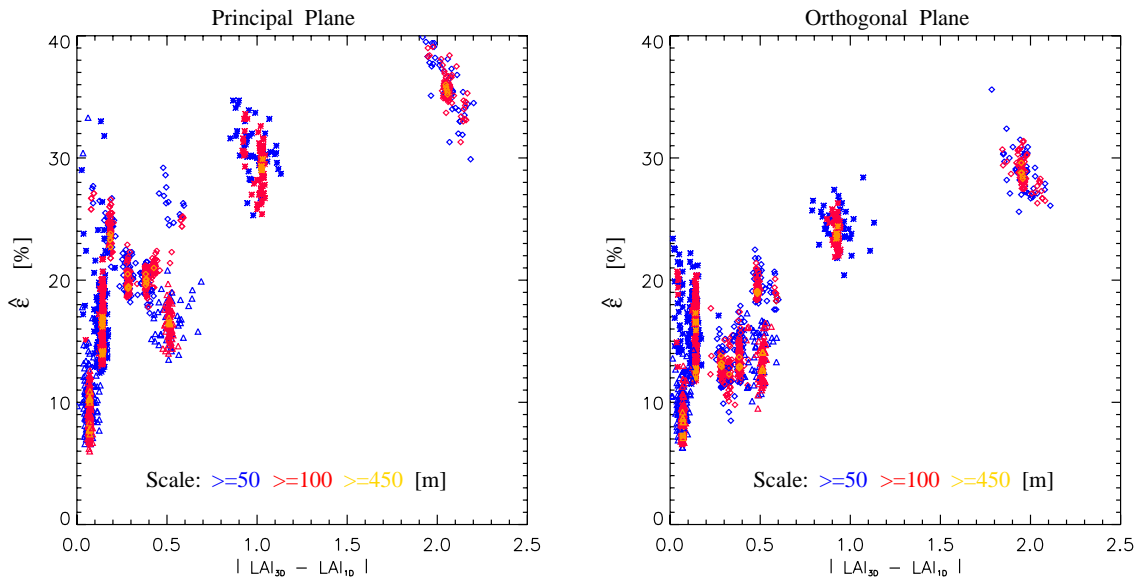


Figure 5.11: Radiative separability limit, $\hat{\epsilon}$, versus absolute LAI difference for the 300 (triangle), 600 (stars) and 1200 (diamonds) stem/hectare coniferous forest under experimental conditions A,B,C and D (see Table 5.2), for three different scale ranges (colors). The 7 innermost MISR view zenith angles in the principal (left graph) or orthogonal (right graph) plane in both the red and NIR spectral bands were utilized to select the radiatively most alike 1-D' surface type.

5.3 Discussion

The issues in this chapter were introduced to discuss the question as to whether 1-D' RT models could be appropriate to interpret satellite observations, if they were capable of retrieving the same type of information as 3-D RT models. As it turned out, the level of LAI error that is to be expected when plane-parallel RT models are to interpret satellite measurements (or the 3-D simulations in this chapter), is somewhat related to the accuracy with which they can fit these observations (compare with Figure 5.11). However, the examples that were presented in this chapter were especially suited to enhance the effects of a 3-D canopy architecture. This is because conifers have vertically elongated tree-crown shapes, and the reflectance and transmission

values of their needles are much lower than those for other kinds of foliage (Gates et al. 1965). Other surface types with relatively brighter foliage and less obliterated crown volumes can thus be expected to yield reduced separability values, especially for closed vegetation covers when the LAI is high (*e.g.*, rainforests), or—in the case of open canopies—if the opacity of the tree crowns is less pronounced. Such configurations might thus have yielded weaker relationships between the radiative separability limit and the LAI retrieval error in Figure 5.11.

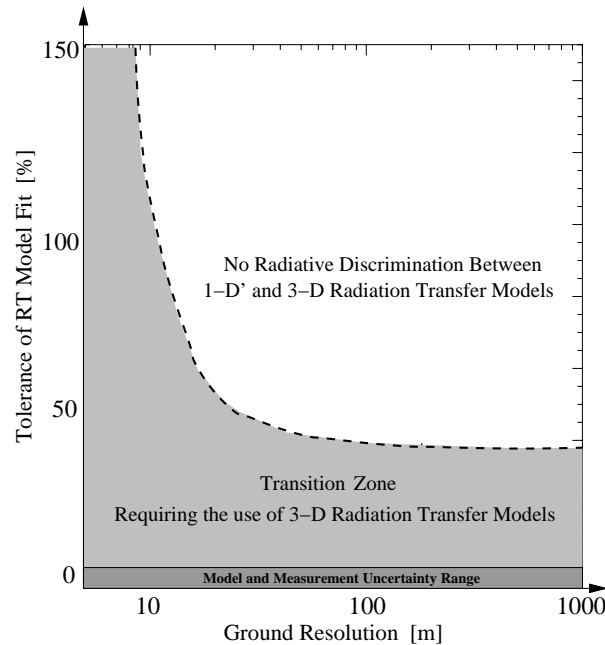


Figure 5.12: Conceptual subdivision of the ‘accuracy requirements’ versus ‘sensor resolution’ space in the context of interpreting terrestrial remote sensing observations with physically based RT models. The bottom zone is dominated by the instrument and model uncertainty, whereas the top right zone asserts the validity of 1-D’ RT model to interpret the observed BR_F values. In between the two lies a transition zone (grey) where due to the lack of any other indicators 3-D RT models must be used even though 1-D’ might be sufficient in some cases.

If one were to add the spatial resolution dependent separability ranges of all existing land cover types into the left hand panel of Figure 5.5, then—from the above note about the spectral and structural properties of coniferous forests—one could expect that the minimum values of $\hat{\epsilon}$ approach the model and measurement uncertainty zone in that conceptual graph. Thus, Figure 5.12 serves as an indicator of the radiative equivalence between 1-D’ RT models and actual (multispectral and multiangular) remote sensing observations at a user specified BR_F accuracy and the spatial resolution of the sensor of choice. Obviously the instrument and modelling uncertainties (dark grey area) prevent any interpretation of remotely sensed data if the fitting requirements for the observations and simulations fall below this limit. On the other hand, if the RT model fitting requirements are sufficiently lax, then 1-D’ RT models will always be capable of reproducing the (multispectral and multidirectional) BR_F observations. It is anticipated that the 1-D’ zone (white area) will have its smallest levels of fitting tolerance at the largest spatial resolutions. This is because naturally vegetated areas—unlike the simulations in this chapter—are composed of a multitude of structural entities with different dimensions, optical properties, and degrees of spatial variations, such that the overall signature of the surface leaving radiation field at coarse spatial resolution is less likely to feature strong markings due to local, radiative surface heterogeneity configurations. In between the 1-D’ and the model and measurement uncertainty zones there is a large transition zone, where both 1-D’ and 3-D RT models could be appropriate for a satisfactory interpretation of the BR_F signals, depending on the underlying

surface type and the exact placement of the area of observation above it. In absence of any *a priori* information as to what surface type is actually being observed, or how the FOV of the sensor is placed above the features on the ground, the interpretation of satellite gathered data strings within the radiative separability limit range of the (grey shaded) transition zone will thus in general require the usage of 3-D RT models.

Nevertheless, the question as to the complexity of the most appropriate RT model could be resolved even in these cases (at least in regional applications) through relationships like the one implied in Figure 5.11. Indeed, the radiative separability limit can always be related to a given state variable, for different illumination and observation conditions, as well as land cover types. But such relationships will only be able to give a broad indication as to the retrieval error, with a large spread of estimates as soon as the resolution of the instrument is smaller than the spatial scale at which the surface type statistics is being conserved within the FOV of the sensor. Furthermore these relationships are susceptible to atmospheric aerosol types and load, and will depend on the assumptions and formulations contained within the RT models that were used to derive them. Alternatively, the maximum radiative separability limit amidst all the 1-D' surface types in the LUTs could serve as a discriminator between plane-parallel and 3-D RT models provided, however, that the set of potential surface types in the LUTs is sufficiently large.

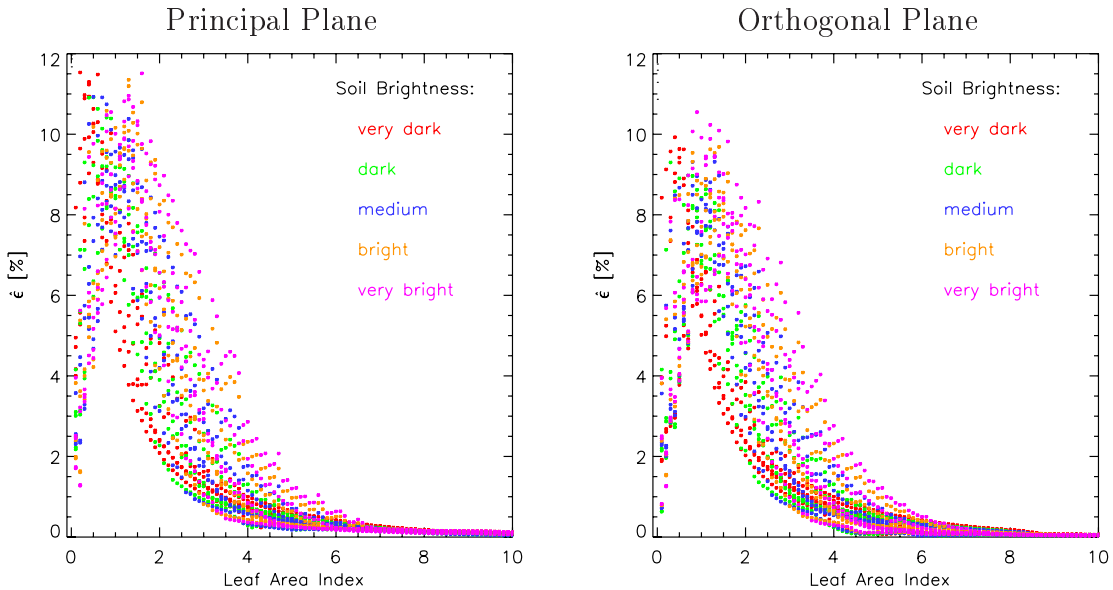


Figure 5.13: The radiative separability limit of the 2505 1-D' surface types (contained within the LUTs) as a function of their LAI content for different soil brightness conditions (colours) in the principal (left) and orthogonal (right) plane - if the 7 innermost MISR view zenith angles in both the red and NIR spectral bands were utilized ($\theta_0 = 30^\circ$).

The graphs in Figure 5.11 do not contain any direct reference as to the origin of the BRF differences. In particular it could be the discretization of the LUTs rather than the three-dimensionality of the observed surfaces that caused the measured separability values. Indeed Figure 5.13, which displays the separability of the 1-D' surface types, shows that the BRF values of these solutions are least alike when their LAI conditions correspond to those of the 1200 stem/hectare surface type under experimental conditions A, B and D. A closer inspection, reveals however that the level of separability between the 1-D' and 3-D reflectance fields corresponds to 20–25% (15–20%) rather than the 10–12% (8–10%) separability maximum of the LUT solutions in the principal (orthogonal) plane. In addition whereas the LUT separability falls (on average) as the LAI is raised from 1 to 3.5, a dramatic increase ($\sim 10\%$) in the separability of the 1200 stem/hectare solution is observed when the LAI is tripled between experimental

conditions A and C. Hence, since both the optical properties and the orientation distributions of the leaves (as well as the soil brightness values) in the heterogeneous forest scenes are contained within the LUT solutions, the differences between their reflectance fields must be entirely due to the clumping of the foliage (and to some degree also to the presence of tree trunks). In section 5.2.1, the correspondence between the value of the separability in Figure 5.7 (at 900 m) and the degree of bell-shapedness of the angular reflectance anisotropy in the red spectral band (especially in the orthogonal plane) of Figure 5.8 was noticed. This bell shaped anisotropy is even more pronounced if the LAI of the tree crown is tripled (experimental condition C). This can be explained by the fact that the tree density and the foliage content of the tree crowns are responsible for the reduction in surface leaving radiation as the view zenith angles increases from nadir (where most of the brighter underlying soil is visible) to larger values (where the tree crowns obscure the soil) in this spectral band. In chapter 6 this avenue will be exploited further by extracting the information contained within the shape of the spectral reflectance anisotropy as a possible indicator of surface heterogeneity.

As a final comment on this chapter, it should be noted that other kinds of biases in the retrieved LAI values (or any other state variable of interest) could have been obtained, if a different criteria for the selection of the most appropriate 1-D' surface type had been selected. Some possible options include:

- adding further radiative criteria, like the mean level and shape of the reflectance anisotropies, for the selection of the most suitable 1-D' surface type.
- using a summation rather than a piece-wise χ^2 approach, which would hopefully alleviate the frequent underestimation of the LAI observed here.
- selecting a “most likely” LAI estimate from an ensemble of 1-D' surface type solutions – obtained for error criterion values that are larger than the minimum 1-D'/3-D separability used here.

5.4 Conclusion

The radiative separability limit between structurally heterogeneous and homogeneous vegetation canopies (both in the spectral and angular domain) depends not only on the amount of surface features, but also on their optical properties, and on the illumination conditions. For sufficiently lax accuracy criteria, a 1-D' RT model can always be found to fit the observed reflectance values (to within the specified requirements). Nevertheless, for any fixed value of the accuracy criteria, the surface heterogeneity at the subpixel level—as perceived by remote sensing measurements—appears to be a scale dependent feature. End-users, with their continuing needs for a quasi-comprehensive characterization of terrestrial surfaces at enhanced spatial resolutions and improved radiative accuracies, constitute the main driver behind the inclusion of ever more complex 3-D RT models in interpretation schemes of remotely sensed data. However, the accurate extraction of surface properties from their radiative signatures using physically based RT models, is likely to yield unsatisfactory results at high spatial resolutions since neither the actual placement of the sensors FOV above the features on the ground, nor the exact (diffuse and direct) illumination conditions can be known *a priori*.

Chapter 6

The Reflectance Anisotropy Shape

This chapter will investigate the information contained within the angular ‘shape’ of the spectral reflectance field for both structurally homogeneous and heterogeneous vegetation canopies. Section 6.1 discusses the possibility to describe the reflectance anisotropy shape using the modified Minnaert function parameter k of the parametric RPV model (Rahman et al. 1993a). Section 6.2 interprets the variations of this parameter for structurally homogeneous vegetation canopies with different optical and architectural properties. Section 6.3 then presents the simple physical principles supporting the interpretation of the anisotropy of spectral radiances exiting from structurally heterogeneous terrestrial surfaces in terms of a signature of surface heterogeneity. Finally, section 6.4 highlights some of the benefits that this surface heterogeneity detection concept might offer to the interpretation of remotely sensed data.

6.1 Characterization of the spectral reflectance anisotropy shape

Our interest in the shape of the reflectance anisotropy of BRF fields stems from the discussion in chapter 5 where, for a given spatial resolution and uncertainty level, a criterion was required to decide whether a plane-parallel or 3-D RT model was needed to interpret multi-angular remote sensing data in one or more spectral bands. Clearly, in absence of any additional information, the multi-directionality of the data itself has to be examined for possible clues to address this issue. An often cited example for the impact of canopy architecture on the reflectance signature is the hot spot effect (see page 10 in section 2.2.2), and a variety of works have addressed the issue of retrieving the structural parameters that caused it, *e.g.*, Goel et al. (1997). Observations in the retro-reflection direction are, however, limited with the current fleet of Earth-orbiting satellites¹. As will be shown in the remainder of this chapter, a certain degree of structural information may be contained within the angular shape of the overall reflectance field. This is because multi-directional remote sensing observations are not only dependent on the optical properties but also on the size, shape and spatial arrangement of the objects that are contained within the FOV of the sensor. However, whether such a structural footprint may be noticeable in the characteristics of multi-directional data-strings, depends (even in the absence of an overlying atmosphere) on the structural and optical properties of the surface building blocks, the conditions of observation and illumination, as well as on the degree of spatial consistency of the landscape patterns within the FOV of the observing instrument.

¹ *Triana*—which is planned to orbit the Sun at the Lagrange-1 (L1) point—will be capable of continuously sampling the hot spot effect at a resolution of 8 km in five visible/NIR bands (<http:// triana.gsfc.nasa.gov>).

Classical radiation transfer theory for optically dense media predicts bowl-shaped reflectance anisotropy patterns. For the large majority of field measurements and RT model simulations with finite-sized leaf canopies, that are documented in the scientific literature, a similar behaviour has been noted. Occasionally, however, the inverse pattern, that is a bell-shaped anisotropy, has been observed, *e.g.*, Gerard and North (1997), Ni and Jupp (2000). It is this latter circumstance—which seems to manifest itself only under very specific conditions—that prompted our interest in investigating the information contained within (some aspect) of the shape of the spectral reflectance anisotropy. Indeed in section 5.3 it was noted that the degree of bowl-shapedness of the reflectance field in the red spectral domain appeared somewhat related to the BRF separability level between the radiative most alike plane-parallel and 3-D canopy architecture representations. These observations gave rise to the conjecture that the “shape” of the spectral reflectance anisotropy (in the red)—if quantified appropriately—could potentially be exploited for the purpose of discriminating between different types of surface heterogeneity as well as amidst RT models (of different complexity) when aiming at the extraction of quantitative information from these data.

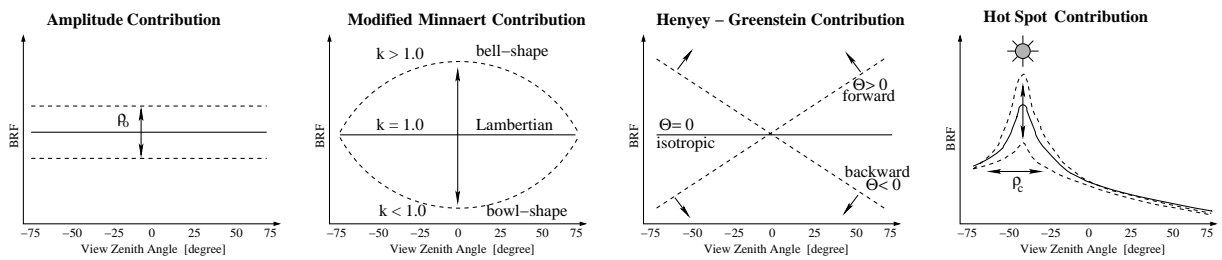


Figure 6.1: The RPV model performs a functional decomposition of any BRF field into an amplitude function (controlled by the ρ_0 parameter), a modified Minnaert function (controlled by the k parameter), a Henyey-Greenstein function (controlled by the Θ parameter), and a hot spot function (controlled by the ρ_c parameter). The modified Minnaert function contributes towards the ‘bowl’ and ‘bell’ shapedness, and the Henyey-Greenstein function towards the skewness of the resulting graph.

Although the concept of such an approach is straightforward, its practical application appears however complicated by the fact that spectral reflectance patterns are highly asymmetric at elevated solar zenith angles. An issue, that can, however, be resolved by utilizing an appropriate parametric model capable of adequately characterizing the angular distribution of the surface leaving radiances. As discussed in section 3.1, such models do not need to be based on physical principles, rather they must be capable of representing the anisotropy effects from a large variety of media in the simplest possible manner, that is with a minimum number of input parameters (Verstraete et al. 1996). The RPV model (Rahman et al. 1993b) proposes to achieve this by representing the reflectance field on the basis of four parameters (k , Θ , ρ_0 , ρ_c) entering a product of angular functions (see equations C-2 to C-7). Through its mathematical formulation², the RPV model splits a BRF field into its amplitude component ρ_0 , its associated (symmetric) $M_I(\theta_0, \theta_v; k)$ and (asymmetric) $F_{HG}(g; \Theta)$ angular shape functions, as well as a hot spot descriptor function $H(\rho_c; G)$. With the exception of the amplitude function, all other parameters of the RPV model affect the overall reflectance field non-linearly across the hemisphere of possible viewing conditions. The main effects of the RPV model parameters on the overall signal shape are schematically depicted in Figure 6.1. Of specific interest here is the so-called modified Minnaert’s function $M_I(\theta_0, \theta_v; k)$, (Minnaert 1941), which allows for the mathematical representation of the overall shape of the angular field through the parameter k :

²The ρ_c parameter is commonly set equal to ρ_0 (Rahman, et al. 1993b).

$$M_I(\theta_0, \theta_v; k) = \frac{\cos^{k-1} \theta_0 \cos^{k-1} \theta_v}{(\cos \theta_0 + \cos \theta_v)^{1-k}}$$

where θ_0 and θ_v represent the zenith angles of the incoming and outgoing directions, respectively. In its present form the modified Minnaert function is based on 1) the observations carried out, around the beginning of the 20th century, by Oepik, who described the variability of the Moon illumination as: $\rho_{Moon}(\theta_0; k) = \rho_0 \cos^k(\theta_0)$, 2) (Minnaert 1941) who subsequently imposed the reciprocity³ principle as a criterion to be satisfied: $\rho_{Moon}(\theta_0; \theta_v; k) = \rho_0 \cos^{k-1}(\theta_0) \cos^{k-1}(\theta_v)$, and 3) Rahman et al. (1993b) who modified Minnaert's function to account for the findings of Kieffer et al. (1977), Thorpe (1977) and Pinty and Ramond (1986). In Figure 6.2, $M_I(\theta_0, \theta_v; k)$ is plotted as a function of the k parameter value and the view zenith angle for a solar zenith angle of 0° (left) and 50° (right). For any given value of k , the magnitudes of the troughs and crests of $M_I(\theta_0, \theta_v; k)$ are enhanced for small solar zenith angles, as expected. More specifically, k is close to 1.0 for a quasi Lambertian surface (very limited angular variations in the spectral BRDF field), k is lower than 1.0 when a bowl-shaped reflectance pattern dominates (the spectral BRDF values increase with the view zenith angle) and, conversely, k is greater than 1.0 when a bell-shaped reflectance pattern is observed (the spectral BRDF values decrease with the view zenith angle).

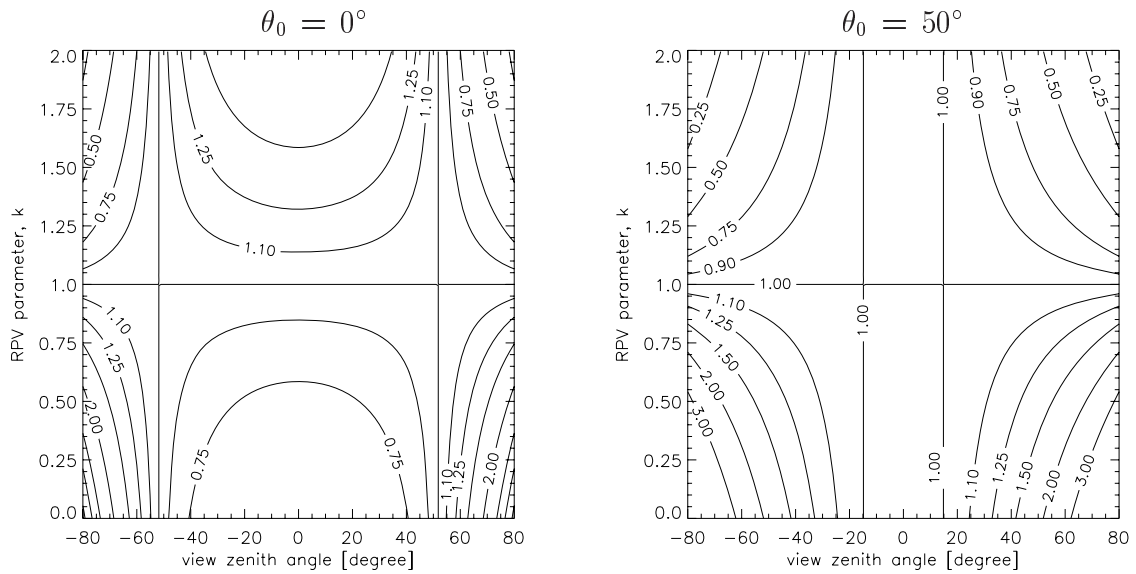


Figure 6.2: The modified Minnaert function, $M_I(\theta_0, \theta_v; k)$ as a function of the k parameter value and the view zenith angle θ_v , for a solar zenith angle, θ_0 of 0° (left) and 50° (right).

The RPV model was extensively evaluated by Engelsen et al. (1996) and can be inverted in a fast and reliable manner as demonstrated in a recent article by Gobron and Lajas (2001). Their approach yields not only an ensemble of possible RPV parameter value combinations but also the accuracy with which these k , Θ and ρ_0 parameters are capable of representing the observed BRDF field. Furthermore, a “most likely” parameter set is normally selected by identifying the k and Θ values that are associated with the ρ_0 closest to the mean of the retrieved amplitude values.

³The principle of reciprocity as it applies to diffuse reflection and transmission can be stated as: *The scattering and the transmission functions are unaltered when the direction of incidence and emergence are interchanged* (Chandrasekhar 1960).

Pinty et al. (2000a) showed that maps of the parameter k derived from an analysis of broadband METEOSAT data exhibit spatially consistent fields and features corresponding to known gradients in surface types which may or may not be represented by variations in the amplitude component of the BRF fields. This strongly suggests that the parameter k can be used as one additional and possibly independent axis of information to better identify and separate various surface types than is feasible on the sole basis of spectral measurements. This requires, however, to understand how the anisotropic signature of geophysical media can be interpreted and, in particular, what practical information could be derived from such a simple parameterization scheme. To this end, section 6.2 will investigate the variations of the most likely k parameter values⁴ over structurally homogeneous canopies both in the red and NIR spectral bands for a series of canopy architecture conditions. Hence in section 6.3 the potential of the k parameter to serve as a discriminator between structurally homogeneous and heterogeneous vegetation canopies (under identical foliage characteristics and illumination conditions) will be investigated.

6.2 The reflectance anisotropy shape of homogeneous canopies

For plane-parallel vegetation canopies—consisting of a homogeneous ‘cloud’ of disc-like scatterers uniformly distributed both along the vertical and horizontal directions (referred to as 1-D’)—the canopy architecture can be entirely described using the typical leaf size, the TOC height, the LAI and a suitable leaf normal distribution (LND) function, $g_L(\theta_L)$ (see section B-3). LNDs are important since they determine how much radiation is being intercepted by the canopy along any particular direction. Erectophile LNDs, with their predominantly vertically oriented leaves, are most effective at intercepting radiation at large view zenith angles whereas planophile LNDs, with their leaves tending to be oriented in a horizontal-like manner, have their largest interception capabilities at low view zenith angles. Quite intuitively, the LND of a structurally homogeneous vegetation canopy, can thus be expected to exert a major influence on the anisotropy of the reflected radiation field. The latter is, however, also conditioned by the optical properties of both the leaves and the soil as well as the illumination conditions.

6.2.1 The Minnaert function parameter of homogeneous leaf canopies

To assess the impact of both spectral and structural canopy properties on the shape of the BRF anisotropy, a series of reflectance fields were simulated at the TOC using the **Semi-Discrete** RT model for which the most likely Minnaert function parameter value was subsequently retrieved by inversion of the **RPV** model using the approach of Gobron and Lajas (2001). In Figure 6.3 the shape of the reflectance anisotropy is thus represented in terms of the most likely k parameter for canopy LAI values ranging from 0.1 to 5, as well as for five different LNDs. Both the leaves and the soil optical properties are analogous to those (not in *italics*) in Table 5.1, and the solar zenith angle was 30° . Going from left to right, every column refers to increasingly brighter soils, with the top (bottom) row referring to the corresponding leaf and soil properties of the red (NIR) spectral band. The jagged appearance of these curves is due to the fact that k was discretized in steps of 0.05 for the inversion of the **RPV** model. Nevertheless, the absence of widely fluctuating deviations provides confidence in the documented behaviour of the retrieved values as well as the selection mechanism that allowed to obtain them.

However, when interpreting the information contained in graphs like those in Figure 6.3 one has to remain aware that k is but a descriptor of one shape attribute of spectral reflectance

⁴Although the parameter k is defined by the ‘modified’ Minnaert function $M_I(\theta_0, \theta_v; k)$ it will be referred throughout this work as the *Minnaert function parameter*.

fields, that themselves were generated with physically-based RT models accounting for the influences of many state variables. The parameter k originates from a parametric model and has, as such (until proven otherwise), to be presumed devoid of any physical meaning. Correlations with state variables, however obvious they might appear in such graphs, are in all likelihood induced by a combinations of factors, and consequently might vanish as soon as some condition of the system under study is being changed. The aim of the various figures in this section is thus not to imply that the parameter k , has in fact a physical interpretation, but, rather, to allow for a better understanding of the conditions under which the shape of the angular reflectance anisotropy might become an indicator of a specific (spectral and optical) type of canopy.

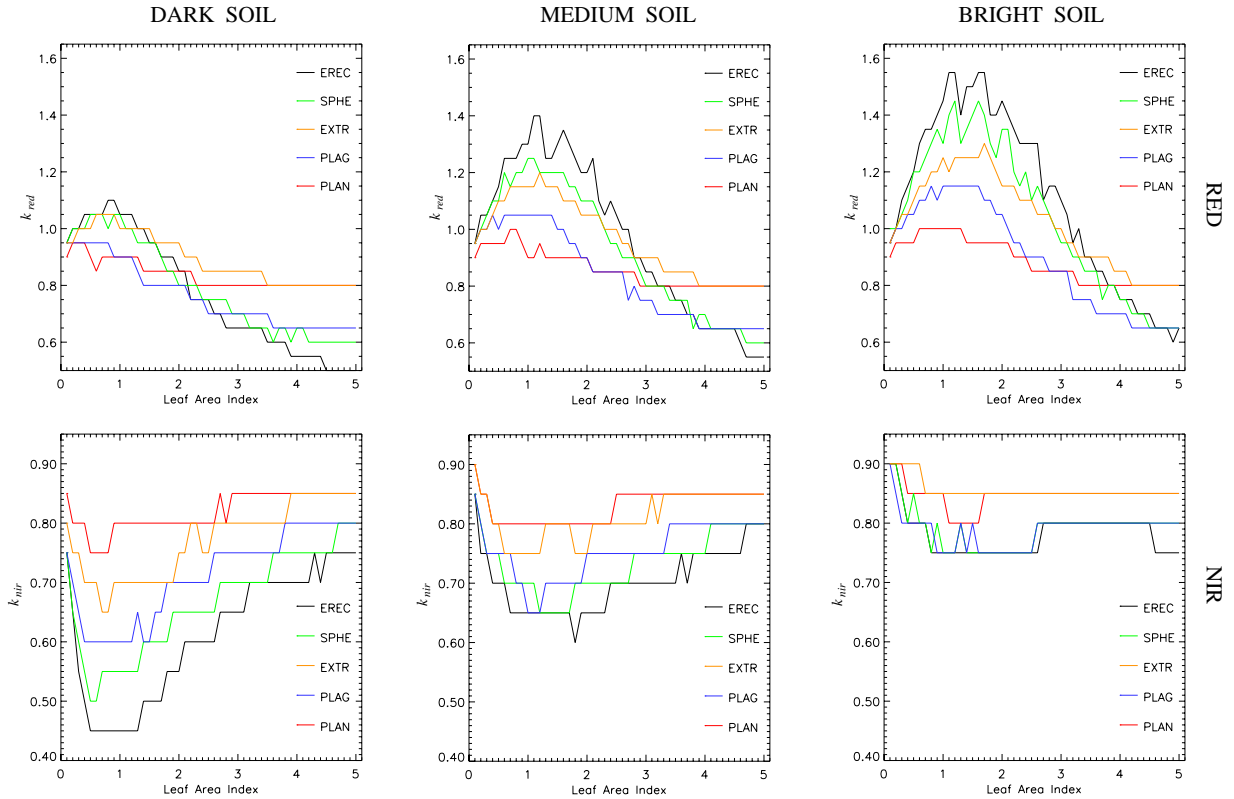


Figure 6.3: The change in the most likely Minnaert function parameter k as the canopy LAI is increased from 0.1 to 5, for different spectral bands (rows), soil brightness conditions (columns) and leaf normal distributions (colours). The leaves and the soil have Lambertian scattering phase functions and $\theta_0 = 30^\circ$. The TOC is at 10 m and the leaf radius 5 cm.

From the simulations contained in Figure 6.3—which are only valid if both the soil and the foliage possess Lambertian scattering phase functions—one can see that, in the red spectral band, increased soil brightness accentuates the differences between the various leaf normal distributions whereas in the NIR the opposite is the case. In the NIR both the leaf transmission and reflectance are $\sim 50\%$ whereas in the red they are much smaller and the leaf reflectance is about 5 times the leaf transmission. Whereas an increase in soil brightness yields also an increase in the values of k Figure 6.3, it should be noted that the soil brightness conditions in the red (NIR) spectral band are continuously larger (smaller) than the corresponding leaf optical properties in that spectral band in Table 5.1. It will be seen later on that the brightness level of the underlying soil (when compared to that of the foliage elements) is a crucial factor in the generation of bell- or bowl-shaped reflectance anisotropy patterns. In Figure 6.3 the maxima of the most likely Minnaert function parameter values in the red can be seen to rise and shift towards larger LAI values as the soil brightness is increased. This is especially the case for an erectophile LND.

For a planophile LND, on the other hand, these effects are significantly dampened: Irrespective of the simulated LAI and soil brightness conditions this LND tends to be characterized by bowl-shaped reflectance anisotropies ($k < 1$), peaking only occasionally under Lambertian-like conditions ($k = 1$) if the soil is bright enough. The k values of most of the other LNDs, however, tend to rise from Lambertian (soil) conditions to distinctly bell shaped reflectance anisotropies ($k > 1$) as the LAI value is gradually increased. Having reached their highest level of k at some intermediate canopy LAI, the “wings” of these reflectance anisotropies begin to rise (with respect to the near-zenith BRF values) until Lambertian-like reflectance conditions and eventually also increasingly bell-shaped anisotropy patterns are occurring (for optically dense canopies). In the NIR, on the other hand, k is less than 1 for all simulations. For dark soil conditions an initial rapid decrease in the values of k is followed by a more gradual rise to levels comparable to, or slightly above, its starting value. This behaviour is most (least) noticeable for erectophile (planophile) LNDs, and is somewhat retained even for brighter soil conditions when the LAI value is increased. However, as the soil becomes brighter, the magnitude of both the initial decrease and subsequent recovery of the values of k is reduced. Additionally, these troughs are gradually becoming broader and the minima of k shift to larger LAI conditions as the soil brightness is increased in the NIR.

6.2.2 The Minnaert function parameter for the uncollided, single-collided and multiple collided BRF components.

Given the optical and structural canopy properties of Table 5.1, the range of values that the Minnaert function parameter spans is larger in the red spectral domain than in the NIR. Additionally, the occurrence of bell-shaped anisotropy patterns in Figure 6.3 manifests itself only in the red wavelength regime (where the soil brightness is always greater than the leaf reflectance and transmission values), most notably at low to medium LAI conditions and then predominantly if the LNDs favour vertically oriented leaves. The latter is an indication that k_{red} might (under certain conditions) be susceptible to the canopy structure. To pursue this hunch a bit further, the **Semi-Discrete** model was utilized to separate the total BRFs (ρ_{TOT}) in the red spectral band into their uncollided ρ_{UC} (radiation not scattered by the leaves), single collided ρ_{SC} (radiation scattered once by the leaves), and multiple collided ρ_{MC} (radiation scattered more than once by the leaves) components. The corresponding most likely Minnaert function parameter values were subsequently retrieved by inversion of the RPV model. Figure 6.4 thus documents the change in k_{red} for the uncollided, single- and multiple collided BRF components (rows) as the LAI is increased from 0.1 to 5, for different soil brightness conditions (columns) and leaf normal distributions (colours). Although such an exercise is of interest to understand the spectral and structural prerequisites necessary for bell-shaped reflectance anisotropies, it should be noted that the (most likely) Minnaert function parameter of the overall reflectance field is not a linear combination of the various k components in Figure 6.4. In fact the (most likely) value of k_{red} of the overall reflectance field can only be related (qualitatively) to the k value of its uncollided, single- and multiple collided BRF components through the relative contributions of these latter (compare with section 6.2.3).

- The **uncollided** BRF component (top row) in Figure 6.4 is characterized by bell-shaped anisotropy patterns ($k > 1$). The order in which the k_{UC} values of the various LNDs appear at any given LAI value can be somewhat anticipated from their corresponding $g_L(\Omega_L)$ and $G(\Omega)$ functions in Figure B-1. Those that provide the largest interception cross-section at increased zenith angles favour the occurrence of bowl-shaped anisotropy patterns in the uncollided BRF component. Obviously, in the case of anisotropically scattering soils, the actual values of the k_{UC} parameter in Figure 6.4 would be different. This is because the

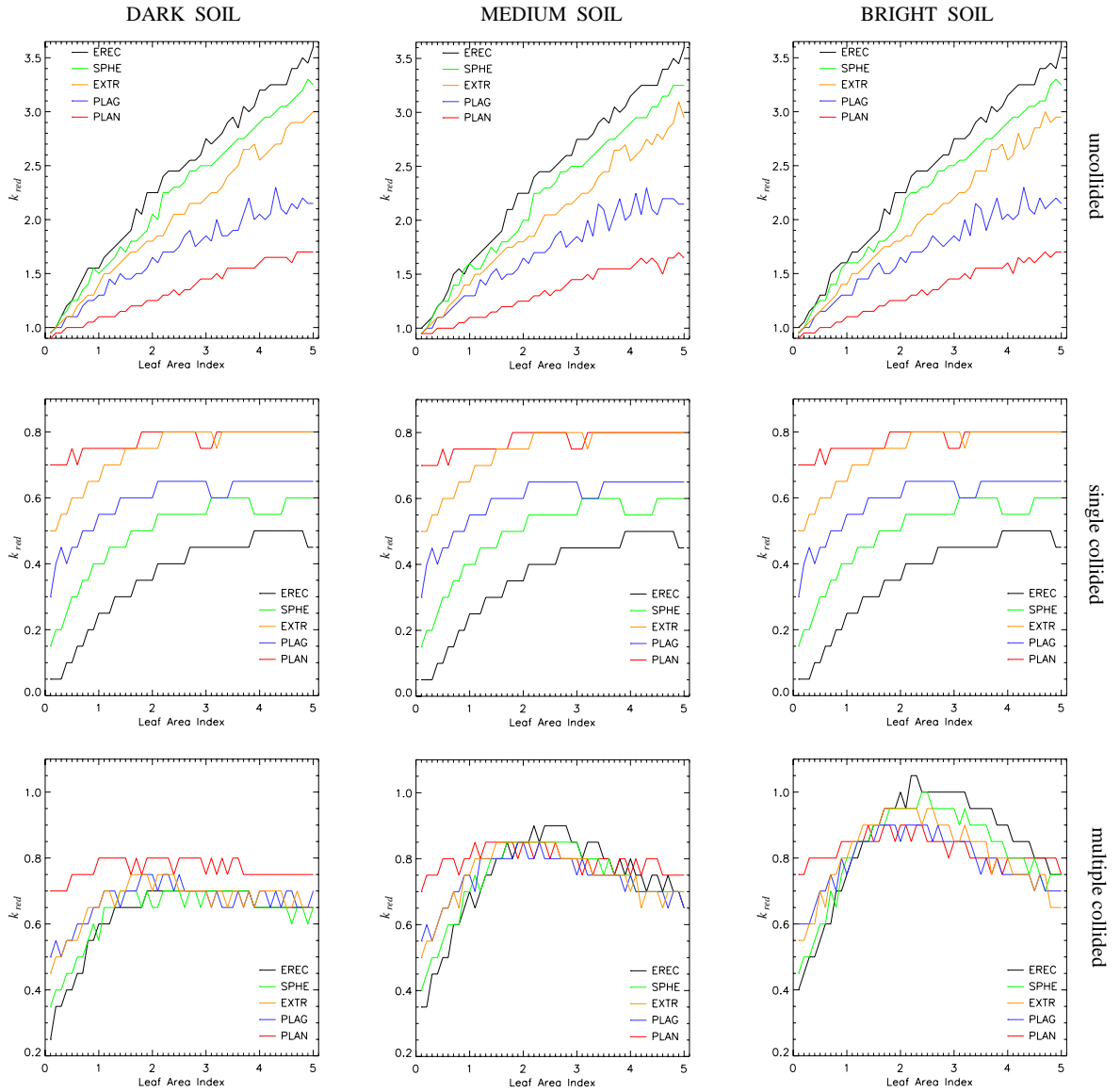


Figure 6.4: Graphs showing the change in the most likely Minnaert function parameter k_{red} for un-, single- and multiple collided BRF components (rows) as the canopy LAI is increased from 0.1 to 5, for different soil brightness conditions (columns) and leaf normal distributions (colours). All scattering phase functions are Lambertian ($\theta_0 = 30^\circ$).

ρ_{UC} component is modulated by the BRF of the underlying soil, as described in Equation 3.1. In the case of Lambertian soils, however, the shape of the uncollided BRF field is entirely controlled by the probability that a photon may travel along any specific direction from the soil through the overlying canopy without being intercepted by the leaves.

- The **single collided** BRF components (middle row) in Figure 6.4 are characterized by k_{SC} values that are smaller than 1. With increasing LAI the bowl-shaped appearance of the angular reflectance anisotropy is however gradually lessened and remains relatively constant for optically thick canopies. In Equation 3.2 the canopy was subdivided into K separate layers, each of which was receiving and reflecting radiation in accordance with the canopy transmission probabilities for the given LND at the height level z_k . For every layer four different factors thus come into play, whose combined effects, when vertically integrated, determine the reflectance anisotropy shape of the single collided BRF component. These factors are 1) the amount of radiation that reaches a given canopy layer, 2)

the amount of radiation that exits the canopy from a given layer, 3) the leaf reflectance and transmittance levels, and 4) the leaf scattering phase function. Which ones of these contributing factors are finally responsible for the observed values of the k_{SC} parameter in the middle row of Figure 6.4 is not obvious to determine. In the end this does not matter for the purpose at hand since the occurrence of $k_{red} > 1$ for the overall reflectance field, appears entirely determined by canopy conditions favouring the relative contribution of ρ_{UC} .

- The **multiple collided** BRF component (lower row) in Figure 6.4 are found to be varying both with the spectral properties of the leaves and the soil. k_{MC} , which is almost always smaller than 1, rises from very low values (bowl-shaped reflectance anisotropy) to peak at medium LAI conditions and to decrease thereafter again. This behaviour is most (least) pronounced for the erectophile (planophile) LND and can be readily explained by the large leaf absorption values in the red such that photons do not experience more than 2–3 interactions (on average) before contributing towards ρ_{MC} . Consequently, their exiting directions will still be somewhat conditioned by their incident direction and the LND of the medium, especially for bright soil conditions. At low to medium LAI conditions the increase in k_{MC} can presumably be related to those photons that were contributed towards ρ_{MC} directly from the soil. Hence the rise in k_{MC} is strongest for erectophile LNDs because here the downward scattering from the leaves is enhanced, and the upward scattering from the soil is least obstructed at small zenith angles. At large LAI values however, this contribution is reduced again due to the increased leaf area density of the canopy.

6.2.3 The relative contributions of ρ_{UC} , ρ_{SC} and ρ_{MC}

In the context of identifying vegetation canopies with bell-shaped reflectance anisotropy patterns in the red spectral band, the most prominent result in Figure 6.4 is that only the shapes of the uncollided BRF component (top row) deliver Minnaert function parameter values greater than 1. However, unless the relative contribution of the uncollided BRF component is dominating, no bell-shaped reflectance anisotropy patterns will be observed. Figure 6.5 indicates how the relative contributions at nadir for the ρ_{UC} , ρ_{SC} and ρ_{MC} components are changing with increasing LAI conditions for both erectophile (left) and planophile (right) LNDs, in the red spectral domain and for different soil brightness conditions. Although the retrieval of the Minnaert function parameter is by no means a linear process, the analysis of the relative contributions of ρ_{UC} in Figure 6.5 can help identifying the conditions under which a bell-shaped reflectance anisotropy is to be expected (for the erectophile (black) and planophile (red) LNDs in the top panels of Figure 6.3).

Initially the overall BRF at nadir for the 1-D' canopy with an erectophile LND is almost entirely dominated by the contributions from the uncollided component. As the LAI values increase, however, the relative weight of ρ_{UC} is diminished and that of ρ_{SC} (and to a lesser extend also ρ_{MC}) begin to rise until eventually the single-collided BRF component is almost exclusively responsible for the retrieved canopy reflectance values. With this behaviour in mind, the development of k_{red} in the upper panels of Figure 6.3 can be explained using the variations of the three components of k in Figure 6.4. Initially it is the $k_{UC} \sim 1$ value that dominates the overall reflectance anisotropy shape. However, although k_{UC} is rapidly rising above 1 as the LAI is increased, its relative contribution is offset against that of k_{SC} which is less than 1. Eventually, the relative weights of these two (and to a lesser extend also k_{MC}) will be in balance, causing the peak in the k_{red} values of the upper panels of Figure 6.3. As the LAI is further increased k_{SC} will dominate and the Minnaert function parameter of the overall anisotropy shape is gradually decreasing to values that asymptotically approach that of k_{SC} . The shifting to higher LAI values

of the crossover point between ρ_{UC}/ρ_{TOT} and ρ_{SC}/ρ_{TOT} (in Figure 6.5) as the soil brightness is increased, thus reflects itself Figure 6.3 by 1) higher k_{red} values due to the continuing dominance of k_{UC} , and 2) the peaking of k_{red} at higher LAI values than for dark soil conditions.

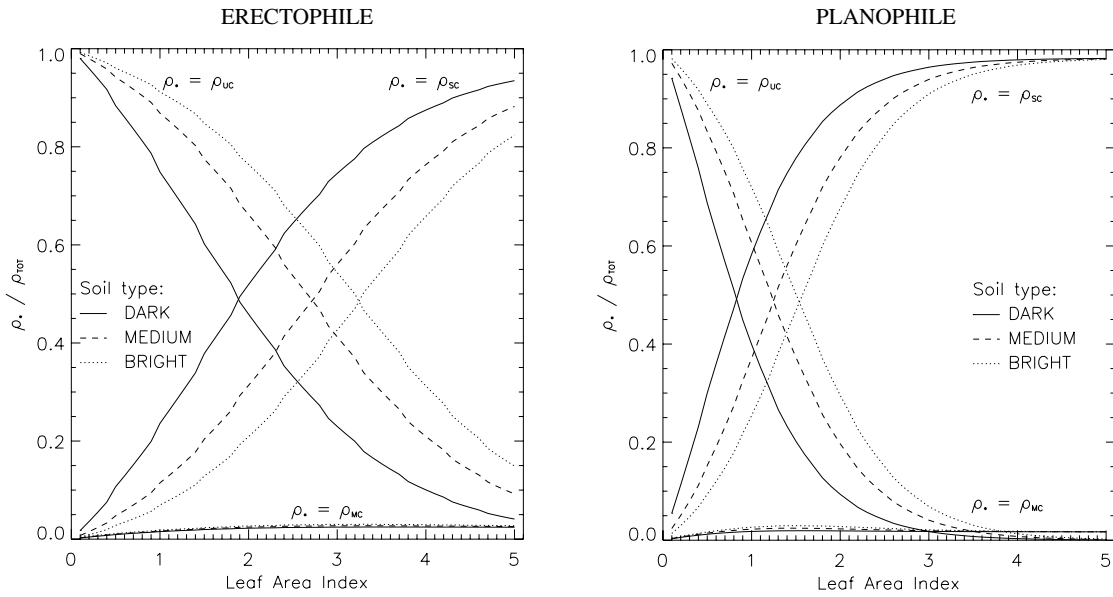


Figure 6.5: The relative contribution of ρ_{UC} , ρ_{SC} and ρ_{MC} towards the overall BRF (ρ_{TOT}), with increasing LAI conditions for erectophile (left panel) and planophile (right panel) LNDs, in the red spectral band and for the different soil brightness conditions indicated in Table 4.1 ($\theta_v = 0^\circ$ and $\theta_0 = 30^\circ$).

6.2.4 The effect of θ_0 on the Minnaert function parameter

Whereas sections 6.2.2 and 6.2.3 documented the change of the Minnaert function parameter for different surface type conditions (*i.e.*, the LAI state variable was varied), in the following, the state of the system under observation will be kept fixed and variations of k_{red} will be monitored as a function of the conditions of observations. More specifically, in the left hand panel of Figure 6.6 the most likely Minnaert function parameter in the red spectral band is plotted as a function of the solar zenith angle, for structurally homogeneous canopies of various LNDs, medium bright soil conditions and a canopy LAI of 1.5. The most prominent result of this graph is the fact that the variations of k_{red} , as θ_0 is increased from 0° to 80° , are characteristic of the LNDs of the various leaf canopies. This suggests that the solar illumination condition could provide a means to discriminate between different degrees of vertical orientations of the dominant structures (*i.e.*, the leaves in the case of the structurally homogeneous canopies here).

A continuous decrease in the value of k_{red} can be observed for predominantly vertically oriented LNDs as the solar zenith angle is increased. For LNDs with predominantly horizontally oriented leaves, an initial fall in the value of k_{red} is compensated by a slight rising (after $\sim 20^\circ$) which continues until 60° or beyond. Interestingly, the k_{red} values of all LNDs cross each other as well as the $k = 1$ line around 60° . This can be related to the fact that the value of the Ross function $G(\Omega)$ at $\theta_0 = 60^\circ$ is almost the same regardless of the LNDs (compare with Figure B-1). Tests have indicated that $k_{UC} > 1$ at this canopy LAI and stays almost constant with θ_0 , whereas k_{SC} (always less than 1) decreases rapidly until $\theta_0 \sim 20^\circ$ before increasing gradually again to its initial values. k_{MC} follows a similar pattern.

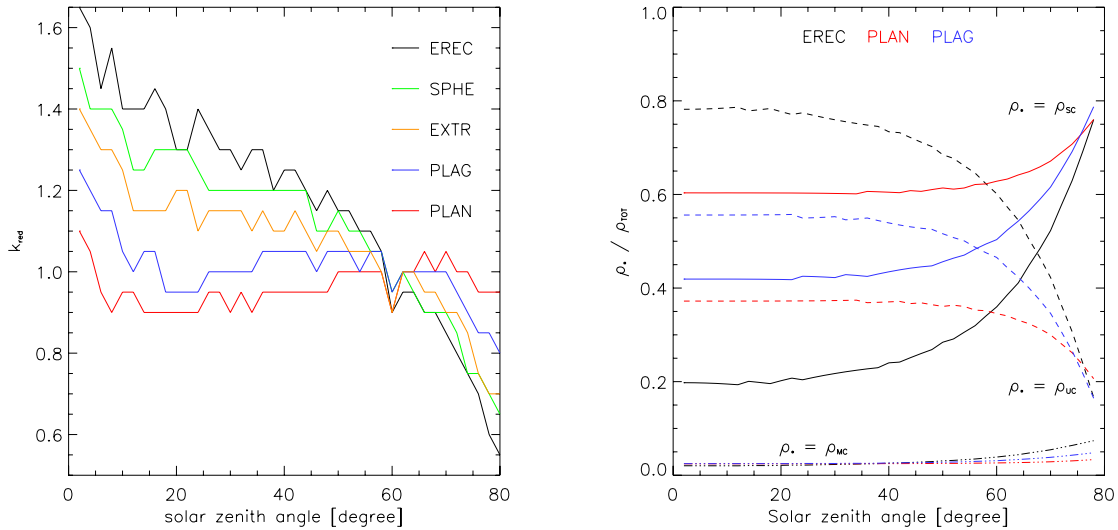


Figure 6.6: Left Panel: The most likely Minnaert function parameter k_{red} as a function of solar zenith angle in the red spectral band, for medium soil brightness conditions, various leaf normal distributions (colours), and a canopy LAI value of 1.5. All scattering phase functions are Lambertian. Right Panel: The relative contribution of ρ_{uc} , ρ_{sc} and ρ_{mc} towards the overall BRF (ρ_{TOT}), with increasing solar zenith angles for erectophile (black), plagiophile (blue) and planophile (red) LNDs under identical conditions as in the left panel.

In the right hand graph of Figure 6.6 the fractions of uncollided, single- and multiple collided nadir BRFs (linestyle) in the red spectral band, are plotted as a function of solar zenith angle, for erectophile, plagiophile and planophile LNDs under identical conditions than in the left hand graph. In the planophile case (red curve) the single collided BRF component (solid line) in the red band is dominating (at 60%) throughout all illumination conditions. In fact its contribution is even increasing when $\theta_0 > 40^\circ$. The uncollided contribution (dashed line), on the other hand, is about 37% at $\theta_0 = 0^\circ$, before gradually decreasing to about 15% as the illumination zenith reaches 80° . Consequently the behaviour of k_{red} for the planophile LND in the left panel of Figure 6.6 follows closely that of the single scattering component (with its absolute value increased due to the uncollided contribution). For an erectophile LND (black curve) the uncollided BRF contribution (dashed line) is about four times as large as the single collided contribution (solid line) at low θ_0 conditions. This is however gradually changing as the solar zenith angle is increased with the relative contributions of the single and uncollided BRF components reaching almost exactly the inverse of their initial proportions. Consequently the k_{red} of the erectophile LND in the left panel starts at a higher value (than the planophile LND), and decreases gradually from bell-shaped to bowl-shaped anisotropy conditions as θ_0 reaches 80° . A more comprehensive overview of the values of k_{red} as a function of canopy LAI and solar zenith angle is given in Figure 6.7 for both erectophile (left graph) and planophile (right graph) LNDs under medium bright soil conditions. The distinct patterns of k_{red} in both panels suggest that multi-directional observations of a non-changing target under different conditions of illumination may provide important clues as to the preferred alignment (with respect to the vertical) of its dominant structural elements (*i.e.*, leaves in this case). Notice that when the solar zenith angle coincides with 60° MISR view zenith angle the fitting accuracy of the RPV model fell to 15–19% versus 3–7% in other cases. The retrieved values of k_{red} tend to be lower in that case (~ 0.1), and this artifact is most noticeable in the planophile case (where the dynamic range of k is less).

At this point we would like to stress out once more that an in-depth identification of the causes for the above reflectance anisotropy shapes is a daunting and somewhat debatable task. Firstly the RPV model is a parametric model whose individual functions are neither orthogonal

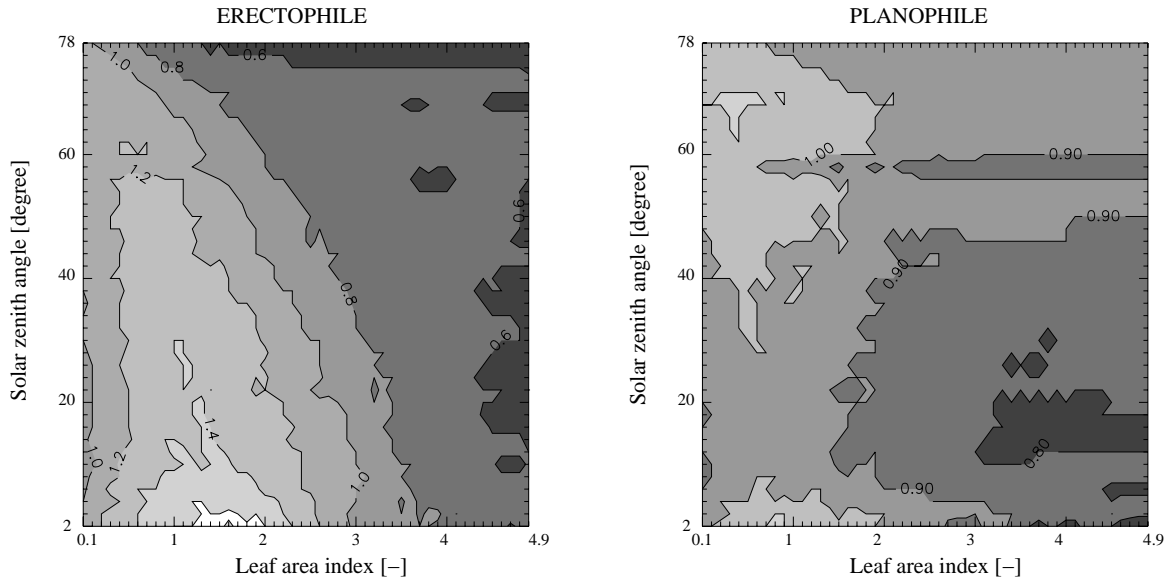


Figure 6.7: The retrieved Minnaert function parameter k_{red} as a function of solar zenith angle and leaf area index for 1-D' leaf canopies of erectophile (left graph) and planophile (right graph) LNDs under medium bright soil conditions. Both the leaves and the soil possess Lambertian scattering phase functions.

nor are its parameters among the state variables of radiation transfer theory in plane-parallel leaf canopies. In essence this implies that—although the main contributions of k and Θ are those depicted in Figure 6.1—the information content of any given reflectance anisotropy shape is to some degree contained in both the k and Θ parameters (and to a lesser extend also in the wings of the hot spot function controlled by ρ_c). In addition, the “goodness of fit” when performing the RPV model inversion also affects the confidence that may be associated with its retrieved parameter estimations. Secondly, a physical interpretation of these parameters should be avoided. Indeed a great many state variables may actually influence the retrieved value of the Minnaert function parameter, such that it will not be obvious to identify the most contributing one(s) of these – even in a case where all optical and structural canopy properties were known. Different factors will dominate the reflectance anisotropy shape under different illumination, structural and optical conditions – as any physically based RT model will be capable of documenting.

The graphs in this section should therefore be seen only as a means to identify 1) the range of variation in the spectral reflectance anisotropy shapes (expressed through the Minnaert function parameter), 2) a broad class of surface type conditions where a bowl-shaped reflectance anisotropy pattern may be observed, and 3) the effects that canopy structure may have on the shape of the observed reflectance signatures. The various reflectance simulation in Figure 6.3 featured bell-shaped anisotropy patterns only in the red spectral domain. In this wavelength regime the soil is generally brighter than the foliage which favours such a development in structurally homogeneous leaf canopies if 1) sufficient radiation can reach the soil and leave the canopy unhindered again, *i.e.*, at low to medium LAI and θ_0 conditions, and 2) predominantly vertically oriented structures exist that obstruct the passage of light at larger view zenith angles, *i.e.*, an erectophile LND.

6.3 Reflectance anisotropy as a surface heterogeneity indicator

The anisotropy pattern of the solar radiation field scattered by vegetation in the red spectral domain is largely controlled by the physical properties and geometric arrangement of the elements that constitute the terrestrial surface. This is because multiple scattering contributions

are relatively insignificant at these wavelengths (Verstraete et al. 1990), and the soil brightness tends to be greater than that of the strongly absorbing foliage elements. Unlike the plane parallel leaf canopies of the previous section, natural vegetated surfaces are made up of foliage agglomerations embedded within distinct envelopes of specific opacity and distributed spatially in a variety of densities and manners. Annex C explains in detail how, under such conditions, the presence of relatively sparse vertical foliage structures (of high LAI values) may yield a typical bell-shaped anisotropy pattern – in contrast to the more bowl-shaped pattern that will be observed over structurally homogeneous (plane-parallel) foliage distributions under identical LAI, LND and vegetation coverage conditions (compare with Figure C-1). In essence, the mechanism for the generation of bell-shaped anisotropy patterns is the same as for the findings in section 6.2, namely the gradual concealment of the underlying soil by vertical foliage structures (tree crowns) as the view zenith angle increases. However, in the case of 3-D canopy representations, it is not so much the LND of the foliage elements within the tree crowns, but rather the size of the inter-tree gaps (together with the vertical elongation of the tree crowns and the leaf area density (LAD) within them) that determine the magnitude of k_{red} . This is because the clumping of leaves into spatially finite foliage structures enhances 1) the LAD in these volumes (under the assumption that TOC level remains the same with respect to the corresponding plane-parallel canopy) and hence also their radiation interception capability at larger view zenith angles, and 2) the radiative contribution of the soil at small view zenith angles. A very high spatial density of optically dense vertical structures yields anisotropy patterns analogous to those of plane-parallel 1-D' media, *i.e.*, bowl-shaped pattern. On the other hand, a very low spatial density of such structures does not significantly affect the anisotropy pattern of the brighter background (which was assumed to be Lambertian in annex C). Only at intermediate vegetation densities can a bell-shaped reflectance pattern be generated – which is similar to what was observed in the 1-D' case. High sun conditions limit the presence of shadows and the associated darkening of the background which favours the exposure of the surface heterogeneity using the Minnaert function parameter (compare with Figure C-4). Increased soil brightness can have a similar effect on the retrieved values of k_{red} , as demonstrated in Figure C-5.

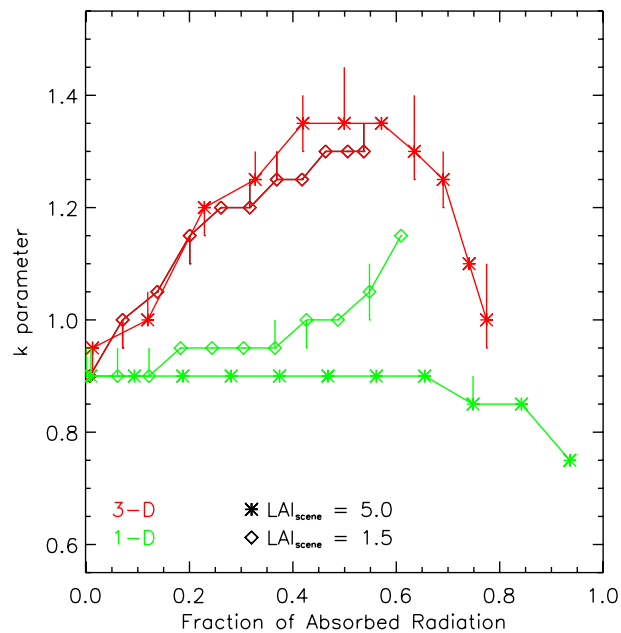


Figure 6.8: Variations of the values of the k_{red} parameter as a function of the fraction of absorbed radiation for vegetation structures equivalent to those in Figure C-2. The spherical foliage clumps (3-D) and plane-parallel canopy representations (1-D) were generated with LAI values of 5.0 (diamonds) and 1.5 (stars). The soil was of medium brightness ($\theta_0 = 30^\circ$).

In annex C, spherical foliage “clumps” with an LAI of 5 were used to gradually increase the LAI average over a 250 m² scene until this reached a value of 5. From Figure 6.3 one can see that under such LAI conditions an otherwise equivalent 1-D’ canopy does not favour bell-shaped anisotropy patterns. Figure 6.8 displays the results when the experiment in Figure C-3 is repeated with a medium soil brightness in the red (0.1724) and for spherical foliage clumps with an LAI value of 5 (diamonds) and 1.5 (stars). Thus as the vegetation coverage reaches 100%, the lower LAI 1-D’ canopy type will have a value of $k_{red} > 1$ (compare with the top row, middle graph of Figure 6.3). Indeed the Minnaert parameter value for the 1-D’ canopy is ~ 1.15 , but the one of the 3-D canopy under the same conditions of LAI, LND and fractional cover has a value of about 1.3! This simulation together with the findings of annex C, thus indicate that the degree of bell-shapedness of the spectral reflectance field for a 3-D (heterogeneous) vegetation canopy will always tend to be larger than that of a 1-D’ canopy with otherwise equivalent properties of LAI, LND, LAD, vegetation coverage, soil brightness, z^{TOC} , etc. This is because both the contribution of the soil at small view zenith angles and the effective blocking of the foliage at larger view zenith angles is enhanced in the structurally heterogeneous case. Finally, the findings displayed in Figure 6.8 do not affect the conclusions of annex C, namely that any value of $k_{red} > 1.05$ requires the usage of three dimensional RT models – since the **Semi-Discrete** RT model accounts for structurally homogeneous vegetation canopies with *finite sized* leaves.

6.4 Concluding remarks

In this chapter evidence was presented that surfaces composed of a bright substratum covered with dark and vertically elongated structures, of preferably high opacity and low to medium spatial density, lie at the origin of bell-shaped reflectance anisotropy patterns. Although the spectral properties of most soils and leaves favour the occurrence of $k > 1$ in the red spectral domain (compare with Figure 2.2), geophysical situations where $k_{NIR} > 1$ might nevertheless exist, such that k_{NIR} could also function (either alone or in conjunction with k_{red}) as an indicator of some kind of subpixel heterogeneity. From the results in section 6.2 and annex C it can be concluded that both structurally homogeneous (1-D’) and heterogeneous (3-D) surface types are capable of producing such reflectance signatures. To determine whether a string of multidirectional satellite measurements with $k > 1$ should be interpreted with a 1-D’ or 3-D surface type solution (in a LUT based inversion scheme) is in essence but a reformulation of the questions at the end of chapter 4 and 5. Does the shape of the angular reflectance anisotropy contain information about the degree of heterogeneity that is present at the surface? And if so, does a certain type of reflectance anisotropy demand the usage of 3-D RT models for its interpretation?

As to the first question the answer is clearly yes. However, whereas for structurally homogeneous “clouds” of disc-like scatterers the value of k_{red} is predominantly determined by the interplay of soil/leaf brightness, LAI, LND and illumination angle, in the case of structurally heterogeneous agglomerations of foliage clumps at the nominal scale of the MISR instrument (275 m), it is predominantly the shape and number of the clusters of leaves as well as their LAI values (in addition to soil/leaf brightness and illumination angle) that affect the magnitude of the Minnaert function parameter. Now, given the fact that terrestrial surfaces are inherently three-dimensional in appearance, 3-D RT models can thus be employed to interpret the variations of k_{red} in terms of the structure of the surface type. In the context of MISR/AirMISR observations, this approach will be dealt with in greater detail in chapter 7.

On the other hand if the user-required information does not relate to 3-D aspects of vegetated surfaces, will it be possible to utilize the value of the Minnaert function parameter in the red as a discriminator between 1-D’ and 3-D RT models? To address this issue, it should be recalled

that the k parameter quantifies only one aspect of the shape of the reflectance anisotropy. It provides a convenient measure of the symmetric curvature properties of the spectral BRDF field. However, both the skewness and hot spot parameters of the RPV model (Θ and ρ_c) also contain valuable information as to the overall shape of the reflectance field. Furthermore, the goodness-of-fit of the best RPV model solution is an important piece of information in its own right since it transmits a notion of the degree of validity that the various RPV parameters convey. But even so, it is possible to anticipate conditions under which the separation of the hot spot (ρ_c) effect from the overall reflectance shape (k , Θ) may become ambiguous or even unfeasible. Such anisotropy patterns are often characterized by somewhat conical shapes and as such could be decomposed alternatively into a very broad hot spot region together with a neutral (Lambertian) k Minnaert function parameter, or, a highly bell-shaped Minnaert function ($k > 1$) with a neutral of insignificant hot spot contribution. Tests have indicated that under surface type conditions favouring such a reflectance field pattern, the RPV model inversion scheme of Gobron and Lajas (2001) tends to favour the first of the above solutions, *i.e.*, it is the hot spot (ρ_c) that accounts for most of the observed BRDF variations. Nevertheless, the BRDF shape in its entirety can always be described by the RPV model parameters and it can thus also be expected that the information contained within k , Θ , ρ_0 and σ_{FIT} in all spectral bands might be related to the radiative separability of chapter 5. On the other hand, relating k alone to $\hat{\epsilon}$, whether retrieved from the red, or, the red and the NIR spectral bands is not likely to provide any conclusive indications as to the Minnaert function parameters' capability to act as a discriminator of 1-D' to 3-D surface types. At this stage the Minnaert function parameter in the red spectral band should thus only be utilized to discriminate between purely 1-D ($k < 1$) and higher order RT models ($k > 1$).

In chapter 5, the separability between the BRDF signatures of a three-dimensional boreal forest representation and some radiatively equivalent plane-parallel surface type was not found to vary anymore beyond a scale of ~ 100 m. The reason for this was that during the creation process of the 3-D canopy representation its "statistics" were conserved at the hectare level. Hence, regardless of the exact pointing of the sensor, it always "saw" similar tree sizes, gaps and optical properties. This implies also that k would not change any more for these forest scenes beyond spatial resolutions of ~ 100 m. Nature however is much less uniform and thus if the spatial resolution of a sensor becomes very large the radiative contributions from all sorts of different structures with their own optical properties and shapes will intermingle to obscure the three-dimensional effects that specific parts of the canopy might have revealed if observed individually and at a higher spatial resolutions. Thus one could expect the radiative separability in the various graphs in chapter 5 to decrease at coarser spatial resolutions if the 3-D conifer forests had been modelled in a more realistic way. This effect was noted in Figure C-8, where k_{red} was gradually decreasing as the sensor resolution was degraded. Specific biome types could thus be characterized by their change in the value of k as a function of the spatial resolution of the observing instrument. A proposal that is in line with the comments made in chapter 5, namely that the subpixel surface heterogeneity (at a specific level of radiative accuracy) will only be exposed at some spatial scales using remote sensing observations, whereas at others it will remain hidden, *i.e.*, 1-D' surface types can fit the measurements equally well.

As a final comment to the findings in this chapter, it should be noted that the variations of k_{red} as a function of the illumination conditions (Figures 6.6 and 6.7) may provide a new avenue for the assessment of subpixel structure, *i.e.*, the retrieval of the most likely LNDs in the context of 1-D' RT models. Given the results of Figure C-5 it can be anticipated that variations in Ω_0 may also improve the retrieval of information relating to the shape and density of the dominant subpixel structures. Indeed, one of the findings of chapter 7 will be exactly along these lines. Hence, it can be envisaged having a configuration of three or more MISR like instruments flying

with the same orbital parameters, but temporally offset, such that their overpass times (at any given location) would correspond to different illumination conditions. Under the assumption that the state of the terrestrial target does not change in between successive observations (1 day), important structural aspects within the confines of the FOV of these sensors could thus be retrieved in addition to documenting the errors associated in current single-view approaches.

Chapter 7

Surface Reflectance and Structure: Combining Anisotropy Indicators

This chapter will investigate quantitative means of characterizing vegetation heterogeneity prior to relating these measures to the reflectance anisotropy indicator, k_{red} . Section 7.1 provides an overview of the various efforts currently underway to describe spatial inhomogeneity. Section 7.2 then introduces the concepts of intermittency and non-stationarity as a means of describing scale-invariant geophysical signals. Section 7.3 shows initial results obtained from superimposing the modified Minnaert function parameter onto the information contained within these structural descriptors. Finally, section 7.4 discusses these findings as well as their implications.

7.1 Surface Heterogeneity Descriptors

The existence of vertically elongated structures was found germane for the occurrence of bell-shaped reflectance anisotropy patterns (under certain spectral conditions) in chapter 6. In annex C, the degree of heterogeneity within the spatial arrangement of foliage clumps was identified as a major structural influence to the reflectance anisotropy signature of natural vegetation canopies. What is thus needed at this point, is the establishment of some quantitative link between the observed reflectance anisotropy shape, on the one hand, and the spatial heterogeneity of the vegetation architecture that gave rise to these observations on the other.

The concept of spatial heterogeneity permeates the fields of ecology and hydrology, most notably in conjunction with GIS or remote sensing applications, *e.g.*, Turner (1987), O'Neill et al. (1988), Kolasa and Pickett (1991), Fotheringham and Rogerson (1994), Kalma and Sivapalan (1995). Just like the concept of scale in chapter 5, spatial heterogeneity possesses no single universal definition, although it is mostly related to the notion of spatial variability (which in turn is scale-dependent). In the context of point patterns spatial heterogeneity means variations in the density of points (*e.g.*, trees in a forest), whereas from a surface pattern perspective it refers to the variability of a spatially continuous parameter (Dutilleul 1993). Alternatively spatial homogeneity might be defined as *remaining similar upon subdivision* which implies a characteristic upper and lower limit of scales within which this property applies (Palmer 1988). In other words, both the resolution (or measurement interval), and the range (or sampling extent) determine the degree of spatial heterogeneity that can be associated with a specific data set. Changing any one of these two aspects may induce a change in the perceived degree of heterogeneity or homogeneity.

A multitude of research projects have been devoted to the extraction and contextual assessment of spatial patterns that were derived from specific variables of interest and scales (resolution and range) of investigation. In the context of remotely sensed image interpretation over forested surfaces, image texture has been related to stand structure – especially when the nominal pixel resolution is equal or less than 1 m (Jupp et al. 1988, St-Onge et al. 1991). More specifically, texture analysis employs pattern recognition techniques that can be categorized into 1) statistical methods (co-occurrence matrix, Fourier transform, auto-correlation function, *etc.*), 2) geometric methods (Voronoi tessellation, texture primitives), 3) model based methods (Markov random fields, fractals), and 4) signal processing methods (spatial domain filtering, Fourier domain filtering, Gabor and wavelet models), (Tuceryan and Jain 1998). However, any conclusion that might be drawn from such an analysis of high resolution digital imagery must obviously be subject to the particular illumination and viewing conditions at the time of observation since these are instrumental for the perceived patterns of interpixel variability and contrast variations. The quantification of spatial heterogeneity is also a key focus in many ecological studies, and a large variety of (global and distributed) metrics exist to quantify landscape patterns in terms of their composition, adjacency, connectedness, shape complexity, dispersion and size distribution, *e.g.*, O’Neill et al. (1988), Ripple et al. (1991), Griffith and Amrhein (1991), Getis and Ord (1992). Many of these, however, are correlated or have been developed solely for specific applications and thus detect individual patterns with varying degrees of accuracy (Hargis et al. 1998).

7.1.1 The Semivariogram

The variogram is a statistical tool—originally derived in mining geology (Matheron 1971)—that has been widely used in geostatistics to measure the spatial variation in a dataset, $\phi(\mathbf{r})$ where \mathbf{r} indicates a vector of spatial coordinates. The semivariogram, which is just half the variogram, is a second order statistics that measures the dissimilarities between two observations $\phi(\mathbf{r})$ and $\phi(\mathbf{r}+\mathbf{h})$ separated by a distance $|\mathbf{h}|$ (the lag) between them. For a one dimensional dataset, $\phi(x)$ with sampling interval ℓ and total length L , the experimental semivariogram along the transect direction x is defined as:

$$\gamma(h) = \frac{\ell}{2(L-h+\ell)} \sum_{i=0}^{(L-h)/\ell} \left[\phi(x_i) - \phi(x_i+h) \right]^2 \quad i = 0, \dots, (L/\ell) - j$$

where $h = j\ell$ is an integer multiple of the sampling interval ℓ ($j = 1, \dots, L/\ell$). Conceptually, the shape of the semivariogram can be characterized by three parameters: the range (which is the distance at which $\gamma(h)$ stops increasing), the sill (which is the value of $\gamma(h)$ for distances equal or greater than the range), and the nugget effect (which is the level of $\gamma(0)$). Figure 7.1 indicates their relevance for a conceptual semivariogram (red) that was overlaid onto an experimental semivariogram (black) obtained from a transect of canopy height data.

A non-zero nugget effect relates to measurement errors and spatial sources of variability that are smaller than the shortest sampling interval (Journel and Huijbregts 1978). In the context of high-resolution, remotely sensed imagery of forested areas, the range was shown to relate to tree size (Woodcock et al. 1988, Cohen et al. 1990), tree density (St-Onge et al. 1991) and increases generally with a coarsening of the texture of digital images. Similarly, the sill has been related to pixel contrast (Cohen et al. 1990) and general variance of the dataset (St-Onge and Cavayas 1995). Hyppänen (1996) used the semivariogram to differentiate Norway Spruce from Scots Pine on the basis of their sill values. It was found that these differences were related both to the vertical layering and the crown shapes, which were different for these two species. The semivariogram has also been shown to be related to the auto-correlation function,

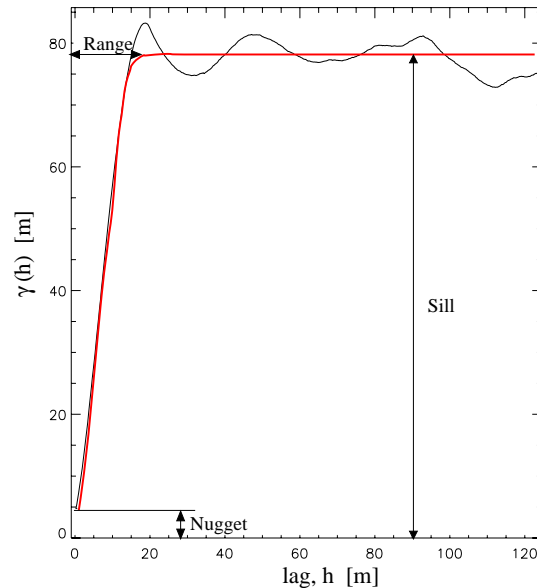


Figure 7.1: Experimental (black) and conceptual (red) semivariogram for a transect of tree heights. The range is the distance at which $\gamma(h)$ stops increasing. The sill is the value of $\gamma(h)$ for distances equal or greater than the range, and the nugget effect is the value of $\gamma(0)$.

the Fourier spectrum, as well as the (mono)fractal dimension of the data (Ramstein and Raffy 1989). However, despite their potential as ‘integrated’ descriptors of some signal properties, none of these measures is capable of providing for an unambiguous characterisation of a given dataset. In section 7.2 this issue is illustrated further and subsequently overcome by utilizing two complementary aspects of a given dataset.

7.1.2 Fractals

Fractals are conceptual objects that show structures at all spatial scales with a scale-dependent self-similarity (Mandelbrot 1982). For example, a circle is not a fractal but a cloud is, since the latter does not become linear upon repeated magnification (Palmer 1988). The fractal dimension can be used as a quantifier for the roughness of a surface or data set. Recent studies have included measures of the fractal geometry of landscapes in patch¹ pattern analyses such as, soil and landscape data analysis, forest fire and cluster growth, tree and habitat structures as well as spatial habitat and landscape pattern analysis, *e.g.*, Burrough (1981), MacKay and Jan (1984), Gardner et al. (1987), Goodchild and Mark (1987), Milne (1988), Bartoli et al. (1991), Williamson and Lawton (1991), Zeide (1991).

In recent years the concept of multifractals (*e.g.*, Grassberger 1983, Hentschel and Procaccia 1983, Parisi and Frisch 1985) have helped to clarify the fuzzy notion of inhomogeneity by introducing and quantifying the effects of intermittency (Davis et al. 1993). Whereas singularity analysis techniques (*e.g.*, Meneveau and Sreenivasan 1987, Schertzer and Lovejoy 1987, Chhabra et al. 1989, Meneveau and Sreenivasan 1989, Lavallée et al. 1991) allow for the extraction of the latter information, the more traditional structure function approach (Monin and Yaglom 1975, Mandelbrot 1982) constitutes a proper framework for addressing the non-stationarity behaviour of geophysical data or processes. In the following section both structure functions and singular analysis techniques will be introduced and subsequently combined for the characterization of

¹A landscape patch can be defined as a relatively homogeneous spatial cell or body (two and three dimensions) differing in appearance from its surrounding matrix (Wu et al. 1992).

geophysical data or processes in terms of their non-stationarity and intermittency properties, respectively. More specifically, the approach of Davis et al. (1993), Davis et al. (1994b), Marshak et al. (1997) and Davis et al. (1999) will be presented.

7.2 Intermittency and non-stationarity of geophysical data

A property of fundamental importance to data analysis is the notion of statistical homogeneity, or *stationarity*, that is defined as invariance of the statistical properties under translation. When this condition is not verified, no meaningful (stable) spatial statistics may be derived from a given data set, or even ensembles of data sets if the spatial statistics of the latter do not converge to their ensemble average values, that is, if they violate ergodicity (Davis et al. 1996). Stationarity can be linked to the geometric appearance of (one-dimensional) datasets, with *smooth*-looking transects being more non-stationary than *rough*-looking ones. To characterize the (non-)stationarity properties of a dataset, structure function analysis, or more specifically, the first order exponent of this technique (H_1) can be utilized. However, statistical stationarity is not a sufficient criteria for the unambiguous characterisation of geophysical datasets. Hence, to overcome this limitation the degree of intermittency (*i.e.*, the occurrence of larger than average jumps) can be quantified in geophysical datasets. Intermittency properties can also be related to the geometric appearance of (one-dimensional) datasets: Transects with a high degree of intermittency are characterized by relatively *sparse* occurrences of variability between adjacent datapoints, whereas for transects with a low degree of intermittency the occurrence of variability is rather *dense*. Intermittency can be characterized by singularity analysis, or more specifically by the first order exponent of this technique (C_1).

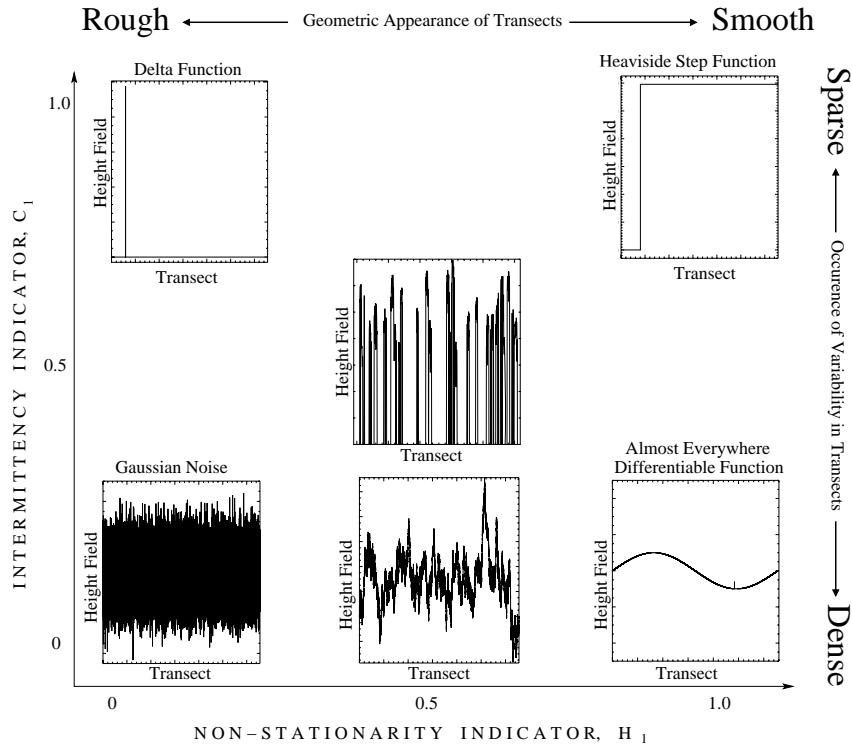


Figure 7.2: Conceptual $H_1 - C_1$ graph: Both Gaussian noise and randomly positioned Dirac δ functions appear geometrically rough and thus are stationary signals. Heaviside step functions and functions that are (varying and) differentiable almost everywhere appear geometrically smooth and hence non-stationary. The Heaviside step function and the Dirac δ function are characterized by highly singular occurrence of variability, *i.e.*, high intermittency. Gaussian noise, fractional Brownian motion and functions that are differentiable almost everywhere possess variability (between adjacent datapoints) almost everywhere, *i.e.*, low intermittency.

Figure 7.2 is an adaptation from Davis et al. (1993) and provides a conceptual classification of various data transects in terms of their non-stationarity and intermittency properties. Stationary and non-intermittent Gaussian noise is positioned at (0,0). It's integral—Fractional Brownian motion—is non-intermittent but also somewhat non-stationary (0.5,0). Functions that are (varying and) differentiable almost everywhere occur at (1,0). Random Dirac Delta functions are highly intermittent but stationary processes (0,1). Heaviside step functions on the other hand are both non-stationary and highly intermittent constructs (1,1). In subsections 7.2.1 and 7.2.2 the procedures for computing both H_1 (structure function analysis) and C_1 (singularity analysis) will be described in greater detail. In section 7.3 actual vegetation canopy height fields will then be characterized using these two indicators.

7.2.1 Structure-function analysis

We consider a generic geophysical signal $\phi(x)$ that represents the “field” we are interested in. Furthermore we assume that $\phi(x)$ is sampled at intervals of length ℓ along the segment $[0, L]$:

$$\phi_i = \phi(x_i) \quad x_i = i\ell \quad i = 0, 1, \dots, \Lambda - 1$$

with the number of datapoints $\Lambda = (L + \ell)/\ell \gg 1$. Next, it is assumed that the geophysical signal behaves in a scale-invariant manner over a range of scales $\eta \leq r \leq R$, that is, power laws will prevail for all scale-conditioned statistics within this range. Thus, for a scale-invariant signal, free of characteristic scales, the corresponding energy spectrum $E(k)$ is expected to follow:

$$E(k) \propto k^{-\beta}$$

where the wavenumber, $k = 1/r$. Davis et al. (1996) have shown that $\beta < 1$ implies stationarity, whereas $1 < \beta < 3$ relates to non-stationarity in geophysical fields that could however be stationary over some range of scales, $\eta \leq r \leq R$. In the following, only the latter type of geophysical signals are considered, and the absolute increment across the scale $r_j = j\ell$ with $j = 1, \dots, \Lambda - 1$ is defined as:

$$|\Delta\phi(r_j; x_i)| = |\phi(x_i + r_j) - \phi(x_i)| \quad i = 0, \dots, \Lambda - j - 1$$

which will be independent of position x_i due to the power-law behaviour. This obviously applies to all q -th order structure functions:

$$\langle |\Delta\phi(r_j)|^q \rangle = \frac{1}{\Lambda - j} \sum_{i=0}^{\Lambda-j-1} |\Delta\phi(r_j; x_i)|^q$$

where $\langle \cdot \rangle$ indicates ensemble averaging over all possible positions ($0 \leq x_i \leq L - r_j$) within the dataset. Due to the scale-invariance it can be expected that for $\eta \leq r \leq R$:

$$\langle |\Delta\phi(r)|^q \rangle \propto r^{\zeta(q)} \quad q \geq 0 \quad (7.1)$$

with $\zeta(q)$ being concave² as long as the proportionality factors in equation 7.1 depend only weakly on q (Parisi and Frisch 1985). Furthermore, it is also non-decreasing if the increments $\Delta\phi(r_j; x_i)$ are bounded (Frisch 1991, Marshak et al. 1994), and finally, due to normalisation one has: $\zeta(0) = 0$. Thus, given the concavity of $\zeta(q)$ a hierarchy of non-increasing exponents $H(q)$ can be defined (Davis et al. 1994b):

²A twice differentiable function $f(x)$, is *concave* (over the interval X) if its second derivative is nonpositive, and is *convex* if its second derivative is nonnegative (for all x within the interval X).

$$H(q) = \frac{\zeta(q)}{q} \quad q \geq 0$$

Obtaining $H(q)$ is the goal of the structure function analysis. Processes with a constant $H(q)$ are called “monoaffine” or “non-stationary monofractals” whereas those with a variable $H(q)$ are called “multiaffine” or “non-stationary multi-fractals” (Viscek and Barabási 1991, Marshak et al. 1994). At least two $\zeta(q)$ are well known: For non-stationary scaling processes with stationary increments the second order structure function $\langle |\Delta\phi(r)|^2 \rangle$ —which is also known as the variogram in geostatistics—can be related to the slope of the power spectrum using the Wiener-Khintchine theorem (Monin and Yaglom 1975):

$$1 \leq \beta = \zeta(2) + 1 = 2H(2) + 1 < 3$$

Furthermore, the $q = 1$ structure function can be related to the fractal dimension $D_{g(\phi)}$ of the graph $g(\phi)$ of $\phi(x)$, when the latter is being viewed as an object in two dimensional Euclidean space (Mandelbrot 1977):

$$0 \leq H_1 = H(1) = \zeta(1) = 2 - D_{g(\phi)} \leq 1 \quad (7.2)$$

H_1 , which is known as the “roughness” or “Hurst” exponent, is thus bounded in the range $[0, 1]$. At its lower limit, H_1 relates to graph filling ($D_{g(\phi)} = 2$) stationary processes whilst at $H_1 = 1$ it indicates the presence of non-fractal signals that are differentiable almost everywhere ($D_{g(\phi)} = 1$), Marshak et al. (1994). Additionally, H_1 , which is also known as the codimension of $g(\phi)$, allows for a geometric interpretation of the data set under study: Low values ($H_1 \rightarrow 0$) relate to increased roughness in the signal whereas high values ($H_1 \rightarrow 1$) indicate the presence of smoothness. According to Davis et al. (1994a), H_1 constitutes the single most important exponent in the whole $H(q)$ hierarchy, not necessarily because of the geometric significance of Equation 7.2 but due to the fact that H_1 defines the linear trend in $\zeta(q)$ (compare with the right hand panel in Figure 7.3). In summary, these authors view H_1 as a direct quantifier of the system’s non-stationarity whereas the complete hierarchy of $\zeta(q)$ or $H(q)$ exponents may serve as a means to qualify this non-stationarity. As such H_1 will provide one of the information axes when classifying the height-field structure of vegetation canopies in section 7.3 where this information will be related to the radiation field that emerges from within these surface types.

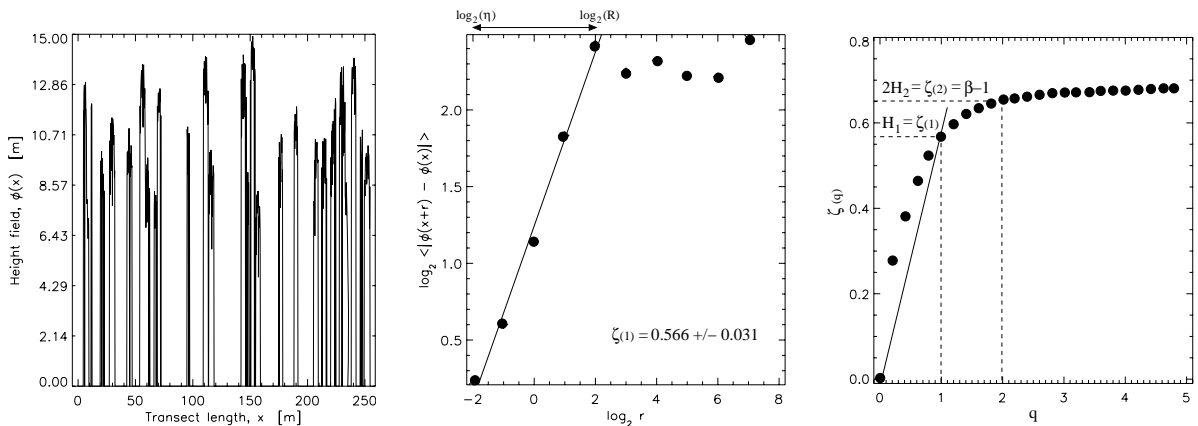


Figure 7.3: Left hand panel: A tree height transect corresponding to a scene with LAI=2.5 that is structurally equivalent to those in the right hand column of Figure C-2 and that was sampled at ~ 25 cm interval over the nominal resolution of MISR (275 m). Middle panel: The corresponding \log_2 - \log_2 plot of the first order structure function versus the scale r . Right hand panel: The resulting $\zeta(q)$ function plotted against q with H_1 being indicated.

Figure 7.3 provides an overview of the structural function analysis: The left hand panel shows a tree height transect (corresponding to a 3-D scene with LAI=2.5, that is structurally equivalent to those in the right hand column of Figure C-2) sampled at ~ 25 cm interval over the spatial sampling frequency of MISR (275 m); the middle panel displays the corresponding \log_2 - \log_2 plot of the first order structure function versus the scale r ; and in the right hand panel the resulting $\zeta(q)$ function is plotted against q .

7.2.2 Singularity analysis

Although structure functions can be used to characterize the non-stationary multifractal structure of geophysical data-sets, such information is, however, not necessarily unique – especially for monofractal processes or when only H_1 is being considered. In order to remove this indetermination it has been suggested to characterize the role of *intermittency* in the observed signal (Marshak et al. 1997). In other words, it would be of interest to analyze the occurrence of “spikiness” (or larger-than-average jumps) – ideally in a stationary dataset. One way to obtain a stationary field from a non-stationary one with stationary increments ($1 < \beta < 3$) is by computing nearest-neighbour differences (Davis et al. 1996). This operation reduces the power spectrum slope of the resulting (absolute) gradient field β^* by two ($\beta^* = \beta - 2$). For the dataset in Figure 7.3 with $\beta \approx 1.65$, such an approach yields irregular gradient fields with $\beta^* < 0$ – which does, however, not make a difference to the outcome of the singularity analysis (Lavallée et al. 1993, Tessier et al. 1993). The “singular measures” approach of Davis et al. (1994b) and Marshak et al. (1997) will be presented here, although other approaches have been proposed, *e.g.*, Meneveau and Sreenivasan 1987, Schertzer and Lovejoy 1987, Chhabra et al. 1989, Meneveau and Sreenivasan 1989, Lavallée et al. 1991.

The m -th order normalized absolute gradient field $\epsilon(\eta; x_i)_m$, is defined over the smallest scale (η) for which a power-law behaviour persists within the dataset (compare with Figure 7.3):

$$\epsilon(\eta; x_i)_m = \frac{|\Delta\phi(\eta; x_i)|^m}{\langle |\Delta\phi(\eta; x_i)|^m \rangle} \quad i = 0, 1, \dots, \Lambda - e - 1$$

where the scale $\eta = e\ell$ with $e > 0$, the number of datapoints $\Lambda = (L + \ell)/\ell \gg 1$ and ℓ is the sampling interval of the datapoints along the segment $[0, L]$. Also:

$$\langle |\Delta\phi(\eta; x_i)|^m \rangle = \frac{1}{\Lambda - e} \sum_{i=0}^{\Lambda - e - 1} |\Delta\phi(\eta; x_i)|^m$$

Setting $m = 1$ for simplicity, the normalized absolute gradient field can be “coarse grained” for any position $0 \leq x \leq L - \eta - r$ and scale $0 \leq r \leq L - \eta$:

$$\epsilon(r_j; x_i) = \frac{1}{j+1} \sum_{i=i}^{i+j} \epsilon(\eta; x_i) \quad \begin{array}{l} i = 0, \dots, \Lambda - e - j - 1 \\ j = 0, \dots, \Lambda - e - 1 \end{array} \quad (7.3)$$

which when raised to the q -th power, before being averaged over all possible positions ($i = 0, \dots, \Lambda - e - j - 1$) along the normalized absolute gradient field, yields:

$$\langle \epsilon(r_j)^q \rangle = \frac{1}{\Lambda - e - j} \sum_{i=0}^{\Lambda - e - j - 1} \epsilon(r_j; x_i)^q$$

These $\langle \epsilon(r_j)^q \rangle$ are presumably stationary and can be related (for some range of scales r) to the convex exponent function $K(q)$ (Schertzer and Lovejoy 1987):

$$\langle \epsilon(r)^q \rangle \propto \left(\frac{r}{L} \right)^{K(q)} \quad q \geq 0 \quad (7.4)$$

where the restriction on q is in general required only when some $\epsilon(\eta; x_i) = 0$ occur within the dataset (Marshak et al. 1997). This was, however, the case for the height field transect shown in the left hand panel of Figure 7.3. Under such conditions a discontinuity in $K(q)$ may occur as $q \rightarrow 0$ (compare with the right hand panel in Figure 7.4). It is important to note that the scale ratio $r/L \ll 1$ in the small scale limit, which is always the most reliable (Davis et al. 1994b). Both $K(0)$ and $K(1)$ are equal to zero, which follows from the normalization of the probability distribution function for $\epsilon(r_j; x_i)$, and from Equation 7.3 which implies that $\langle \epsilon(r_j) \rangle = 1$ and hence $K(1) = 0$ (Marshak et al. 1997).

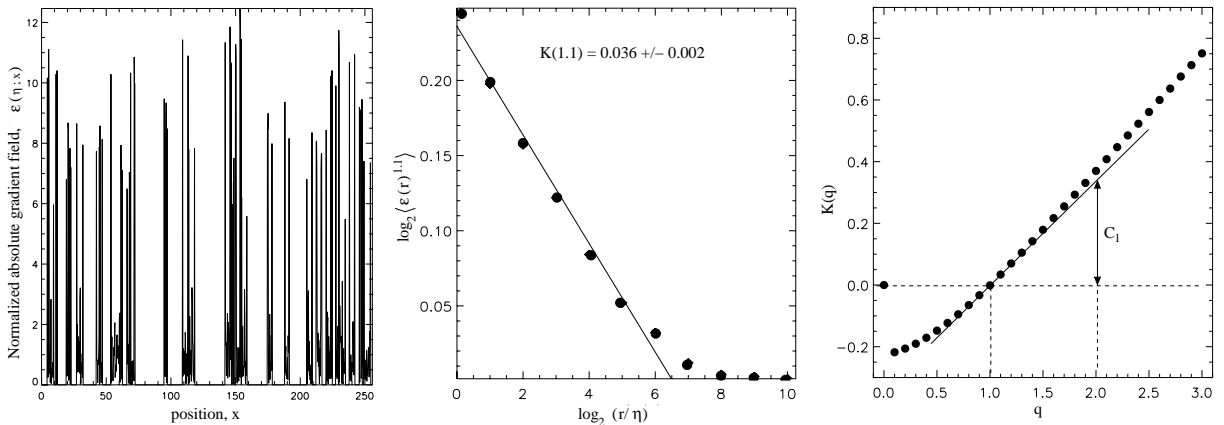


Figure 7.4: Left hand panel: The normalized absolute gradient field, $\epsilon(\eta; x)$ for the tree-height transect indicated in the left hand panel in Figure 7.3. Middle panel: The corresponding \log_2 - \log_2 plot of the $q = 1.1$ singularity measure, $\langle \epsilon(r)^{1.1} \rangle$ versus the scale r/η . Right hand panel: The resulting $K(q)$ function. Notice the discontinuity as $q \rightarrow 0$ and the quasi-linear increase beyond $q \approx 1.5$.

As was the case for structure functions, a non-decreasing hierarchy of exponents can be defined $C(q) = K(q)/(q - 1)$ which is related to the well-known non-increasing hierarchy of “generalized dimensions” $D(q)$, first introduced by Grassberger (1983) and Hentschel and Procaccia (1983) in the context of deterministic chaos theory:

$$C(q) = 1 + D(q) = K(q)/(q - 1) \quad (7.5)$$

Given that $D(q)$ or $C(q)$ are constant then the process under study is termed “uniform” as opposed to “multifractal” if they are changing. Applying l’Hopital’s rule for $q \rightarrow 1$ in Equation 7.5 yields a straightforward measure for the inhomogeneity in the sense of singular measures, which is the currently accepted way of characterizing intermittency (Davis et al. 1994b):

$$0 \leq C_1 = C(1) = K'(1) \leq 1$$

where the upper limit of C_1 has been set equal to 1 thus excluding degenerate gradient fields. At $C_1 = 0$ the data exhibits weak variability (low intermittency), whereas at its upper limit the signal becomes extremely intermittent (*e.g.*, random Dirac δ function). In the latter case, the signal may be characterized geometrically by the adjective ‘sparse’ whereas in the former, with information available almost everywhere along the data set ($D(1) = 1$), it may be labeled as ‘dense’. As was the case with structure functions, Davis et al. (1994a) argue that C_1 quantifies intermittency whereas the full hierarchy of exponents is required to qualify it. Furthermore, they propose to utilize the $H_1 - C_1$ plane as a means of characterizing geophysical datasets

when scale-invariance is present. Figure 7.2 displayed such a conceptual $H_1 - C_1$ plane with the position of some specific data-sets being indicated. Note also that the central graph in this figure corresponds to the canopy height transect depicted in the left hand panel of Figure 7.3 with $C_1 \approx 0.37$ and $H_1 \approx 0.57$. In the following section the $H_1 - C_1$ approach will thus be applied to the characterisation of canopy height fields as a surrogate for the three-dimensional structure of vegetated surfaces. These structural statistics will then be related to the shape of the spectral reflectance anisotropy (as characterized by the Minnaert function parameter, k) that was simulated for these vegetation canopy types.

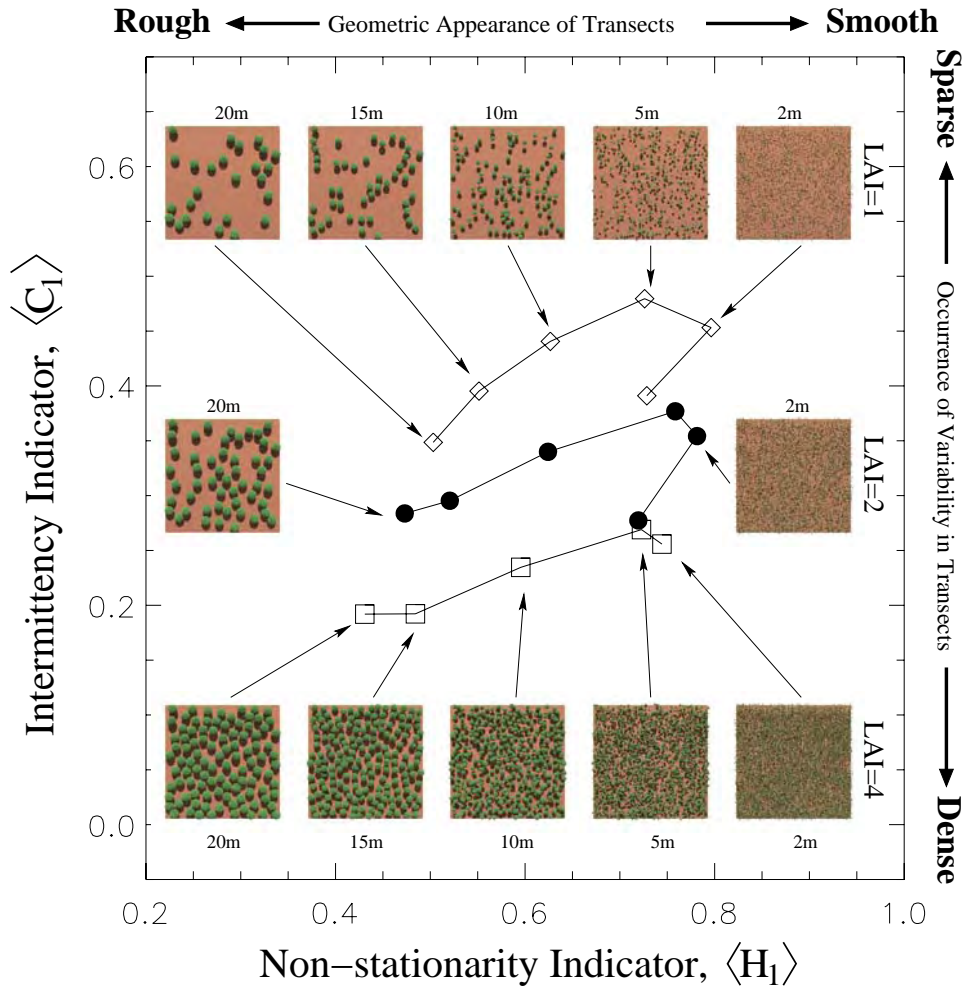


Figure 7.5: $\langle H_1 \rangle$, $\langle C_1 \rangle$ statistics for heterogeneous vegetation canopies composed of ‘floating’ spherical foliage clumps (with an LAI of 5). The diameter of the spherical envelopes is gradually increased from 1 m (right) to 20 m (left) to cover the scene with an overall LAI of 1 (diamonds), 2 (filled circles) and 4 (squares).

7.3 Combining surface structure and reflectance information

In order to derive the necessary canopy height data, the model of Govaerts and Verstraete (1998) was applied to a large variety of 3-D vegetation canopy representations including those of annex A and C. The sampling interval of the subsequent height measurements ($\ell \simeq 25$ cm), was chosen such as to be greater than the characteristic scale of the leaves, yet smaller than the typical dimension of the tree crowns or the gaps in between them. Some 40 transects of equal length (2^{10} data points) but with different origins and orientations were sampled. For each of these,

the H_1 , C_1 statistics were computed in the small scale limit following the approach of Davis et al. (1994b). The structure functions were fitted (on a \log_2 - \log_2 plot) from scale $\eta = \ell$ to the first detected scale break (~ 1 – 2 orders of magnitude), or, in its absence, through all the data. C_1 was computed from a normalized absolute gradient field of step size η . Ultimately, these H_1 , C_1 statistics were ensemble-averaged to yield a directionally independent estimate of the non-stationarity $\langle H_1 \rangle$ and intermittency $\langle C_1 \rangle$ of the vegetation height at the resolution of the MISR pixel (275 m). Figure 7.5 indicates the changes in H_1 , C_1 as the diameter of spherical foliage agglomerations (with a LAI of 5) is increased from 1 m to 20 m, to generate scenes with three different overall LAI values: 1 (diamonds), 2 (filled circles) and 4 (squares). It can be seen that the lower the scene-LAI the higher the value of the intermittency indicator C_1 . As the sphere size is decreased both H_1 and C_1 are increasing until, for sphere diameters smaller than ~ 5 m, the occurrence and size of “soil-to-tree jumps” is becoming too frequent on the one hand, and too regular on the other such that both indicators start to decrease again. Further examples are presented in Figure D-1.

By computing the values of the Minnaert function parameter k_{red} for a large set of vegetation canopies whose $\langle H_1 \rangle$, $\langle C_1 \rangle$ statistics are known (compare with Figure D-2), both types of information can be compared. Figure D-4 shows that indeed, there exists a clustering in $\langle H_1 \rangle$, $\langle C_1 \rangle$ space of surface types with bell-shaped reflectance anisotropies ($k_{red} > 1.05$). The same can also be observed from Figure 7.6 which shows how the individual values of the Minnaert function parameter (for some of the surface types in Figure D-4) change as the solar zenith angle is altered from 0° (left panel) to 30° (right panel). The former illumination conditions enhance both the bell-shape of structurally heterogeneous surfaces and the bowl-shape of structurally homogeneous surfaces (and IPA thereof).

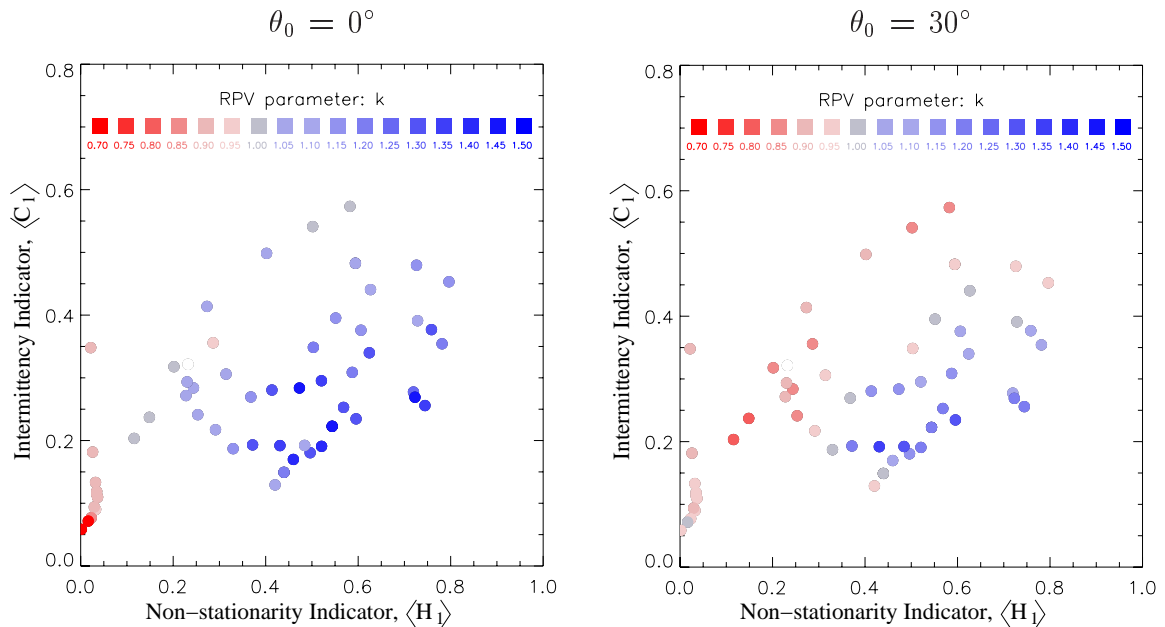


Figure 7.6: The Minnaert function parameter k_{red} (colour) in relation to the $\langle H_1 \rangle$, $\langle C_1 \rangle$ statistics for a series of surface types with the solar zenith angle being zero (left panel) and thirty degree (right panel).

7.4 Discussion

The work presented in this chapter provides a quantitative linkage between the spectral reflectance anisotropy pattern (quantified through the Minnaert function parameter, k), and the canopy height field structure (quantified by the non-stationarity and intermittency indicators,

$\langle H_1 \rangle$ and $\langle C_1 \rangle$ respectively). The examples shown relate to situations where the underlying soil brightness is sufficiently larger than that of the canopy foliage – a situation commonly encountered in the red spectral domain. An immediate consequence of these findings is thus the derivation of subpixel heterogeneity (in terms of their $\langle H_1 \rangle, \langle C_1 \rangle$ statistics) from multiangular remote sensing observations. However, before discussing such an undertaking we would like to address the issue of alternative measures for the characterisation of the spatial heterogeneity/variability. Two of the most used measures include the fractal dimension and the semivariogram. However, fractal dimensions are directly linked to H_1 and hence do not account for any information relating to the intermittency of the data, which is why they have been combined with “lacunarity” measures in an attempt to overcome this ambiguity (Tuceryan and Jain 1998). The slope of the semi-variogram, on the other hand, is related to H_2 and hence suffers from the same drawback as the spectral slope and the fractal dimension. In most ecological applications, however, the range and (sill – nugget) distances are exploited as independent information for the characterisation of the spatial variability of a dataset. Figure 7.7 compares such an approach with the one proposed in annex D, and shows that the information contained within the semivariogram measures (right panel) is not capable of reproducing a similar clustering of $k > 1$ as can be observed in the $\langle H_1 \rangle, \langle C_1 \rangle$ approach (left panel).

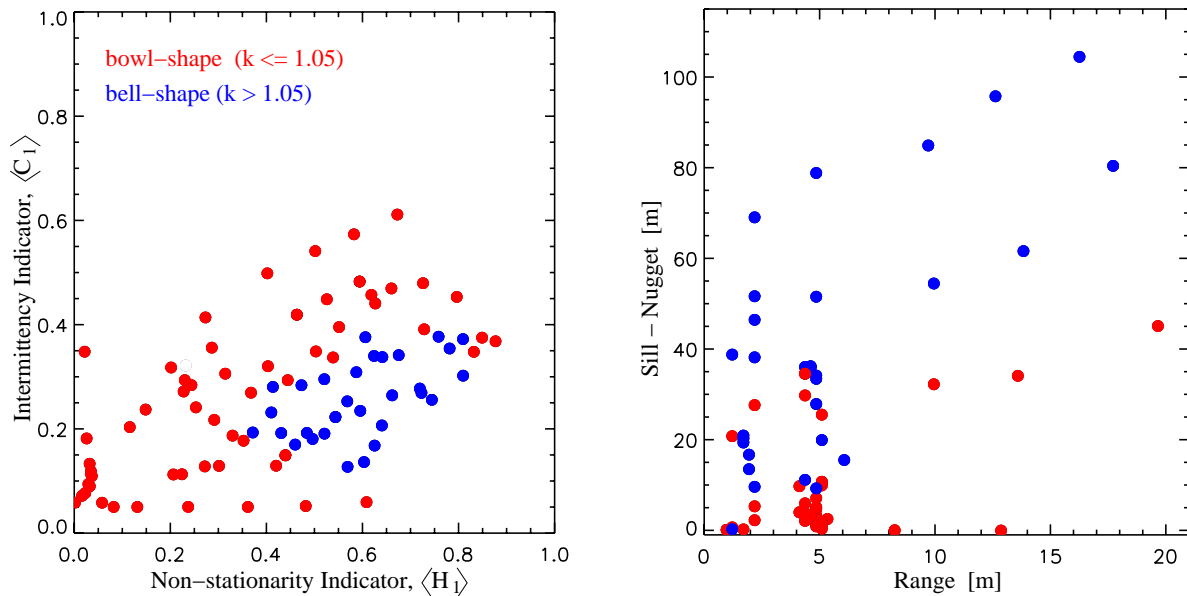


Figure 7.7: Left Panel: The Minnaert function parameter k_{red} (colour) in relation to the $\langle H_1 \rangle, \langle C_1 \rangle$ statistics obtained from height field transects for a series of different surface types. Right panel: The Minnaert function parameter k_{red} (colour) in relation to the range and (sill-nugget) information obtained from experimental semi-variograms on the same height field transects. The solar zenith angle being thirty degree.

The implications of the results in Figures 7.6 and D-4 are mainly twofold. First there is indeed a quantifiable linkage between vegetation canopy height fields and the reflectance anisotropy that might originate from these surface types in the red spectral domain – in other words the reasoning in chapter 6 and annex C about the indicative potential of the k parameter with respect to surface heterogeneity is correct. Secondly, multidirectional satellite observations could thus be exploited to yield such structural information, which in turn might help select the structurally and spectrally most alike candidate from a set of predefined 3-D surface types. One possible approach to achieve such a structural characterization at the subpixel level could be by relating the vegetation coverage or FAPAR (of the scene) to the value of the intermittency indicator $\langle C_1 \rangle$ (compare with Figure D-1). The algorithm of Gobron et al. (2001a), which is

capable of delivering both the FAPAR and the value of k_{red} at the TOC, could thus provide a first clue as to what the value of the intermittency indicator might be. Beware, however, that such a relationship might actually be far from obvious in reality, *i.e.*, height variations in annex D were always induced by foliage elements and not by tree trunks, dead branches or rocky outcrops. Indeed the presence of topography could seriously bias the findings reported in this chapter and annex D. After all, the vegetation height field is taken only as a proxy to describe the three-dimensional aspects of vegetation canopy structure. Alternative variables, like the local LAI, surely exist, but might be less convenient for validation purposes. From both panels in Figure 7.6 it can be seen that fixing k and $\langle C_1 \rangle$ might not be sufficient to retrieve the corresponding non-stationarity indicator $\langle H_1 \rangle$. This could be achieved if two measurements at two different solar illumination positions were available. Alternatively, by combining optical and radar sensors to yield instantaneous reflectance anisotropy and canopy height field estimates, respectively (Treuhaft et al. 1996, Treuhaft and Siquera 2000), one might substantiate any relationships between FAPAR and $\langle C_1 \rangle$, or directly provide the $\langle H_1 \rangle$, $\langle C_1 \rangle$ statistics of the scene of interest. Such an approach would not only remove the bias of topography in estimating $\langle H_1 \rangle$, $\langle C_1 \rangle$ but also add further constraints (like tree height and biomass) on the selection of the most appropriate 3-D surface type in a LUT based inversion scheme.

A few additional comments are required at this stage. First, both H_1 and C_1 depend on the sampling interval as well as the length of the dataset. Regularization models are, however, available to convert between different sampling intervals and dataset lengths (assuming that the governing geophysical mechanisms are known), *e.g.*, Marshak et al. (1994). The second comment relates to the values of $k < 1$ for the structurally homogeneous scenes in the lower left corner of both panels in Figure 7.6 (compare also with the left hand panel in Figure D-1): In section 6.2 it was shown that the Minnaert function parameter could easily be greater than 1 if the LAI, LND and soil brightness conditions were appropriate. Since the $\langle H_1 \rangle, \langle C_1 \rangle$ of structurally homogeneous canopy types cannot be expected to change substantially for different LNDs (although their k values do) their appears to be a breakdown in the previously mentioned linkage between canopy height and reflectance anisotropy. The reasons for this are however related to the fact that in Figure 7.6 the sampling size ($\ell \approx 25\text{cm}$) was greater than the size of the scatterer (5 cm). For ℓ being of the order of 0.1 cm, say, the $\langle H_1 \rangle, \langle C_1 \rangle$ between erectophile and planophile LNDs would in all likelihood be different. Finally it should also be noted that all 3-D scenes for which the $\langle H_1 \rangle, \langle C_1 \rangle$ statistics had been retrieved were azimuthally homogeneous, *i.e.*, there were no rows or other structural artifacts that would have made the value of k_{red} dependent on the azimuth of observation. This latter factor can thus either be seen as an additional source of information since it allows for the exploitation of the azimuthal organization of landscapes, or else as a source of noise since it might adversely affect the retrieval of representative structural characteristics for a given pixel.

7.5 Conclusion

In this chapter it was shown that first order structure function and singularity measure exponents provide an appropriate basis for the characterization of canopy height fields. Furthermore, when relating these statistics to the modified Minnaert function parameter k_{red} , a distinct clustering of surface types favouring bell-shaped reflectance anisotropy patterns becomes apparent. Such a relationship can be utilized to derive quantitative structural information of terrestrial surfaces at the subpixel scale from multidirectional satellite measurements like those of MISR. The semivariogram, on the other hand, did not permit the establishment of such a link between k_{red} and the information contained within its ‘range’ and the ‘sill – nugget’ axes.

Chapter 8

Summary and Outlook

This research has been motivated by the need to improve our understanding and exploitation of space-borne observations over terrestrial surfaces. More specifically, this work aimed at providing **new avenues for the extraction of quantitative information about the subpixel-scale surface heterogeneity from optical remote sensing data**. Accurate knowledge of the spatial (and temporal) variability of the biosphere's characteristics is not only useful to address critical scientific issues (climate change, environmental degradation, biodiversity preservation, *etc.*) but also to provide appropriate initial and boundary conditions for general circulation or landscape succession models. In this context, satellite remote sensing provides a convenient, efficient and cost-effective way to acquire data repetitively over large areas and at spatial resolutions adequate to address many key ecological and climate change related issues. Two different approaches were pursued to achieve the characterization of surface heterogeneity at the subpixel scale.

The first one was a LUT-based inversion scheme, where an accurate 3-D representation of the structural and optical canopy properties (obtained from field and laboratory measurements) were used to generate a series of TOA spectral reflectance fields for that specific surface type and for a set of atmospheric states at the spatial resolution of the specified sensor. From amongst these predefined surface type/atmospheric depth solution pairs, the method selects an optimal solution such that both the temporal consistency and the user-specified accuracy requirements are guaranteed. Once such a pre-defined surface type solution has been selected, all optical and structural properties used to generate this simulated 3-D vegetation canopy can be retrieved. This, in turn, allows the derivation of structural information on that canopy. The method has been successfully applied to the identification and characterization of boreal coniferous forests over Northern Europe. One implication of such a high level of structural detail is, however, that the possible number of parameter value combinations increases, and thus also the potential number of the predefined surface types in the LUT. This has the obvious consequence that the radiative discrimination between these various candidate solution becomes smaller and smaller, *i.e.*, it may be no longer possible to distinguish between some of the predefined solutions on the sole basis of their spectral reflectance values. It was shown that multidirectional BRDF measurements may enhance the radiative uniqueness of the predefined 3-D surface type candidates. However, under certain conditions of illumination, accuracy requirements and atmospheric depth the explicit representation of all structural properties of vegetation canopies may not be needed to simulate reflectance fields that are sufficiently similar to those measured from space. Indeed, Occam's razor, when applied to two competing, physically-based RT models of different complexity (*i.e.*, 1-D' versus 3-D) that are both capable of delivering equivalent reflectance fields

(within the required accuracy limits), states that the simpler RT model should be given preference in the absence of any other advantageous property of one or the other approach. It was subsequently shown that the need for 3-D RT models (in a LUT based inversion scheme) was primarily necessary when the required tolerance of the fit between the modelled and measured BRF values was becoming very small, and this even more so at higher spatial resolutions. The latter conditions, however, have the adverse effect that both the exact placement of the sensors FOV with respect to the features on the ground, and the actual conditions of illumination (both direct and diffuse) significantly influence the observed reflectance fields, and thus also on the information retrieval accuracy. Alternatively, for any fixed value of the accuracy level, the explicit simulation of the three-dimensionality of any given surface type is (from a radiative point of view) only required over a specific range of scales. This is because there will always be a scale/accuracy combination at which a structurally homogeneous surface type solution can provide equivalent BRF values, hence effectively reducing the amount of structural information that may be retrieved from that pixel location.

The second approach to quantify the degree of surface heterogeneity involved the characterization of its relation with the reflectance anisotropy shape. This was achieved in terms of the modified Minnaert function parameter, k , retrieved through inversion of the parametric RPV model (Rahman et al. 1993a) against multidirectional reflectance data. The k parameter allows to differentiate between primarily ‘bowl-shaped’ reflectance anisotropy patterns ($k < 1$), and ‘bell-shaped’ reflectance anisotropy patterns ($k > 1$). Under Lambertian soil conditions, $k < 1$ is, for example, indicative of optically-thick plane-parallel leaf canopies, whereas $k > 1$ may relate to both structurally homogeneous and heterogeneous vegetation canopies with their dominant structures being vertically elongated, sufficiently dark, opaque and sparsely distributed over a brighter background surface. Given the spatial sampling frequency of the Multiangle Imaging Spectro-Radiometer (275 m), it was shown that observation made under low Sun zenith angles favor the detectability of such heterogeneous vegetation conditions, especially in the red spectral domain where the spectral contrast between the (darker) foliage elements and the (brighter) underlying soil tends to be maximized. Furthermore, the value of k_{red} was documented to increase with soil brightness and decrease with the spatial resolution of the observing sensor. Variations of k_{red} as a function of the solar zenith angle turned out to be characteristic of the leaf normal distributions in a series of structurally homogeneous leaf canopies. This suggests that multiangular Earth-Observation under varying illumination conditions might provide additional information on the preferred orientation/shape of the dominant subpixel structures. Similarly, the fact that surface heterogeneity at the subpixel level is a scale dependent feature (as far as its reflectance signature is concerned) could be utilized to characterize the spatial organization of landscape patterns and ecosystems in terms of k_{red} at multiple spatial resolutions. One attempt at linking the surface reflectance anisotropy to its structural configuration was provided. As a first step, vegetation canopy structure was characterized in the small scale limit by non-stationarity ($\langle H_1 \rangle$) and intermittency ($\langle C_1 \rangle$) exponents using an ensemble of canopy height transects of different orientations and origins. In a second step, the reflectance anisotropy quantifier k_{red} , when retrieved from the top of the canopy reflectance fields of the corresponding surface types, was found to form clusters with $k > 1$ in $\langle H_1 \rangle, \langle C_1 \rangle$ space. The extend of these clusters was shown to increase with low illumination zenith angles. For Lambertian soil properties, one can thus conjecture that the exposure of subpixel scale surface heterogeneity ($k > 1$) from the analysis of an angular signature identifies regions for which, at the scale of observation, inversion procedures should preferably be based on three-dimensional radiation transfer models (simulating structurally homogeneous or heterogeneous vegetation canopies). The evidence presented for the detection of significantly heterogeneous surfaces from a straightforward analysis of multi-angular satellite observations, thus provides the rationale for proposing the parameter k as a new axis of

information, in addition to the classical spectrally-derived information, for applications where land cover characterizations are sought.

Further research could be performed on a variety of issues, most obviously on establishing a link between heterogeneous surface structures and the variations of k with respect to the solar illumination conditions. This parameter could also be related to a more ‘user-friendly’ concept like ‘gapiness’ or some form of ‘aspect ratio’ rather than the more abstract information on intermittency and non-stationarity. Ultimately however the goal is to derive surface heterogeneity information at the subpixel scale, from multispectral and multidirectional remote sensing observations in the optical domain. Applications of both the LUT-based inversion approach and the retrieval of the modified Minnaert function parameter are obvious candidates to spread the benefit gained from this research. This appears especially promising in the context of the Multiangle Imaging Spectro-Radiometer instrument on board TERRA, where the higher spatial resolution and the multispectral, multidirectional sampling of the Earth’s reflectance field provides for a better identification and characterization of the underlying surfaces than what is feasible with current sensors. Land cover characterizations using k_{red} and the fraction of absorbed photosynthetically active radiation (FAPAR) have already been shown to deliver promising results (Gobron et al. 2001a).

Bibliography

- Adams, J., D. Sabol, V. Kapos, R. Filho, D. Roberts, M. Smith, and A. Gillespie (1995). Classification of multispectral images based on fractions of endmembers: application to land-cover change in the Brazilian Amazon. *Remote Sensing of Environment* 52, 137–154.
- Antyufeev, V. S. and A. L. Marshak (1990). Monte Carlo method and transport equation in plant canopies. *Remote Sensing of Environment* 31, 183–191.
- Arvo, J. and D. Kirk (1989). A survey of ray tracing acceleration techniques. In A. S. Glassner (Ed.), *An Introduction to Ray Tracing*, pp. 201–262. London, U.K.: Academic.
- Asner, G. P., B. H. Braswell, D. S. Schimel, and C. A. Wessman (1998). Ecological research needs from multiangle remote sensing data. *Remote Sensing of Environment* 63, 155–165.
- Asrar, G. (1989). *Theory and Applications of Optical Remote Sensing*. New York: John Wiley & Sons.
- Avissar, R. and M. M. Verstraete (1990). The representation of continental surface processes in mesoscale atmospheric models. *Reviews of Geophysics* 28, 35–52.
- Baret, F. and G. Guyot (1991). Potentials and limits of vegetation indices for LAI and APAR assessment. *Remote Sensing of Environment* 35, 161–173.
- Barker, H. W. (1996). A parametrization for computing grid-averaged solar fluxes for inhomogeneous boundary layer clouds - part 1: Methodology and homogeneous biases. *Journal of the Atmospheric Sciences* 53, 2289–2303.
- Bartoli, F., R. Philippy, M. Doirisse, S. Niquet, and M. Dubuit (1991). Structure and self-similarity in silty and sandy soils: The fractal approach. *Journal of Soil Science* 42, 167–185.
- Bastin, L. (1997). Comparison of fuzzy c-means classification, linear mixture modelling and mlc probabilities as tools for unmixing coarse pixel. *International Journal of Remote Sensing* 18, 3629–3648.
- Belward, A., J. C. Taylor, M. J. Stuttard, E. Bignal, J. Mathews, and D. Curtis (1990). An unsupervised approach to the classification of semi-natural vegetation from Landsat thematic mapper data. *International Journal of Remote Sensing* 11, 429–445.
- Belward, A. S. e. (1999). The IGBP-DIS Global 1-km Land Cover Data Set DISCover: A project overview. *Photogrammetric Engineering & Remote Sensing* 65, 1013–1020.
- Benson, B. J. and M. D. MacKenzie (1995). Effects of sensor spatial resolution on landscape structure parameters. *Landscape Ecology* 10, 113–120.
- Berthelot, B., L. Adam, L. Kergoat, F. Cabot, P. Maisongrande, and G. Dedieu (1997). A global dataset of surface reflectances and vegetation indices derived from AVHRR/GVI time series for 1989–1990: the land surface reflectances (LASUR) data. In *Proceedings of the 7th ISPRS International Symposium on Physical Measurements and Signatures in Remote Sensing, Courchevel, France, 7–11 April 1997*. CNES.

- Borel, C. C., S. A. W. Gerstl, and B. J. Powers (1991). The radiosity method in optical remote sensing of structured 3-D surfaces. *Remote Sensing of Environment* 36, 13–44.
- Borel, C. and S. Gerstl (1994). Nonlinear spectral mixing models for vegetative and soil surfaces. *Remote Sensing of Environment* 47, 403–416.
- Brakke, T. W., J. A. Smith, and H. J. M. (1989). Bidirectional scattering of light from tree leaves. *Remote Sensing of Environment* 29, 175–183.
- Breece, H. T. and R. A. Holmes (1971). Bidirectional scattering characteristics of healthy green soybeans and corn leaves in vivo. *Applied Optics* 10, 119–127.
- Brown, P. S. and J. P. Pandolfo (1969). An equivalent-obstacle model for the computation of radiation flux in obstructed layers. *Agricultural Meteorology* 6, 407–421.
- Bunnik, N. J. J. (1978). The multispectral reflectance of shortwave radiation of agricultural crops in relation with their morphological and optical properties. Technical report, Mededelingen Landbouwhogeschool, Wageningen, The Netherlands.
- Burrough, P. A. (1981). Fractal dimensions of landscapes and other environmental data. *Nature* 294, 241–243.
- Cahalan, R., W. Ridgeway, and W. J. Wiscombe (1994a). Independent pixel and Monte Carlo estimates of stratocumulus albedo. *Journal of the Atmospheric Sciences* 51, 3776–3790.
- Cahalan, R. F., W. Ridgeway, W. J. Wiscombe, T. L. Bell, and J. B. Snider (1994b). The albedo of fractal stratocumulus clouds. *Journal of Atmospheric sciences* 51, 2434–2455.
- Camillo, P. (1987). A canopy reflectance model based on an analytical solution to the multiple scattering equation. *Remote Sensing of Environment* 23, 453–477.
- Cermák, J., F. Riguzzi, and R. Ceulemanns (1998). Scaling up from individual tree to the stand level in Scots pine. I. Needle distribution, overall crown and root geometry. *Annales des sciences forestières* 55, 63–88.
- Chambers, L. H., B. A. Wielicki, and K. F. Evans (1997). On the accuracy of the independent pixel approximation for satellite estimates of oceanic boundary layer cloud optical depth. *Journal of Geophysical Research* 102, 1779–1794.
- Chandrasekhar, S. (1960). *Radiative Transfer*. New York: Dover Publications, Inc.
- Chen, J. M. and S. G. Leblanc (1997a). A four-scale bidirectional reflectance model based on canopy architecture. *IEEE Transactions on Geoscience and Remote Sensing* 35, 1316–1337.
- Chen, J. M., P. M. Rich, S. T. Gower, J. M. Norman, and S. Plummer (1997b). Leaf area index of boreal forests: Theory, techniques and measurements. *Journal of Geophysical Research* 102, 29,429–29,443.
- Chen, J. M., X. Li, T. Nilson, and A. Strahler (2000). Recent advances in geometrical optical modelling and its applications. *Remote Sensing Review* 18, 227–262.
- Chhabra, A. B., C. Meneveau, R. V. Jensen, and K. R. Sreenivasan (1989). Direct determination of the $f(\alpha)$ singularity spectrum. *Physical Review A* 40, 5284–5294.
- Cierniewski, J. (1987). A model for soil surface roughness influence on the spectral response of bare soils in the visible and near infrared range. *Remote Sensing of Environment* 23, 97–115.
- Clevers, J., C. Büker, H. van Leuwen, and B. Bouman (1994). A framework for monitoring crop growth by combining directional and spectral remote sensing information. *Remote Sensing of Environment* 50, 161–170.

- Coakley, J. J. A. (1991). Reflectivities of uniform and broken layered clouds. *Tellus 43B*, 420–433.
- Cohen, W. B., T. A. Spies, and G. A. Bradshaw (1990). Semivariograms of digital imagery for analysis of conifer canopy structure. *Remote Sensing of Environment 34*, 167–178.
- Coulson, K. L., G. M. Bouricius, and E. L. Gray (1965). Optical reflectance properties of natural surfaces. *Journal of Geophysical Research 70*, 4601–4611.
- Coulson, K. L. (1966). Effects of reflection properties of natural surfaces in aerial reconnaissance. *Applied Optics 5*, 905–917.
- Curran, P. (1981). The relationship between polarized visible light and vegetation amount. *Remote Sensing of Environment 11*, 87–92.
- Cushnie, J. L. (1987). The interactive effect of spatial resolution and degree of variability within land-cover types on classification accuracies. *International Journal of Remote Sensing 8*, 15–29.
- Davis, A. B., A. L. Marshak, and W. J. Wiscombe (1993). Bi-multifractal analysis and multi-affine modelling of non-stationary geophysical processes, application to turbulence and clouds. *Fractals 1*, 560–567.
- Davis, A. B., A. Marshak, and W. J. Wiscombe (1994a). Wavelet-based multifractal analysis of non-stationary and/or intermittent geophysical signals. In E. Foufoula-Georgiou and P. Kumar (Eds.), *Wavelets in Geophysics*, pp. 249–298. San Diego: Academic Press.
- Davis, A. B., A. Marshak, W. J. Wiscombe, and R. F. Cahalan (1994b). Multifractal characterization of nonstationarity and intermittency in geophysical fields: Observed, retrieved, or simulated. *Journal of Geophysical Research 99*, 8055–8072.
- Davis, A. B., A. Marshak, W. J. Wiscombe, and R. F. Cahalan (1996). Scale invariance in liquid water distributions in marine stratocumulus. Part i: Spectral properties and stationarity issues. *Journal of the Atmospheric Sciences 53*, 1538–1558.
- Davis, A. B., A. Marshak, R. F. Cahalan, and W. J. Wiscombe (1997). The LANDSAT scale-break in stratocumulus as a three-dimensional radiative smoothing effect, implications for cloud remote sensing. *Journal of Atmospheric Sciences 54*, 241–260.
- Davis, A. B., A. Marshak, H. Gerber, and W. J. Wiscombe (1999). Horizontal structure of marine boundary layer clouds from centimeter to kilometer scales. *Journal of Geophysical Research 104*, 6123–6144.
- De Reffye, P. and F. Houllier (1997). Modelling plant growth and architecture: Some recent advances and applications to agronomy and forestry. *Current Science 73*, 984–992.
- Deering, D. W. (1989). Field measurements of bidirectional reflectance. In G. Asrar (Ed.), *Theory and Applications of Optical Remote Sensing*, pp. 14–65. New York: John Wiley & Sons.
- DeFries, R., M. Hansen, M. Steininger, R. Dubayah, R. Sohlberg, and J. Townshend (1997). Subpixel forest cover in Central Africa from multisensor, multitemporal data. *Remote Sensing of Environment 60*, 228–246.
- Deschamps, P. Y., F.-M. Bréon, M. Leroy, A. Podaire, A. Bricaud, J.-C. Buriez, and G. Sèze (1994). The POLDER mission: Instruments characteristics and scientific objectives. *IEEE Transactions on Geosciences and Remote Sensing 32*, 586–615.
- Devroye, L. (1986). *Non-Uniform Random Variate Generation*. New York: Springer-Verlag.
- Dickinson, R. E., B. Pinty, and M. M. Verstraete (1990). Relating surface albedos in GCM to remotely sensed data. *Agricultural and Forest Meteorology 52*, 109–131.

- Diner, D. J. et al. (1991). A Multi-Angle Imaging SpectroRadiometer for terrestrial remote sensing from the Earth Observing system. *International Journal of Imaging Systems and Technology* 3, 92–107.
- Diner, D. J., W. A. Abdou, H. R. Gordon, R. A. Kahn, Y. Knyazikhin, J. V. Martonchik, S. McMuldroch, R. B. Myneni, and R. A. West (1997). MISR Level 2 Ancillary products and Datasets Algorithm Theoretical Basis. Technical Report JPL D-13402, Rev. A, NASA Jet Propulsion Laboratory.
- Diner, D. J., R. Davies, L. Di Girolamo, A. Horvath, C. Moroney, J.-P. Muller, S. R. Paradise, D. Wenkert, and J. Zong (1997). MISR Level 2 Cloud Detection and Classification Algorithm Theoretical Basis. Technical Report JPL D-11399, Rev. C, NASA Jet Propulsion Laboratory.
- Diner, D. J., L. M. Barge, C. J. Bruegge, T. G. Chrien, J. E. Conel, M. L. Eastwood, J. D. Garcia, H. M. A., C. G. Kurzweil, W. C. Ledebor, P. N. D., C. M. Sarture, and B. G. Smith (1998a). The airborne multi-angle imaging spectroradiometer AirMISR instrument description and first results. *IEEE, Transactions on Geoscience and Remote Sensing* 36, 1339–1349.
- Diner, D. J., J. C. Beckert, T. H. Reilly, C. J. Bruegge, J. E. Conel, R. Kahn, J. V. Martonchik, T. P. Ackerman, R. Davies, S. A. W. Gerstl, H. R. Gordon, J. P. Muller, R. B. Myneni, P. J. Sellers, B. Pinty, and M. M. Verstraete (1998b). Multiangle imaging spectroradiometer (MISR) description and experiment overview. *IEEE, Transactions on Geoscience and Remote Sensing* 36, 1072–1087.
- Diner, D. J., G. P. Asner, R. Davies, Y. Knyazikhin, J.-P. Muller, A. W. Nolin, B. Pinty, C. B. Schaaf, and J. Stroeve (1999). New directions in earth observing: Scientific applications of multiangle remote sensing. *Bulletin of the American Meteorological Society* 80, 2209–2228.
- Dirmhirn, I. and F. D. Eaton (1975). Some characteristics of the albedo of snow. *Journal of Applied Meteorology* 14, 375–379.
- Disney, M. I., P. Lewis, and P. R. J. North (2000). Monte Carlo raytracing in optical canopy reflectance modelling. *Remote Sensing Review* 18, 163–196.
- Dutilleul, P. (1993). Spatial heterogeneity and the design of ecological field experiments. *Ecology* 74, 1646–1658.
- Egan, W. G. (1985). *Photometry and polarization in Remote Sensing*. New York: Elsevier.
- Egbert, D. D. (1977). A practical method for correcting bidirectional reflectance variations. In *Proceedings of the Machine Processing Remotely Sensed Data Symposium*, pp. 178–189.
- Engelsen, O., B. Pinty, M. M. Verstraete, and J. V. Martonchik (1996). Parametric bidirectional reflectance factor models: Evaluation, improvements and applications. Technical Report EUR 16426 EN, EC Joint Research Centre.
- Flasse, S., M. M. Verstraete, B. Pinty, and C. Bruegge (1993). Modeling Spectralon’s bidirectional reflectance for in-flight calibration of Earth-orbiting sensors. In *Proceedings of the SPIE Conference on Recent Advances in Sensors, Radiometric Calibration, and Processing of Remotely Sensed Data, Orlando, Florida, 14–16 April 1993*, pp. 100–108. SPIE 1938.
- Fotheringham, S. and P. E. Rogerson (1994). *Spatial analysis and GIS*. London: Taylor and Francis.
- Fournier, R. A., P. M. Rich, and R. Landry (1997). Hierarchical characterization of canopy architecture for boreal forest. *Journal of Geophysical Research* 102, 29,445–29,454.
- Franklin, J., J. Michaelsen, and A. H. Strahler (1985). Spatial analysis of density pattern in coniferous forest stands. *Vegetatio* 64, 29–36.

- Franklin, J. and A. H. Strahler (1988). Invertible canopy reflectance modeling of vegetation structure in semiarid woodland. *IEEE Transactions on Geoscience and Remote Sensing* 26, 809–825.
- Friedl, M. A. (1997). Examining the effects of sensor resolution and sub-pixel heterogeneity on spectral vegetation indices: Implications for biophysical modeling. In D. A. Quattrochi and M. F. E. Goodchild (Eds.), *Scale in Remote Sensing and GIS*, pp. 113–139. New York: CRC Press Inc.: Lewis Publishers.
- Frisch, U. (1991). From global scaling à la Kolmogorov, to local multifractal in fully developed turbulence. *Proceedings of The Royal Society London, section A* 434, 89–99.
- Froehlich, C. and J. Lean (1998). The sun's total irradiance: Cycles and trends in the past two decades and associated climate change uncertainties. *Geophysical Research Letters* 25, 4377–4380.
- Gabriel, P. M. and K. F. Evans (1996). Simple radiative-transfer methods for calculating domain-averaged solar fluxes in inhomogeneous clouds. *Journal of the Atmospheric Sciences* 53, 858–877.
- Gardner, R. H., B. T. Milne, M. G. Turner, and R. V. O'Neill (1987). Neutral models for the analysis of broadscale landscape patterns. *Landscape Ecology* 1, 19–28.
- Gastellu-Etchegorry, J.-P., V. Demarez, V. Pinel, and F. Zagolski (1996). Modeling radiative transfer in heterogeneous 3-d vegetation canopies. *Remote Sensing of Environment* 58, 131–156.
- Gates, D. M., H. J. Keegan, J. C. Schleter, and V. R. Weidner (1965). Spectral properties of plants. *Applied Optics* 4, 11–20.
- Gaussman, H. W. (1977). Reflectance of leaf components. *Remote Sensing of Environment* 6, 1–9.
- Genda, H. and H. Okayama (1978). Estimation of soil moisture and components by measuring the degree of spectral polarization with a remote sensing simulator. *Applied Optics* 17, 3439–3443.
- Gerard, F. F. and P. R. J. North (1997). Analyzing the effect of structural variability and canopy gaps on forest BRDF using a geometric-optical model. *Remote Sensing of Environment* 62, 46–62.
- Gerstl, S. A. W. (1988). Angular reflectance signature of the canopy hotspot in the optical regime. In *4th Intl. Coll. On Spectral Signatures of Objects in Remote Sensing, Aussois, France*, pp. 129. ESA report SP-287.
- Gerstl, S. A. W. (1990). Physics concepts of optical and radar reflectance signatures: A summary review. *International Journal of Remote Sensing* 11, 1109–1117.
- Gerstl, S. A. W. and C. C. Borel (1992). Principles of radiosity method versus radiative transfer for canopy reflectance modeling. *IEEE Transactions on Geoscience and Remote Sensing* 30, 271–275.
- Gervin, J., A. Kerber, R. Witt, Y. Lu, and R. Sekhon (1985). Comparison of Level 1 land cover classification accuracy for MSS and AVHRR data. *International Journal of Remote Sensing* 6, 47–57.
- Getis, A. and J. K. Ord (1992). The analysis of spatial association by distance statistics. *Geographical Analysis* 24, 189–206.
- Gill, P. and W. Murray (1972). Quasi-newton methods for unconstrained optimization. *Journal of the Institute of Mathematics and its Applications* 9, 91–108.

- Glassner, A. S. (1989). Surface physics for ray tracing. In A. S. Glassner (Ed.), *An Introduction to Ray Tracing*, pp. 121–160. London, U.K.: Academic.
- Gobron, N., B. Pinty, and M. M. Verstraete (1997a). Presentation and application of an advanced model for the scattering of light by vegetation in the solar domain. In *Proceedings of the 7th ISPRS International Symposium on Physical Measurements and Signatures in Remote Sensing, Courchevel, France, 7–11 April 1997*, pp. 267–273. Balkema/Rotterdam/Brookfield.
- Gobron, N., B. Pinty, and M. M. Verstraete (1997b). Theoretical limits to the estimation of the leaf area index on the basis of optical remote sensing data. *IEEE Transactions on Geoscience and Remote Sensing* 35, 1438–1445.
- Gobron, N., B. Pinty, M. M. Verstraete, and Y. Govaerts (1997c). A semi-discrete model for the scattering of light by vegetation. *Journal of Geophysical Research* 102, 9431–9446.
- Gobron, N., B. Pinty, M. M. Verstraete, and J.-L. Widlowski (1998). Development of spectral indices optimized for the VEGETATION instrument: Phase 1 report. Technical report, EC Joint Research Centre.
- Gobron, N., B. Pinty, and M. M. Verstraete (1999a). A new algorithm to characterize the land surface at the global scale with AVHRR data. In M. M. Verstraete, M. Menenti, and J. Peltoniemi (Eds.), *Observing Land from Space: Science, Customers and Technology*, pp. 143–150. Dordrecht, The Netherlands: Kluwer Academic Publishers.
- Gobron, N., B. Pinty, M. M. Verstraete, and Y. Govaerts (1999b). The MERIS Global Vegetation Index (MGVI): description and preliminary application. *International Journal of Remote Sensing* 20, 1917–1927.
- Gobron, N., B. Pinty, M. M. Verstraete, J. V. Martonchik, and D. J. Diner (2000a). The potential of multi-angular spectral measurements to characterize land surfaces: Conceptual approach and exploratory application. *Journal of Geophysical Research* 105, 17539–17550.
- Gobron, N., B. Pinty, M. M. Verstraete, and J.-L. Widlowski (2000b). Advanced spectral algorithm and new vegetation indices optimized for up coming sensors: Development, accuracy and applications. *IEEE Transactions on Geoscience and Remote Sensing* 36, 2489–2505.
- Gobron, N., B. Pinty, M. M. Verstraete, J.-L. Widlowski, and D. J. Diner (2001a). Uniqueness of multi-angular measurements - Part 2: Joint retrieval of vegetation structure and photosynthetic activity from MISR. *IEEE Transactions on Geoscience and Remote Sensing MISR special issue*, submitted.
- Gobron, N., B. Pinty, M. M. Verstraete, J.-L. Widlowski, and D. J. Diner (2001b). Joint retrieval of vegetation structure and photosynthetic activity from MISR. In *Proceedings of IGARSS 2001, July 9-13, Sydney, Australia*.
- Gobron, N., F. Mélin, B. Pinty, M. M. Verstraete, J.-L. Widlowski, and G. Bucini (2001c). A global vegetation index for SeaWiFS: Design and applications. In M. Beniston and M. M. Verstraete (Eds.), *Remote Sensing and Climate Modeling: Synergies and Limitations*, pp. 5–21. Dordrecht, The Netherlands: Kluwer Academic Publishers.
- Gobron, N. and D. Lajas (2001). A fast scheme to invert the RPV model against multiangle data. *Canadian Journal of Remote Sensing*, submitted.
- Goel, N. S. and D. E. Strebel (1983). Inversion of vegetation canopy reflectance models for estimating agronomic variables. i. problem definition and initial results using Suits model. *Remote Sensing of Environment* 13, 487–507.

- Goel, N. S. and D. E. Strebel (1984). Simple beta distribution representation of leaf orientation in vegetation canopies. *Agronomy Journal* 76, 800–803.
- Goel, N. S. and R. L. Thompson (1984). Inversion of vegetation canopy reflectance models for estimating agronomic variables. V. Estimation of leaf area index and average leaf angle using measured canopy reflectances. *Remote Sensing of Environment* 14, 77–111.
- Goel, N. (1988). Models of vegetation canopy reflectance and their use in estimation of biophysical parameters from reflectance data. *Remote Sensing Reviews* 4, 1–212.
- Goel, N. S. (1989). Inversion of canopy reflectance models for estimation of biophysical parameters from reflectance data. In *Wiley Series in Remote Sensing. Theory and Applications of Optical Remote Sensing*, edited by Ghassem Asrar, pp. 205–251. John Wiley & Sons, Inc. ISBN 0-471-62895-6.
- Goel, N. S., L. B. Knox, and J. M. Norman (1991a). From artificial life to real life: Computer simulation of plant growth. *International Journal of General Systems* 18, 291–319.
- Goel, N. S., I. Rozehnal, and R. L. Thompson (1991b). A computer graphics based model for scattering from objects of arbitrary shapes in the optical region. *Remote Sensing of Environment* 36, 73–104.
- Goel, N. S. and W. Qin (1994). Influences of canopy architecture on relationships between various vegetation indices and LAI and FPAR: A computer simulation. *Remote Sensing Reviews* 10, 309–347.
- Goel, N. S., W. Qin, and B. Wang (1997). On the estimation of leaf size and crown geometry for tree canopies from hotspot observations. *Journal of Geophysical Research* 102, 29,543–29,554.
- Goodchild, M. F. and D. M. Mark (1987). The fractal nature of geographic phenomena. *Annals, Association of American Geographers* 77, 265–278.
- Govaerts, Y. and M. M. Verstraete (1994). Applications of the L-systems to canopy reflectance modelling in a Monte Carlo ray tracing technique. In *Fractals in Geosciences and Remote Sensing, Proceedings of a Joint JRC/EARSeL Expert Meeting, Ispra, Italy, 14–15 April 1994*, pp. 211–236. European Commission.
- Govaerts, Y. (1995). *A Model of Light Scattering in Three-Dimensional Plant Canopies: A Monte Carlo Ray Tracing Approach*. Ph. D. thesis, Université Catholique de Louvain-la-Neuve, Département de Physique, 2, Chemin du Cyclotron, B–1348 Louvain-la-Neuve, Belgique.
- Govaerts, Y., S. Jacquemoud, M. M. Verstraete, and S. Ustin (1996). Three-dimensional radiation transfer modeling in a dicotyledon leaf. *Applied Optics* 35, 6585–6598.
- Govaerts, Y. and M. M. Verstraete (1996). Development and parallelization of a monte carlo ray tracing code for radiative transfer modelling: Initial lessons from using the Cenju-3 machine. *Speedup Journal* 10, 62–67.
- Govaerts, Y., O. Engelsen, B. Pinty, and M. M. Verstraete (1997). Identification of a particular tropical forest environment on the basis of simulated NOAA-AVHRR reflectance factors. In *Proceedings of the 7th ISPRS International Symposium on Physical Measurements and Signatures in Remote Sensing, Courchevel, France, 7–11 April 1997*, pp. 727–734. Balkema/Rotterdam/Brookfield.
- Govaerts, Y. and M. M. Verstraete (1998). Raytran: A Monte Carlo ray tracing model to compute light scattering in three-dimensional heterogeneous media. *IEEE Transactions on Geoscience and Remote Sensing* 36, 493–505.

- Govaerts, Y., M. M. Verstraete, B. Pinty, and N. Gobron (1999). Designing optimal spectral indices: a feasibility and proof of concept study. *International Journal of Remote Sensing* 20, 1853–1873.
- Grant, L., C. S. T. Daughtry, and V. C. Vanderbilt (1987). Polarized and nonpolarized leaf reflectance of *Coleus Blumei*. *Environmental and Experimental Botany* 27, 139–145.
- Grassberger, P. (1983). Generalized dimensions of strange attractors. *Physical Review Letters A* 97, 227–230.
- Griffith, D. A. and C. G. Amrhein (1991). *Statistical Analysis for Geographers*. New York: Prentice Hall.
- Gross, P. R. and N. Levitt (1997). *Higher Superstition: The Academic Left and Its Quarrels with Science*. John Hopkins University Press.
- Guyot, G. (1989). *Signatures spectrales des surfaces naturelles, 178p*. Paradigme: Collection Télédétection satellitaire N°5.
- Hafley, W. I. and H. T. Scheuner (1977). Statistical distributions for fitting diameter and height data in even aged stands. *Canadian Journal of Forest Research* 7, 481–489.
- Hall, G. F., Y. E. Shimabukuro, and K. F. Huemmerich (1995). Remote sensing of forest biophysical structure using mixture decomposition and geometric reflectance models. *Ecological Applications* 5, 993–1013.
- Hame, T., A. Lohi, M. Kohl, R. Paivinen, E. Carfagna, H. Jean-Jean, I. Spence, T. leToan, S. Quegnan, C. Estreguil, S. Folving, and P. Kennedy (1999). Validated forest variable mapping across Europe using multi-resolution data—results of the FMERS study. *Remote Sensing and forest monitoring IUFRO Conference, Rogow, Poland, June 1-3*.
- Hansen, M., R. Dubayah, and R. DeFries (1996). Classification trees: an alternative to traditional land cover classifiers. *International Journal of Remote Sensing* 17, 1075–1081.
- Hapke, B. (1981). Bidirectional reflectance spectroscopy. I. Theory. *Journal of Geophysical Research* 86, 3039–3054.
- Hapke, B. (1993). *Theory of Reflectance and Emittance Spectroscopy*. Cambridge: Cambridge University Press.
- Hapke, B., D. DiMucci, N. Nelson, and W. Smythe (1996). The cause of the HotSpot in vegetation canopies and soils: shadow hiding versus coherent backscatter. *Remote Sensing of Environment* 58, 63–68.
- Hargis, C. D., J. A. Bissonette, and J. L. David (1998). The behavior of landscape metrics commonly used in the study of habitat fragmentation. *Landscape Ecology* 13, 167–186.
- Henry, P. and A. Meygret (2000). Calibration of VEGETATION cameras on board SPOT 4. In *VEGETATION 2000 Proceedings, Belgirate, Italy, 3-6 April 2000*, Ispra, Italy, pp. 23–31. Space Applications Institute, JRC.
- Hentschel, H. G. E. and I. Procaccia (1983). The infinite number of generalized dimensions of fractals and strange attractors. *Physica D* 8, 435–444.
- Heney, L. G. and T. L. Greenstein (1941). Diffuse radiation in the galaxy. *Astrophysics Journal* 93, 70–83.
- Hunt, J. R. and J. W. Salisbury (1970). Visible and near infrared spectra of minerals and rocks: I Silicate minerals. *Modern Geology* 1, 283–300.
- Hyppänen, H. (1996). Spatial autocorrelation and optimal resolution of optical remote sensing data in boreal forest environment. *International Journal of Remote Sensing* 17, 3441–3452.

- Iaquinta, J. (1995). *Champ de rayonnement émergeant des surfaces terrestres : modélisation et inversion dans le cas de milieux optiquement finis et couplés avec une couche atmosphérique*. Ph. D. thesis, Université Blaise Pascal, 24 Av. des Landais, F-63177, Aubière, Cedex, France.
- Jackson, R., P. Teillet, P. N. Slater, G. Fedosejevs, J. K. Jasinski, M. F. Aase, and M. S. Moran (1990). Bidirectional measurements of surface reflectance for view angle corrections of oblique imagery. *Remote Sensing of the Environment* 32, 189–202.
- Jacobowitz, H., H. V. Soule, H. L. Kyle, F. B. House, and the Nimbus 7 ERB Experiment Team (1984). The earth radiation budget (ERB) experiment: an overview. *Journal of Geophysical Research* 89, 5021–5038.
- Jacquemoud, S. and F. Baret (1990). PROSPECT: A model of leaf optical properties spectra. *Remote Sensing of Environment* 34, 75–91.
- Jacquemoud, S., F. Baret, and J. F. Hanocq (1992). Modelling spectral and bidirectional soil reflectance. *Remote Sensing of Environment* 41, 123–132.
- Journel, A. and C. Huijbregts (1978). *Mining Geostatistics*. London: Academic Press.
- Judd, D. (1967). Terms, definitions and symbols in reflectometry. *Journal of the Optical Society of America* 57, 445–452.
- Jupp, D. L. B., A. H. Strahler, and C. E. Woodcock (1988). Auto-correlation and regularization in digital images. *IEEE Transactions on Geoscience and Remote Sensing* 26, 463–473.
- Jupp, D. L. B. and A. H. Strahler (1991). A hot spot model for leaf canopies. *Remote Sensing of Environment* 38, 193–210.
- Justice, C., J. Townshend, B. Holben, and C. Tucker (1985). Analysis of the phenology of global vegetation using meteorological satellite data. *International Journal of Remote Sensing* 6, 1271–1281.
- Kahn, R., R. West, D. McDonald, and B. Rheingans (1997). Sensitivity of multiangle remote sensing observations to aerosol sphericity. *Journal of Geophysical Research* 102, 16861–16870.
- Kahn, R., P. Banerjee, D. McDonald, and J. Martonchik (2001). Aerosol properties derived from aircraft multiangle imaging over Monterey Bay. *Journal of Geophysical Research* 106.
- Kalma, J. D. and M. E. Sivapalan (1995). *Scale issues in hydrological modelling*. London: John Wiley & Sons.
- Kaufman, Y. J. (1989). The atmospheric effect on remote sensing and its correction. In *Wiley Series in Remote Sensing. Theory and Applications of Optical Remote Sensing*, edited by Ghassem Asrar, pp. 336–428. John Wiley & Sons, Inc. ISBN 0-471-62895-6.
- Kieffer, H. H., T. Z. Martin, A. R. Peterfreund, and B. M. Jakosky (1977). Thermal and albedo mapping of Mars during the Viking primary mission. *Journal of Geophysical Research* 82, 4249–4291.
- Kimes, D. and P. Sellers (1985). Inferring hemispherical reflectance of the Earth's surface for global energy budgets from remotely sensed nadir or directional radiance values. *Remote Sensing of the Environment* 18, 205–211.
- Kimes, D. S., W. W. Newcomb, R. F. Nelson, and J. B. Schutt (1986). Directional reflectance distribution of a hardwood and pine forest canopy. *IEEE Transactions on Geoscience and Remote Sensing* GE-24, 281–293.
- Kimes, D. S., Y. Knyazikhin, J. L. Privette, A. A. Abuelgasim, and F. Gao (2000). Inversion methods for physically-based models. *Remote Sensing Review* 18, 381–439.

- Knipling, E. B. (1970). Physical and physiological basis for the reflectance of visible and near-infrared radiation from vegetation. *Remote Sensing of the Environment* 1, 155–159.
- Knorr, W., N. Gobron, P. Martin, B. Pinty, M. M. Verstraete, and G. Dedieu (1995). Constraining a climate driven vegetation model with satellite data. In G. Guyot (Ed.), *Proceedings of the International Colloquium on Photosynthesis and Remote Sensing, Montpellier, 28–30 August 1995*, pp. 269–279. EARSeL.
- Knyazikhin, Y. V. and A. L. Marshak (1991). Fundamental equations of radiative transfer in leaf canopies, and iterative methods for their solution. In R. Myneni and J. Ross (Eds.), *Photon-Vegetation Interactions*, pp. 9–43. New York: Springer-Verlag.
- Knyazikhin, Y., J. Kranigk, R. B. Myneni, O. Panfyrov, and G. Gravenhorst (1998). Influence of small-scale structure on radiative transfer and photosynthesis in vegetation canopies. *Journal of Geophysical Research* 103, 6133–6144.
- Knyazikhin, Y., J. V. Martonchik, D. J. Diner, R. B. Myneni, M. M. Verstraete, B. Pinty, and N. Gobron (1999). Estimation of vegetation canopy leaf area index and fraction of absorbed photosynthetically active radiation from atmosphere-corrected MISR data. *Journal of Geophysical Research* 103, 32,239–32,256.
- Koehler, C., B. Hosgood., G. Andreoli, G. Schmuck, J. Verdebout, A. Pegoraro, J. Hill, W. Mehl, D. Roberts, and M. Smith (1994). The European goniometer facility: Technical description and first experiments on spectral unmixing. In *Proc. IGARSS'94, Pasadena, California*, pp. 2375–2377. IEEE, No 94CH3378-7.
- Kolasa, J. and S. T. E. Pickett (1991). *Ecological Heterogeneity*. New York: Springer-Verlag.
- Kranigk, J. and G. Gravenhorst (1993). Ein dreidimensionales Modell für Fichtenkronen. *Allgemeine Forst und Jagd Zeitung* 164, Jg. 8, 146–149.
- Kranigk, J., F. Gruber, J. Heimann, and A. Thorwest (1994). Ein Modell für die Kronenraumstruktur und die räumliche Verteilung der Nadeloberfläche in einem Fichtenbestand. *Allgemeine Forst und Jagd Zeitung* 165, Jg. 10-11, 193–197.
- Kriebel, K. T. (1978). Measured spectral bidirectional reflection properties of four vegetated surfaces. *Applied Optics* 17, 253–259.
- Kuusk, A. (1991). The hot spot effect in plant canopy reflectance. In R. Myneni and J. Ross (Eds.), *Photon-Vegetation Interactions*, pp. 139–159. New York: Springer-Verlag.
- Kuusk, A. (1995). A markov chain model of canopy reflectance. *Agricultural and Forest Meteorology* 76, 221–236.
- Lavallée, D., D. Schertzer, and S. Lovejoy (1991). On the determination of the codimension function. In D. Schertzer and S. Lovejoy (Eds.), *Nonlinear variability in geophysics*, pp. 99–109. Amsterdam: Kluwer.
- Lavallée, D., D. Schertzer, S. Lovejoy, and P. Ladoy (1993). Nonlinear variability and simulation of landscape topography. In L. De Cola and M. Lam (Eds.), *Fractal in geography*, pp. 158–192. Amsterdam: Kluwer.
- Lewis, P. (1999). Three-dimensional plant modelling for remote sensing simulation studies using the botanical plant modelling system. *Agronomie: Agriculture and Environment* 19, 185–210.
- Li, X. and A. H. Strahler (1985). Geometric-optical modeling of a conifer forest canopy. *IEEE Transactions on Geoscience and Remote Sensing* GE-23, 705–721.
- Liang, S. and A. H. Strahler (1993). Calculation of the angular radiance distribution for a coupled atmosphere and canopy. *IEEE Transactions on Geoscience and Remote Sensing* 31, 491–502.

- Liang, S. and A. H. Strahler (1995). An analytic radiative transfer model for a coupled atmosphere and leaf canopy. *Journal of Geophysical Research* 100, 5085–5094.
- Loeb, N. G. and R. Davies (1996). Observational evidence of plane-parallel model bias. *Journal of Geophysical Research* 101, 1621–1634.
- Loeb, N. G., T. Várnai, and R. Davies (1997). Effect of cloud inhomogeneities on the solar zenith angle dependence of nadir reflectance. *Journal of Geophysical Research* 102, 9387–9395.
- Loeb, N. G. and J. A. J. Coakley (1998). Inference of marine stratus cloud optical depths from satellite measurements: Does 1D theory apply? *Journal of Climate* 11, 215–233.
- Lovejoy, S. and D. Schertzer (1990). Fractals, raindrops and resolution dependence of rain measurements. *Journal of Applied Meteorology* 29, 1167–1170.
- Loveland, T., J. Merchant, D. Ohlen, and J. Brown (1991). Development of a land-cover characteristics database for the conterminous U.S. *Photogrammetric Engineering and Remote Sensing* 57, 1453–1463.
- Lucht, W. (1998). Expected retrieval accuracies of bidirectional reflectance and albedo from EOS-MODIS and MISR angular sampling. *Journal of Geophysical Research* 103, 8763–8778.
- Lucht, W. and J.-L. Roujean (2000). Considerations in the parametric modeling of BRDF and albedo from multiangular satellite sensor observations. *Remote Sensing Reviews* 18, 343–379.
- Lyapustin, A. I. (1999). Atmospheric and geometrical effects on land surface albedo. *Journal of Geophysical Research* 104, 4127–4143.
- MacKay, G. and N. Jan (1984). Forest fires as critical phenomena. *Journal of Physics A* 17, L757–760.
- Mandelbrot, B. B. (1977). *Fractals: Form, Chance, and Dimension*. San Francisco: W. H. Freeman.
- Mandelbrot, B. B. (1982). *The Fractal Geometry of Nature*. San Francisco: W. H. Freeman.
- Marshak, A. L. (1989). The effect of the hot spot on the transport equation in plant canopies. *Journal of Quantitative Spectroscopy and Radiation Transfer* 42, 615–630.
- Marshak, A., A. Davis, R. Cahalan, and W. Wiscombe (1994). Bounded cascade models as nonstationary multifractals. *Physical Review E* 49, 55–69.
- Marshak, A., A. Davis, W. Wiscombe, and R. Cahalan (1995a). Radiative smoothing in fractal clouds. *Journal of Geophysical Research* 100, 26,247–26,261.
- Marshak, A., A. Davis, W. Wiscombe, and G. Titov (1995b). The verisimilitude of the independent pixel approximation used in cloud remote sensing. *Remote Sensing of Environment* 52, 71–78.
- Marshak, A., A. Davis, W. Wiscombe, and R. F. Cahalan (1997). Scale invariance in liquid water distributions in marine stratocumulus. part ii: Multifractal properties and intermittency issues. *Journal of the Atmospheric Sciences* 54, 1423–1444.
- Marshak, A., A. Davis, R. F. Cahalan, and W. Wiscombe (1998). Nonlocal independent pixel approximation: Direct and inverse problems. *IEEE Transactions on Geoscience and Remote Sensing* 36, 192–205.
- Martonchik, J. V., D. J. Diner, R. A. Kahn, T. P. Ackerman, M. M. Verstraete, B. Pinty, and H. R. Gordon (1998a). Techniques for the retrieval of aerosol properties over land and ocean

- using multi-angle imaging. *IEEE Transactions on Geoscience and Remote Sensing* 36, 1212–1227.
- Martonchik, J. V., D. J. Diner, B. Pinty, M. M. Verstraete, R. B. Myneni, Y. Knyazikhin, and H. R. Gordon (1998b). Determination of land and ocean reflective, radiative, and biophysical properties using multiangle imaging. *IEEE Transactions on Geoscience and Remote Sensing* 36, 1266–1281.
- Martonchik, J. V., C. J. Bruegge, and A. H. Strahler (2000). A review of reflectance nomenclature for remote sensing. *Remote Sensing Reviews* 19, 9–20.
- Massman, J. W. (1982). Foliage distribution in old-growth coniferous tree canopies. *Canadian Journal of Forest Research* 12, 10–17.
- Matheron, G. (1971). *The theory of regionalized variables and its applications*. Fontainebleau: Les Cahiers du Centre de Morphologie Mathématique, Fasc. 5, Centre de Géostatistique.
- Meerkoetter, R. (1989). Reflection functions for inhomogeneous land surfaces. *Applied Optics* 29, 4192–4198.
- Mélin, F., C. Steinich, N. Gobron, B. Pinty, and M. M. Verstraete (2001). Optimal merging of LAC and GAC data from SeaWiFS. *International Journal of Remote Sensing (in press)*.
- Meneveau, C. and K. R. Sreenivasan (1987). The multifractal spectrum of the dissipation field in turbulent flows. *Nuclear Physics B* 2, 49–76.
- Meneveau, C. and K. R. Sreenivasan (1989). Measurement of $f(\alpha)$ from scaling of histograms and application to dynamical systems and fully developed turbulence. *Physica Letters A* 137, 103–112.
- Meyer, D., M. M. Verstraete, and B. Pinty (1995). The effect of surface anisotropy and viewing geometry on the estimation of NDVI from AVHRR. *Remote Sensing Reviews* 12, 3–27.
- Milne, B. T. (1988). Measuring the fractal geometry of landscapes. *Applied Mathematics and Computation* 27, 67–79.
- Minnaert, M. (1941). The reciprocity principle in lunar photometry. *Astrophysical Journal* 93, 403–410.
- Monin, A. S. and A. M. Yaglom (1975). *Statistical Fluid Mechanics: Mechanics of Turbulence*. London: MIT Press.
- Moody, A. and C. E. Woodcock (1995). The influence of scale and the spatial characteristics of landscapes on land-cover mapping using remote sensing. *Landscape Ecology* 10, 363–379.
- Muecher, C. A., J. G. Veldkamp, C. Heunks, P. Loudjiani, V. Perdigao, K. Steinnocher, F. Kressler, V. van Katwijk, M. Barkhof, J. P. Goutorbe, J. L. Champeaux, R. Leemans, S. Griguolo, K. Wester, and O. Furberg (1998). Pan-european land cover monitoring (PEL-COM). *18th EARSEL Symposium, Enschede, 11-13th June 1998*.
- Myneni, R., J. Ross, and G. Asrar (1989). A review on the theory of photon transport in leaf canopies. *Journal of Agricultural and Forest Meteorology* 45, 1–153.
- Myneni, R. (1991). Modeling radiative transfer and photosynthesis in three-dimensional vegetation canopies. *Agricultural and Forest Meteorology* 55, 323–344.
- Myneni, R., A. L. Marshak, and Y. Knyazikhin (1991). Transport theory for a leaf canopy of finite-dimensional scattering centers. *Journal of Quantitative Spectroscopy and Radiation Transfer* 46, 259–280.
- Myneni, R. B. and G. Asrar (1993). Radiative transfer in 3-dimensional atmosphere vegetation media. *Journal of Quantitative Spectroscopy and Radiative Transfer* 49, 585–598.

- Myneni, R. B., F. G. Hall, P. J. Sellers, and A. L. Marshak (1995a). The interpretation of spectral vegetation indexes. *IEEE Transactions on Geoscience and Remote Sensing* 33, 481–486.
- Myneni, R. B., S. Maggion, J. Iaquina, J. L. Privette, N. Gobron, B. Pinty, D. S. Kimes, M. M. Verstraete, and D. L. Williams (1995b). Optical remote sensing of vegetation: Modeling, caveats, and algorithms. *Remote Sensing of Environment* 51, 169–188.
- Myneni, R. B., R. R. Nemani, and S. W. Running (1997). Estimation of global leaf area index and absorbed PAR using radiative transfer models. *IEEE Transactions on Geoscience and Remote Sensing* 35, 1380–1393.
- Nelder, A. and R. Mead (1965). A simplex method for function optimization. *Computation Journal* 7, 308–313.
- Ni, W. and D. Jupp (2000). Spatial variance in directional remote sensing imagery - recent developments and future perspectives. *Remote Sensing Reviews* 18, 441–479.
- Nicodemus, F. E., J. C. Richmond, J. J. Hsia, I. W. Ginsberg, and T. Limperis (1977). Geometrical considerations and nomenclature for reflectance. NBS Monograph 160, National Bureau of Standards, U.S. Department of Commerce, Washington, DC.
- Nilson, T. and A. Kuusk (1989). A reflectance model for the homogeneous plant canopy and its inversion. *Remote Sensing of Environment* 27, 157–167.
- Nilson, T. and U. Peterson (1991). A forest reflectance model and a test case. *Remote Sensing of Environment* 37, 131–142.
- Nolin, A. W. and S. Liang (2000). Progress in bidirectional reflectance modeling and applications for surface particulate media: Snow and soils. *Remote Sensing Review* 18, 307–342.
- North, P. R. J. (1996). Three-dimensional forest light interaction model using a Monte Carlo method. *IEEE Transactions on Geoscience and Remote Sensing* 34, 946–956.
- Oetking, P. (1966). Photometric studies of diffusely reflecting surfaces with applications to the brightness of the Moon. *Journal of Geophysical Research* 71, 2505–2513.
- Oker-Blom, P. and H. Smolander (1988). The ratio of shoot silhouette area to total needle areain Scots Pine. *Forest Science* 34, 894–906.
- O'Neill, R. V., J. R. Krummel, R. H. Gardner, G. Sugihara, B. Jackson, D. L. DeAngelis, B. T. Milne, M. G. Turner, B. Zygmunt, S. W. Christensen, V. H. Dale, and R. L. Graham (1988). Indices of landscape pattern. *Landscape Ecology* 1, 153–162.
- Oreopoulos, L., A. Marshak, R.F. Cahalan, and G. Wen (2000). Cloud three-dimensional effects evidenced in Landsat spatial power spectra and autocorrelation functions. *Journal of Geophysical Research* 105, 14777–14788.
- Oreskes, N., K. Shrader-Frechette, and K. Belitz (1994). Verification, validation, and confirmation of numerical models in the earth sciences. *Science* 263, 641–646.
- Otterman, J. (1983). Absorption of insolation by land surfaces with sparse vertical protrusions. *Tellus* 35B, 309–318.
- Päivinen, R. and M. Köhl (1996). Systems of nomenclature in european forest resource assessments - is harmonisation needed? In *Proceedings of the International Workshop: Application of Remote Sensing in European Forest Monitoring, Vienna, Austria, 14th - 16th October 1996*, ECSC-EC-EAEC Brussels, pp. 9–20. EUR 17685, European Commission.
- Palmer, M. W. (1988). Fractal geometry: A tool for describing spatial patterns of plant communities. *Vegetatio* 75, 91–102.

- Parisi, G. and U. Frisch (1985). A multifractal model of intermittency. In M. Ghil, R. Benzi, and G. E. Parisi (Eds.), *Turbulence and Predictability in Geophysical Fluid Dynamics*, pp. 84–88. Amsterdam: North Holland.
- Peltoniemi, J. I. (1993). Radiative transfer in stochastically inhomogeneous media. *Journal of Quantitative Spectroscopy and Radiation Transfer* 50, 655–671.
- Pinty, B. and D. Ramond (1986). A simple bidirectional reflectance model for terrestrial surfaces. *Journal of Geophysical Research* 91, 7803–7808.
- Pinty, B., M. M. Verstraete, and R. E. Dickinson (1989). A physical model for predicting bidirectional reflectances over bare soil. *Remote Sensing of Environment* 27, 273–288.
- Pinty, B. and M. M. Verstraete (1991). Extracting information on surface properties from bidirectional reflectance measurements. *Journal of Geophysical Research* 96, 2865–2874.
- Pinty, B. and M. M. Verstraete (1992). On the design and validation of bidirectional reflectance and albedo models. *Remote Sensing of Environment* 41, 155–167.
- Pinty, B., M. M. Verstraete, J. Iaquina, and N. Gobron (1996). Advanced modeling and inversion techniques for the quantitative characterization of desertification. In *The Use of Remote Sensing for Land Degradation and Desertification Monitoring in the Mediterranean Basin: State of the Art and Future Research*, pp. 79–93. European Commission.
- Pinty, B. and M. M. Verstraete (1998). Modeling the scattering of light by vegetation in optical remote sensing. *Journal of the Atmospheric Sciences* 55, 137–150.
- Pinty, B., F. Roveda, M. M. Verstraete, N. Gobron, Y. Govaerts, J. Martonchik, D. Diner, and R. Kahn (2000a). Surface albedo retrieval from METEOSAT - Part 2: Application. *Journal of Geophysical Research* 105, 18113–18134.
- Pinty, B., F. Roveda, M. M. Verstraete, N. Gobron, Y. Govaerts, J. Martonchik, D. Diner, and R. Kahn (2000b). Surface albedo retrieval from METEOSAT - Part 1: Theory. *Journal of Geophysical Research* 105, 18099–18112.
- Pinty, B., J.-L. Widlowski, N. Gobron, M. M. Verstraete, O. Engelsen, H. Johnsen, and Y. Govaerts (2000c). Monitoring boreal forest resources in northern europe. Technical report, EC Joint Research Centre.
- Pinty, B., J.-L. Widlowski, N. Gobron, M. M. Verstraete, and the MISR Team (2000d). Detection of land surface structure and heterogeneity from MISR/Terra data. In *Proceedings of the Fall Meeting of the American Geophysical Union, December 15-19, San Francisco, California*, pp. Vol 81, No 48, F275. Published as a supplement to EOS, Transactions, AGU.
- Pinty, B., N. Gobron, J.-L. Widlowski, S. A. W. Gerstl, M. M. Verstraete, M. Antunes, C. Bacour, F. Gascon, J.-P. Gastellu, N. Goel, S. Jacquemoud, P. North, W. Qin, and R. Thompson (2001a). The RADIATION transfer Model Intercomparison (RAMI) exercise. *Journal of Geophysical Research* 106, 11937–11956.
- Pinty, B., J.-L. Widlowski, N. Gobron, and M. M. Verstraete (2001b). Uniqueness of multi-angular information - Part 1: A surface heterogeneity indicator from MISR. *IEEE Transactions on Geoscience and Remote Sensing MISR special issue*, submitted.
- Price, J. C. (1995). Examples of high resolution visible to near-infrared reflectance spectra and a standardized collection for remote sensing studies. *International Journal of Remote Sensing* 16, 993–1000.
- Privette, J. L., R. B. Myneni, W. J. Emery, and B. Pinty (1995). Inversion of a soil bidirectional reflectance model for use with vegetation reflectance models. *Journal of Geophysical Research* 100, 25,497–25,508.

- Privette, J. L., T. F. Eck, and D. W. Deering (1997). Estimating spectral albedo and nadir reflectance through inversion of simple BRDF models with AVHRR/MODIS-like data. *Journal of Geophysical Research* 102, 29,529–29,542.
- Puech, C. (1994). Thresholds of homogeneity in targets in the landscape. relationship with remote sensing. *International Journal of Remote Sensing* 15, 2421–2435.
- Qin, W. and Y. Xiang (1994). On the hotspot effect of leaf canopies: Modeling study and influence of leaf shape. *Remote Sensing of the Environment* 50, 95–106.
- Qin, W. and S. A. W. Gerstl (2000). 3-D scene modeling of semi-desert vegetation cover and its radiation regime. *Remote Sensing of Environment* 74, 145–162.
- Qin, W. and S. Liang (2000). Plane-parallel canopy radiation transfer modelling: Recent advances and future directions. *Remote Sensing Review* 18, 281–305.
- Rahman, H., M. M. Verstraete, and B. Pinty (1993a). Coupled surface-atmosphere reflectance (CSAR) model. 1. Model description and inversion on synthetic data. *Journal of Geophysical Research* 98, 20,779–20,789.
- Rahman, H., B. Pinty, and M. M. Verstraete (1993b). Coupled surface-atmosphere reflectance (CSAR) model. 2. Semiempirical surface model usable with NOAA Advanced Very High Resolution Radiometer data. *Journal of Geophysical Research* 98, 20,791–20,801.
- Ramstein, G. and M. Raffy (1989). Analysis of the structure of radiometric remotely-sensed images. *International Journal of Remote Sensing* 10, 1049–1073.
- Ranson, K. J., L. L. Biehl, and C. S. T. Daughtry (1984). Soybean canopy reflectance modeling data sets. Technical Report No. 071584, Purdue University, Laboratory for Applications of Remote Sensing, Purdue University, West Lafayette, Indiana, 25 pp.
- Renders, J.-M. and S. Flasse (1996). Hybrid methods using genetic algorithms for global optimizations. *IEEE Transactions on Systems, Man and Cybernetics - Part B: Cybernetics* 26, 243–258.
- Richardson, A. J., E. C. Wiegand, H. Gausman, J. Cuellar, and A. Gerberman (1975). Plant, soil, and shadow reflectance components of row crops. *Photogrammetric Engineering* 41, 1401–1407.
- Ripple, W., G. Bradshaw, and T. Spies (1991). Measuring forest landscape patterns in the cascade range of Oregon, USA. *Biological Conservation* 57, 73–88.
- Ross, J. (1981). *The Radiation Regime and Architecture of Plant Stands*. Boston: W. Junk.
- Ross, J. and A. L. Marshak (1988). Calculation of the canopy bidirectional reflectance using the Monte-Carlo method. *Remote Sensing of Environment* 24, 213–225.
- Roujean, J.-L., M. Leroy, and P.-Y. Deschamps (1992). A bidirectional reflectance model of the Earth's surface for the correction of remote sensing data. *Journal of Geophysical Research* 97, 20,455–20,468.
- Sandmeier, S., C. Mueller, B. Hosgood, and G. Andreoli (1998). Physical mechanisms in hyperspectral BRDF data of grass and watercress. *Remote Sensing of Environment* 66, 222–233.
- Schertzer, D. and S. Lovejoy (1987). Physical modelling and analysis of rain and clouds by anisotropic scaling and multiplicative processes. *Journal of Geophysical Research* 92, 9693–9714.
- Sellers, P. J. (1987). Canopy reflectance, photosynthesis and transpiration II. the role of biophysics in the linearity of their interdependence. *Remote Sensing of Environment* 21, 143–183.

- Sellers, P. J., J. Berry, G. Collatz, C. Field, and F. Hall (1992). Canopy reflectance, photosynthesis and transpiration III. a reanalysis using improved leaf models and a new canopy integration scheme. *Remote Sensing of Environment* 42, 187–216.
- Sellers, P. J., S. O. Los, C. J. Tucker, C. O. Justice, D. A. Dazlich, G. J. Collatz, and D. A. Randall (1996). A revised land surface parameterization (SiB2) for atmospheric GCMs. Part ii: The generation of global fields of terrestrial biophysical parameters from satellite data. *Journal of Climate* 9, 706–737.
- Settle, J. and N. Campbell (1998). On the errors of two estimators of sub-pixel fractional cover when mixing is linear. *IEEE Transactions on Geoscience and Remote Sensing* 36, 163–170.
- Shugart, H. and E. Nielsen (1994). Te-22 allometric forest survey data. *BOReal Ecosystem-Atmosphere Study (BOREAS) Dept. of Environmental Sciences, University of Virginia*.
- Shugart, H. H. (2000). Importance of structure in the longer-term dynamics of landscapes. *Journal of Geophysical Research* 105, 20065–20075.
- Shultis, J. K. and R. B. Myneni (1988). Radiative transfer in vegetation canopies with anisotropic scattering. *Journal of Quantitative Spectroscopy and Radiation Transfer* 39, 115–129.
- Smith, B. H. and A. E. Plotnitsky (1997). *Mathematics, Science, and Postclassical Theory*. Durham, North Carolina: Duke University Press.
- Sokal, A. and J. Bricmont (1997). *Impostures Intellectuelles*. France: Editions Odile Jacob.
- Spanier, J. and E. M. Gelbard (1969). *Monte Carlo principles and Neutron Transport Problems*. Reading: Addison-Wesley.
- St-Onge, B. A., F. Cavayas, and P. M. Teillet (1991). Etude de la signature spatiale des couverts forestiers par modélisations géométrique-optique. In *Proceedings of the 5th International Colloquium on Physical Measurements and Signatures in Remote Sensing held in Courchevel, France, 14-18 January 1991*, pp. 671–674. ESA SP-319 (ESA Paris).
- St-Onge, B. A. and F. Cavayas (1995). Estimating forest stand structure from high resolution imagery using the directional variogram. *International Journal of Remote Sensing* 16, 1999–2021.
- Stenberg, P., T. Kuuluvainen, T. Kellomaeki, J. C. Grace, E. J. Jokela, and H. L. Gholz (1994). Crown structure, light interception and productivity of pine trees and stands. In H. L. Gholz, R. McMurthie, and S. Linder (Eds.), *A comparative analysis of pine forest productivity*, pp. 20–43. Copenhagen: Ecological Bulletins (43).
- Stenberg, P., S. Linder, H. Smolander, and J. Flower-Ellis (1994). Performance of the LAI-2000 plant canopy analyzer in estimating leaf area index of some Scots pine stands. *Tree Physiology* 14, 981–995.
- Stoner, E. R. and M. F. Baumgardner (1981). Characteristic variations in reflectance of surface soils. *Soil Science Society of America Journal* 45, 1161–1165.
- Strahler, A. H. and D. L. B. Jupp (1990). Modeling bidirectional reflectance of forests and woodlands using boolean models and geometric optics. *Remote Sensing of Environment* 34, 153–166.
- Strebel, D. E., N. S. Goel, and K. J. Ranson (1985). Two-dimensional leaf orientation distributions. *IEEE Transactions on Geoscience and Remote Sensing* 23, 640–647.
- Tanré, D., C. Deroo, P. Duhaut, M. Herman, and J. J. Marquette (1990). Description of a computer code to simulate the satellite signal in the solar spectrum: the 5s code. *International Journal of Remote Sensing* 11, 659–668.

- Tessier, Y., S. Lovejoy, and D. Schertzer (1993). Universal multifractals: Theory and observations for rain and clouds. *Journal of Applied Meteorology* 32, 223–250.
- Thompson, R. L. and N. S. Goel (1998). Two models for rapidly calculating bidirectional reflectance: Photon spread (PS) model and statistical photon spread (SPS) model. *Remote Sensing Reviews* 16, 157–207.
- Thorpe, T. E. (1977). Viking orbiter photometric observations of the Mars phase function July through November 1976. *Journal of Geophysical Research* 82, 4161–4165.
- Tomppo, E. (2000). Remote sensing requirements to support forest inventories. In M. M. Verstraete, M. Menenti, and J. Peltoniemi (Eds.), *Observing Land from Space: Science, customers and technology; Advances in Global Change Research, Vol. 4*, pp. 207–248. Kluwer Academic Publishers.
- Torrance, K. E. and E. M. Sparrow (1967). Theory for off-specular reflection from roughened surfaces. *Journal of the Optical Society of America* 57, 916–925.
- Treuhaft, R. N., N. S. Madsen, M. Moghaddam, and J. J. van Zyl (1996). Vegetation characteristics and underlying topography from interferometric data. *Radio Science* 31, 1449–1495.
- Treuhaft, R. N. and P. R. Siquera (2000). The vertical structure of vegetated land surfaces from interferometric and polarimetric radar. *Radio Science* 35, 141–177.
- Tuceryan, M. and A. K. Jain (1998). Texture analysis. In C. H. Chen, L. F. Pau, and P. S. P. Wang (Eds.), *The Handbook of Pattern Recognition and Computer Vision (2nd Edition)*, pp. 207–248. World Scientific Publishing Co.
- Tucker, C. J., J. R. G. Townshend, and T. E. Goff (1985). African land-cover classification using satellite data. *Science* 227, 369–375.
- Turner, M. G. E. (1987). *Landscape heterogeneity and disturbance*. New York: Springer-Verlag.
- Vanderbilt, V. C., L. Grant, and S. L. Ustin (1991). Polarization of light by vegetation. In R. Myneni and J. Ross (Eds.), *Photon-Vegetation Interactions*. New York: Springer-Verlag.
- Várnai, T. and R. Davies (1999). Effect of cloud inhomogeneities on the shortwave radiation: Comparison of cloud-top variability and internal heterogeneity. *Journal of Atmospheric Sciences* 41, 3085–3103.
- Várnai, T. (2000). Influence of three-dimensional radiative effects on the spatial distribution of shortwave cloud reflection. *Journal of Atmospheric Sciences* 57, 216–229.
- Verhoef, W. (1984). Light scattering by leaf layers with application to canopy reflectance modeling: The SAIL model. *Remote Sensing of Environment* 16, 125–141.
- Vermote, E., D. Tanré, J. L. Deuzé, M. Herman, and J. J. Morcrette (1997). Second simulation of the satellite signal in the solar spectrum: An overview. *IEEE Transactions on Geoscience and Remote Sensing* 35-3, 675–686.
- Verstraete, M. M. (1987). Radiation transfer in plant canopies: Transmission of direct solar radiation and the role of leaf orientation. *Journal of Geophysical Research* 92, 10,985–10,995.
- Verstraete, M. M., B. Pinty, and R. E. Dickinson (1990). A physical model of the bidirectional reflectance of vegetation canopies. 1. Theory. *Journal of Geophysical Research* 95, 11,765–11,775.
- Verstraete, M. M. (1994). The contribution of remote sensing to monitor vegetation and to evaluate its dynamical aspects. In F. Veroustraete and R. Ceulemans (Eds.), *Vegetation, Modelling and Climatic Change Effects*, pp. 207–212. The Hague: SPB Academic Publishing.

- Verstraete, M. M. and B. Pinty (1996). Designing optimal spectral indices for remote sensing applications. *IEEE Transactions on Geoscience and Remote Sensing* 34, 1254–1265.
- Verstraete, M. M., B. Pinty, and R. B. Myneni (1996). Potential and limitations of information extraction on the terrestrial biosphere from satellite remote sensing. *Remote Sensing of Environment* 58, 201–214.
- Verstraete, M. M. and B. Pinty (1999). Environmental information extraction from satellite remote sensing data. In P. Kasibhatla, M. Heimann, P. Rayner, N. Mahowald, R. G. Prinn, and D. E. Hartley (Eds.), *Inverse Methods in Global Biogeochemical Cycles*, pp. 125–137. Washington DC, US: American Geophysical Union.
- Viscek, T. and A.-L. Barabási (1991). Multi-affine model for the velocity distribution in fully developed flows. *Journal of Physics A: Mathematics and General* 24, L845–851.
- Vogt, P., M. M. Verstraete, B. Pinty, M. Menenti, A. Caramagno, M. Rast, and D. Lajas (2000). The impact of multi-angular measurements on the accuracy of land-surface albedo retrieval: Preliminary results for the proposed ESA LSPIM mission. *Remote Sensing Reviews* 19, 191–204.
- Walter-Shea, E. A. (1989). Leaf bidirectional reflectance and transmission in corn and soybean. *Remote Sensing of the Environment* 29, 161–174.
- Walthall, C. L., J. M. Norman, J. M. Welles, G. Campbell, and B. Blad (1985). Simple equation to approximate the bidirectional reflectance for vegetative canopies and bare soil surfaces. *Applied Optics* 24, 383–387.
- Wanner, W., X. Li, and A. H. Strahler (1995). On the derivation of kernels for kernel-driven models of bidirectional reflectance. *Journal of Geophysical Research* 100, 21,077–21,089.
- Wanner, W., A. H. Strahler, B. Hu, P. Lewis, J.-P. Muller, X. Li, C. L. Barker-Schaaf, and M. J. Barnsley (1997). Global retrieval of bidirectional reflectance and albedo over land from EOS MODIS and MISR data: theory and algorithm. *Journal of Geophysical Research* 102, 17,143–17,162.
- Welch, R. M. and B. A. Wielicki (1984). Stratocumulus cloud field reflected fluxes: The effect of cloud shape. *Journal of Atmospheric Sciences* 41, 3085–3103.
- Wehrli, C. (1985). Extraterrestrial Solar Spectrum. Physikalisches-Meteorologisches Observatorium and World Radiation Center (PMO/WRC), Document 615, Davos-Dorf, Switzerland
- Widlowski, J.-L., B. Pinty, N. Gobron, and M. M. Verstraete (2001a). Detection and characterization of boreal coniferous forests from remote sensing data. *Journal of Geophysical Research (in print)*.
- Widlowski, J.-L., B. Pinty, N. Gobron, M. M. Verstraete, and A. B. Davies (2001b). Characterization of surface heterogeneity detected at the MISR/TERRA subpixel scale. *Geophysical Research Letters* 28, 4639–4642.
- Williams, D. L. (1991). A comparison of spectral reflectance properties at the needle, branch, and canopy level for selected conifer species. *Remote Sensing of Environment* 35, 79–93.
- Williamson, M. H. and J. H. Lawton (1991). Fractal geometry of ecological habitats. In S. S. Bell, E. D. McCoy, and H. R. E. Mushinsky (Eds.), *Habitat Structure*, pp. 69–86. London: Chapman and Hall.
- Woessner, P. and B. Hapke (1978). Polarization of light scattered by clover. *Remote Sensing of the Environment* 21, 243–261.
- Woodcock, C. E., A. H. Strahler, and D. L. B. Jupp (1988). The use of variograms in remote sensing: I - scene models and simulated images. *Remote Sensing of the Environment* 25, 323–348.

- Wu, J., B. L. Li, and Y. Wu (1992). Patchiness and patch dynamics: I. Concept and mechanism. *Chinese Journal of Ecology* 11, 41–45.
- Wu, Y. and A. H. Strahler (1994). Remote estimate of crown size, stand density and biomass on the Oregon transect. *Ecological Applications* 4, 299–312.
- Zeide, B. (1991). Fractal geometry in forestry applications. *Forest Ecology and Management* 46, 179–188.
- Zuidema, P. and F. K. Evans (1998). On the validity of the independent pixel approximation for boundary layer clouds observed during ASTEX. *Journal of Geophysical Research* 103, 6059–6074.

Annex A

Detection and Characterization of Boreal Coniferous Forests from Remote Sensing Data

Jean-Luc Widlowski, Bernard Pinty, Nadine Gobron and Michel M. Verstraete

*Institute for Environment and Sustainability of the EC Joint Research Centre,
TP 440, I-21020 Ispra (VA), Italy*

Abstract: Advanced radiation transfer models capable of representing the reflectance of coupled surface and atmosphere system have been used to generate look-up tables of simulated remote sensing measurements at the top of the atmosphere, for typical conditions of forest cover and atmospheric composition found in Northern Europe. These simulations were evaluated against actual observations under identical viewing and illumination geometries, available for the blue, red and near-infrared spectral bands of the VEGETATION instrument, to retrieve the most likely of a set of pre-defined solutions to the inverse problem. The accumulation of results over multiple days in the summer of 1999 permitted the establishment of maps showing the likelihood of identifying the pre-defined forest types, their corresponding structural characteristics as well as the associated atmospheric optical depth on the day of retrieval. The proposed methodology is completely generic, and thus can easily be prototyped for different biomes and instruments.

A-1 Introduction

Current ecological and climatological research interests place considerable emphasis on the magnitude and dynamics of the physical and chemical processes that control the exchanges of water, energy and carbon at the interface between the biosphere and atmosphere. Accurate knowledge of the spatial and temporal variability of the world's forest characteristics is not only mandatory to verify the implementation of international treaties (climate change, environmental degradation, biodiversity preservation, *etc.*) but also to provide appropriate initial and boundary conditions for general circulation or global climate models (*e.g.*, Knorr et al. 1995).

In particular, the boreal ecosystem, which covers extensive and often inaccessible areas, has become the target of an intensified effort to quantify the whereabouts of the missing CO₂ in the context of the global carbon budget. Satellite remote sensing, in principle, can provide a convenient, efficient and cost-effective way to gather this information, because data can be acquired repetitively over large areas and at a spatial resolution adequate to address many key ecological and climate change related issues (Verstraete 1994). A variety of land-cover information extraction schemes have thus been applied to satellite gathered measurements in the past. These include (un)supervised image classification techniques of single,

multi-temporal and/or multi-sensor data, or metrics derived thereof, as well as spectral unmixing, the use of expert knowledge, simple spectral vegetation indices and a wide variety of ancillary validation data (Gervin et al. 1985, Justice et al. 1985, Tucker et al. 1985, Belward et al. 1990, Loveland et al. 1991, Borel and Gerstl 1994, Hansen et al. 1996, DeFries et al. 1997, Belward 1999).

Although many important results have been obtained with these methodologies, they are often largely empirical or only regionally applicable; some require long-term statistics, extensive human interactions or are prone to errors due to atmospheric, topographic and seasonal disturbances; others neglect the reflectance anisotropy of natural surfaces, the influence of the canopy structure and background on the satellite gathered data strings or even saturation problems of the vegetation indicator itself (for a documentation of these effects, see for example, Baret and Guyot 1991, Goel and Qin 1994, Meyer et al. 1995, Gobron et al. 1997b). Optimized vegetation indices (*e.g.*, Verstraete and Pinty 1996, Gobron et al. 2000b), on the other hand, attempt to overcome or at least minimize these drawbacks and have been applied on a quasi-operational basis to the detection of vegetation on a global scale (Mélin et al. 2001). The retrieval of one particular variable of interest, however, is often not sufficient, and more recent approaches have relied directly on the inversion of physically-based models to retrieve the state variables that control the radiation transfer processes and hence also the observed satellite measurements. The many problems to be faced when addressing such an inversion have been extensively discussed by Goel and Strebel (1983), Pinty and Verstraete (1991), Privette et al. (1995), Verstraete and Pinty (1999) and Kimes et al. (2000) among others. One-dimensional physically-based radiation transfer models, which typically comprise from five to seven state variables, find their usage primarily for geophysical and measurement conditions where the usual homogeneous plane-parallel assumptions are acceptable (Gobron et al. 1997a). Three-dimensional models, on the other hand, describe in more detail the structure of vegetation canopies and thus may require a much larger number of input parameters *e.g.*, Kranigk and Gravenhorst (1993), North (1996), Chen et al. (1997b) and Govaerts and Verstraete (1998). These explicit canopy architecture models, however, have only recently been employed for designing retrieval methodologies (Govaerts et al. 1997, Myneni et al. 1997 and Knyazikhin et al. 1999). As pointed out by Gobron et al. (2000a), the choice of the model depends firstly on the nature of the application, but also on the accuracy that is required by the end-user of the derived information, as well as the availability and quality of the data, and the allowable cost of producing the desired information.

Of interest here will be coniferous forests, where a realistic description of the canopy structure and an accurate representation of the radiative transfer are essential to a better understanding of the canopy light interception properties and the retrieval of other biophysical canopy parameters. In this paper we will thus explore the potential use of a Look Up Table (LUT) based approach to retrieve an exhaustive set of vegetation characteristics from remotely sensed data. This is achieved by pre-computing directional reflectances over explicitly modelled forest scenes, and for a large range of model parameter value combinations, before the actual inversion process is attempted (Gobron et al. 1997a, Govaerts et al. 1997, Kahn et al. 1997). This then allows not only for the solving of the inverse problem within operational computing constraints, but also to estimate the accuracy of the retrieved surface type information, by controlling the largest tolerable discrepancy between the satellite measured and the model pre-computed reflectance values. Consequently the reliability of this retrieved information will increase as further (spectral or directional) instantaneous measurements become available for a given observed target (Gobron et al. 2000a). More specifically, the proposed inversion methodology will be applied over Northern Europe, using remote sensing data gathered in the blue, red and near-infrared bands of the VEGETATION instrument. Section A-2 presents the conceptual ideas, the physics and mathematics supporting the retrieval strategy. In section A-3 the application of the retrieval methodology to a set of VEGETATION-P¹ products over Scandinavia is presented.

A-2 Strategy of the retrieval

The physical interpretation of a multispectral and/or multidirectional data string collected by a spaceborne sensor over terrestrial surfaces reduces ultimately to the solution of an inverse problem. Inverse problems are notoriously ill-posed and often lead to the identification of multiple solutions, hereafter

¹Top of atmosphere bidirectional reflectance factors.

referred to as “probable” solutions, that are all statistically equivalent to the extent that they permit the simulation of this series of observations within the range of the remote sensing data uncertainty (see, Kahn et al. 1997, Gobron et al. 1997a, Martonchik et al. 1998a, Knyazikhin et al. 1999, Pinty et al. 2000a and Gobron et al. 2000a). Conceptually, these probable solutions are simply part of a very large ensemble of “potential” solutions that must be regarded as infinite, without any *a priori* knowledge on the type of solutions to be found. For all practical purposes, however, this ensemble becomes finite as soon as a LUT of potential solutions with defined boundaries and increments on the values of the variables is specified. The size of this LUT can be limited by importing additional, so called ancillary information to prevent the searching for very improbable geophysical or ecological events. Apart from the identification of a large ensemble of potential solutions, the quantification of the desired accuracy on the retrieved information and the knowledge of the remote sensing data and algorithm uncertainties have to be addressed. This is mandatory in order to best select both the models to be applied and the source of the data to be used in the inversion. However, assessing the accuracy required on the desired information may not always be an easy task unless the further impacts related to the cost of the tolerated errors are thoroughly evaluated. In practice, most end-users request the most accurate information that can be provided, given the performance of the algorithm and the intrinsic uncertainties associated to the input remote sensing data.

Due to the non-uniqueness of solutions to an inversion problem, the interpretation of remotely sensed data strings requires finding the set of probable solutions rather than the “true” solution. This strategy is, in fact, dictated by 1) inherent limits of radiation transfer regimes which do not guarantee the existence of a unique one-to-one relationship between the sets of state variables of the geophysical system and its measured outgoing radiance fields (Verstraete et al. 1996) and 2) intrinsic uncertainties in both the inversion algorithm and the data sources. This implies that identifying the ensemble of the probable solutions must be constrained by the various levels of uncertainties associated to the various constituents entering the inverse procedure. A practical and elegant method has been devised by Kahn et al. (1997) to extract aerosol load and properties from data acquired by the Multi-angle Imaging SpectroRadiometer (MISR) instrument on board TERRA. It has been applied by Pinty et al. (2000a) to estimate surface bidirectional reflectance factor (BRF) and albedo values using METEOSAT data. This approach is based on an ensemble of metrics which permit the isolation of the set of probable solutions that are all equivalent in terms of their ability to represent the observations within the limits of the imposed uncertainties.

A-2.1 Forest canopy modelling

The inverse problem to be solved in the context of this study consisted in the identification and primary characterization of boreal forests over Northern European regions. As such, it was necessary to first identify the ensemble of potential surface types that could occur within the region of study prior to the simulation and subsequent storage of their reflectance fields at the top of the atmosphere (TOA) in an appropriate set of LUTs.

Coniferous trees exhibit non-uniform foliage distributions, highly convoluted needle surfaces and significant clumping of their individual crown elements (needles, shoots and branches). They may well have in excess of 100,000 needles per tree and can occur in stands with densities above 1000 trees/hectare. Ecological factors like soil type and moisture, tree density and maturity as well as the exact geographic location, wind regime and climatic conditions also play an important role in the crown structure characteristics of individual trees. The number of possible combinations for the parameter values available for the generation of realistic 3-D tree representations thus increases dramatically if each and every measurable structural detail (*e.g.*, branching angles, needle growth lengths and the sprouting behavior of different buds and shoots) is taken into consideration. Even more so if several tree species are to be considered and the nature of the modelled scene is such as to include significant allometric variations. Consequently, the accurate three dimensional description of conifers has either been limited to relatively small spatial areas (Kranigk and Gravenhorst 1993, Kranigk et al. 1994) or else, substituted with statistical descriptions of the various canopy structure elements (Li and Strahler 1985, Chen and Leblanc 1997a, Gerard and North 1997). Since many of the individual tree-structural properties have no obvious connection to the light interception regime (Stenberg et al. 1994) and thus should not be modeled in isolation, some degree of canopy abstraction becomes necessary to avoid prohibitive requirements on computational power and memory, especially if large spatial areas are to be modelled.

The approach adopted here attempts at minimizing the level of structural abstraction when representing a typical Northern European coniferous forest at a spatial resolution of 1 km². At the same time every effort was made to remain as faithful as possible to the documented statistical behaviour of those variables that are primarily responsible for the radiative transfer processes within three-dimensional vegetation canopies. More specifically the forest modelling process utilizes the tree height, the crown dimensions and spatial distribution of the trees, the size, amount, orientation and distribution of the foliage in the tree crowns as well as the various spectral properties of the needles, trunks and soil. A schematic description of the tree modeling approach, which focuses entirely on surface types composed of a single dominant tree species, is given in Figure A-1. For a given stem density and scene dimension, the number of trees that are to be distributed was computed. In accordance with Hafley and Scheuner (1977) and Li and Strahler (1985), among others, a lognormal tree height model was generated for a given average tree height and height standard deviation. The allometric equations of Cermák et al. (1998) were used to retrieve the corresponding values for the height to the crown base, the crown and trunk radius, and the leaf area index (LAI). Although these allometric equations were originally derived from a medium density plot of Scots pine (*Pinus Sylvestris*) in Belgium, comparison of the individual variables with data from BOREAS (Fournier et al. 1997, Shugart and Nielsen 1994) suggested their appropriateness for the modeling of a typical boreal coniferous forest at a scale of 1 km². In addition the data from BOREAS were collected from stands with a broad range of tree density, maturity and species composition (see Figure A-2), thus being somewhat similar to the non-uniform stand conditions that are to be expected within the scales of interest here. The LAI from Cermák et al. (1998) varies between ~ 2 and 6 for individual trees of 17.5 to 25 m height; this is comparable to the LAI values reported by Chen et al. (1997b) during the BOREAS campaign and those that Stenberg et al. (1994) found for Scots Pine trees in Sweden.

Limitations in available computer memory (~ 0.5 Gb) required a simplifying of the canopy architecture representation, such as to allow for the simulation of realistic stem density ranges (10,000 – 120,000 trees/km²) within the nominal spatial resolution of the VEGETATION instrument. From Figure A-1 it can be seen that in order to reduce the number of geometrical objects in the canopy simulation, each tree crown was assembled using a single cone and cylinder (Chen et al. 1997b), both of equal radius and height. This partitioning was somewhat arbitrary but nevertheless justifiable since 1) apex angle² variations are known to be highly variable (Li and Strahler 1985) and 2) because this structural subdivision allows for the approximation of the vertical leaf area distribution, which in conifers is often skewed towards the light source (Massman 1982, Chen et al. 1997b). The latter was accounted for by placing 75% of the total LAI for a given tree into the volume of the cone and 25% into that of the cylinder. For simplicity, a uniform foliage distribution was assumed within the tree crowns and individual needles were simulated with a surface area equivalent to that of a 5 cm long and 2 mm wide cylinder without endcaps. Additionally, an azimuthally independent (uniform) needle orientation distribution was adopted throughout the crown volume (Oker-Blom and Smolander 1988), even though the shoot orientations for Scots Pines are dependent on the stand age and canopy depth (Stenberg et al. 1994).

Table A-1: Actual canopy biophysical characteristics.

| Tree Density [stem/ha] | $\overline{\text{LAI}}_{\text{Scene}}$ [m ² /m ²] | Fractional Cover [†] | $\overline{H}_{\text{Crown_Base}}$ [m] | $\overline{\text{Rad}}_{\text{Crown}}$ [m] | $\overline{\text{Rad}}_{\text{Trunk}}$ [cm] | $\overline{H}_{\text{Tree}}$ [m] |
|---------------------------|---|----------------------------------|--|---|--|-------------------------------------|
| 100 | 0.15 | 0.04 | 10.43 | 1.14 | 6.73 | 15.00 |
| 200 | 0.30 | 0.08 | 10.43 | 1.14 | 6.73 | 15.00 |
| 400 | 0.63 | 0.16 | 10.42 | 1.14 | 6.73 | 15.01 |
| 801 | 1.26 | 0.33 | 9.93 | 1.12 | 6.54 | 14.76 |
| 1209 | 1.83 | 0.48 | 9.93 | 1.12 | 6.54 | 14.76 |

[†] Ratio of the vertically downward projected area of all trees in the scene to the area of the scene.

²The apex angle is half of the solid angle of the cone with respect to the downward vertical.

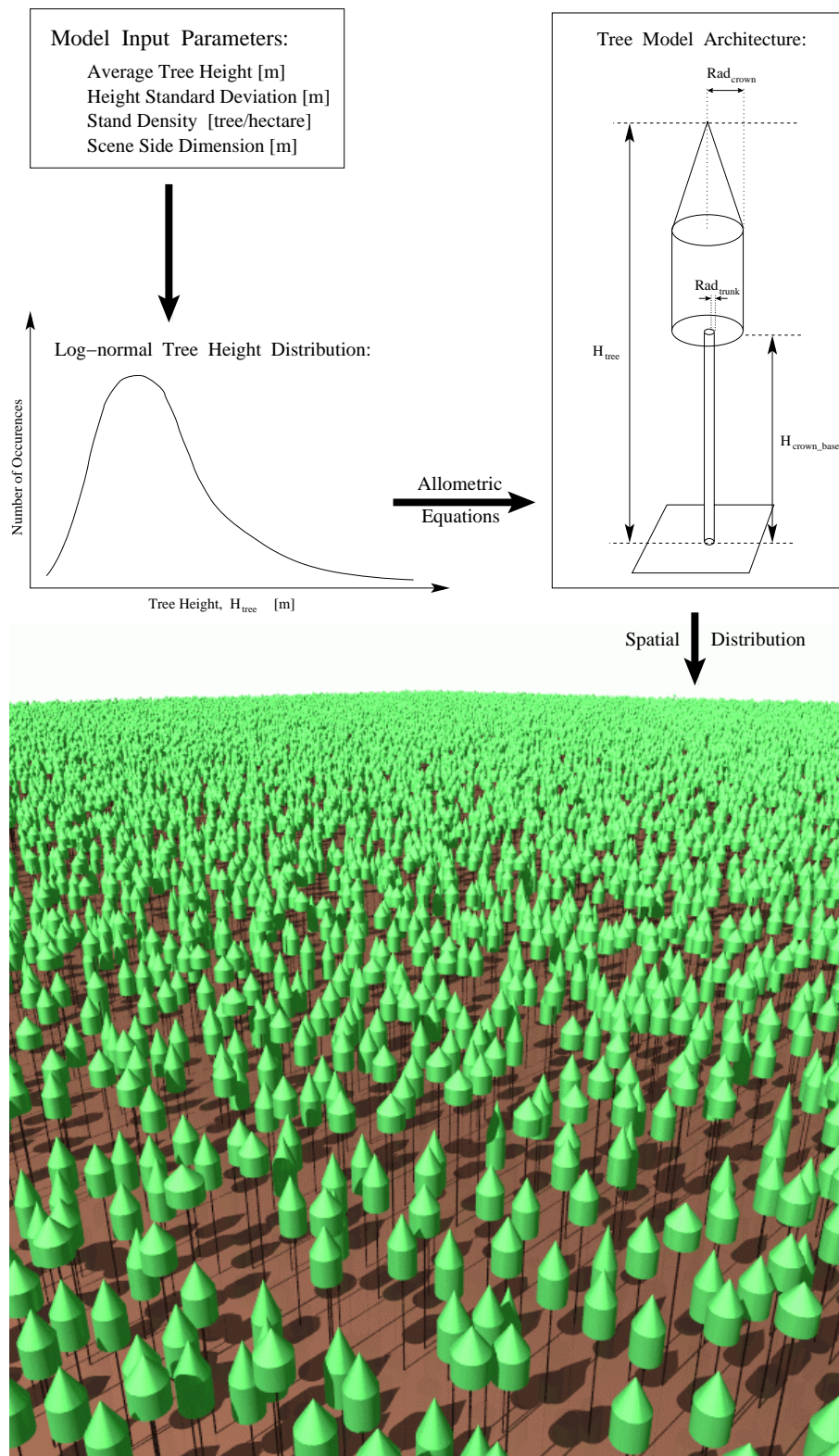


Figure A-1: Schematic representation of the canopy architecture model. The input parameters are used to generate a log-normal tree height distribution. Every value of which is then related, via a set of allometric equations, to the remaining architectural parameters that are needed to construct the corresponding tree representation in the modelled scene. The trees are then randomly distributed over a 1 km² area to provide the required tree density (shown is an oblique view of a coniferous forest with a mean height of 15 m, a height standard deviation of 1 m and a stand density of 400 trees/hectare)

Table A-2: Spectral characteristics.

| $\hat{\lambda}$ | ρ_{Needle} | τ_{Needle} | ρ_{Trunk} | ρ_{Soil} |
|-----------------|------------------------|------------------------|-----------------------|----------------------|
| 459 nm | 0.0097 | 0.0153 | 0.0800 | 0.0670 |
| 662 nm | 0.0505 | 0.0532 | 0.1425 | 0.1270 |
| 834 nm | 0.4900 | 0.4620 | 0.2350 | 0.1590 |

$\hat{\lambda}$ = weighted Wavelength ρ = Reflectance τ = Transmittance

The spatial distribution of the conifers was simulated with a Poisson model regardless of the stand densities (Wu and Strahler 1994, Franklin et al. 1985). Five different tree densities from 100 to 1200 stem/hectare were chosen to generate the coniferous forest scenes. For tree density values greater than 400 stem/hectare (which is equivalent to 40,000 trees in a scene of 1 km²), individual trees were grouped into height classes of 0.5 m interval and their biophysical properties were aligned to those of that respective class. This explains why in Table A-1 the average values for the tree height, the height to the crown base, and the crown and trunk radii are different at higher stem density values. Finally, the spectral properties of the needles of Norway Spruce trees (Williams 1991) were weighted with the spectral bands of the VEGETATION instrument to yield an estimate of typical coniferous needle reflectances and transmittance in the blue, red and near-infrared (NIR) domains. The lower boundary condition of the surface was chosen such as to mirror the reflectance values of a darkish, moist soil (see Table A-2 for all spectral properties).

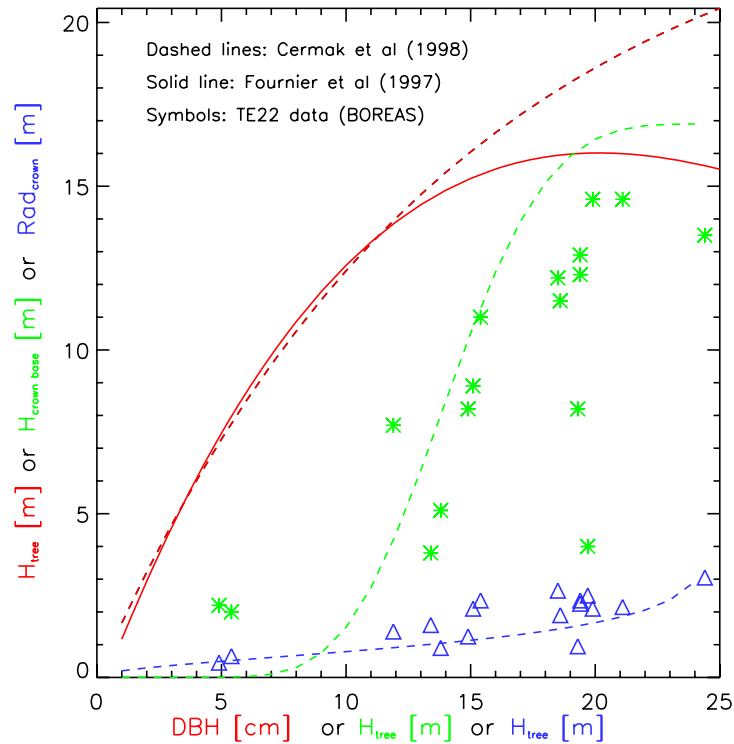


Figure A-2: Comparison of allometric equations for Scots Pine in a medium density stand in Belgium (Cermak et al, 1998) with the corresponding data from the Terrestrial Ecology (TE)-22 group of the BOREal Ecosystem-Atmosphere Study (BOREAS): height to crown base versus tree height (green) and crown radius versus tree height (blue). The divergence between the relationship for the tree height and diameter at breast height (DBH) for Scots pine and that of Fournier et al (1997) for Old Jack pine (red line) could be related to the low correlation coefficient ($R^2 \simeq 0.52$) of the latter and its reduced amount of datapoints above 18 m.

A-2.2 Physics of the retrieval

The identification of a particular terrestrial environment or biome type on the basis of data taken from space involves the reckoning of the spectral BRFs at the surface level. Once these surface BRFs are known they can be compared to a series of LUTs in order to identify the geophysical systems best able to replicate them. This implies, however, that the surface BRFs can be obtained from TOA BRF data, and also, that a model exists to establish the link between the directional surface reflectances and the associated geophysical systems. The modelling tools required to achieve this task therefore include 1) an atmosphere radiative transfer model allowing the simulations of TOA BRF values in the desired spectral bands of the sensor and with a prescribed set of atmospheric and surface properties, 2) a model approximating the surface reflectance fields in order to represent the lower boundary condition for the atmospheric model and 3) a radiative transfer model capable of representing the radiation transfer regime and the top-of-canopy (TOC) BRF fields for various surface types. More specifically, the implementation of our retrieval scheme made use of 1) the Second Simulation of the Satellite Signal in the Solar Spectrum (6S) model from Vermote et al. (1997) which permits the simulation of TOA BRF fields under varying surface and atmospheric conditions, 2) the parametric RPV model from Rahman et al. (1993b), capable of representing TOC BRF fields over a large variety of terrestrial surfaces, and 3) the Raytran model from Govaerts and Verstraete (1998) implementing a ray-tracing approach to simulate the radiation transfer regime of complex three-dimensional surface environments at any spatial scale.

On the basis of the information and hypotheses of section A-2.1, the canopy types characterized in Table A-1 were generated over a ground area of 1 square kilometer (see bottom panel in Figure A-1 for a visual representation of a 400 stem/hectare coniferous forest). The Raytran model was subsequently used to simulate the transfer of radiation in all forest scenes and, in particular, to generate the TOC BRFs at discrete observation angles in the blue, red and near-infrared bands of the VEGETATION instrument, and at various solar zenith angles that could occur over high latitudes. For every forest scene the generated TOC BRF fields were approximated by the RPV model (Rahman et al. 1993b), which, on the sole basis of three parameters permits to interpolate/extrapolate between the BRF data points simulated at discrete observation angles by the Raytran model. The RPV model also provides a very efficient mathematical way to express the BRF fields which can then be entered into the 6S model (Vermote et al. 1997) to generate an ensemble of potential solutions at the TOA. The latter were used to interpret the VEGETATION data acquired under any angular conditions and for a range of atmospheric properties. A novel technique to estimate the set of optimal RPV parameters and their associated range of uncertainty was developed (Gobron and Lajas 2001), and applied to each and every forest scene. Table A-3 summarizes the various geophysical scenarios adopted to simulate the TOA reflectance fields.

Table A-3: Geophysical scenarios used to construct the look-up-tables.

| Medium / Model | Variable | Range of values |
|---|--|---|
| Atmosphere / 6S model (Vermote <i>et al.</i> , 1997) | Aerosol optical depth @ 550 nm for a subarctic summer model ^(*) | 0.05 to 0.45 in steps of 0.1 |
| Forest / Raytran model (Govaerts & Verstraete, 1997) | Tree density (stem/hectare) Mean conifer height (m) Mean Crown LAI (m ² /m ²) | 100, 200, 400, 800 and 1200 15 3.81 |

^(*) Water vapor and ozone content of 1.0 g/cm² and 320 DU are used.

As an example of the information stored in the LUTs, Figure A-3 shows the simulated TOA reflectance factors for the blue, red and NIR VEGETATION channels (upper three rows), for a solar zenith angle of 49° and a relative azimuth of 45° over low, medium and high tree density boreal conifer-forest scenarios (left, middle and right column, respectively). The large dynamical ranges occurring at all wavelengths of the VEGETATION sensor illustrate both the importance of the angular effects on the measured signal, and more interestingly, the existing potential in using these angular signatures to better constrain the inversion procedure.

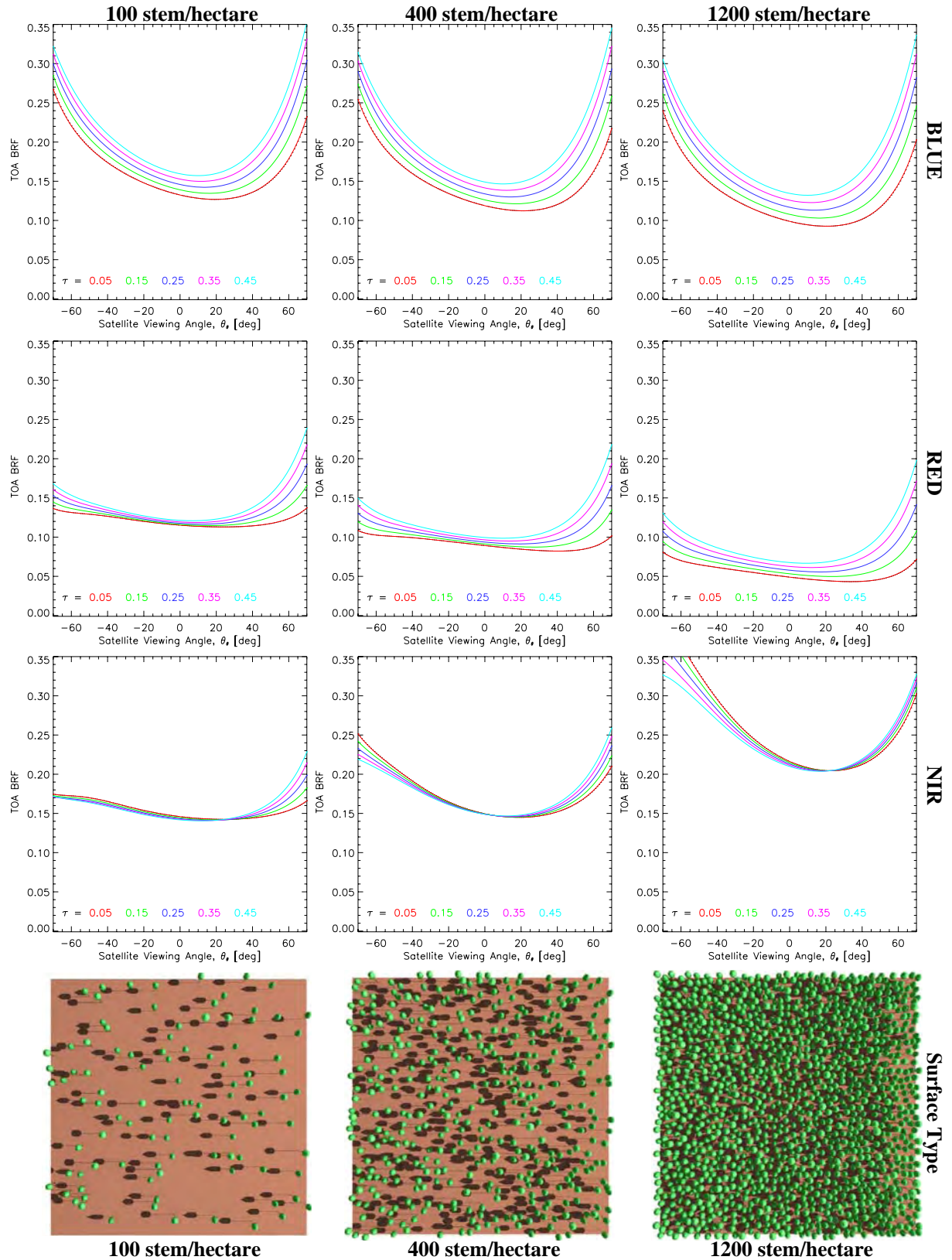


Figure A-3: Example of pre-computed spectral BRF values at the top of the atmosphere between $-70^\circ \leq \theta_v \leq 70^\circ$, for a variety of atmospheric optical depths τ at 550 nm, at illumination conditions of $\theta_o = 49^\circ$ and $|\phi| = 45^\circ$. Every column refers to a different surface type (dark soil) which is visualized from the local zenith in the bottom panel. The first three rows (top to bottom) refer to the blue, red and near-infrared channels of the VEGETATION instrument.

A-2.3 Mathematical approach

Identification of the ensemble of probable solutions

In order to apply the simulated spectral signatures in a boreal forest identification algorithm an efficient measure must be devised in order to extract the probable solutions from the ensemble of potential solutions. This can be achieved by evaluating all potential solutions with the following spectral metrics (Kahn et al. 1997, Martonchik et al. 1998a and Pinty et al. 2000b):

$$\chi_{(\lambda, \theta_v)}^2 = \frac{W_{cost}(\lambda, \theta_v) [\rho^{SAT}(\lambda, \mu, \mu_0, \phi - \phi_0) - \rho^{LUT}(\lambda, \mu, \mu_0, \phi - \phi_0)]^2}{[\sigma_{total}(\lambda, \theta_v)]^2} \quad (\text{A-1})$$

where μ and μ_0 are the cosine of the observation and illumination zenith angles, respectively and $\phi - \phi_0$ denotes the relative azimuth angle between the directions of observation and illumination.

In Equation A-1, $\rho^{SAT}(\lambda, \mu, \mu_0, \phi - \phi_0)$ is the spectral TOA BRF value measured by the space-borne instrument at the current band λ and view zenith angle θ_v , $\rho^{LUT}(\lambda, \mu, \mu_0, \phi - \phi_0)$ is the model-generated spectral TOA BRF value at the current band λ and view zenith angle θ_v stored in the LUTs of the potential solutions. $W_{cost}(\lambda, \theta_v)$ is a spectral and directional weighting factor, that can be chosen in order to account for either desired or undesired effects, or else set equal to 1 as was done here. The $\sigma_{total}(\lambda, \theta_v)$ value accounts for the expected uncertainty in both the measured and model-generated spectral TOA BRF values for a given spectral band and view zenith angle. This latter string of values is difficult to assess precisely for a given instrument using a theoretical approach, since it accumulates all kinds of limitations of the instrument, as well as uncertainties on calibration coefficients, the stability of the instrument and geometrical rectification, and the inaccuracies inherent to the modelling of the spectral TOA BRF values. The choice of the $\sigma_{total}(\lambda, \theta_v)$ values impacts the number of combinations of surface and atmospheric variables which represent acceptable solutions to the inverse problem for every processed pixel: the larger its value, the greater the number of solutions that may be considered acceptable from the radiative point of view. However, rather than using the uncertainty values of the BRF, the maximum tolerable deviation between observed and modelled spectral BRF values will be expressed throughout this paper in terms of the error criterion, ϵ which is set to a percentage of the satellite measured spectral BRF values.

All potential solutions that have $\chi_{(\lambda, \theta_v)}^2 < 1$ for a specific value of the error criterion ϵ , belong to the set of probable solutions $S\{\chi_{(\lambda, \theta_v)}^2 < 1 \mid \epsilon\}$ at that particular view zenith angle and spectral band condition. However, for a potential solution to be identified as a probable solution to all valid instantaneous directional and spectral observations (O) of a given instrument, it needs to be included in the intersection of all of the above available sets of probable solutions:

$$S\{probable\ solutions \mid O, \epsilon\} = \bigcap_{\lambda, \theta_v} S\{\chi_{(\lambda, \theta_v)}^2 < 1 \mid \epsilon\} \quad (\text{A-2})$$

In the case of a monodirectional satellite like VEGETATION a probable solution is thus one whose $\chi_{(\lambda)}^2$ values over the blue, red and NIR bands³ are simultaneously less than 1.

This permits identifying, for each overpass and pixel of the VEGETATION sensor, a set of radiatively consistent atmospheric and surface conditions that are accurate enough to interpret the VEGETATION spectral data strings, with an accuracy at least equal to the error criterion, or equivalently, to the corresponding $\sigma_{total}(\lambda)$ in the denominator of Equation A-1. This procedure thus yields at once the values of the model state variables documenting 1) the aerosol load provided as an effective aerosol optical depth at 550 nm, and 2) the state of the coniferous forests as described in the geophysical scenes entering the Raytran model. The latter corresponds to the surface boundary condition which is also mathematically expressed by the RPV model with pre-determined sets of RPV parameter values, namely, the spectral amplitude and shapes of the surface scattering function ($\rho_0(\lambda), k(\lambda), \Theta_{HG}(\lambda)$).

³For clarity the subscript θ_v will be omitted whenever referring to the monodirectional VEGETATION satellite.

Selection of the most likely solution

For a number of practical reasons it is appropriate to select only one candidate from amongst the set of probable solutions identified in Equation A-2 that sufficiently account for the satellite gathered BRF values at a particular pixel location. To find the most likely of these probable solutions, we follow Pinty et al. (2000a) and compute the mean value, $\overline{\rho_0(\lambda_{NIR})}$ and average deviation, Δ_{ρ_0} of the associated spectral amplitudes of the RPV model in the near-infrared. The most likely candidate to represent the underlying surface $\tilde{\rho}_0(\lambda_{NIR})$, is the one associated with spectral amplitude $\rho_0(\lambda_{NIR})$, that is, firstly, amongst those probable solutions that are not further away from $\overline{\rho_0(\lambda_{NIR})}$ than Δ_{ρ_0} , and secondly, that minimizes the quantity $|\rho_0(\lambda_{NIR}) - \overline{\rho_0(\lambda_{NIR})}|$. If due to different associated atmospheric optical depths several probable solutions with $\tilde{\rho}_0(\lambda_{NIR})$ exist, then the one with the smallest value of $\langle \chi^2_{(\lambda_{NIR})} \rangle$ —computed as the average over all n valid instantaneous bidirectional measurements in the NIR—will be selected from amongst them to represent the most likely solution. In the case of the VEGETATION instrument this means finding the probable solution that is associated to the $\tilde{\rho}_0(\lambda_{NIR})$ with the smallest value of $\chi^2_{(\lambda_{NIR})}$ (see Figure A-4 for a graphical illustration). While this selection procedure is aimed at handling large sets of probable solutions, and to reduce the influence of atmospheric and data related perturbations, it is clear that various other means of extraction could be devised, all of which with their own degree of arbitrariness.

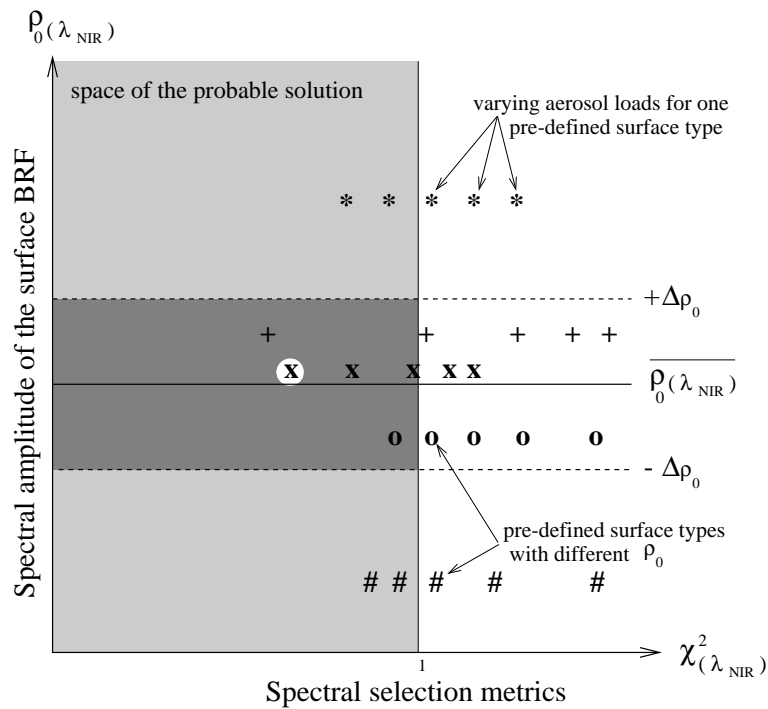


Figure A-4: Graphical illustration of the implemented procedure to retrieve the most likely candidate from the ensemble of probable solutions (*i.e.*, for symbols that lie within the grey shaded areas). The **x** symbol corresponds to the surface type that minimizes the quantity $|\rho_0(\lambda_{NIR}) - \overline{\rho_0(\lambda_{NIR})}|$. The white circular area identifies what associated atmospheric aerosol load yields the lowest $\chi^2_{(\lambda_{NIR})}$ value for this particular surface type, *i.e.*, the selected solution.

Selection of the temporally most representative solution

The output of the procedure in subsection A-2.3 and can be mapped in order to locate those pixels that belong to at least one of the broad surface type categories pre-defined in the LUTs. However, in the presence of clouds and other unfavorable atmospheric conditions, the situation may arise where none of the acceptable values of ϵ allows for a given pixel to be associated with one of the predefined surface type solutions. This is especially the case if multiple sets of spectral BRF values, gathered at different viewing conditions, have to be in agreement. Conversely, monodirectional instruments might

very well allow for the retrieval of a most likely solution in that case, but only at the risk of identifying a different surface type than would be retrieved under clear sky conditions. Thus, in the absence of relevant simultaneous angular sampling of the spectral TOA BRF values, the effects due to the coupling between the surface and atmospheric scattering properties are not always separable in a reliable manner. Indeed, each individual set of spectral VEGETATION measurements may correspond to different geophysical systems, all of them equi-probable in the sense of Equation A-1 to explain the observations. The selection of the most likely solution from the ensemble of probable solutions (in Figure A-4) may therefore very well be impaired by the particular illumination, viewing and atmospheric conditions at the time of observation. A supplemental step in the data interpretation is thus required in order to provide a coherent characterization of the underlying forest type. More specifically, the identification of the most representative solution, that best summarizes the state of the underlying surface, has to rely on the analysis of retrievals obtained during a short time period if no additional information or ecological models are available to compensate for the lack of appropriate simultaneous data. This assumes however, that the surface conditions during the data accumulation period (typically a few weeks) are not changing significantly enough to impact the retrieved sets of probable solutions. Furthermore, it is surmised that the number of probable solutions on any particular day is merely controlled by the occurrence of a changing atmosphere, which forces the surface type to be chosen so that the radiative coupling produces acceptable fits to the data measured by the instrument. The selection of the most representative surface type can thus be achieved on the identification of the most frequent surface type belonging to the ensemble of likely solutions found over the given time period. Mathematically, the selection of the most representative forest type is done by estimating first the temporal average of the most likely $\tilde{\rho}_0(\lambda_{NIR})$ over a fixed number of days, N :

$$\overline{\tilde{\rho}_0(\lambda_{NIR})} = \frac{1}{T} \sum_{t=1}^T \tilde{\rho}_0(\lambda_{NIR})(t) \quad (\text{A-3})$$

where T is the number of available values during the N -day period of temporal accumulation and $\overline{\tilde{\rho}_0(\lambda_{NIR})}$ is the temporal averaged value estimated for parameter $\tilde{\rho}_0(\lambda_{NIR})(t)$.

The N -day representative value for the ρ_0 parameter is the value of $\tilde{\rho}_0(\lambda_{NIR})(t)$ that minimizes the quantity $|\tilde{\rho}_0(\lambda_{NIR})(t) - \overline{\tilde{\rho}_0(\lambda_{NIR})}|$. Since this solution corresponds to one of the individual solutions selected in the complete N -day time series, the associated discrete values for the k and Θ_{HG} parameters are easily assessed. This procedure defines the most representative N -day values of the three surface parameters characterizing the surface radiative properties, namely, $\hat{\rho}_0(\lambda_{NIR})$, $\hat{k}(\lambda_{NIR})$ and $\hat{\Theta}_{HG}(\lambda_{NIR})$. It also ensures that these selected values are able to produce radiation fields consistent with at least one of the radiation fields, measured during the N -day period by the instrument.

A-2.4 Simulation tests of the inverse procedure

A series of experiments were performed in order to 1) quantify the intra-variability of the set of pre-defined potential solutions⁴, 2) identify, in the case of mono-directional instruments, one or more optimal viewing conditions that consistently increase the separability of the pre-defined solutions over all spectral bands, and 3) test the expected performance of the proposed inversion methodology in terms of the limits and quality of the retrieved forest types and associated aerosol load for a VEGETATION like instrument. These tests (see Pinty et al. 2000c) lead to the conclusion that, 1) the intra-variability of the pre-defined solutions is dependent on the spectral band of observation, 2) different optimal viewing conditions exist for individual surface types, illumination angles and atmospheric aerosol conditions, and 3) no single value of the error criterion, greater than the absolute calibration error of the VEGETATION instrument, can guarantee the complete separability of all pre-defined solutions in Table A-3 under all illumination and viewing conditions tested. The latter refer to solar zenith angles of 40°, 50° and 60°, satellite zenith angles going from 0° to 80° in steps of 1°, and relative azimuth angles spanning 0° to 180° in steps of 5°.

Multi-angular observations like those of the Multi-angle Imaging SpectroRadiometer (Diner et al. 1991), on the other hand, would almost completely eliminate the viewing angle dependency of the separability of the pre-defined solutions. In addition, the increased number of spectral and directional

⁴The term solution refers here to both an underlying surface type and its associated atmospheric optical depth.

constraints in Equation A-2, would almost certainly increase the level of separability between the predefined solutions. However, the use of only one value for the error criterion in operational retrievals is still inappropriate because of the dependency of the solutions with respect to the changes in illumination angle and aerosol conditions. The approach adopted here will therefore consist of gradually incrementing the value of the error criterion until either a valid solution is retrieved or else an upper limit of ϵ is reached. In the case of multiple solutions to an instantaneously gathered data string, the methodology of subsection A-2.3.2 will be applied to retrieve the most likely of the probable solutions, whereas the procedure of subsection A-2.3.3 will be used to identify the temporally most representative of the predefined surface types at every pixel position.

A-3 Application to actual data

The identification and characterization procedure presented in section A-2.3 has been applied to a VEGETATION TOA data set (P-products), acquired over Northern Europe during the first 20 days of June 1999. Given that Henry and Meygret (2000) claim that the absolute calibration error over the first three spectral bands of the VEGETATION instrument lies in the range of 3 to 5%, the inversion procedure at every pixel position was started with an initial error criterion value of 3%. If no probable solution out of the pre-computed set of potential forest types could be retrieved, the error criterion was increased by 1% and Equation A-1 was evaluated anew, for all three spectral bands considered. This iterative procedure either identified one or more probable solutions at some specified degree of confidence (error level), or ended with no solution if the error criterion reached 20% and no probable solution had been identified yet. From results summarized in Figure A-5, it can be seen however, that the number of probable solutions did not exceeded unity in 87.7% of the processed pixels for which acceptable solutions were identified.

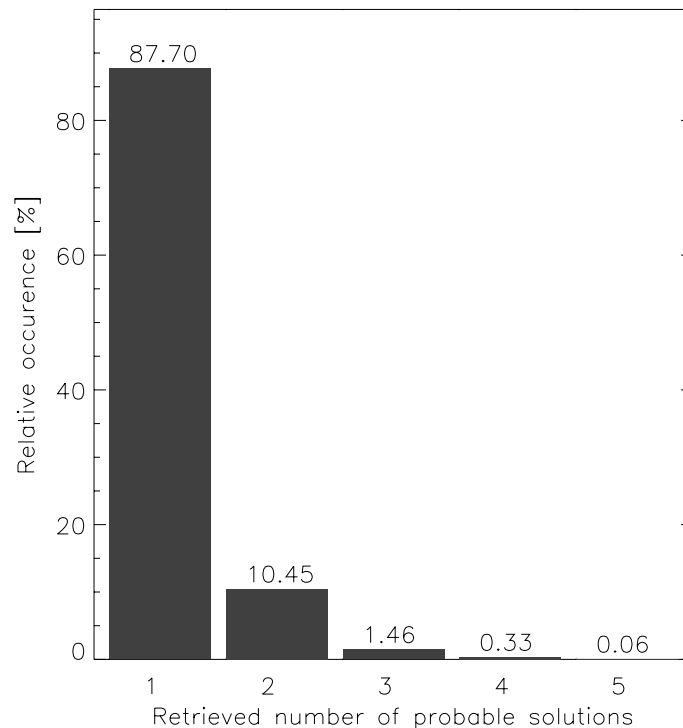


Figure A-5: Histogram of the retrieved number of probable solutions over Scandinavia during the first 20 days of June 1999 for all values of the error criteria between 3 and 20% together.

This procedure can be applied in a stand-alone mode in the sense that it does not require any pre-screening for cloud/cloud shadow contamination or other spurious geophysical situations because these geophysical situations can hardly lead to the finding of a probable solution as defined by Equation A-1. However, in order to limit the unnecessary processing of too many pixels, we adopted a conservative

screening procedure which is based on the Optimized VEGETATION Normalized Index (OVNI) (Gobron et al. 2000b). This vegetation index provides the ability to assess the presence of vegetation of the basis of TOA BRF values sampled by the blue, red and near-infrared bands of the VEGETATION instrument. We thus first labeled all pixels of the processed VEGETATION data set before applying our inversion procedure only on those pixels corresponding to a vegetation class.



Figure A-6: Forest identification map for the first twenty days of June 1999 with a maximum tolerable BRF deviation at various accuracy levels between 5 and 20%. Vegetation coverage (grey areas) increases as the error criterion increases. White areas indicate the presence of water bodies or locations for which no probable solution could be retrieved at that particular value of the error criterion.

A-3.1 Forest identification

Figure A-6 shows, for a series of values of the error criterium, the spatial distribution of those pixels, whose most representative spectral BRF values at TOA (over the period from 1st–20th June 1999) were sufficiently close to those in the LUTs, such that at least one of the predefined surface types would represent a probable solution⁵. White areas indicate the presence of water bodies or pixels for which no probable solution could be retrieved for any allowable value of the error criterion. From panel to panel the maximum tolerable BRF deviation was increased with the consequence that more pixels satisfied the

⁵For the latitude and longitude ranges of interest here (4°E to 30°E and 55°N to 71.25°N), the VEGETATION 1 km “Plate carrée” projection had an average pixel size of ~ 994 m in the latitudinal direction, whilst that of the longitudinal direction varied from ~ 486 m at 55°N to ~ 600 m at 71.25°N , such that it had to be reprojected—using a nearest neighbor sampling scheme—to obtain a true 1 km^2 pixel size map.

imposed conditions, and thus became part of the ensemble of probable solutions (grey color). Clearly the likelihood that one of the pre-defined surface types is truly responsible for the observed measurements decreases as the constraints on the error criterion are being relaxed. Depending on the application, a compromise has to be found between highly accurate yet mostly empty maps, on the one hand, and relatively inaccurate but well covered maps on the other. In any case, the reliability of the adopted retrieval methodology can be assessed over sparsely forested regions like Denmark (4–12% forest cover, Päivinen and Köhl 1996), where only very few forest covered pixel locations were identified in Figure A-6, even for $\epsilon = 20\%$.

The right panel of Figure A-7 shows the atmospheric optical depth field associated with the retrieved forest type solutions in Figure A-6, while the left panel displays the spatial distribution of the error criterion values yielding at least 1 solution. The associated optical depth field is actually a temporal mosaic of optical depth values, each one associated with a particular day of the compositing period but not necessarily being statistically representative of that period.

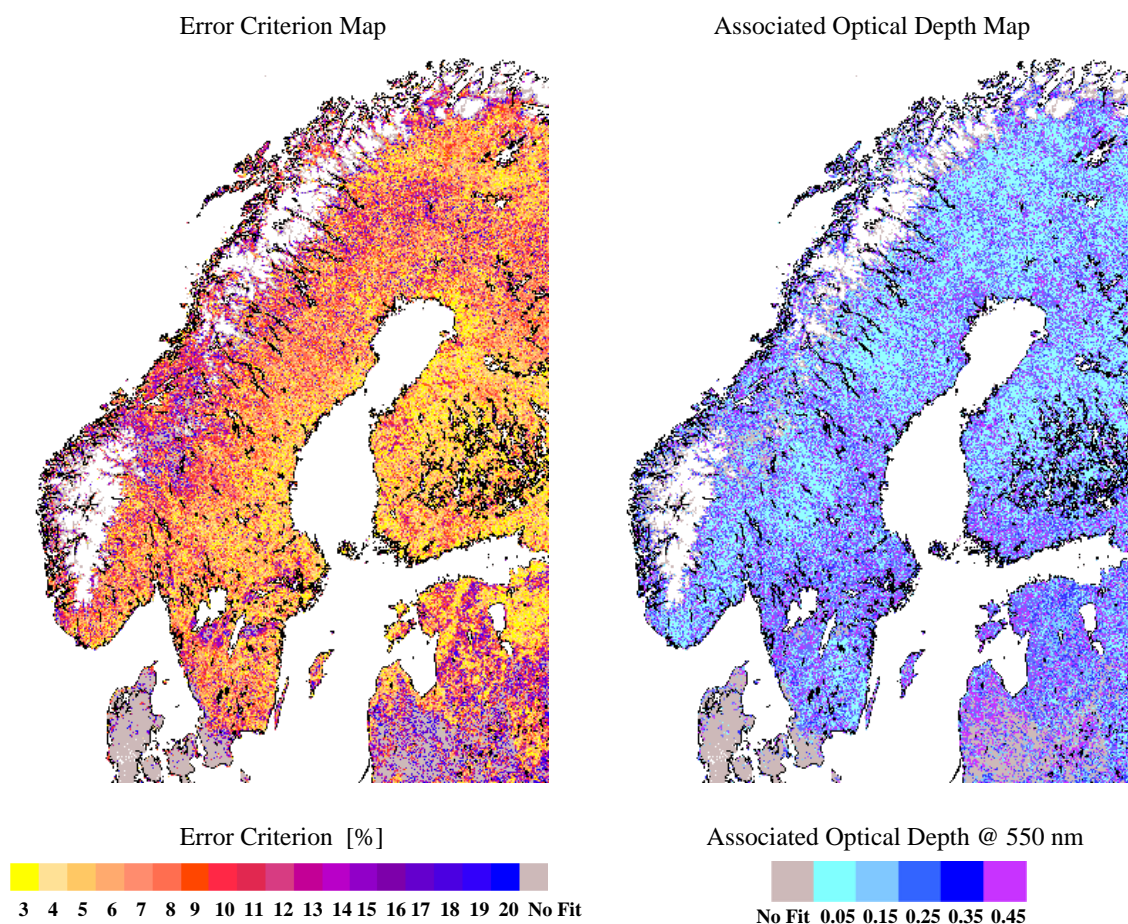


Figure A-7: Left panel: Accuracy map for the first twenty days of June 1999 with the maximum tolerable spectral BRDF deviation varying between 3 and 20% of the observed values. White patches indicate the presence of water bodies or bright surfaces. Right panel: Optical depth map for the first twenty days of June 1999. These values are those associated to the most representative surface type (and day) of the compositing period.

As the error criterion value is increased and more and more pixels are associated to the pre-defined surface types, the probability that the actual biophysical characteristics of these pixel locations are in agreement with the ones of the pre-defined solutions will decrease. The goal is thus to generate a forest cover map where the correspondence between pixels with valid retrievals and the actual presence of forested areas at these locations is maximized. This can be achieved by selecting a cutoff value for the maximum tolerable error criterion that adequately delineates the presence of wooded areas similar to

those included in the set of pre-defined forest types. Clearly such a value is dependent on the adequacy, the number and range of surface types that are included in the set of potential solutions. More limiting however, because less quantifiable with respect to the inversion procedure, are processing and measurement related uncertainties, like data interpolation for mapping purposes, adjacency effects and spectral mixing, that all affect the denominator of Equation A-1. As a compromise to the above arguments it was decided to present the following results at a maximum value of 8% for the error criterion. This value corresponds to the in-flight, root-mean-square deviation from the VEGETATION reference calibration over bright sands and deserts in the blue, red and near-infrared bands (Henry and Meygret 2000). Additionally, the 8% specifically take account of the bounded envelope of the pre-defined spectral reflectances in the LUTs. In other words, it captures the inaptitude of the five pre-defined forest scenes to account for the natural ranges of structural and spectral variability in the land-cover and soil types that are likely to be encountered within the region of study.

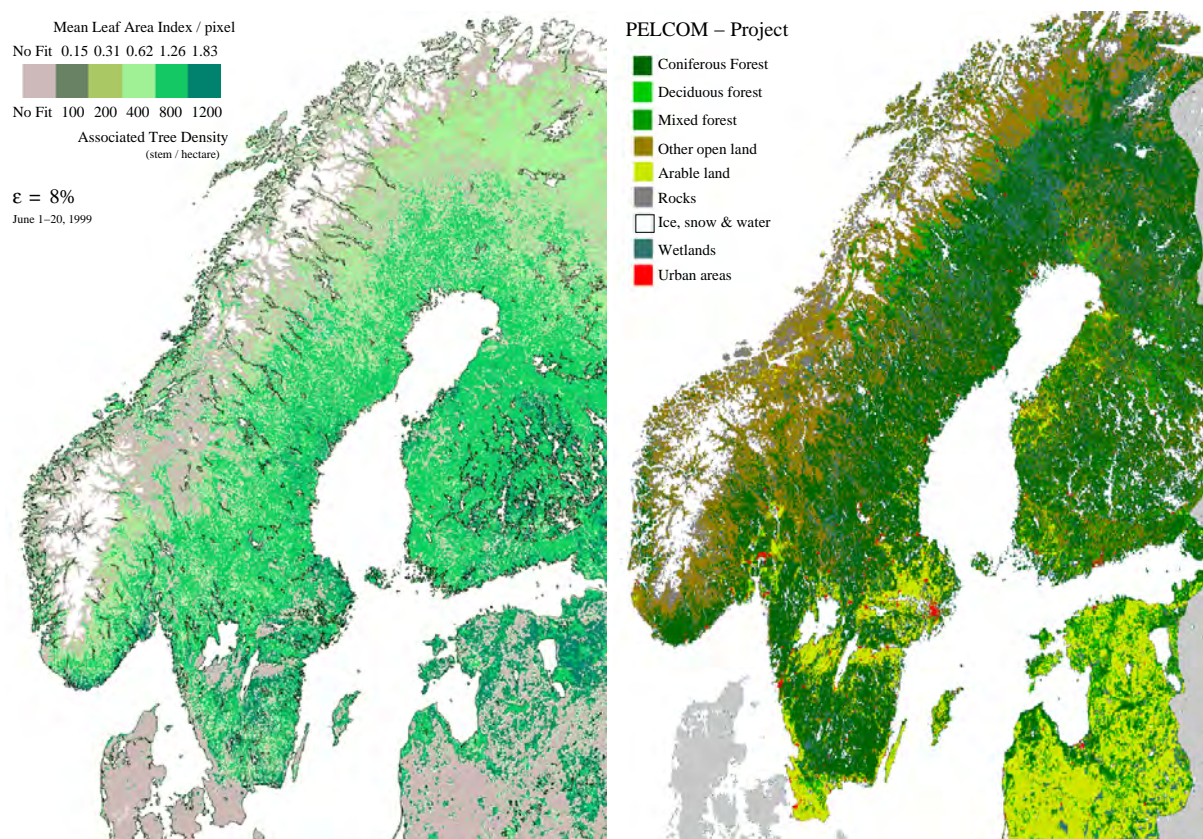


Figure A-8: Left panel: Forest characterization map for the first twenty days of June 1999 with a maximum tolerable BRF deviation of 8%. White patches indicate the presence of water bodies or bright surfaces. Right panel: Land cover characterization map derived in the context of the Pan-European Land Use and Land Cover Monitoring (PELCOM) project.

A-3.2 Forest characterization

Beyond the task of forest identification, the inversion methodology also aims at characterizing the underlying wooded surface types. The left panel of Figure A-8 shows a forest characterization map of Scandinavia, derived from VEGETATION data for the first 20 days of June 1999, with the $\sigma_{total}(\lambda)$ value set to 8% of the spectral BRF values. A general thinning of tree density with latitude can be observed in Finland. The same effect is also apparent over Sweden with the addition of orography-induced tree density reductions in its western regions. The right panel of Figure A-8 exhibits a map derived in the context of the Pan-European Land Use and Land Cover Monitoring (PELCOM) project (Muecher et al. 1998). That map was generated by integrating multiple sources of land use information with information resulting from the classification of multitemporal NOAA-AVHRR satellite data and thus cannot be easily

associated to one specific time period or year. A visual inspection of the two reveals a high degree of correlation, especially in the delineation of the contours of the broad vegetation classes (e.g., the presence of the “arable land” class for example, is well respected by our forest identification algorithm). It should be stressed that the VEGETATION derived map was generated from three weeks of data only, and does not require any further ancillary information. The summer period was primarily selected in order to ensure a sufficient number of cloud-free conditions over Northern Europe and, therefore, to provide the best possible spatial coverage over this region.

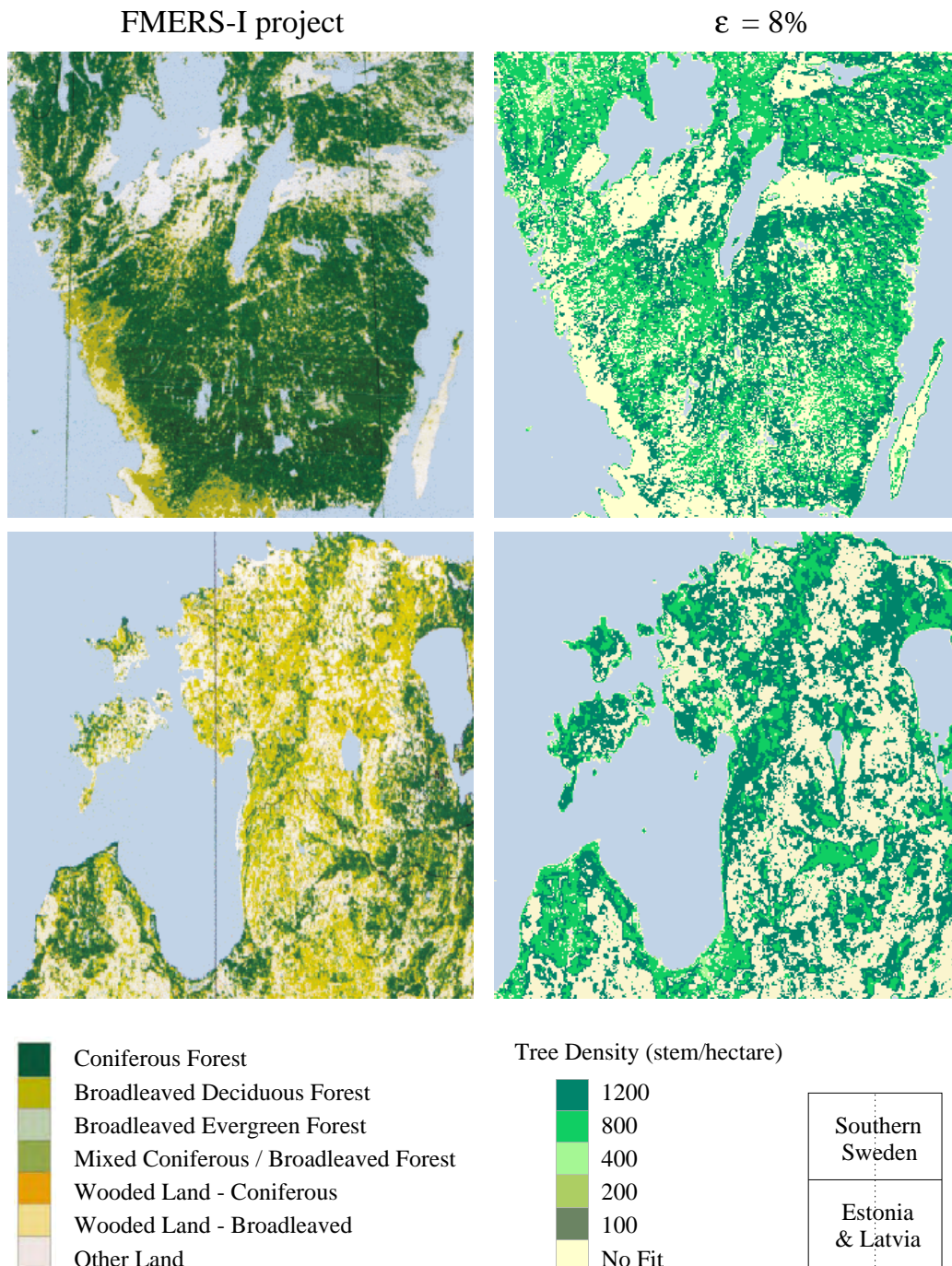


Figure A-9: Comparison between our forest characteristics map for June 1st-20th 1999 (with an error criterion of 8%) and the land-cover map produced in the context of the FMERS-I project over southern Sweden (top panels) and Estonia & Latvia (bottom panels).

Figure A-9 compares two regions of Figure A-8 with the corresponding areas of a land-cover map derived in the context of the Forest Monitoring in Europe with Remote Sensing (FMERS) project. The FMERS-I maps were derived from the analysis of one year of data gathered in 1997 from the high resolution IRS 1C WIFS sensor and ancillary ground controlled observations (see Hame et al. 1999). Again, a high degree of agreement between the forested structures in both regions is evident. In the top panels (Southern Sweden) our methodology appears to account for the transition between coniferous and deciduous forests along the south-western coastal region. The possibly spurious location of forested pixels along some of the coastlines is presumably due to the way the original VEGETATION data are interpolated when projected onto the user-specified grids.

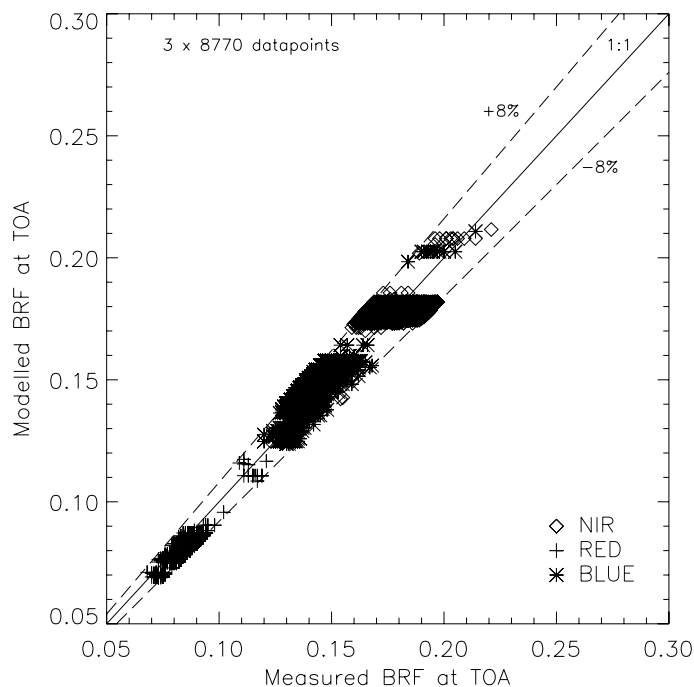


Figure A-10: Relationship between modelled and measured BRF values at the top of the atmosphere for the first three bands of the VEGETATION sensor for a section of the forest characterization map in the left panel of Figure A-8 (error criterion = 8%).

Figure A-10 indicates the relationship between the measured and modelled BRFs at the top of the atmosphere. Indeed, it can be seen that the selected probable solutions all lie within the uncertainty level of Equation A-1, expressed by an error criterion of 8%. When comparing the maps in Figures A-8 and A-9, one should however keep in mind the various uncertainties due to data derived from different sources, with disparate reliabilities, spatial accuracies and temporal acquisition periods, as well as those due to the sets of criteria that are not always related to measurable quantities but instead to ecological classes that have been defined *a priori*. Two of the main issues in such an intercomparison exercise are the selection of a tolerable error level and the lack of quantification of the uncertainties in the associated classes. By precomputing the radiative signature of a series of explicitly described, three-dimensional representations of potential land cover types, prior to the identification of the most probable one of these as a representative solution for a given period of observation, the ambiguities of interpretation are ultimately delegated to the end-user of the derived information. It is his task to decide upon the value of the error criterion beyond which the pre-defined solutions can no longer be tolerated as probable in the sense of the application at hand. In the case of the presented inversion methodology the retrieved information will not only contain biophysical structure parameters but also the allometric equations that relate them, since these were an implicit part of the input information.

Nevertheless, a number of issues related to the derivation of the forest characterization map in the left panel of Figure A-8, still have to be addressed here. The length of the compositing period and the number of days with at least one probable solution within that period both have an effect onto

the selection of the most representative surface type. The reasons for this are twofold at least: firstly the VEGETATION instrument is mono-directional, which clearly reduces its capability in differentiating between similarly vegetated surfaces at the scale of observation (Diner et al. 1999), and secondly, it is also possible that the viewing conditions for a given pixel location may change from relatively oblique angles to virtually nadir in subsequent overpasses, which can easily influence the separability of the pre-defined surface type solutions (Pinty et al. 2000c). Additionally, one has to keep in mind that with the rapidly changing atmospheric conditions over northern latitudes, the mono-directionality of this instrument and the associated measurement errors, it is possible to mistakenly retrieve a unique solution to the inversion problem that may be characterized by an elevated aerosol load and an “erroneous” surface type.

A-4 Conclusions

The retrieval of an exhaustive set of boreal forest characteristics from remote sensing data was investigated. For that purpose, the BRF fields at TOC and subsequently at TOA, for a series of three-dimensional representations of typical coniferous forests were simulated, for a pre-defined set of aerosol, viewing and illumination conditions. These spectral BRF values were stored in LUTs, from where they could easily be retrieved for a comparative evaluation against actual satellite data, under identical viewing and illumination geometries. If an acceptable match between observed and pre-computed spectral BRF values was found, the physical parameters that had been involved in the generation of the corresponding LUT entries were considered as a possible solution to the satisfactory interpretation of the observed satellite measurements. By retaining the most likely of the so retrieved solutions over a period of 20 days in June 1999, the generation of maps showing the likelihood of identifying various forest types, their most representative corresponding structural characteristics as well as the associated atmospheric optical depth at the day of retrieval was performed. A visual comparison with two independent land cover maps confirmed the usefulness of this approach, especially with respect to the delineation of forest-covered zones. In addition, however, the proposed retrieval methodology is completely generic, and thus can easily be prototyped for different instruments, such as MODIS, MERIS, SeaWiFS, etc.

Of particular interest here is the latest of the generation of multispectral and multiangular instruments (*e.g.*, MISR). Indeed, Diner et al. (1999) and Gobron et al. (2000a), showed that with multi-angular MISR data, a more detailed, reliable and accurate description of different surface types is achievable than from mono-directional instruments. More specifically, its nine viewing angles would allow for a much more stringent identification criteria to be imposed, when looking for probable solutions in the LUT entries. This, in turn, would clearly translates into a better separability of the set of pre-defined solutions and hence also the acceptable size of that ensemble. Another point to consider is that at the nominal ground resolution of MISR (275 m), the use of three dimensional canopy representations for the simulation of the exiting BRF field at TOC intuitively appears to be more warranted. All of these considerations then indicate that the potential of the methodology described here should become fully exploitable with the availability of instantaneous multi-angular and multi-spectral data.

Acknowledgements

Some of the results shown in this paper were presented at the VEGETATION 2000 Symposium at Belgirate, Italy in June 2000. The authors acknowledge the support of the VEGETATION preparatory programme financed by France, the European Commission, Belgium, Italy and Sweden, and the inputs from V. Gond (Space Applications Institute, Joint Research Centre, Italy) and D. L. Williams (Biospheric Sciences Branch, NASA/Goddard Space Flight Center, USA) who helped with their knowledge of the various conifer species in Europe and provided data on the optical properties of needle spectral reflectance and transmittance. Part of this work has been achieved in the framework of Jean-Luc Widlowski's Ph.D. thesis, who currently benefits from a JRC doctoral fellowship.

Annex B

Radiation Transfer Fundamentals

B-1 The radiation transfer equation in vegetation canopies

Consider a flat, horizontal leaf canopy of depth H , that is being illuminated in a spatially uniform manner from the top ($z = 0$). The radiation transfer equation (under steady state conditions and neglecting any polarization effects) can then be expressed along the local downward vertical, such that, the change in radiation intensity, travelling at depth level z and in the direction $\mathbf{\Omega}$, is controlled by the amounts that are being intercepted by the foliage, and that are being scattered from direction $\mathbf{\Omega}'$ into $\mathbf{\Omega}$:

$$-\mu \frac{\partial I(z, \mathbf{\Omega})}{\partial z} + \tilde{\sigma}_e(z, \mathbf{\Omega}, \mathbf{\Omega}_0) = \oint_{4\pi} \tilde{\sigma}_s(z, \mathbf{\Omega}' \rightarrow \mathbf{\Omega}) I(z, \mathbf{\Omega}') d\mathbf{\Omega}' \quad 0 < z < H \quad (\text{B-1})$$

where I represents the intensity [$\text{W m}^{-2} \text{sr}^{-1}$] at point z in the exiting direction $\mathbf{\Omega}$, and $\tilde{\sigma}_e$ [m^{-1}] is the extinction coefficient taken at the same point and along the same direction. $\tilde{\sigma}_s$ [sr^{-1}] is the differential scattering coefficient for photons scattering from direction $\mathbf{\Omega}'$ into a unit solid angle about direction $\mathbf{\Omega}$ at point z , where the unit vector $\mathbf{\Omega}(\theta, \phi)$ has an azimuthal angle ϕ and a polar angle $\theta = \cos^{-1} \mu$ with respect to the outward normal.

For representing the case of finite sized scatterers, when mutual shading between foliage elements affects the interception capability of the canopy, the probability, per unit pathlength of travel, that photons may hit a leaf depends not only on the amount and orientation of the scatterers but also on the direction of travel of the photons, and that of the solar illumination, $\mathbf{\Omega}_0$. Pinty and Verstraete (1998) have proposed to write the extinction coefficient as:

$$\tilde{\sigma}_e(z, \mathbf{\Omega}, \mathbf{\Omega}_0) = \sigma_e(z, \mathbf{\Omega}) \tilde{O}(z, \mathbf{\Omega}, \mathbf{\Omega}_0) = \Lambda(z) G(\mathbf{\Omega}) \tilde{O}(z, \mathbf{\Omega}, \mathbf{\Omega}_0) \quad (\text{B-2})$$

where $\sigma_e(z, \mathbf{\Omega})$ is the extinction coefficient for a purely turbid medium, *i.e.*, an infinite number of oriented point scatterers. $\Lambda(z)$ [m^2/m^3] is the leaf area density (LAD) at level z , $G(\mathbf{\Omega})$ is the well known Ross (1981) function accounting for the projection of the leaf-normal distributions in the direction $\mathbf{\Omega}$ (see section B-4), and $\tilde{O}(z, \mathbf{\Omega}, \mathbf{\Omega}_0)$ is a correction factor that aims at accounting for the increased transmission in the retro-reflection direction through the gaps in between finite sized leaves (see section B-2).

The probability for radiation coming from an arbitrary direction Ω' to be scattered into a particular direction Ω clearly depends both on the leaf normal distribution $g_L(z, \Omega_L)$ (see section B-3), and the rotationally invariant leaf scattering distribution function $f(\Omega' \rightarrow \Omega; \Omega_L)$ (see section B-5), describing the scattering behaviour of both sides of a leaf. The differential scattering coefficient can thus be written as:

$$\tilde{\sigma}_s(z, \Omega' \rightarrow \Omega) = \frac{\Lambda(z)}{2\pi} \oint_{2\pi^+} g_L(z, \Omega_L) |\Omega' \cdot \Omega_L| f(\Omega' \rightarrow \Omega, \Omega_L) d\Omega_L \quad (\text{B-3})$$

B-2 The hot-spot formulation of Verstraete et al. 1990

The physical mechanism behind the hot spot effect was studied in detail by Verstraete et al. (1990) who idealised the free space in between scatterers by considering two cylindrical volumes $\|\mathcal{V}_1\|$ and $\|\mathcal{V}_2\|$ drawn along the incoming Ω_0 and outgoing Ω directions. $\|\mathcal{V}_1\|$ and $\|\mathcal{V}_2\|$ have a common base defined by a circular Sun fleck of radius r and therefore share a common volume free of scatterers. Denoting $\|\mathcal{V}_\bullet\|$ the volume that is not in common between $\|\mathcal{V}_1\|$ and $\|\mathcal{V}_2\|$ it can be demonstrated that the actual optical path of the scattered radiation can be estimated as:

$$\tau(z, \Omega, \Omega_0) = \frac{\|\mathcal{V}_\bullet\|}{\|\mathcal{V}_2\|} \int_z^0 \sigma_e(z', \Omega) dz' \quad (\text{B-4})$$

where $\sigma_e(z', \Omega)$ is the purely turbid extinction coefficient taken at level z' along the direction Ω . The correction factor is given by:

$$\frac{\|\mathcal{V}_\bullet\|}{\|\mathcal{V}_2\|} = 1 - \frac{2}{\pi\zeta_T} \left[\zeta_* \cos^{-1} \zeta_* - (1 - \zeta_*^2)^{-1/2} + \frac{1}{3} \sin^3(\cos^{-1} \zeta_*) + \frac{2}{3} \right] \quad (\text{B-5})$$

where $\zeta_* = \min(1, \zeta_T)$ with $\zeta_T = zG_f/2r$. Gobron et al. (1997c) describes how to retrieve an estimate of r , and G_f —being a geometric factor—is defined as:

$$G_f = \left[\tan^2 \theta_0 + \tan^2 \theta - 2 \tan \theta_0 \tan \theta \cos(\phi_0 - \phi) \right]^{1/2} \quad (\text{B-6})$$

With the assumption that the leaf area density Λ and the Ross function $G(\Omega_x)$ are constant along the coordinate z , the correction function for the extinction coefficient $\tilde{O}(z, \Omega, \Omega_0)$ is given by $\partial(\|\mathcal{V}_\bullet\| / \|\mathcal{V}_2\|) / \partial z$ which is equal to (Pinty and Verstraete 1998):

$$\tilde{O}(z, \Omega, \Omega_0) = 1 - \frac{2}{\pi} \left\{ \cos^{-1} \zeta_* - \zeta_* [1 - \zeta_*^2]^{1/2} \right\} \quad (\text{B-7})$$

and unity if $\zeta_T > 1$ i.e., $\zeta_* = 1$.

B-3 The distribution function of leaf normal orientations

The spatial orientation of a leaf is described by the direction of its normal $\Omega_L(\theta_L, \phi_L)$ to the upper surface, where θ_L is the inclination angle of the leaf normal, and ϕ_L is the azimuthal angle of the outward normal. Consider a horizontally homogeneous leaf layer of unit thickness at height z , and let the sum of areas of all leaves (or parts thereof) whose normals fall within an incremental solid angle around the direction Ω_L be $\hat{g}_L(z, \Omega_L)$. Upon integration over the space of leaf normals one obtains (Asrar 1989):

$$\frac{1}{2\pi} \oint_{2\pi^+} \hat{g}_L(z, \Omega_L) d\Omega_L = \frac{1}{2\pi} \int_0^{2\pi} d\phi_L \int_0^{\pi/2} \hat{g}_L(z, \Omega_L) \sin \theta_L d\theta_L \equiv s_L^*(z) \quad (\text{B-8})$$

where all leaves are assumed to face upward, so that all leaf normals are confined to the upper hemisphere ($2\pi^+$), and $s_L^*(z)$ is the total one sided area of all leaves in this horizontal layer. The leaf-normal distribution (LND) function $g_L(z, \mathbf{\Omega}_L) = \hat{g}_L(z, \mathbf{\Omega}_L)/s_L^*(z)$, denotes the fraction of total leaf area in the horizontal layer of unit thickness at height z whose normals fall within a unit solid angle around the direction $\mathbf{\Omega}_L$, and must satisfy the following normalization criterion (Ross 1981):

$$\frac{1}{2\pi} \oint_{2\pi^+} g_L(\mathbf{\Omega}_L) d\mathbf{\Omega}_L = \frac{1}{2\pi} \int_0^{2\pi} d\phi_L \int_0^{\pi/2} g_L(\theta_L, \phi_L) \sin \theta_L d\theta_L \equiv 1 \quad (\text{B-9})$$

Although plants are known to change their orientations in response to solar illumination conditions, heliotropisms (and other two-dimensional LND functions) are only rarely treated in theoretical studies (Strebel et al. (1985), Verstraete (1987)) since the assumption of azimuthally random leaf distributions significantly reduces the mathematical complexity of the function $g_L(\theta_L, \phi_L)$:

$$\int_0^{\pi/2} g_L(\theta_L) \sin \theta_L d\theta_L = \int_0^{\pi/2} g_L^*(\theta_L) d\theta_L = 1 \quad (\text{B-10})$$

Out of the various models to describe the leaf normal distribution functions, the two most commonly used are 1) the trigonometric functions of Bunnik (1978):

$$g_L(\theta_L) = (a + b \cos 2\theta_L + c \cos 4\theta_L) / \sin \theta_L \quad (\text{B-11})$$

and 2) the beta functions of (Goel and Strebel 1984):

$$g_L(\theta_L) \sim \beta(\xi, \nu) = \frac{\pi x^{\xi-1}(1-x)^{\nu-1}}{2 B(\xi, \nu)} \quad 0 < x < 1 \quad (\text{B-12})$$

where $B(\xi, \nu) = \Gamma(\xi)\Gamma(\nu)/\Gamma(\xi + \nu)$ is the beta function, Γ is the gamma function and $x = 2\theta_L/\pi$.

In Table B-1 the parameters for the above two representations of $g_L(\theta_L)$ are given for a variety of leaf normal distributions. Note however, that the descriptive term of the LNDs refers to g_L^* rather than g_L . This is most notably seen in what are termed *uniform* and *spherical* leaf normal distributions, namely:

$$\begin{aligned} g_L(\theta_L) &= \frac{2}{\pi} (\sin \theta_L)^{-1} & g_L^*(\theta_L) &= \frac{2}{\pi} & \text{uniform} \\ g_L(\theta_L) &= 1 & g_L^*(\theta_L) &= \sin \theta_L & \text{spherical} \end{aligned}$$

Table B-1: Parameter values for the trigonometrical (a, b, c) and beta (ξ, ν) function representation of the probability density function, $g_L(\theta_L)$ for 6 different leaf-normal distributions.

| | uniform | spherical | planophile | erectophile | plagiophile | extremophile |
|-------|---------|----------------------------|---------------|---------------|-------------|--------------|
| a | $2/\pi$ | $\sin \theta_L$ | $2/\pi$ | $2/\pi$ | $2/\pi$ | $2/\pi$ |
| b | 0 | 0 | $2/\pi$ | $-2/\pi$ | 0 | 0 |
| c | 0 | 0 | 0 | 0 | $2/\pi$ | $-2/\pi$ |
| ξ | 1.000 | 1.101 (1.066) [†] | 2.770 (2.531) | 1.172 (1.096) | 3.326 | 0.433 |
| ν | 1.000 | 1.930 (1.853) | 1.172 (1.096) | 2.770 (2.531) | 3.326 | 0.433 |

[†] The values used by Raytran are shown in brackets if different from Goel and Strebel (1984).

B-4 The Ross function, $G(\boldsymbol{\Omega})$

For plane-parallel leaf canopies the $G(\boldsymbol{\Omega})$ function of Ross (1981) describes the projection of the leaf normal orientations in a particular direction of interest, and hence is an indicator of the likelihood that radiation may be intercepted by the canopy if travelling in that direction. More specifically, $G(\boldsymbol{\Omega})$, is the mean projection of a unit foliage area, in the direction $\boldsymbol{\Omega}$, per unit volume of canopy:

$$G(\boldsymbol{\Omega}) = \frac{1}{2\pi} \oint_{2\pi^+} g_L(\boldsymbol{\Omega}_L) |\boldsymbol{\Omega}_L \cdot \boldsymbol{\Omega}| d\boldsymbol{\Omega}_L \quad (\text{B-13})$$

where for azimuthally independent leaf normal distributions $G(\boldsymbol{\Omega})$ simplifies to $G(\theta)$ and the probability distribution function (PDF) of the leaf normal orientations $g_L(\boldsymbol{\Omega}_L)$ reduces to $g_L(\theta_L)$.

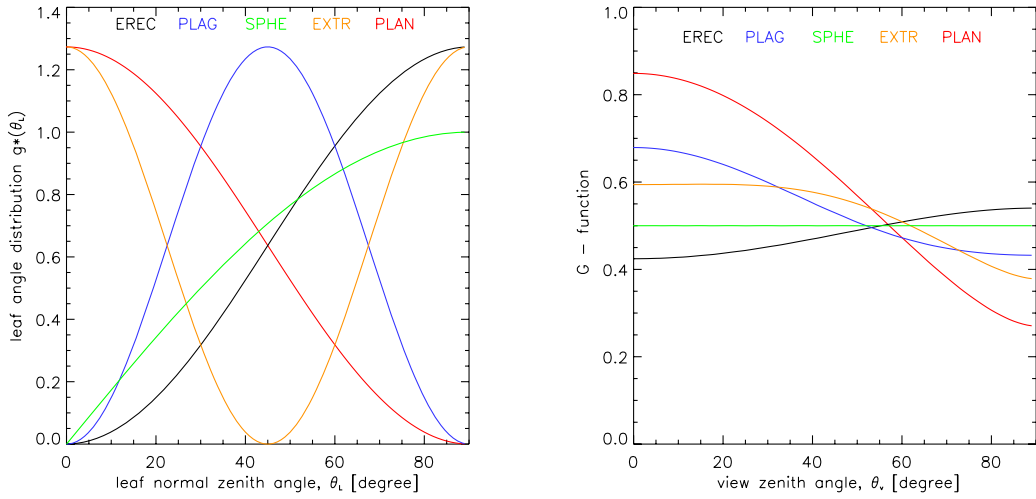


Figure B-1: Left panel: $g_L^*(\boldsymbol{\Omega}_L)$ of the azimuthally independent leaf normal distribution $\boldsymbol{\Omega}_L$ according to Bunnik's formulation. Right panel: mean projection of a unit foliage area in the direction $\boldsymbol{\Omega}$ per unit volume canopy: $G(\boldsymbol{\Omega})$

B-5 The leaf scattering transfer function, $f(\boldsymbol{\Omega}' \rightarrow \boldsymbol{\Omega}, \boldsymbol{\Omega}_L)$

The leaf scattering transfer function $f(\boldsymbol{\Omega}' \rightarrow \boldsymbol{\Omega}; \boldsymbol{\Omega}_L)$, describes the fraction of intercepted energy (from photons that initially travelled in the direction $\boldsymbol{\Omega}'$) that is reradiated from a leaf with outward normal $\boldsymbol{\Omega}_L$) into a unit solid angle about the direction $\boldsymbol{\Omega}$. When integrating $f(\boldsymbol{\Omega}' \rightarrow \boldsymbol{\Omega}; \boldsymbol{\Omega}_L)$ over all exiting direction yields the single-scattering albedo ω_o per leaf (Shultis and Myneni 1988):

$$\oint_{4\pi} f(\boldsymbol{\Omega}' \rightarrow \boldsymbol{\Omega}; \boldsymbol{\Omega}_L) d\boldsymbol{\Omega} = \omega_o \quad (\text{B-14})$$

such that ω_o may depend on both the initial photon direction $\boldsymbol{\Omega}'$ and the leaf normal orientation $\boldsymbol{\Omega}_L$. In the case of isotropic scattering Equation B-14 simplifies to $f(\boldsymbol{\Omega}' \rightarrow \boldsymbol{\Omega}; \boldsymbol{\Omega}_L) = \omega_o/4\pi$. On the other hand, by assuming the leaf scattering phase functions to be Lambertian, the specification of the relative fractions r_L and t_L of the intercepted energy that is to be reflected and transmitted following a simple cosine distribution around the leaf normal, leads to the following formulation of the leaf scattering transfer function (Shultis and Myneni 1988):

$$f(\boldsymbol{\Omega}' \rightarrow \boldsymbol{\Omega}; \boldsymbol{\Omega}_L) = \frac{r_L |\boldsymbol{\Omega} \cdot \boldsymbol{\Omega}_L|}{\pi} \quad (\boldsymbol{\Omega} \cdot \boldsymbol{\Omega}_L)(\boldsymbol{\Omega}' \cdot \boldsymbol{\Omega}_L) < 0 \quad (\text{B-15})$$

$$f(\Omega' \rightarrow \Omega; \Omega_L) = \frac{t_L |\Omega \cdot \Omega_L|}{\pi} \quad (\Omega \cdot \Omega_L)(\Omega' \cdot \Omega_L) > 0 \quad (\text{B-16})$$

where, the photon hits the lower (upper) surface of the leaf if $(\Omega' \cdot \Omega_L) > 0$ ($(\Omega' \cdot \Omega_L) < 0$), and the photon exits from the lower (upper) surface of the leaf when $(\Omega \cdot \Omega_L) > 0$ ($(\Omega \cdot \Omega_L) < 0$), respectively (Pinty and Verstraete 1998). Furthermore the single scattering albedo $\omega_o = r_L + t_L$.

B-6 The area scattering transfer function, $\Gamma(z_k; \Omega' \rightarrow \Omega)$

Shultis and Myneni (1988) define the area scattering transfer function in a canopy where the leaf normal distribution $g_L(z, \Omega_L)$ is independent of depth as:

$$\frac{1}{\pi} \Gamma(z_k; \Omega' \rightarrow \Omega) \equiv \frac{1}{\pi} \Gamma(\Omega' \rightarrow \Omega) = \frac{1}{2\pi} \oint_{2\pi} g_L(\Omega_L) |\Omega' \cdot \Omega_L| f(\Omega' \rightarrow \Omega; \Omega_L) d\Omega_L \quad (\text{B-17})$$

where from Equations B-13 and B-14, one can see that $\Gamma(\Omega' \rightarrow \Omega)$ has to be normalized as follows in the case of $f(\Omega' \rightarrow \Omega; \Omega_L)$ being independent of both Ω' and Ω_L :

$$\frac{1}{\pi} \oint_{4\pi} \Gamma(\Omega' \rightarrow \Omega) d\Omega = \omega_o G(\Omega') \quad (\text{B-18})$$

By introducing the leaf area index L [m^2/m^2] as a new variable ($dL = \Lambda(z) dz$) the radiation transfer equation (B-1) can be rewritten as:

$$-\mu \frac{\partial I(L, \Omega)}{\partial L} + G(\Omega) \tilde{O}(L, \Omega, \Omega_0) = \frac{1}{\pi} \oint_{4\pi} \Gamma(\Omega' \rightarrow \Omega) I(L, \Omega') d\Omega' \quad (\text{B-19})$$

Annex C

Uniqueness of Multiangular Measurements Part 1: An Indicator of Subpixel Surface Heterogeneity from MISR

Bernard Pinty, Jean-Luc Widlowski, Nadine Gobron and Michel M. Verstraete

*Institute for Environment and Sustainability of the EC Joint Research Centre,
TP 440, I-21020 Ispra (VA), Italy*

Abstract: The recent availability of quasi-simultaneous multispectral and multidirectional measurements from space, as provided by the Multiangle Imaging Spectro-Radiometer (MISR) on board the Terra platform, offers new and unique opportunities to document the anisotropy of land surfaces at critical solar wavelengths. This paper presents simple physical principles supporting the interpretation of the anisotropy of spectral radiances exiting terrestrial surfaces in terms of a signature of surface heterogeneity. The shape of the anisotropy function is represented with two model parameter values which may be mapped and interpreted in their own right. The value of one of these parameters also permits identifying geophysical conditions where the surface heterogeneity becomes significant and where three-dimensional radiation transfer effects have to be explicitly accounted for. This paper documents these findings on the basis of results from a number of three-dimensional radiation transfer model simulations. The latter are used to perform an extensive sensitivity study which includes issues related to the scale of investigation. A preliminary validation of these results, conducted with a dataset collected by the AirMISR instrument over the Konza prairie, is also discussed.

C-1 Introduction

The recent availability of quasi-simultaneous multispectral and multiangular measurements from the Along-Track Scanning Radiometer-2 (ATSR-2), the Polarization and Directionality of the Earth's Reflectances (POLDER) and the Multiangle Imaging Spectro-Radiometer (MISR), brings new and unique opportunities to develop and apply operational algorithms that capitalize on the understanding of radiation transfer processes within the atmosphere and vegetation layers, as well as at their interfaces (see for instance Diner et al. 1999, for a series of examples). The primary benefits from multiangular measurements lie in an improved accuracy and reliability of the derived products thanks to the addition of appropriate constraints for identifying the solutions to a series of inverse radiation transfer problems. Although this aspect constitutes, *a priori*, a definite conceptual advantage over algorithms that can be

applied on data strings gathered by single angle sensors, accuracy improvements might not always be systematically required for all geophysical applications. The main issue that will be addressed here is to establish whether and to what extent the acquisition of multiangular data from space permits the assesment of new and unique information on the status of terrestrial surfaces.

This and a companion paper demonstrate that such unique information can in fact be obtained by coupling new approaches with more traditional spectral analyses. This first paper describes the simple physical principles supporting the interpretation of the measured anisotropy of spectral radiances exiting from terrestrial surfaces in terms of a signature of surface heterogeneity at the subpixel scale. The angular distribution of surface leaving radiances exhibits a degree of anisotropy which can be characterized through the parameter values entering the angular function of the RPV model (Rahman et al. 1993b). The degree of anisotropy of these surface radiance fields can therefore be assessed, mapped and interpreted in its own right. The conceptual developments presented in this first paper also demonstrate that one of these parameters has the potential to expose significant surface heterogeneity at the subpixel scale. Beyond information about the heterogeneity of the surface, the value of this parameter also permits identifying geophysical conditions where the three-dimensional radiation transfer effects have to be explicitly accounted for. In a companion paper (Gobron et al. 2001a, hereafter referred to as part 2), we show that the angular domain of measurement can be combined with the spectral domain in order to deliver jointly information about the photosynthetic activity and structure of vegetation: A spectral axis yields a quantitative estimate optimally related to the FAPAR through the combined use of the blue, red and near-infrared spectral bands; a structural axis, independent from the first one, corresponds to the surface heterogeneity parameter optimally retrieved from an analysis of the angular measurements made in the red band only. The approach presented in these two papers has been prototyped for the AirMISR and MISR instruments, providing a good compromise between the desired angular and spectral sampling of the radiance field and the spatial resolution of data acquisition.

C-2 Interpretation of the anisotropy of surface leaving radiance fields

C-2.1 Surface anisotropy as a unique feature

All surfaces, natural or man-made, show some degree of spectral anisotropy when illuminated by a point source of light in the solar domain, *i.e.*, the Bidirectional Reflectance Factors (BRFs) of these media vary with both the illumination and observation angular locations (Martonchik et al. 2000). Since this surface anisotropy depends on the structure and optical properties of the observed medium, it constitutes an angular signature of the target. To the extent that this signature results from the interaction of the radiation field with the medium, a proper understanding of the relevant processes may lead to the characterization of the medium on the basis of remote sensing data. These radiative processes can be modelled and understood using radiation transfer theory and implementing the adaptation necessary to account for specific effects such as specularly and hot spot scattering enhancements (see Pinty and Verstraete 1998). Depending on the application, surface anisotropy can be perceived either as a source of noise, *e.g.*, when developing vegetation indices, or alternatively, as an additional source of information to the spectral dimension since the anisotropy exhibited by surface BRF fields is fully controlled by radiation transfer processes. In the first case, the surface anisotropy effects have to be eliminated to produce information not contaminated by the observation and illumination conditions. In the second case, the anisotropy is exploited with adequate radiation transfer tools to provide better constraints when solving the inverse remote sensing problems. This second alternative allows more parameters to be assessed and therefore enhances the capability of deriving accurate and reliable documentation of geophysical systems from measurements gathered in space (see for instance Gobron et al. 2000a).

Surface anisotropy patterns can adequately be represented by suitable parametric models. These models do not need to be based on or rigorously follow from basic physical principles to the extent that they must only be able to represent the anisotropy effects from a large variety of media in the simplest possible manner, that is with a minimum number of input parameters (Verstraete et al. 1996). The recent developements of multiangle sensors has promoted the refinement of such parametric models (Lucht and Roujean 2000) and two broad families have emerged : the linear-kernel driven models (Wanner et al.

1995) and the RPV model (Rahman et al. 1993b). The former assumes that the spectral BRF fields can be described as a sum of three contributions; the latter, which has a long historical development dating back to early investigations of the scattering properties of celestial bodies, proposes a representation of the same fields on the basis of three parameters entering a product of angular functions. Through its mathematical formulation, the RPV model splits a BRF field into its amplitude component and the associated angular field describing the anisotropic behavior of the surfaces under investigation when illuminated by the Sun, that is:

$$\rho_{sfc}(z_0, \Omega_0 \rightarrow \Omega; \rho_0, \rho_c, \Theta, k) = \rho_0 \check{\rho}_{sfc}(z_0, \Omega_0 \rightarrow \Omega; \rho_c, \Theta, k) \quad (C-1)$$

where Ω_0 and Ω represent the direction of incoming and outgoing radiation, respectively and where ρ_0 and $\check{\rho}_{sfc}(z_0, \Omega_0 \rightarrow \Omega; \rho_c, \Theta, k)$ describe the amplitude and the angular variations of the surface BRF, respectively. This latter quantity is expressed by:

$$\check{\rho}_{sfc}(z_0, \Omega_0 \rightarrow \Omega; \rho_c, \Theta, k) = M_I(\theta_0, \theta; k) F_{HG}(g; \Theta) H(\rho_c; G) \quad (C-2)$$

where:

$$M_I(\theta_0, \theta; k) = \frac{\cos^{k-1} \theta_0 \cos^{k-1} \theta}{(\cos \theta_0 + \cos \theta)^{1-k}} \quad (C-3)$$

$$F_{HG}(g; \Theta) = \frac{1 - \Theta^2}{[1 + 2\Theta \cos g + \Theta^2]^{3/2}} \quad (C-4)$$

$$H(\rho_c; G) = 1 + \frac{1 - \rho_c}{1 + G} \quad (C-5)$$

$$\cos g = \cos \theta \cos \theta_0 + \sin \theta \sin \theta_0 \cos \phi \quad (C-6)$$

$$G = [\tan^2 \theta_0 + \tan^2 \theta - 2 \tan \theta_0 \tan \theta \cos \phi]^{1/2} \quad (C-7)$$

where ρ_c is the hot spot parameter, and where θ and θ_0 are the observation and illumination zenith angles respectively. The relative azimuth angle, ϕ , is zero when the source of illumination is behind the sensor.

Engelsen et al. (1996) report in detail on the performance and limits of applicability of this parametric model. The angular function $M_I(\theta_0, \theta; k)$, *i.e.*, the so-called modified Minnaert's function (Minnaert 1941), permits the mathematical representation of the overall shape of the angular field through the parameter k . Specifically, k is close to 1.0 for a quasi Lambertian surface (very limited angular variations in the spectral BRF field), k is lower than 1.0 when a bowl-shape pattern dominates (the spectral BRF values increase with the view zenith angle) and, conversely, k is greater than 1.0 when a bell-shape pattern is observed (the spectral BRF values decrease with the view zenith angle). The other angular functions controlling Equation C-2 are adding more complexity/flexibility to the anisotropy classes described above; they allow the accounting for asymmetrical shapes around the local normal to the sampled area, due to the possible imbalance between the backward and forward scattering regions, as well the backscattering enhancement due to the hot spot effect. $F_{HG}(g; \Theta)$ is based on the Heney-Greenstein function (Heney and Greenstein 1941), and the parameter Θ establishes the degree of forward or backward scattering, depending on its sign.

A recent article by Pinty et al. (2000a) revealed that maps of the parameter k derived from an analysis of Meteosat data exhibit spatially consistent fields and features corresponding to known gradients in surface types which may or may not be represented by variations in the amplitude component of the BRF fields. It strongly suggests that the parameter k can be used as one additional and possibly independent axis of information to better identify and separate various surface types than is feasible on the sole basis of spectral measurements. This preliminary statement does not constitute, in itself, a new finding since, for instance, the analysis of low resolution Nimbus 7 data acquired during the Earth Radiation Budget experiment already showed that different anisotropic factor values can be assigned to different cloud and broad surface types (see for instance Jacobowitz et al. 1984). One can thus easily foresee that, thanks to their capability to measure quasi-instantaneously the angular radiance fields emerging at the top of the atmosphere, multiangle instruments such as POLDER, ATSR and MISR should improve the identification of surface types through the unique assessment of their individual surface anisotropy. For instance, maps of the ρ_0 and k parameters obtained by inversion of the RPV model at various wavelengths can be ingested by classification techniques to produce revised land cover maps and better detect changes

occurring at the surface. We may anticipate that such exercises will soon become quite frequent due to the operational availability of such surface anisotropy information (Martonchik et al. 1998b). It is thus important to understand how the anisotropic signature of geophysical media can be interpreted and, in particular, what practical information could be derived from simple parameterizations such as the one used here.

C-2.2 Anisotropy pattern as an indicator of surface heterogeneity

The parameter k of the RPV model plays a fundamental role in representing the anisotropy of the surface:

- $k < 1.0$ corresponds to a bowl-shape anisotropy pattern where BRDF values close to nadir are lower than for larger exiting angles,
- $k = 1.0$ corresponds to a Lambertian surface, an idealized case rarely found in practice, and
- $k > 1.0$ corresponds to a bell-shape anisotropy pattern where BRDF values measured at large exiting angles are lower than those measured at angles close to nadir.

The vast majority of terrestrial surfaces, whose anisotropy patterns have been investigated using laboratory, field, or airborne measurements, exhibit a bowl-shape anisotropy pattern. Models describing the scattering of light by homogeneous plane-parallel turbid geophysical media also typically generate this type of anisotropy pattern. Indeed, under such conditions, radiative transfer theory and, in particular, the multiple scattering component, predicts an increase of the BRDF values together with the exiting zenith angle. This situation is also generally observed for closed (large values of the leaf area index) homogeneous plant canopies, bare soils and other planetary surfaces as well.

Observations of bell-shape anisotropy patterns have been occasionally reported in the literature (see for instance Ni and Jupp 2000 and Gerard and North 1997). It is thus interesting to investigate under which conditions this type of anisotropy occurs. A class of geophysical systems that exhibit a higher reflectance when observed from above than at large zenith angles can easily be conceived of: consider, for example at red wavelengths, a sparse coniferous forest over a snow-covered field, or sparse bushes over a bright sandy desert. In such cases, the high background reflectance dominates at small observation zenith angles, while the absorbing properties of the dark objects control the reflectance of the entire scene at large angles. These BRDF fields should therefore exhibit a bell-shape pattern corresponding to k values greater than 1.0 when analyzed with the RPV model.

A few critical remarks are in order at this point:

- If the density of the dark vertical structures increases sufficiently, the reflectance field of the system will tend towards that of a fully covered but “homogeneous system” of such structures, and the anisotropy pattern will be bowl-shaped.
- If the density of the dark vertical structures decreases to low values, the bright underlying surface will control the anisotropy of the scene at all angles, and the reflectance will also tend to correspond to a bowl-shape.
- Only rather heterogeneous geophysical systems composed of relatively sparse dark vertical structures over a bright background can lead to anisotropy patterns characterized by a bell-shape.

In fact, it is the main thesis of this paper that a bell-shape anisotropy pattern over vegetated surfaces characterized by $k > 1.0$ likely identifies heterogeneous systems composed of sparse dark vertical structures over a relatively brighter surface at the subpixel spatial resolution. This numerical condition can thus be considered as an indicator of surface anisotropy in the sense described above. This, however, does not imply that all forms of heterogeneity will result in a bell-shaped anisotropy pattern. Incidentally, whenever heterogeneity is detected in the sense of this protocol ($k > 1.0$), the principle of reciprocity will likely not be valid. The implications of this fact will be discussed later.

The essence of our interpretation lies in the presence of vertically distributed absorbing material (*e.g.*, vegetation at the red wavelength because of the presence of strongly absorbing chlorophyll bands) overlying a brighter (more reflecting or less absorbing) interface or lower boundary condition (*e.g.*, the vast

majority of soils at the red wavelength). Actual situations are of course very complex: the reflectance of each pixel of a heterogeneous system viewed from the nadir depends on competing factors such as the intrinsic optical properties of the scene elements but also the presence of shadows induced by the vertical stands. However, it should be noted that even one-dimensional models, simulating the radiation transfer regime in vegetation canopies, can generate bell-shaped anisotropy patterns, if the former explicitly account for the finite-size of the elementary scatterers, *i.e.*, the leaves. This may occur when the model input variables are set up to represent, for instance, open (low values of the leaf area index) canopies specially under conditions where the leaf angle distribution favors an erectophile leaf orientation: the heterogeneity of the canopy system is, indeed, inherent to the presence of finite-size oriented leaves. The same conclusion applies for bare soils exhibiting significant roughness that will create well-marked shadows.

For all practical purposes and considering typical values for the vegetation architectural attributes, a medium spatial resolution sensor (a few tens to hundreds of meters) has the potential to expose subpixel scale surface heterogeneity controlled by the presence of clumped vegetation as is the case for open forest and woodland ecosystems. A high spatial resolution sensor (a few tens of centimeters) may reveal a similar degree of heterogeneity when sensing a plant canopy system because of the effects intrinsic to the presence of finite size leaves. Various scales of heterogeneity could then be introduced depending on the sensor spatial resolution, from the microscale (ensemble of leaves) to the medium scale (ensemble of trees) or even larger scales (ensemble of landscapes).

Figure C-1 illustrates the evolution from a quasi one-dimensional to a complex three-dimensional radiative transfer regime due to the significant impact of horizontally distributed vertical structures occurring in the latter case. The top panels provide a visualization of a simulated quasi one-dimensional scene (top left) together with the corresponding BRF values generated in the cross plane (top right), *i.e.*, the plane perpendicular to the principal plane. These BRF values are calculated using a Monte-Carlo ray-tracing model developed by Govaerts and Verstraete (1998) (red line) and the model from Gobron et al. (1997c) applicable for one-dimensional horizontally infinite canopy scenes (green line). In the latter case, the total BRF field emerging from the scene is approximated with a linear mixing of the respective contributions due to the vegetated and bare soil domains composing the scene, *i.e.*, it follows the Independent Pixel Approximation (IPA) scheme promoted by Cahalan et al. (1994b) in the case of cloud scenarios. In this first scenario, the leaves are concentrated and grouped in one part of the scene and, thus, the heterogeneous three-dimensional effects between the canopy and the bare soil are limited to the single straight boundary separating these two media in the horizontal plane. Therefore, since both models by Gobron et al. (1997c) and Govaerts and Verstraete (1998) have already been shown to produce very accurate and reliable solutions in the simulation of the BRF fields in 1-D cases, respectively (Pinty et al. 2001a), they generate essentially similar and thus undiscernible averaged BRF fields.

By contrast, the bottom panels of Figure C-1 show a geophysical situation where the three-dimensional effects are enhanced due to the regrouping of the leaves into clumps scattered throughout the scene. In this second, architecturally more complex scenario, the BRF values are accurately estimated using the Monte-Carlo ray-tracing model (Pinty et al. 2001a).

It is noteworthy that the only difference between the two scenarios lies in the spatial distribution of the leaves in the scene, *i.e.*, the Leaf Area Index (LAI), the spectral and geometrical properties of the leaves and the soil are all set at the same values in both experiments. This structural difference, discernable through the occurrence of vegetation clumps, is, however, at the origin of a significant change in the resulting BRF values and shapes. Indeed, the BRF anisotropy patterns evolve from a bowl-shape in the quasi one-dimensional scenario to a bell-shape when three-dimensional effects become more significant. As a matter of fact, the inversion of the RPV model (following the simple procedure described in Gobron and Lajas (2001) and summarized in the appendix of part 2) against these two simulated BRF strings result in mean values for the parameter k equal to 0.65 (top panel) and 1.18 (bottom panel), respectively.

Results from these simulation scenarios reinforce the suggestion that the k parameter of the RPV model can be further interpreted as a heterogeneity indicator controlled by the occurrence of vertical structures. Although a surface application is considered here for the sake of explanation, a similar rea-

soning can be applied for different geophysical systems showing the required elements and for which the BRF field can be sensed at the appropriate wavelength. According to our conceptual approach, it should be enough for the parameter k to exceed the threshold value 1.0 to indicate reliably the occurrence of significant surface heterogeneity at the subpixel scale. In practice, this threshold becomes a transition zone around the value 1.0 because the inversion procedure often delivers a range of values for the parameter k , *i.e.*, there is often no unique solution, and also because of errors on the retrieved values themselves due to uncertainties on the surface BRF fields. This particular issue is addressed and documented in the next section.

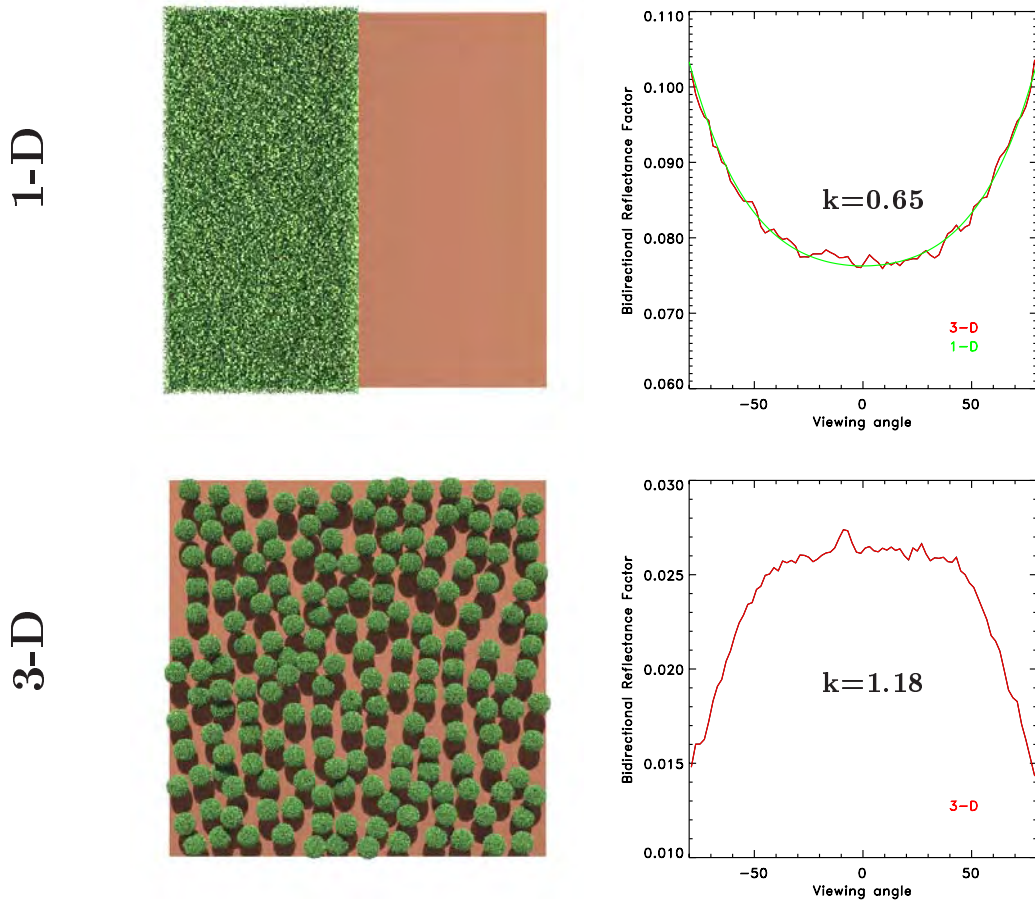


Figure C-1: Typical angular signatures of the BRF field in the red spectral region emerging from quasi one-dimensional (top panels) and three-dimensional (bottom panel) vegetation scenes. Both scenes are composed of identical leaf and soil material exhibiting exactly the same radiometric properties in the two experiments. The scene leaf area index is equal to 4 in both cases. The left panels provide an artistic view of the scenes and the right panels show the corresponding BRF field derived from model calculations in the cross plane. In the right panels, the red (green) lines correspond to the BRF generated by the 3-D (1-D) model.

C-2.3 Potential and limitation in the exposure of surface heterogeneity

Considering further the generic case of an open vegetation layer sensed at the red wavelength it can, therefore, be logically expected that:

- too sparse a vegetation system may not lead systematically to $k > 1.0$ conditions: there might not be enough vegetation to compensate, at large view angles, for the BRF increase due to the illuminated soil in between the vegetation elements. This system could, in fact, be almost indistinguishable from a plane-parallel system, in the sense that the BRF fields estimated with the IPA are extremely close to those obtained with the full three-dimensional model, except in the vicinity of the hot spot angular region.

- too dense (closed) a vegetation system will also hardly translate into $k > 1.0$ estimation: the heterogeneity might not be significant enough to create a detectable BRF increase signature at angles close to nadir, *i.e.*, the latter might always be masked by the shadowing effects. As in the previous case, we may in fact deal with a system that could satisfy the usual plane-parallel assumption from a radiation transfer point of view.

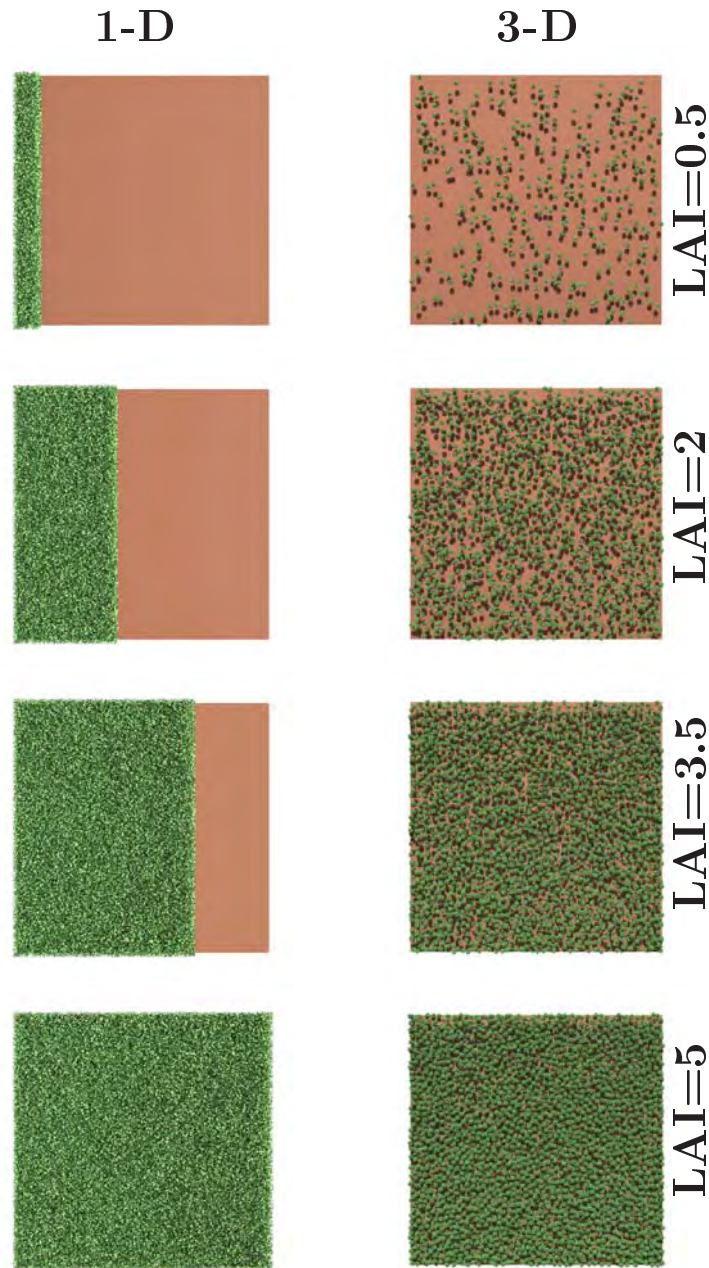


Figure C-2: Visualization of a sample of the series of 11 scenes idealizing the quasi one-dimensional (left panels) and corresponding three-dimensional (right panels) scenes for various values of the Leaf Area Index.

In order to assess our expectations, we replicated the numerical experiment presented in Figure C-1 for 11 different scenarios, simulating the effects of a progressive increase in LAI and, thus of the fractional vegetation cover of the scene. A sample of the corresponding quasi one-dimensional (1-D) and full three-dimensional (3-D) scenes can be visualized in Figure C-2, and detailed information regarding the structural and radiative properties of the scenes are provided in Tables C-1, C-2 and C-3. As already mentioned when presenting results from Figure C-1, the only changes occurring in the characteristics of

the scenes between the quasi 1-D and the 3-D concern the spatial distribution of the leaves into spherical clumps. As a matter of fact, for a given scene, quantities such as LAI are conserved independently from the strategy adopted to spatially distribute the scattering elements. The geometrical projection of the spheres onto the ground can be seen in Figure C-2 specially for scenes implementing low LAI conditions¹. In the following, and as suggested from results shown in Figure C-1, the BRF fields emerging the quasi 1-D scenes were approximated using the model by Gobron et al. (1997c) together with an IPA scheme. In the case of the 3-D scenes, the model from Govaerts and Verstraete (1998) was applied to simulate the BRF fields at the resolution of the scene.

Table C-1: Variables defining the leaf and soil spectral properties

| Variable identification | Values |
|-------------------------|--------|
| Leaf reflectance † | 0.0546 |
| Leaf transmittance † | 0.0149 |
| Soil Lambertian albedo | 0.1270 |

† Using a bi-Lambertian scattering law.

Table C-2: Variables defining the structure of the quasi 1-D scenes

| Variable identification | Values |
|--|--|
| Height of the canopy | 15 m |
| Equivalent leaf diameter | 0.05 m |
| Leaf Angle Distribution | uniform |
| Scene Leaf Area Index (LAI) | 0.05 and from 0.50 to 5.0 in steps of 0.50 m ² /m ² |
| Ground fraction covered by vegetation | 0.01 and from 0.10 to 1.0 in steps of 0.1 |

Table C-3: Variables defining the structure of the 3-D scenes

| Variable identification | Values |
|--|---|
| Sphere diameter | 5 m |
| Leaf Angle Distribution | uniform |
| Leaf Area Index of the spheres | 5 m ² /m ² |
| Maximum height of the canopy | 16 m |
| Minimum height of the canopy | 4 m |
| Scene Leaf Area Index (LAI) | same as in Table C-2 |
| Ground fraction covered by vegetation | 0.01, 0.09, 0.17, 0.26, 0.34, 0.41, 0.49, 0.55, 0.61, 0.66, 0.71 |

The inversion of the RPV model was performed against the simulated BRF fields for these two ensembles of 11 scenes, each scene being considered separately, and the three RPV model parameters were

¹Architectural parameters imposed in Table C-3 may generate full circular shadows onto the ground since the spheres are allowed to “float” between predefined lower and upper levels.

thus optimally retrieved with their corresponding uncertainty levels. Figure C-3 (left panel) shows the mean and the associated uncertainty values obtained for the parameter k in the case of both the quasi 1-D and 3-D scenes, when the direct illumination source is located at 30° zenith angle, as a function of the LAI of each scene such as illustrated in Figure C-2. As could be expected from the preceding qualitative reasoning, this Figure demonstrates the potential to document the structural heterogeneity of the scenes through the value of the parameter k . Indeed, while this parameter takes on values close to unity for both low and high vegetation cover conditions, its values clearly rise to much larger values at intermediate situations, where the heterogeneous effects are maximized by the clumping of leaves into spheres. By contrast, the values of the parameter k remain within the same range, typically from 0.9 to 1.05, independent of the vegetation cover, for the associated quasi 1-D scenes. Variations in the spectral and architectural properties of the vegetation attributes may yield different relationships between the leaf area index of the scenes and the values of the parameter k . The same result holds for different Sun angle conditions as mentioned already in section C-2.2. Nevertheless, the presence of significant heterogeneity (in the 3-D scenarios) will translate into larger k values than would be retrieved from limited heterogeneity (idealized by the quasi 1-D scenarios) situations. Figure C-3 shows that such structural heterogeneity can be exposed over a broad range of realistic leaf area index conditions.

Other sets of analogous Figures can be drawn using other quantitative variables to represent the type of scene as there is always some degree of correlation between the type of scene and, for instance, the LAI of the scene, the fractional cover, as well as the fraction of radiation absorbed by the vegetation. For instance, the right panel of Figure C-3 displays the variation of the k parameter for the quasi 1-D and associated 3-D scenes, as a function of the fraction of radiation absorbed by the vegetation elements composing the scenes. The use of the latter variable to define the x -axis permits us to represent the dependency of the value of the parameter k with respect to a physical quantity characterizing the vegetation. This approach is exploited in the accompanying paper.

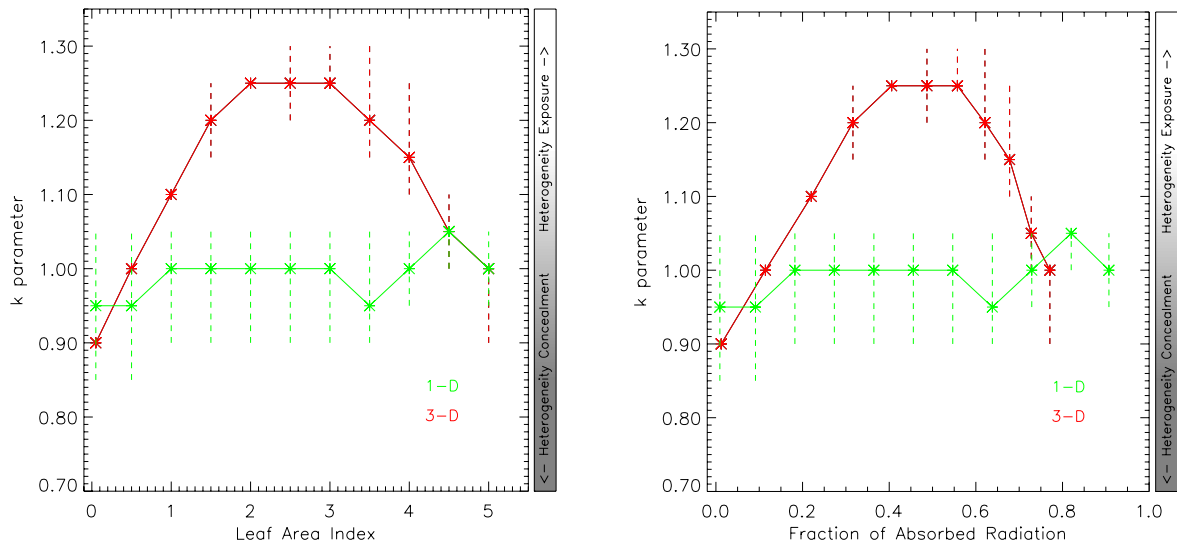


Figure C-3: Variations of the values of the k parameter as a function of the Leaf Area Index (left panel) and the associated Fraction of Absorbed Radiation (right panel) for each individual scene, respectively. The k values are obtained by inversion of the RPV model in the case of quasi one-dimensional (green color) and corresponding three-dimensional (red color) scenes. The input BRF values are those corresponding to the radiative transfer model results derived for each scenes represented in Figure 2. The vertical bars indicate all the possible values for the k parameter which can provide an acceptable fit to the modelled BRF in each case.

These results, obtained from a number of accurate model simulations and based on simple physical reasoning, demonstrate the potential for extracting unique information about structural heterogeneity of the terrestrial surfaces when sensed simultaneously at various viewing geometries and at the appropriate wavelength and spatial resolution. As explained at the beginning of section C-2.2, the wavelength should be chosen so as to maximize the reflectance/absorption contrast between the vertically clumped elements

and the background while the viewing geometries must permit a reliable inversion of the RPV model for the retrieval of the parameter k . Based on these considerations, there is an ensemble of spectral, structural, illumination and spatial scale aspects that will reveal heterogeneous scenes at a given sensor spatial resolution. These aspects are investigated in a quantitative manner in the next sections describing results obtained when performing a sensitivity analysis of the variations of the parameter k value with respect to changes in the brightness of the background, solar zenith angle, and spatial scale of investigation.

C-3 Sun angle and background brightness effects

Following the qualitative reasoning proposed in the previous section, one can thus anticipate that the larger the spectral contrast between the soil and the vegetation (to increase the angular BRF variations between close to nadir and large view angles), and the smaller the Sun zenith angle (to limit the darkening effects of shadows) the more favourable the conditions leading to the observation of k values significantly greater than 1.0.

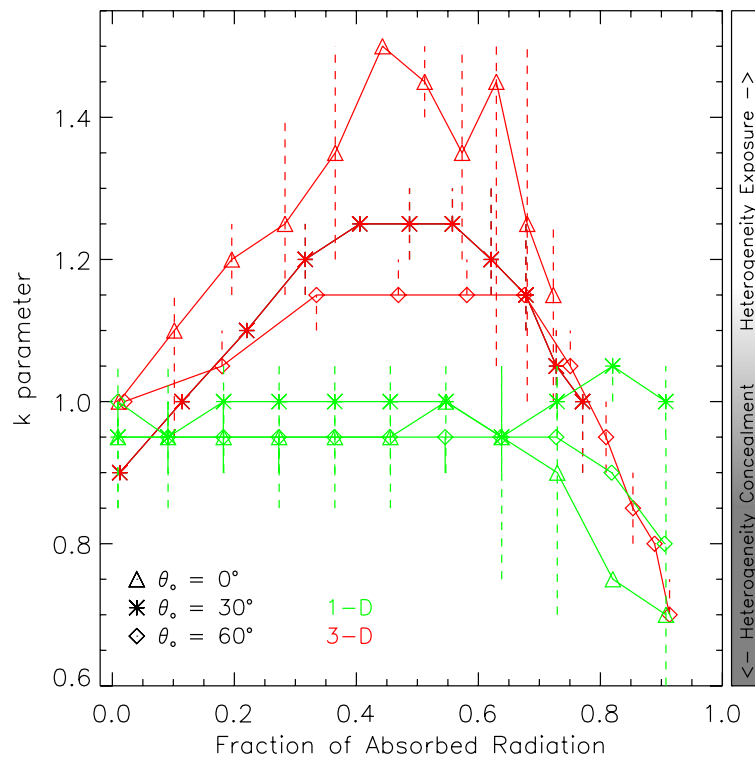


Figure C-4: Variations of the k parameter values as a function of the fraction of absorbed radiation for Sun zenith angle equal to 0° (triangles), 30° (stars) and 60° (diamonds), respectively. Results obtained for the quasi one-dimensional and the corresponding three-dimensional scenes are identified with green and red colors, respectively. The vertical bars indicate the range of possible values for the k parameter that can provide an acceptable fit to the modelled BRF in each case.

The combined effects of changing background reflectance and illumination geometry on the retrieved values of k (or, equivalently, on the bowl or bell shape of the anisotropy) are illustrated in Figures C-4 and C-5 for various types of scenes. Specifically, Figure C-4 exhibits the results obtained by replicating the simulations achieved in the previous section (see Figure C-2 for quasi 1-D and 3-D scenes, respectively) for Sun zenith angle values successively equal to 0° , 30° and 60° . Results shown in Figure C-4 indicate that, as expected, the values of the parameter k decrease with an increase of the Sun zenith angle: the reflectance of the background soil between the vegetation clumps becomes dominated by shadows and cannot deliver large BRF values even for viewing conditions close to nadir. This Figure shows that when the illumination angle becomes as high as 60° , the projected clump shadows are significant enough to damp the large values of the k parameter that would normally be associated with heterogeneous struc-

tures, for the spectral and architectural conditions prescribed in these simulations. By contrast, the quasi 1-D scenes are characterized by values which are always close to the 1.0 critical threshold, and under these conditions, the scene heterogeneity remains concealed.

In the same vein, the three panels in Figure C-5 display the variations in the values of parameter k estimated for three different Sun zenith angles, namely 0, 30 and 60°, and three typical Lambert soil albedo values, namely 0.055 (dark), 0.127 (medium) and 0.242 (bright) (see Price 1995). It can be seen that, independent from the Sun zenith angle, the brighter the soils, the larger the k parameter values, *i.e.*, the easier it is to identify the presence of strongly heterogeneous surfaces. The observed trends followed by the k parameter values due to changes in Sun zenith angle support the findings already discussed on the basis of Figure C-4. It is noticeable that, for Sun zenith angles larger than 30°, a dark soil condition does not allow the anisotropy to exhibit a bell-shaped pattern, even though heterogeneity is present. By contrast, even a medium bright soil condition is sufficient for the faint bell-shaped anisotropy to betray the existing heterogeneity with low Sun conditions (see right panel). These simulated experiments are conducted using various soil brightness conditions for the purpose of illustrating the sensitivity of the parameter k with respect to changes in the spectral contrast between the vertical structures and the background. However, any geophysical situation exhibiting such spectral contrast would yield analogous results, independently from the intrinsic nature of both the background and the vertical elements, *e.g.*, a snow blanket underneath a coniferous forest.

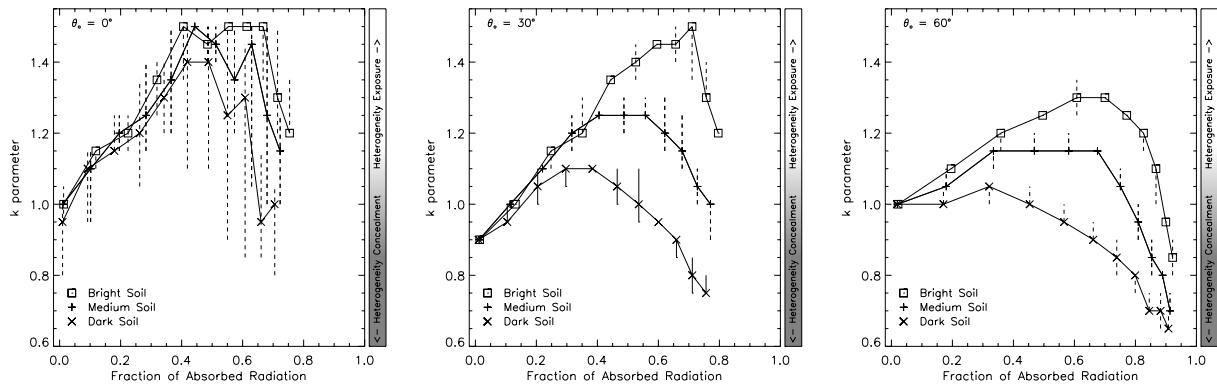


Figure C-5: Variations of the k parameter values as a function of the fraction of absorbed radiation in the case of a bright (square symbol), medium (plus symbol) and dark (cross symbol) soil albedo, respectively. Panels a, b and c show results obtained for illumination zenith angle equal to 0°, 30° and 60°, respectively. The vertical bars indicate the range of possible values for the k parameter which can provide an acceptable fit to the modelled BRF in each case.

Although these results are based on a particular architecture for the specification of the 3-D heterogeneous scenes, *i.e.*, a random distribution of vegetated clumps in the horizontal space, realistic soil and vegetation characteristics have been used; there is, therefore, a genuine potential to actually detect in a simple manner, on the basis of the k parameter value, the occurrence of a class of heterogeneous targets, specifically those made up of dark vertically oriented architecture over a bright background. Since such spectral contrasts often occur in nature, these findings open new opportunities to characterize the heterogeneity of terrestrial ecosystems at the sub-pixel level, for a range of scales.

C-4 Application

The potential to detect structural signatures from BRF measurements is a scale dependent issue and is therefore a function of the spatial resolution of the observing instrument. Accordingly, for a given land terrestrial system, the retrieved value of the k parameter will strongly depend on the spatial scale of investigation, and the higher the spatial resolution, the more opportunities exist to expose radiatively heterogeneous systems at the subpixel resolution, specially in the case where large vertical structures are present, *e.g.*, forest canopies. The scale dependent problem of the heterogeneity exposure with respect to the sensor resolution renders the demonstration of its detectability from an assessment of the parameter

k at once easy and difficult: on the one hand, it is relatively easy by choosing a set of favourable spectral and architectural conditions that can be kept under control at the laboratory scale, *i.e.*, a few tens of centimeters, which, however, does not correspond to the spatial resolution accessible from space remote sensing; on the other hand, although the analysis of multiangle measurements taken from space may suggest the occurrence of heterogeneous conditions, the demonstration of the intrinsic links between the architecture of the vegetation cover and the k parameter values remains difficult to illustrate, even with simple photographic support, due to the spatial resolution of the sensors, *i.e.*, a few hundred of meters or more.

The AirMISR instrument does, however, permit accessing an intermediary spatial resolution (the nominal spatial resolution on the ground of the map-projected product is 27.5 m) which could be large enough to demonstrate the desired mechanism in the field and small enough for this mechanism to be supported from simple ground investigation. This instrument, extensively described in Diner et al. (1998a), was flown by the NASA ER-2 aircraft at an altitude close to 20 km, under almost cloud-free conditions, over the Konza prairie site in Kansas on July 13, 1999 around noon.

Two special processing steps were applied on the map-projected AirMISR data. The first step was a first-order atmospheric correction. Based on Reagan sunphotometry, an aerosol optical depth of 0.135 in the green band was established, and a clean continental aerosol model consisting of 90% (by optical depth fraction) accumulation mode sulfate at 70% relative humidity, and 10% accumulation mode mineral dust was assumed and provided the atmospheric parameters needed to perform the surface retrieval. A surface pressure of 964.3 hPa was used to establish the Rayleigh scattering optical depth. Climatological atmospheric parameters such as ozone abundance were taken from the Terrestrial Atmosphere and Surface Climatology, or TASC dataset, which is an ancillary file set in conjunction with MISR standard data processing. Quantities needed for the radiative transfer calculation were derived from a look-up table generated to support MISR processing, known as the Simulated MISR Ancillary Radiative Transfer, or SMART, dataset (Diner et al. 1997).

The atmospheric correction was done on a camera-by-camera and band-by-band basis, and for this purpose the surface reflectance at angles not observed by the individual camera was assumed Lambertian. This method does not distinguish between the Hemispherical-Directional Reflectance Factor and the Bidirectional Reflectance Factor. The surface BRDF was retrieved by first correcting for ozone absorption, subtracting off the path radiance, dividing by atmospheric direct and diffuse transmittance, and correcting for multiple reflections between the atmosphere and surface assuming reflectance homogeneity. The retrieved surface BRDF was converted back to an equivalent radiance and the results were written out to AirMISR data files in the same format as the original data. The second processing step consisted of a pixel by pixel geometric remapping to improve the camera co-registration. The nadir image was used as a reference, and the Multipoint Matcher (M2) area matching algorithm developed for MISR stereo processing was used to determine the misregistration between each off-nadir camera and the nadir data (Diner et al. 1997). Nine by nine pixel patches were used for the area matcher. For each pixel a cross-track and along-track misregistration, or disparity (in pixels) was determined. A smoothing algorithm consisting of a box filter was passed over the resulting disparity fields to eliminate blunders and fill in areas where the matching failed. The resulting disparity field was then used to “warp” the off-nadir imagery and a new data file consisting of the remapped data was written. For each camera, this processing was done band by band. Additional data fields containing the disparities were written to the data products for the off-nadir cameras.

For the purpose of our investigation the surface-level BRDF dataset will be considered as if it were taken just above the surface without any corruption by atmospheric scattering effects. This dataset was further analyzed with the help of the RPV model in order to estimate, at the pixel resolution, the values of the parameter k .

Figure C-6 shows the map of the parameter k_{red} estimated in the red band, *i.e.*, the spectral band which maximizes the single scattering effect as well as the required reflectance contrast between the soil and the vegetation. This map identifies a number of well-defined patterns which are directly related to the organization of the landscapes, *i.e.*, some of the agricultural, pasture and other lands can be easily

identified on the basis of the values depicted by the k_{red} parameter. As can be seen from the color convention adopted for the anisotropy shape parameter, some of these fields can be classified with respect to their bowl or bell-shape anisotropy pattern. A ground inspection of a number of these fields was conducted just about a year after the AirMISR data acquisition. It confirmed that the fields characterized by a bell-shaped anisotropy pattern exhibited some significant degree of heterogeneity at the scale of a few tens of meters. By contrast, a bowl-shape type of anisotropy was associated with those fields which do not exhibit strong vertical structures and 3-D heterogeneity at the scale of the AirMISR measurements. These features are qualitatively illustrated with the help of a series of photographs taken from the ground over a sample of the Konza fields (see Figure C-7 and further description in Table C-4). A significant degree of heterogeneity, *i.e.*, openings between vertically oriented and dense vegetation cover, was observed for non-mature maize fields as well as other more complex land surface types, indicating that the detected heterogeneous behaviour originates from very different types of land cover. Targets identified as A and E provide good examples of the exposure of heterogeneity due to a strong contrast between the dense vertical vegetated structures and the bright soils which can be seen in the gaps between vegetation. An analogous situation occurs for the growing maize field, target B and C for instance; it can reasonably be anticipated that the heterogeneity will be progressively concealed (*i.e.*, k values should decrease) as plants grow to close the canopy. By contrast, at the scale of the AirMISR pixels, the pasture fields (*e.g.*, target F) which are not contaminated by significant vertical structures are characterized by a bowl-shaped anisotropy. Target D shows a case where the structural heterogeneity apparent from the photograph is not exposed by the analysis of the angular signature of the BRF field in the red domain, *i.e.*, the value of k is close to 0.8; this result suggests that the coverage by green vegetation (instead of bright soil) of the horizontally wide gaps (with respect to the AirMISR spatial resolution) does not favor the detection of structural heterogeneity.

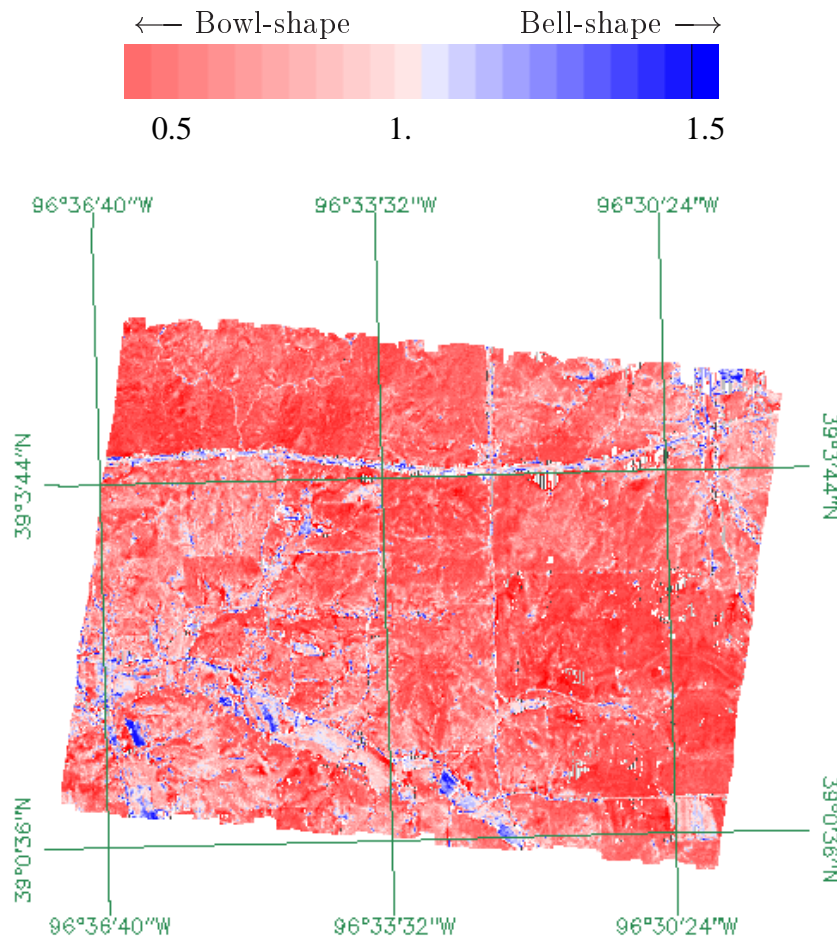


Figure C-6: Map of the parameter k_{red} obtained from an inversion of the RPV model against “surface BRF” data collected in the red band of the AirMISR instrument over Konza prairie on July 13, 1999. This BRF dataset was derived using a simplified atmospheric transfer scheme. The color code goes from red tones for low k values to blue tones for large k values and the intermediate white colors indicate pixels exhibiting values close to unity for the parameter k .

At this preliminary stage of investigation, the quantification of the degree of heterogeneity remains an open issue. Nevertheless, the visual assessment of surface heterogeneity which can be made on the basis of this series of photographs confirms our expectations derived from simple reasoning and supported by extensive radiation transfer model simulations.

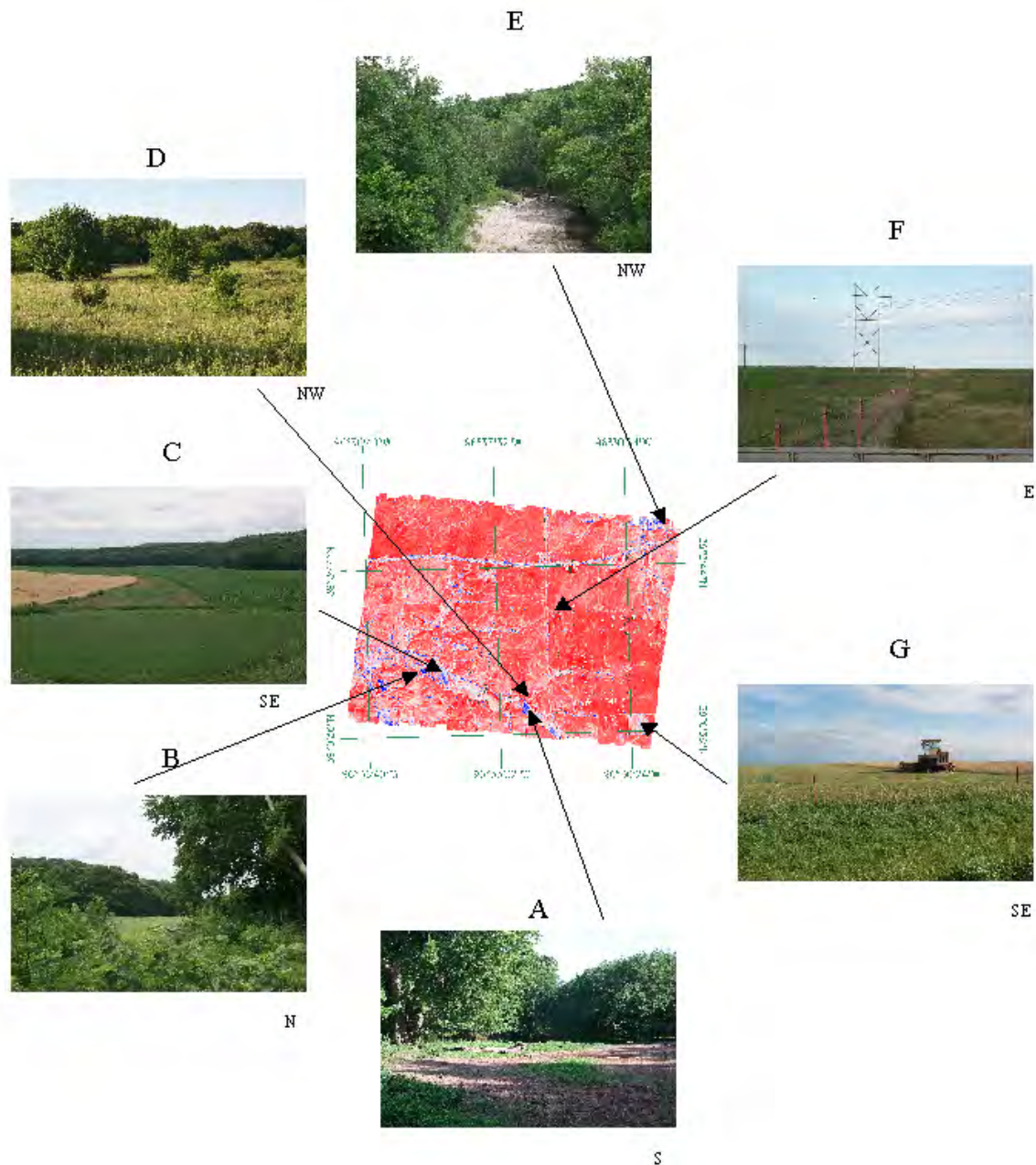


Figure C-7: Photographs illustrating the state of the landscapes over Konza prairie on June 7, 2000. The labelling permits co-locating the photographs with respect to the corresponding value of the parameter k_{red} mapped in figure C-6. The approximate orientation of the views displayed are indicated below each photograph, *i.e.*, N, S, E and W stand for northward, southward, eastward and westward directions, respectively.

The dependency of the estimated values for the parameter k with respect to the resolution of the observing instrument can be examined on the basis of the AirMISR dataset. Indeed, in a first approximation, the local BRDF values available from surface level BRDF dataset can be iteratively aggregated in order to approximate BRDF values that would have been measured by the same sensor but at different spatial resolutions. The upscaling process is achieved by calculating, from the original resolution of 27.5

m, the average values over windows of 2×2 , 4×4 , ..., 32×32 pixels. This procedure thus permits relating the changes of the values of the parameter k against the sensor ground resolution. The series of panels in Figure C-8 display the results of such an upscaling approach when applied to the parameter k_{red} . The progressive increase in the redish hue observed from the top left to bottom right panel confirms our expectation on the scale dependency, *i.e.*, the lower the sensor resolution and the lesser its potential to expose the heterogeneous features invoking the 3-D organization of well-identified surface cover types. The spatial dimensions involved in this exercise, *i.e.*, from ≈ 30 up to 900 meters, are indicative of the expected spatial scale and sensor resolution beyond which the angular signatures can hardly be used to detect a significantly heterogeneous situation even under favourable geophysical conditions.

Table C-4: Target descriptions from the series of photographs in Figure C-7.

| Target | Description | Land category [†] from k values |
|--------|--|---|
| A | Bare soil clearing, used by cattle, in a wooded area | bell-shape |
| B | Clearing used for maize cultivation in a wooded area | bell-shape |
| C | Transitions between senescent cereals (left), maize (middle) and full cover crop (right) | bell-shape for the maize field only |
| D | Natural meadow with shrubs | bowl-shape |
| E | Dry riverbed with shrubs | bell-shape |
| F | Two fields of permanent pasture separated by a fence | bowl-shape on both side of the fence |
| G | harvested and unharvested forage (background) | bell-shape for the harvested part only |

[†] Bowl-shape (bell-shape) is assigned to pixels exhibiting k values belonging to the heterogeneity concealment (exposure) domain.

C-5 Miscellaneous issues

The concepts developed in this paper elicit further remarks on various related issues concerning both fundamental aspects of radiation transfer problems and immediate applications to the characterization of land surface properties, especially in the case of medium resolution sensors. The following issues arise in those regions detected as heterogeneous in the sense defined above:

- there is a discernable breakdown of the reciprocity principle due to the deviation from an homogeneous turbid plane-parallel system (see Chandrasekhar 1960). The application of models satisfying this basic principle must therefore be conducted with care since, for instance, the use of these models against data strings acquired under various illumination conditions is not strictly valid. However, these models can be applied for the analysis of BRDF fields sampled under a constant illumination angle. This conclusion is obviously not specific to the RPV model used here, but it holds for all models of this category.
- the spatio-temporal variations of the parameter k are partly controlled by the direction of illumination with respect to the target (see Figure C-5). Therefore, the value of this parameter cannot

be interpreted directly as if it were an intrinsic surface property, *e.g.*, the value of the parameter k may vary as a function of the season. However, a single instantaneous multiangular set of measurements may be sufficient to expose the heterogeneity of the region at the scale of investigation and to select further appropriate processing schemes.

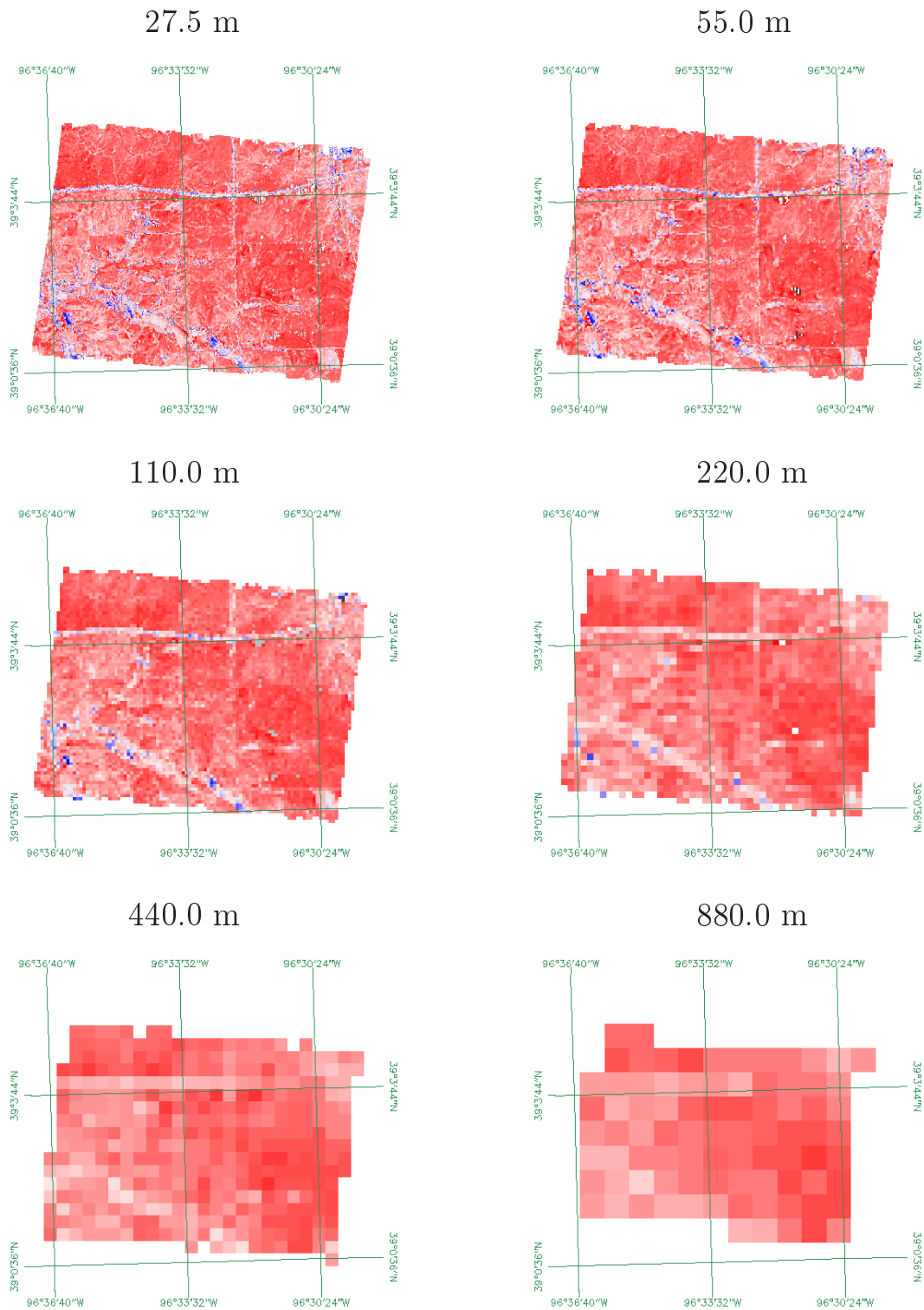


Figure C-8: Maps of the parameter k_{red} derived from an iterative aggregation the “surface BRF” data collected in the red band of the AirMISR instrument over Konza prairie on July 13, 1999. Conventions are the same as in Figure C-6. The simulated sensor resolution indicated on top of each panel decreases from the top left to the lower right panel.

- the acquisition of instantaneous BRF values by single angle view instruments, as available from most of the medium resolution scanning sensors, may fail in delivering accurate and reliable estimates of surface albedo when the algorithm emulates multiangular sampling from a sequential accumulation of BRF measurements over time. Indeed, during this time period of data accumulation, the values of the parameters entering the parametric models are not constant, which is contrary to the basic hypothesis supporting the approach.
- the estimate of bihemispherical reflectance, which requires computing the integral of the directional hemispherical reflectance over all illumination angles (Martonchik et al. 2000), is not strictly valid if based on reciprocal models and thus assumes that the parameter values entering the model are not a function of the illumination angle (see for instance, Martonchik et al. 1998b and Lucht 1998).
- the extrapolation at other Sun zenith angles of the directional hemispherical reflectance value estimated for one solar position may be unreliable following the argument given in the previous item.
- three-dimensional models should be used for inversion purposes whenever state variables are being retrieved from model inversions to the highest possible accuracy. In other words, one-dimensional radiation transfer models can be adopted in inversion procedures only over targets exhibiting a bowl-shaped anisotropy pattern, possibly using an IPA scheme to approximate solutions to the radiation transfer problem for mixed pixels. Depending on the sensor resolution, the choice of the appropriate model dimension to be applied can, however, hardly be made prior to the analysis of the data.

The interpretation of multiangular data acquired by medium and high spatial resolution sensors permits identifying those regions where a number of data analysis issues must be addressed. By contrast, approaches based on reciprocal models may be sufficient to analyse data for those regions where heterogeneity has not been detected. In other words, although all terrestrial surfaces present a degree of heterogeneity over a range of spatial scales, this fact does not imply *a priori* that the complexity of these surfaces has to be explicitly represented, since this complexity does not significantly influence the measured signal.

C-6 Concluding remarks

This paper stresses a unique capability offered by multiangular information for surface cover monitoring. Our approach is based on a straightforward analysis of the BRF field sampled at red wavelengths, as available from data gathered by AirMISR and the MISR/Terra instruments. Our results strongly support the potential to map a class of surface cover heterogeneity from space data at the subpixel scale resolution, by simply setting a critical limit value for the parameter k_{red} estimated by the inversion of the RPV model; the occurrence of values larger than this limit indicates the very probable presence of a structurally heterogeneous surface. For typical vegetation systems, measurements in the red spectral region permit maximizing the required contrast between the scattering/absorption properties over the vegetation stands versus the underlying soil. Given the resolution of the observing instrument, it was also shown that observation conditions made with low Sun zenith angles favor the detectability of such heterogeneous vegetation. In practice, the processing involved to assess the value of the parameter k is straightforward, as the inversion of the RPV model can easily be made operational as discussed in the accompanying paper.

A series of applications, conducted with AirMISR and MISR data (see part 2), illustrate the potential benefit of exploiting the parameter k in land cover classification since it reveals a different but complementary organization of the landscapes than can be already derived from instantaneous spectral information only. The sensor spatial resolution was shown to be of critical importance for determining the geophysical causes for the heterogeneity. The decrease of the sensor spatial resolution renders the interpretation more complex since it diminishes the relative weight of the information due to individual land cover with respect to each other and with respect to the topographical features as well. In other words, the typical dimensions involved in vegetation land cover type (*e.g.*, height, size and interdistance between trees) imposes a choice of sensor resolutions such that the BRF anisotropic shape can be further interpreted in terms of vegetation cover. No unique resolution thus permits documenting the vegetation

heterogeneity for all surface types, but there is a range of resolutions that maximizes the probability of identifying the presence of architecturally organized plant stands. This issue stresses the need to establish the necessary links between the parameter k and a limited but critical set of descriptors of vegetation cover heterogeneity. As a first step, the approach described in Widlowski et al. (2001b) is very promising.

The exposure of subpixel scale surface heterogeneity from the analysis of an angular signature locates regions for which, at the scale of the investigation, 1) the radiation transfer regime violates the reciprocity principle and 2) inversion procedures applied to retrieve vegetation properties to the highest possible accuracy, *e.g.*, the leaf area index, should be based on three-dimensional radiation transfer models. This capability to detect significantly heterogeneous surfaces is important in the studies of long-term evolution of landscapes. Indeed, it has already been stressed that vegetation structure and its intrinsic dynamics can have a profound effect on ecosystem productivity, a key variable in understanding the vegetation response to climate change (Shugart 2000). On the side of applications, it is noteworthy that this simple approach involving only one spectral band and the estimate of the parameter k , should permit monitoring events such as the occurrence of snow on the ground as happens at the end of the Spring season in Boreal coniferous forests. Many other applications can be foreseen including those dealing with urban sprawl and crop monitoring, for instance.

Our analysis only involves the inversion of the RPV model and the further interpretation of the values of the parameter k . The arguments given in this paper are based on results from a conceptual model that were confirmed by extensive three-dimensional radiation transfer simulations. They provide the rationale for using the parameter k as a new axis of information in addition to the classical spectrally-derived information. This issue is further addressed in the accompanying paper (part 2), which proposes a computer efficient method, optimized for the MISR instrument, to derive jointly information about the photosynthetic activity and the structure of the vegetation. It also addresses the practical issue of decontaminating the parameter k from atmospheric effects thereby allowing its fast estimation directly from data collected by the MISR instrument.

C-7 Acknowledgements

The motivation for this conceptual development demonstrating that a unique information can be extracted from multiangular data analysis came after an informal and stimulating discussion with W. Wiscombe. The application part presented here would not have been possible without the dedicated support from the scientific and technical team in charge of the AirMISR data acquisition and analysis.

Annex D

Characterization of surface heterogeneity detected at the MISR/TERRA subpixel scale.

Jean-Luc Widlowski¹, Bernard Pinty¹, Nadine Gobron¹, Michel M. Verstraete¹
and Anthony B. Davis²

*1: Institute for Environment and Sustainability of the EC Joint Research Centre,
TP 440, I-21020 Ispra (VA), Italy*

*2: Los Alamos National Laboratory, Space and Remote Sensing Group,
Los Alamos, NM 87545, USA.*

Abstract: Vegetation structure can have a significant impact on the degree of anisotropy in the reflected radiation field. With the appropriate characterization of these effects, the analysis of multiangular data, such as provided by the Multi-angle Imaging SpectroRadiometer (MISR) instrument on board TERRA, can yield statistical information about the type of surface heterogeneity that exists at the subpixel scale.

D-1 Introduction

Retrieving information about the state of terrestrial vegetation canopies has typically been restricted to the scale of individual pixels, that is, instantaneous (multi) spectral measurements are treated as if the signal contributing surfaces were composed of a single uniformly distributed cover type. To address the issue of subpixel variability, approaches like the independent pixel approximation (IPA), linearly combine the spectral reflectances of two or more homogeneous end-members [*e.g.*, Cahalan et al. (1994a)]. However, in order to account explicitly for the architecture of spatially heterogeneous vegetation canopies, three-dimensional radiation transfer models need to be employed in the retrieval strategy, [*e.g.*, Widlowski et al. 2001a]. This may deliver realistic canopy architecture representations of the potential surface types, but such approaches are generally computationally-intensive and have yet to provide a means of characterizing the spatial structure of the retrieved vegetation types. Pinty et al. (2000d) recently showed that the analysis of multi-angular reflectance data in the red spectral domain may yield information about the heterogeneity of the surface at the sensor subpixel scale. This approach is exploited by Gobron et al. (2001b) to retrieve information on vegetation activity and structure from the Multi-angle Imaging SpectroRadiometer (MISR) instrument (Diner et al. 1998b) on board EOS-TERRA. In the present work, this radiatively derived surface heterogeneity indicator k will be related to actual

vegetation canopy height fields as characterized by their first-order structure-function (Mandelbrot 1982) and singularity measure (Hentschel and Procaccia 1983) exponents. Although the latter have been amply used in the context of multifractal cloud and rain characterizations, [*e.g.*, Lovejoy and Schertzer 1990], this paper utilizes these statistical indicators solely as tools for pursuing new avenues in understanding how vegetation structure affects the reflectance anisotropy that can be measured by the latest generation of multi-directional instruments, like MISR.

D-2 Canopy height field characterization

Other than topography and the leaf and soil optical properties, the abundance, dimensions and spatial aggregations of dominant vegetation types within the footprint area of a space-borne sensor are the primary modulators of the angular anisotropy in the surface-leaving reflectance field, especially in the red spectral domain. Canopy height measurements may provide a convenient way to quantify the degree of spatial heterogeneity within the field of view of an observing instrument. However, several of the techniques to analyze such data transects, like the auto-correlation and statistical moment analysis, become meaningless if the signal does not exhibit spatial *stationarity*, that is, invariance of statistical properties under translation (Davis et al. 1994b). Others, like Fourier spectrum slopes and semi-variograms may suffer from what has been termed the *ambiguity* of data sets, *i.e.*, very different looking geophysical signals may exhibit identical statistics. Davis et al. (1994b) have argued that the first order structure function exponent H_1 proves sufficient to quantify the non-stationarity of any generic geophysical signal $\phi(x)$:

$$\langle |\phi(x+r) - \phi(x)| \rangle \propto \left(\frac{r}{L}\right)^{H_1} \quad (\ell \leq r \leq L) \quad (\text{D-1})$$

where ℓ is the sampling interval of $\phi(x)$ along the segment $[0, L]$, and $\langle \cdot \rangle$ indicates ensemble averaging over the scale r within the length of the data set L . Bound in the range $[0, 1]$, H_1 allows for an intuitive geometric interpretation of the signal under study: Low values relate to increased roughness (more stationarity) in the data set whereas high values indicate the presence of smoothness (more non-stationarity).

However, like the fractal dimension, H_1 becomes an ambiguous descriptor of the variability in the case of multi-affine signals. In order to remove this indetermination Davis et al. (1994b) proposed to additionally characterize the role of *intermittency* in the observed signal. This can be achieved using different flavors of ‘singularity analysis’ to define a hierarchy of exponents from which the intermittency descriptor C_1 can be derived (Schertzer and Lovejoy 1987). Like H_1 , C_1 is confined to the range $[0, 1]$. At $C_1 = 0$ the data exhibit no intermittency but similar variability everywhere (*e.g.*, Gaussian processes), whereas $C_1 = 1$ relates to highly singular occurrences of variability (*e.g.*, random Dirac delta functions). In the latter, extremely intermittent case, the occurrence of dominant signal variations may be characterized as being ‘sparse’ whereas in the former case it is ‘dense’. Analyzing H_1 and C_1 has proven useful in a variety of geophysical situations, [*e.g.*, Marshak et al. 1997].

To gather the necessary canopy height data, the model of Govaerts and Verstraete (1998) was used to generate various 3-D vegetation canopy representations at the nominal ground resolution of the MISR instrument. The sampling interval of the subsequent height measurements ($\ell \simeq 25$ cm), was chosen such as to be greater than the characteristic scale of the leaves, yet smaller than the typical dimension of the tree crowns or the gaps in between them. 40 transects of equal length (2^{10} data points) but with different origins and orientations were sampled. For each of these, the H_1 , C_1 statistics were computed in the small scale limit following the approach of Davis et al. (1994b). The structure functions were fitted (on a log-log plot) from scale $\eta = \ell$ to the first detected scale break (~ 1 – 2 orders of magnitude), or, in its absence, through all the data. C_1 was computed from a normalized absolute gradient field of step size η . Ultimately, these H_1 , C_1 statistics were ensemble averaged to yield a directionally independent estimate of the non-stationarity $\langle H_1 \rangle$ and intermittency $\langle C_1 \rangle$ of the vegetation height at the resolution of the MISR pixel (275 m). Tests have indicated that the actual values of these ensemble averaged statistics vary, from ~ 0.02 at high values to ~ 0.05 at low values of vegetation coverage, if different sets of transects were selected.

In the context of this paper, radiatively homogeneous canopies refer to surface conditions where the bidirectional reflectance factor (BRF) fields produced by plane-parallel radiative transfer (RT) models

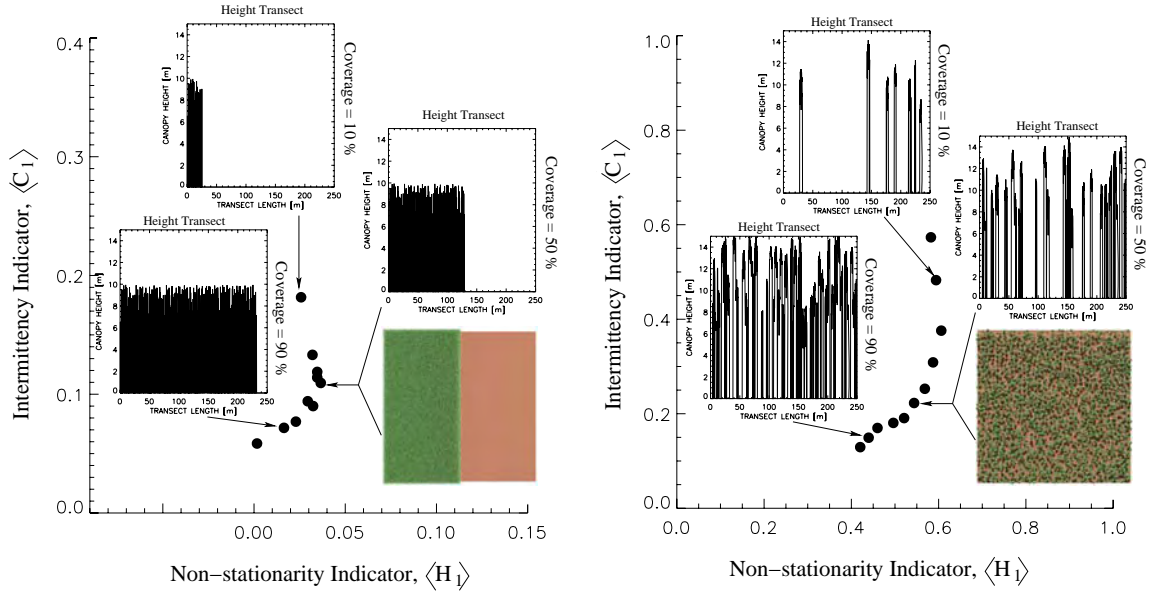


Figure D-1: $\langle H_1 \rangle, \langle C_1 \rangle$ statistics for various canopies of different vegetation coverage. The left (right) panel refers to radiatively homogeneous (heterogeneous) vegetation canopies. Typical height transects of the low (10%), medium (50%) and high (90%) vegetation covers as well as a graphical representation of the intermediate cases are presented.

(together with the IPA) are indiscernible from those generated by a full 3-D RT models. Thus, in Figure D-1, the $\langle H_1 \rangle, \langle C_1 \rangle$ statistics for radiatively homogeneous (left) and heterogeneous (right) vegetation canopies are shown. Typical height transects of the low, medium and high vegetation coverages as well as a graphical representations of the intermediate case are presented. For the documented simulations intermittency naturally decreases with increasing vegetation cover. Non-stationarity, on the other hand, tends to be highest at low to medium vegetation coverages, decreasing at very low coverages due to most transects showing only a few jumps, and also at very high coverages because here stationarity is asymptotically approached (*i.e.*, height-transects and white-noise graphs start looking alike). For radiatively homogeneous vegetation canopies the non-stationarity and intermittency descriptors are remarkably lower than for their heterogeneous counterparts. These findings suggest the ability of $\langle H_1 \rangle, \langle C_1 \rangle$ to characterize different vegetation structures through their corresponding canopy height fields. Figure D-2 corroborates this by documenting the differing intermittency and non-stationarity behaviors of such diverse biome types as **A**, low density deciduous forest of increasing coverage (left to right), **B**, evergreen boreal forest of increasing stand density (top to bottom) and **C**, closed rainforest of equal leaf content and decreasing canopy depth (left to right), for example (Widlowski et al. 2001a).

D-3 Combining canopy height field and reflectance anisotropy descriptors

The angular anisotropy of a surface exiting radiation field in the optical domain can be partly qualified with the Minnaert function parameter, k , of the RPV model (Pinty et al. 2000d). If sufficient spectral contrast exists between the (darker) canopy foliage and the underlying (brighter) ground cover, different types of vegetation structure yield different BRF fields. Figure D-3 shows typical examples of homogeneous (left) and heterogeneous (right) vegetation canopy BRFs in the cross plane. The reflectance field of homogeneous canopies can either be generated using explicit 3-D RT models or equivalently by combining the radiances generated with 1-D plane-parallel RT models using the IPA approach. These BRFs may be characterized by a *bowl-shape* and k values less than 1. For heterogeneous canopies, where the visible (relatively bright) soil fraction decreases from nadir to oblique viewing angles, the corresponding BRF shapes may be *bell-shape* in which case the k value is greater than 1. The latter obviously depends on the foliage orientation, distribution and density, the optical properties of both the leaves and the ground, as well as the illumination angle and the field of view of the sensor.

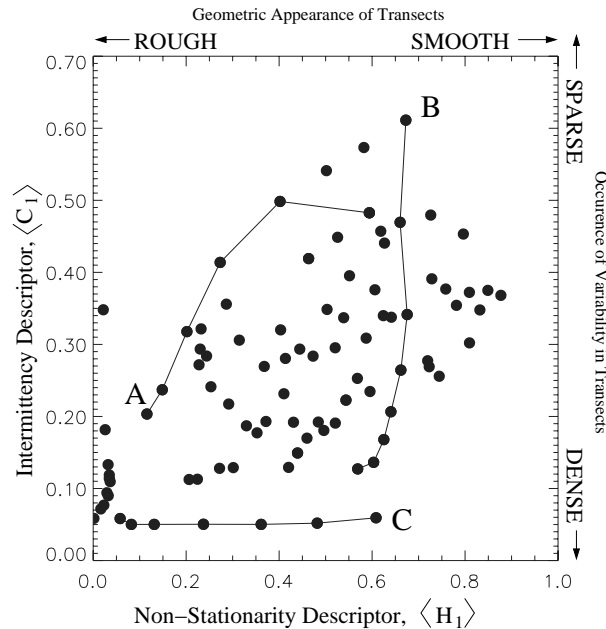


Figure D-2: $\langle H_1 \rangle, \langle C_1 \rangle$ statistics for a large variety of different vegetation canopies, *e.g.*, **A:** low density deciduous forest of increasing coverage (left to right), **B:** boreal forest of increasing stand density (top to bottom), **C:** closed rainforest of decreasing canopy depth (left to right) and equal leaf content.

Simulating the reflectance fields in the red band and at the nominal ground resolution of MISR allows one to retrieve the radiative anisotropy quantifier k for all of the vegetation types characterized in Figure D-2. The BRDF modelling was performed with the Raytran model of Govaerts and Verstraete (1998) for a solar zenith angle of 30° , uniform leaf angle distributions, Lambertian scattering properties of both soil and leaves, and leaf reflectance (transmittance) values of 0.055 (0.015) and 0.127 for the soil albedo. In Figure D-4, the value of k was discriminated with colour against the corresponding $\langle H_1 \rangle$, $\langle C_1 \rangle$ statistics. Shown in red (blue) are all canopy types that generate bowl-shaped (bell-shaped) reflectance fields with $k \leq 1.05$ ($k > 1.05$). Given the simulated conditions a remarkable pattern of organisation can be observed: only the presence of vertically elongated foliage clumps (tree crowns) of medium to high densities can generate bell shaped BRDF fields. Sparse tree coverage and closed vegetation canopies, on the other hand, will have a value of k that is generally less than 1. Thus, based on spectral signatures and the retrieved values of k (Gobron et al. 2001b), it is envisaged that the vegetation structure at the sub-pixel scale of the observing instrument may be deduced (under appropriate sampling conditions) from a set of predefined $\langle H_1 \rangle$, $\langle C_1 \rangle$ statistics, corresponding to typical configurations of the most likely biome types to be encountered within the region of study.

D-4 Conclusion

It has been shown that vegetation canopy structure may be characterized in the small scale limit by non-stationarity ($\langle H_1 \rangle$) and intermittency ($\langle C_1 \rangle$) exponents using an ensemble of canopy height transects of different orientations and origins. More importantly, the reflectance anisotropy quantifier k , obtained by inversion of the parametric RPV model against multiangular terrestrial surface observations, when used in conjunction with the corresponding $\langle H_1 \rangle$, $\langle C_1 \rangle$ statistics, allows to identify specific types of vegetation that are characterized by medium-dense accumulations of vertically elongated foliage clumps. Therefore, if sufficient spectral contrast exists between the (darker) leaves and (brighter) ground cover in the red, k may be employed (in conjunction with spectral information and under appropriate sampling conditions) to characterize the underlying vegetation structure at the scale of the MISR subpixel resolution.

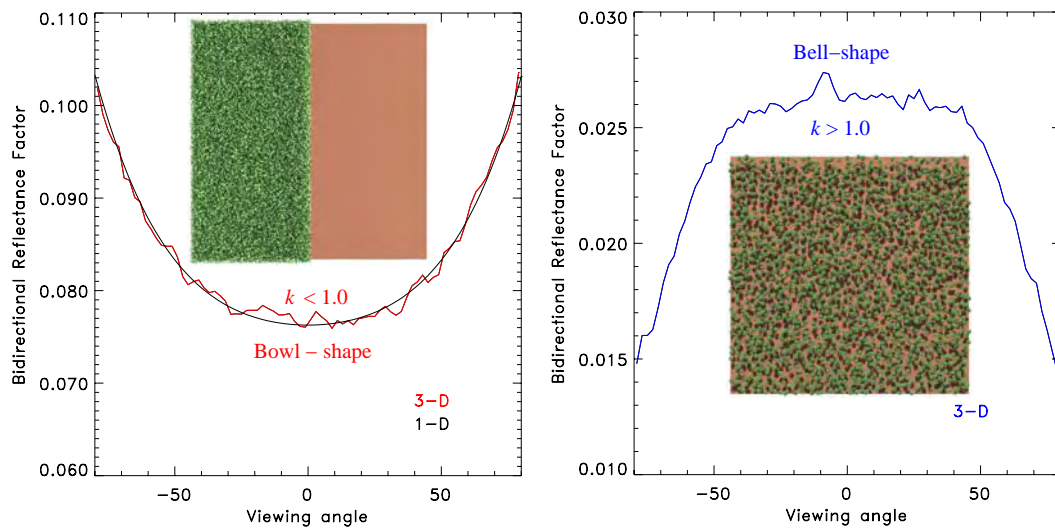


Figure D-3: Typical BRF anisotropy in the red spectral domain for radiatively homogeneous (left) and heterogeneous (right) vegetation canopies. The BRFs of the homogeneous surface are generated using a 3-D RT model and typified by a bowl-shape ($k < 1$). The BRFs of the heterogeneous surface covers are generated using a 3D RT model and a 1D IPA approach, and are generally bowl-shaped ($k < 1$).

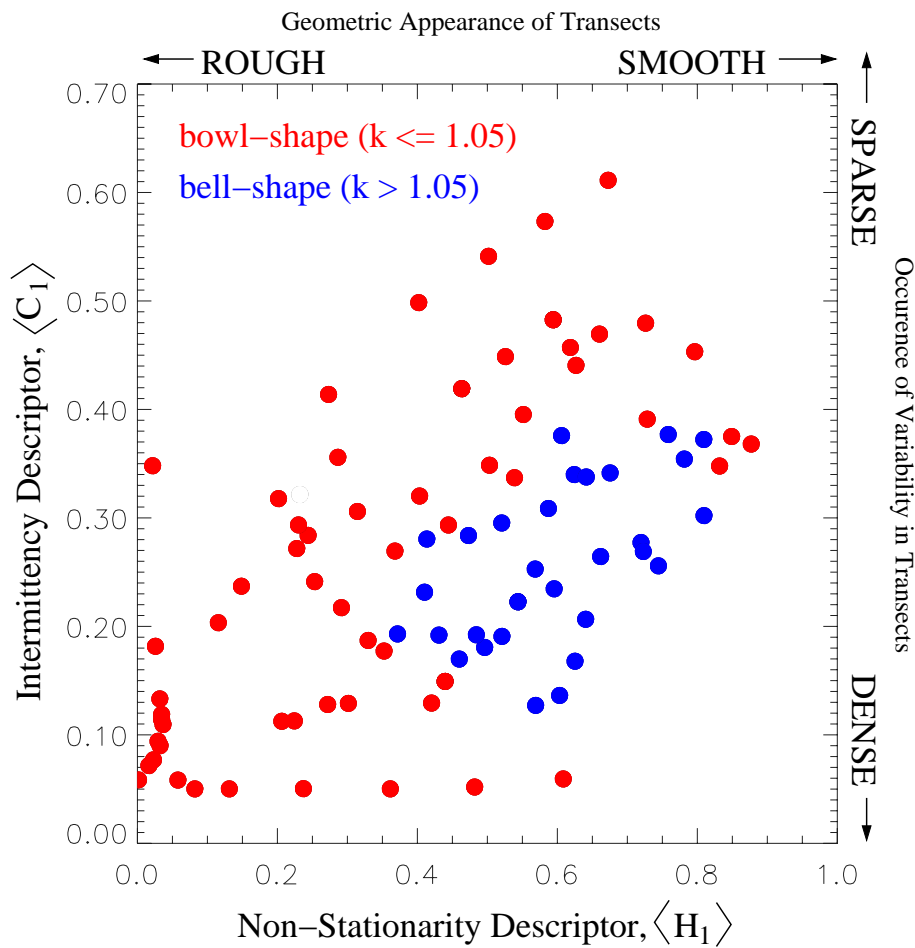


Figure D-4: $\langle H_1 \rangle, \langle C_1 \rangle$ statistics for a large variety of different vegetation canopies overlaid by their corresponding reflectance anisotropy quantifier, k . Shown in red (blue) are all canopy types that generate bowl-shaped (bell-shaped) reflectance fields *e.g.*, $k \leq 1.05$ ($k > 1.05$).

Curriculum Vitæ

PERSONAL DETAILS:

Name: Widlowski Jean-Luc
Date of Birth: 14th July 1969
Nationality: luxembourgish

EDUCATION:

- Since Oct 98:* Institute of Geography, University of Fribourg (Switzerland): Conducting research in the framework of a Ph.D. thesis on **extracting quantitative subpixel-heterogeneity information from optical remote sensing data.**
- Oct 94 - Sep 95:* Department of Meteorology, University of Edinburgh (UK): **Masters of Science** degree with *Distinction* in '**Remote Sensing and Image Processing Technology**'.
- Oct 89 - Jun 94:* Department of Physics, University of Newcastle upon Tyne (UK): *First Class Bachelor of Science* degree with Honours in '**Geophysics and Planetary Physics**'.
- Sep 84 - Jul 88:* Lycée Technique du Centre, Luxembourg: *Diplôme de fin d'études secondaires techniques* in **Applied Chemistry**.

PUBLICATIONS:

Refereed Journals

Gobron N., B. Pinty, M. M. Verstraete, and J.-L. Widlowski (2000). Advanced Spectral Algorithm and New Vegetation Indices Optimized for Up Coming Sensors: Development, Accuracy and Applications., *IEEE Transactions on Geoscience and Remote Sensing*, 36, 2489-2505.

Gobron N., B. Pinty, M. M. Verstraete, and J.-L. Widlowski (2001). Uniqueness of Multi-angular Information - Part 2: Joint Retrieval of Vegetation Structure and Photo-synthetic Activity from MISR, *IEEE Transactions on Geoscience and Remote Sensing*, MISR special issue, submitted.

Pinty B., N. Gobron, J.-L. Widlowski, S. A. W. Gerstl, M. M. Verstraete, M. Antunes, C. Bacour, F. Gascon, J.-P. Gastellu, N. Goel, S. Jacquemoud, P. North, W. Qin, and R. Thompson (2000). The Radiation Transfer Model Intercomparison (RAMI) Exercise, *Journal of Geophysical Research*, 106, 11937-11956.

Pinty B., J.-L. Widlowski, N. Gobron, M. M. Verstraete (2001). Uniqueness of Multi-angular Information - Part 1: A Surface Heterogeneity Indicator from MISR, *Journal of Geophysical Research*, MISR special issue, submitted.

Widlowski J.-L., Pinty B., N. Gobron, and M. M. Verstraete (2001). Detection and characterization of boreal coniferous forests from remote sensing data, *Journal of Geophysical Research*, in print.

Widlowski J.-L., Pinty B., N. Gobron, M. M. Verstraete and A. B. Davies (2001). Characterization of Surface Heterogeneity Detected at the MISR/TERRA Subpixel Scale, *Geophysical Research Letters*, in print.

Proceedings, Reports and Book chapters

Gobron N., F. Mélin, B. Pinty, M. M. Verstraete, J.-L. Widlowski, and G. Bucini (2000). A Global Vegetation Index for SeaWiFS: Design and Applications, in *Satellite Remote Sensing and Climate Modelling: Synergies and Limitations*, Eds. M. Beniston and M. M. Verstraete, Kluwer Academic Publishers, Dordrecht, The Netherlands, pp 5-21.

Gobron N., B. Pinty, M. M. Verstraete, and J.-L. Widlowski (2000). Development of spectral indices optimized for the VEGETATION Instrument, pp 275--280, *Proceedings of VEGETATION 2000*, Belgirate, Italy, 3-6 April.

Gobron N., B. Pinty, M. M. Verstraete, F. Mélin, J.-L. Widlowski, and G. Bucini (2000). An Approach to develop global Vegetation Indices decontaminated from geometric effects: Applications on the series of up-coming instruments, *Second International Workshop on Multiangular Measurements and Models (IWMMM2)*, 15-17 September 1999, Ispra (VA), Italy.

Gobron, N., B. Pinty, J.-L. Widlowski, M. M. Verstraete and D. J. Diner (2001). Joint Retrieval of Vegetation Structure and Photosynthetic Activity from MISR, *IGARSS 2001*, Sydney, Australia, July 9-13.

Pinty B., J.-L. Widlowski, N. Gobron, M. M. Verstraete (2000). Monitoring Boreal Forest Resources in Northern Europe - Final Report, Technical Report, EC Joint Research Centre.

Pinty, B., J.-L. Widlowski, N. Gobron, D. Diner, A. B. Davies, and M. M. Verstraete (2001). Detection of Land Surface Structure and Heterogeneity from Multiangle Remote Sensing Data, *4th International GEWEX conference*, Institut Pierre Simon Laplace, Collège de France, Paris, France, 10-14 September

Verstraete M. M., Pinty B., N. Gobron, and J.-L. Widlowski (2000). Development of spectral indices optimized for the VEGETATION Instrument - Phase 2, Final report, Technical Report, EC Joint Research Centre.

Widlowski J.-L., D. W. Gulik, and C. Best (1998), Z39.50 Search interface in GELOS, published in: J. STROBL and C. BEST (Eds.), *Proceedings of the Earth Observation & Geo-Spatial Web and Internet Workshop '98*, Salzburger Geographische Materialien, Volume 27. Institut für Geographie der Universität Salzburg. ISBN: 3-85283-014-1.

Widlowski J.-L., B. Pinty, N. Gobron, and M. M. Verstraete (2000). Monitoring Boreal Forest Resources in Northern Europe, *Proceedings of VEGETATION 2000 Symposium*, Belgirate, Italy, 3-6 April.

WORKING EXPERIENCE:

Sep 88 - Apr 89: R&D Laboratories, Heintz van Landewijck, Luxembourg: Development of **gaschromatographical methodologies** for the determination of pesticides and menthol.

Oct 95 - May 96: Institute of Building Science, **Federal Institute of Technology**, Zurich, Switzerland: Development and implementation of an image processing software enabling the **classification of pedestrian level wind comfort regimes** within urban areas.

Nov 96 - Dec 97: Computer Research International, Italy: Administration, population and development of the G7-ENRM web-server which aimed at providing on-line information about Environment and Natural Resource Management data.